



The
University
Of
Sheffield.



EPSRC CENTRE FOR DOCTORAL TRAINING
NEW AND SUSTAINABLE
PHOTOVOLTAICS

Developing Industrially Relevant Processing Techniques for Perovskite Solar Cells

Elena Josephine Cassella

A thesis submitted in partial fulfilment of the requirements for the degree of
Doctor of Philosophy

The University of Sheffield
Faculty of Science
Department of Physics and Astronomy

November 22

Declaration of Originality

This thesis summarises the work undertaken during my time in the Department of Physics and Astronomy at the University of Sheffield – from October 2018 until November 2022.

I, the author, confirm that the Thesis is my own work. I am aware of the University's Guidance on the Use of Unfair Means (www.sheffield.ac.uk/ssid/unfair-means). This work has not previously been presented for an award at this, or any other, university. The contributions of my collaborating authors for each publication are described at the appropriate locations within the chapter/publication forewords.

Abstract

This thesis presents a series of technological innovations which show significant promise towards realising an industrially-feasible route to manufacture spray-coated perovskite solar cells (PSCs).

Hybrid metal halide perovskites have very recently emerged as an extremely promising material for photovoltaic (PV) applications. Such perovskites have opened the door to a potential future of sustainable, high-throughput, and low-cost manufacture of solar cells, which will support the expansion of solar deployment and propel the global energy transition towards Net-Zero goals. In order to achieve this, perovskites must concurrently satisfy the golden triangle of PV technologies: high-efficiency, appropriate stability, and commercially viable costs. Whilst there have been many demonstrations of PSCs that achieve market-competitive efficiencies, and that satisfy a number of the International Electrotechnical Commission (IEC) standards, such devices are typically only fabricated over small areas ($< 1 \text{ cm}^2$) via spin coating. Clearly, there must be a transition from “lab to fab,” and PSCs satisfying the golden triangle should be developed using scalable fabrication techniques.

Spray coating is a painting technique now widely used across a huge number of industries. A critical factor dictating the economic viability of perovskite-based PV technologies is the manufacturing throughput speed. Here, spray coating offers very high deposition speeds for a continuous roll-to-roll (R2R) manufacturing process. R2R production is extremely industrially relevant, reducing production costs through the “economy of scale.” Therefore, the R2R production of PSCs is a key objective to realise cost-effective manufacture. The core focus of this thesis is the development of new processes to ultrasonically spray coat efficient PSCs in a manner compatible with R2R manufacturing.

In the first chapter, a new technique is developed to induce crystallisation of the spray-cast perovskite, replacing the typically used processes which are limited to batch-manufacturing. Here, an air-knife attached to a spray gantry creates a gas-jet which induces evaporation of the casting solvent and, accordingly, nucleation. A protocol for the spray deposition of a high-quality, self-assembled molecular hole-transporting layer (MeO-2PACz) is also developed. The combination of these techniques is then used to create state-of-the-art spray-coated PSCs.

To build upon this work, and considering the criticality of device stability, a spray-coated perovskite composition avoiding the use of thermally unstable methylammonium (MA) was also developed. Here, the gas-assisted spray processing technique was used to successfully fabricate a CsFA-based (where FA is formamidinium) perovskite. Such perovskites are typically limited in efficiency due to a high density of defects arising from the poor crystalline quality. Further gains in efficiency were realised by the development of a spray-coated surface-passivating treatment to reduce nonradiative recombination at the perovskite/ charge-transporting layer interface.

The final chapter returns to spin coating in order to address a critical fabrication-speed consideration: typically, both the perovskite active layer and charge-transporting layers require lengthy annealing times which significantly diminish the effective process speed of PSC manufacture. Here, a binary solvent system is engineered to circumvent the post-deposition annealing of the perovskite layer. An annealing-free self-assembled molecular hole-transporting layer is then incorporated into devices, creating fully annealing-free PSCs having stabilised power conversion efficiencies of up to 17%.

Table of Contents

Introduction	11
1.1 Lighting the Way: The Role of Solar in the Pathway to Net-Zero	11
1.2 Thesis Motivation.....	16
1.3 Thesis Overview	16
1.4 References.....	17
Background Theory	19
2.1 Basic Principles of Solar Cells.....	19
2.2 A Decade (and a bit) of Perovskite Solar Cells.....	24
2.3 Solution Processing of Perovskite Solar Cells.....	29
2.4 Materials	40
2.5 Anti-reflective coatings	42
2.6 Characterisation Techniques.....	43
2.7 References.....	46
Experimental Methods	55
3.1 Introduction	55
3.2 Materials	55
3.4 Device Fabrication.....	56
3.5 Device Characterisation	60
Gas-Assisted Spray Coating of Perovskite Solar Cells Incorporating Sprayed Self-Assembled Monolayers	64
4.1 Publication Foreword	64
4.2 Author Contributions.....	65
4.3 Publication Main Text	66
Spray Deposition of an Alkyl-Ammonium Halide Passivating Agent for Spray-Coated, Methyammonium-Free Perovskite Solar Cells	98
5.1 Publication Foreword	98
5.2 Author Contributions.....	99

5.3	Publication Main Text.....	100
A Binary Solvent System Used to Fabricate Fully Annealing-Free Perovskite Solar Cells		127
6.1	Publication Foreword.....	127
6.2	Author Contributions.....	128
6.3	Publication Main Text.....	129
Conclusions and Further Work.....		163

Presentations and Publications

Poster Presentations

Centre for Doctoral Training in New and Sustainable Photovoltaics Showcase Event 2019:
“Integrating perovskite photovoltaics with carbon fibre” (*Bath, UK*).

Centre for Doctoral Training in New and Sustainable Photovoltaics Showcase Event 2021: “Next generation spray-coated perovskite solar cells” (*Sheffield, UK*).

Conference on Hybrid and Organic Photovoltaics (HOPV) 2022:
“Spray-coated self-assembled monolayers” (*Valencia, Spain*).

Centre for Doctoral Training in New and Sustainable Photovoltaics Alumni Event 2022: “Next generation spray-coated perovskite solar cells” (*London, UK*). **Poster prize.**

Publications

Cassella, E. J.; Thornber, T.; O’ Kane, M. E.; Spooner, E. L. K.; Albariqi, I.; Blackburn, D.; Kilbride, R.; Routledge, T. J.; Game, O. S.; Lidzey, D. G. **Spray Deposition of an Alkyl-Ammonium Halide Passivating Agent for Spray-Coated, Methylammonium-Free Perovskite Solar Cells**, *In Preparation [Target Journal: Adv. Mater., Target Submission Date: July 2023]*

Cassella, E. J.*; Spooner, E. L. K.*; Catley, T. E.; Lidzey, D. G. **Air-Knife Assisted Spray Coating of Organic Solar Cells**, *Under Review [ACS Appl. Mater. Interfaces, Submitted March 2023]* (*Authors contributed equally)

Game, O. S.; Thornber, T.; Cepero-Mejias, F.; Infante-Ortega, L. C.; **Cassella, E. J.;** Kilbridge, R. C.; Isherwood, P. J. M.; Fairclough, P.; Walls, J. M.; Lidzey, D. G. **Direct Integration of Perovskite Solar Cells with Carbon Fibre Substrates**, *[Adv. Mater, Accepted March 2023]*

Cassella, E. J.; Spooner, E. L. K.; Smith, J.A.; Thornber, T.; O’ Kane, M. E.; Choudhary, S.; Wood, C.J.; Hammond, D.B.; Snaith, H.J.; Lidzey, D. G. **Binary Solvent System Used to Fabricate Fully Annealing-Free Perovskite Solar Cells**, *Adv. Energy Mater.* 2023, 13, 2203468.

T. Thornber, O. S. Game, **E. J. Cassella**, M. E. O’Kane, J. E. Bishop, T. J. Routledge, T. I. Alanazi, M. Togay, P. J. M. Isherwood, L. C. Infante-Ortega, D. B. Hammond, J. M. Walls, D. G. Lidzey, **Nonplanar Spray-Coated Perovskite Solar Cells** *ACS Appl. Mater. Interfaces* 2022, 14, 37587

Blackburn, D.; Routledge T.J.; O’Kane M.E.; **Cassella E.J.**; Game O.S.; Catley T.E.; Wood C.J.; McArdle T.; Lidzey D.G. **Low-Temperature, Scalable, Reactive Deposition of Tin Oxide for Perovskite Solar Cells**, Solar RRL 2022, 6, 2200263

Cassella, E. J.; Spooner, E. L. K.; Thornber, T.; O’Kane, M. E.; Catley, T. E.; Bishop, J. E.; Smith, J. A.; Game, O. S.; Lidzey, D. G. **Gas-Assisted Spray Coating of Perovskite Solar Cells Incorporating Sprayed Self-Assembled Monolayers**. Adv. Sci. 2022, 2104848.

O’Kane, M. E.; Smith, J. A.; Alanazi, T. I.; **Cassella, E. J.**; Game, O.; Meurs, S. van; Lidzey, D. G. **Perovskites on Ice: An Additive-Free Approach to Increase the Shelf-Life of Triple-Cation Perovskite Precursor Solutions**. ChemSusChem 2021, 14 (12), 2537–2546.

Smith, J. A.; Game, O. S.; Bishop, J. E.; Spooner, E. L. K. K.; Kilbride, R. C.; Greenland, C.; Jayaprakash, R.; Alanazi, T. I.; Alanazi, T. I.; **Cassella, E. J.**; Tejada, A.; Tejada, A.; Chistiakova, G.; Wong-Stringer, M.; Routledge, T. J.; Parnell, A. J.; Hammond, D. B.; Lidzey, D. G. **Rapid Scalable Processing of Tin Oxide Transport Layers for Perovskite Solar Cells**. ACS Appl. Energy Mater. 2020, 3 (6), 5552–5562.

List of Abbreviations

PV – Photovoltaics

PSC – Perovskite solar cell

R2R – Roll-to-roll

MA – Methylammonium

FA – Formamidinium

LCOE – Levelised Cost of Electricity

EPBT – Energy payback time

BoS – Balance of systems

TCO – Transparent conductive oxide

ITO - Indium tin oxide

FTO – Fluorine-doped tin oxide

HTL – Hole-transporting layer

ETL – Electron-transporting layer

DMF – Dimethyl formamide (solvent)

DMSO – Dimethyl sulfoxide (solvent)

NMP – N-methyl-2-pyrrolidone (solvent)

AM1.5 – Air mass 1.5 (spectrum)

EQE – External quantum efficiency

J-V – Current-density

XRD – X-ray diffraction

SEM – Scanning electron microscopy

GIWAXS – Grazing incidence wide-angle X-ray scattering

SAM(s) – Self-assembled monolayer(s)

VASP – Vacuum-flash assisted solution processing

GASP – Gas-assisted spray processing

Introduction

1.1 Lighting the Way: The Role of Solar in the Pathway to Net-Zero

Humans account for just 0.01% of life, yet we have systematically destroyed 80% of wild animals and 50% of plants.^[1] We have increased the CO₂ levels in the atmosphere more effectively than any other planetary event in at least 66 million years.^[2] The Intergovernmental Panel on Climate Change (IPCC) was formed in 1988, comprising of international experts who volunteer their time to analyse the literature and create a number of reports on the drivers of climate change, its expected impact and risks, and how we might expect to mitigate and adapt to such risks. Unfortunately, since the IPCC formed, we have released more CO₂ into the atmosphere than throughout the rest of human history combined.^[3] The 2022 “Mitigation of Climate Change” report by the IPCC’s Working Group III for the Sixth Assessment Report delivers a damning conclusion: the current Nationally Determined Contributions (NDCs) are likely insufficient to limit global warming below the 1.5 °C necessary to avoid catastrophic and irreversible changes.^[4,5] Immediate and extensive emissions reductions are needed in order to achieve net-zero carbon emissions by 2050 and stabilise global temperatures.

Here, the World’s energy system must be fundamentally overhauled and decarbonised. Of the available renewable energy sources, solar power makes an extremely compelling case. Solar power is abundant, annually providing a renewable energy source which exceeds the total annual human energy consumption.^[6] Solar power is safe, clean, and reliable. Solar power is cost competitive, as will be discussed further below. Most notably, solar power can be uniquely deployed at multiple levels across the grid – or even off-grid – and ameliorate a huge number of energy-intensive activities. Solar photovoltaics (PV) can be deployed at utility-scale power stations, as rooftop systems to provide for households at the point-of-use, or as small-scale devices powering the “Internet of Things”. As global temperatures continue to rise, mass-deployed cooling systems will become a pertinent contributor to climate change; one in which could be

alleviated by solar PV integration with cooling systems.^[7] Similarly, integration of solar PV with building windows can assist in temperature regulation, reducing the initial demand for cooling systems. Combining the use of land for both energy generation and food production – a field known as “Agrivoltaics” – has started to show a promising synergy.

Not only is there both an opportunity and critical need for solar power, but also a strong economic case. The Levelised Cost of Electricity (LCOE) is a figure of merit comparing the ratio of the total cost of electrical production against the rate of electrical energy generation. Whilst the LCOE of incumbent fossil-fuel technologies is only a few cents per kWh, there is little room to further reduce this value in such mature technologies. Conversely, the solar “experience curve” demonstrates a 20% reduction in the average cost of installing 1 MW of solar PV, every time that the installed solar capacity is doubled.^[8] Representing only 2.4 % of total energy generation in the UK in Q1 of 2022, there is clearly still plenty of room for further reductions in price as solar technologies scale up.^[9]

Crystalline silicon-based solar panels continue to dominate the market, holding a 95% majority of worldwide solar energy production.^[10] The large Earth-abundance of silicon has facilitated over half a century of research, which has achieved a peak cell efficiency of just over 26%.^[11] Silicon solar cells are regarded as the “first generation” of solar technologies. Nevertheless, there are significant drawbacks to silicon as a photovoltaic material. Relatively thick absorber layers are required due to the indirect bandgap. Further, the bandgap is narrow and leads to a large degree of thermalisation losses. The manufacture of “solar grade” silicon requires high-grade precursor materials for the Czochralski process, which requires temperatures above the melting point of silicon (1,425 °C).^[12] As a result of this, further decreases in module production costs, and therefore the LCOE, are limited by such high energy requirements. The Energy Payback Time (EPBT) refers to the amount of time it takes for a module to recoup the equivalent amount of energy that it took to produce the module. Whilst the EPBT of silicon solar modules has decreased by 12.8% over the last 24 years,^[10] the energy-intensive manufacturing process again limits any further improvements.

Such drawbacks of silicon-based technologies drove the emergence of “second generation” photovoltaics, namely thin-film technologies such as cadmium telluride (CdTe), copper indium gallium diselenide (CIGS), and amorphous-silicon (a-Si). With a

higher absorption coefficient than silicon, these materials allow the production of cells and modules with thinner absorber layers – hence “thin-film” technologies. Despite demonstrating lower EPBTs, such second generation technologies hold only a 5% market share. This is attributed to the continued lower overall price of silicon cells, presumably driven by their larger market scale due to technological maturity.

Further improvements in LCOE and EPBT values are now mostly expected from so-called “third generation” solar technologies. This generation encompasses a number of emerging technologies including perovskite solar cells, organic solar cells; quantum dot solar cells; dye-sensitised solar cells; copper zinc tin selenide (CZTS) cells, and derivatives thereof; and more advanced concepts expected to overcome the theoretical efficiency limit, such as multijunction solar cells.

Perovskite solar cells (PSCs) are a disruptive third generation technology which have dramatically redirected the photovoltaic field. Since their emergence in 2009, cell efficiencies for single-junction devices have increased from 3.9% to 25.7% at the time of writing.^[11,13] The National Renewable Energy Laboratory (NREL) produces a chart mapping the best performing cells from each solar technology (**Figure 1.1**). Here, it can be clearly seen that the gradient of the “Cell Efficiency” developments curve of both PSCs and perovskite/Si tandems have outpaced all other solar materials, so far. PSCs have a rare combination of optoelectronic properties that are extremely favourable for solar devices. Further, PSCs hold the promise for low-cost, facile manufacture of cells with market-competitive efficiencies, thereby presenting a clear opportunity for commercialisation. However, long-term stability of the perovskite absorber remains a significant challenge for the field. Currently, the operational lifetime of PSCs prevents sufficiently low LCOE values and remains a significant barrier to market entry.

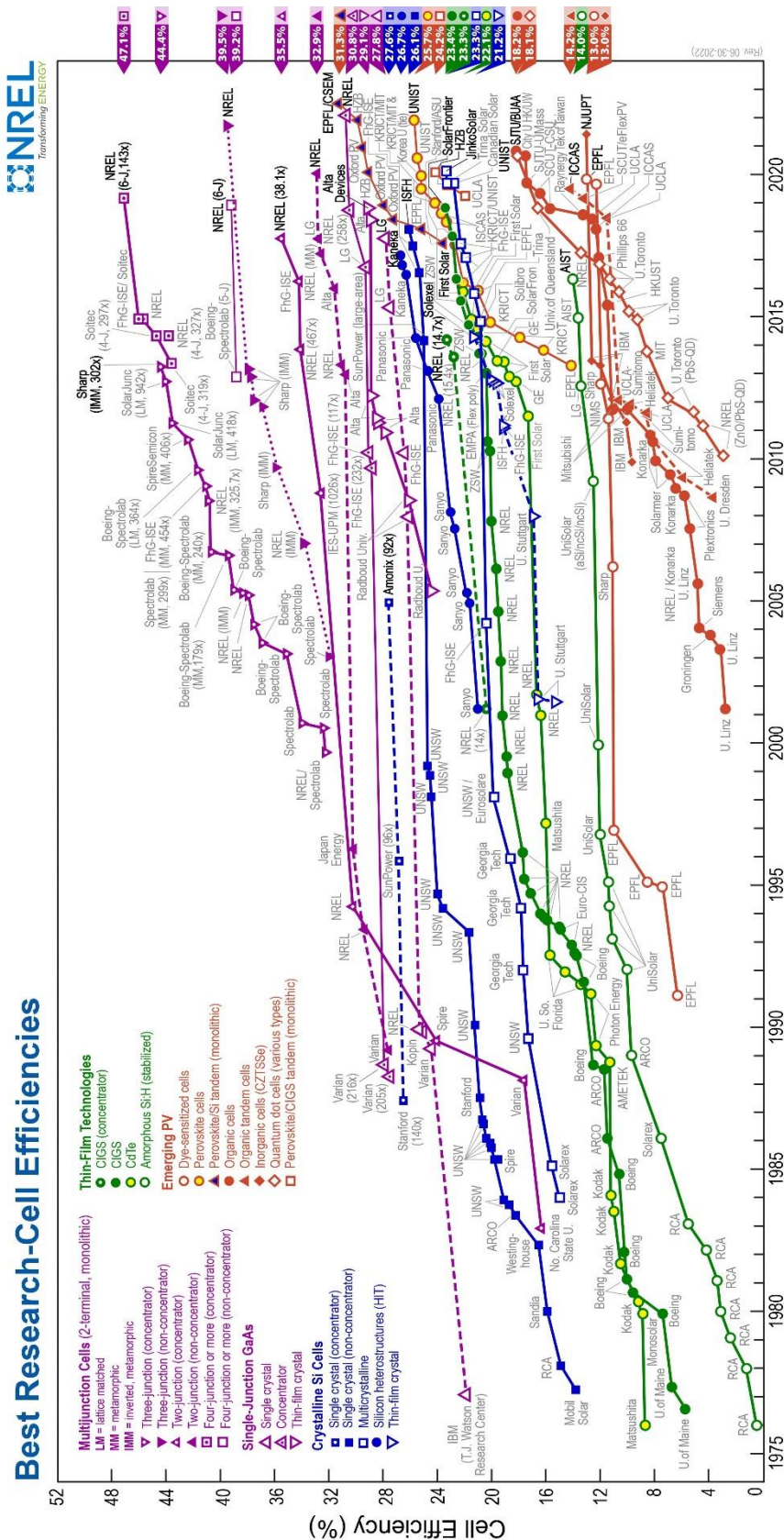


Figure 1.1: The National Renewable Energy Laboratory “best research-cell efficiency chart” (Accessed August 2022).^[1]

Moreover, whilst the device efficiencies of PSCs are competitive with commercial cells, such demonstrations are only for laboratory-scale cells – typically $< 1 \text{ cm}^2$. The field is now moving to develop such competitive efficiencies at competitive scales. The solution-processable nature of PSCs (and other third generation technologies) opens the door to high-throughput, roll-to-roll (R2R) manufacture. Here, a continuous web of flexible substrate is fed through a coating system allowing high-speed, high-volume production. R2R printing is the “holy grail” of cost-effective printing and is considered a key target for the PV community. Unfortunately, the cell-to-module losses remain significant for perovskite-based technologies. The current state-of-the-art perovskite minimodule delivers only ~ 21.4% efficiency with an active area of just 19.32 cm^2 ,^[14] whilst an 804 cm^2 module delivers only 17.9% efficiency.^[15]

In order to demonstrate the economic viability of PSCs, deposition techniques to scale up PSC manufacture must now also demonstrate cost-effective, market-competitive efficiencies. Whilst a number of scalable deposition techniques exist, each has its own respective merits and drawbacks. Amongst these techniques, spray coating has emerged as a technique capable of achieving unparalleled deposition speeds.^[16] Despite this, progress has been limited in this research area, with state-of-the-art spray-coated device efficiencies falling behind those of other scalable technologies. This technological lag is attributed to the complexity of the spray coating process, as will be discussed in further detail. Considering the extremely strong correlation between the economics of solar cell manufacturing and production throughput speed, spray coating remains a technique worthy of further research interest.

1.1. Thesis Motivation

The aim of this thesis is to develop five industrially-relevant technologies for the fabrication of PSCs, taking inspiration from technologies which are driving the high-performance of spin-coated PSCs. These five technologies are spray-coated self-assembled molecules; a gas-quenching technique to control the crystallisation of spray-coated perovskite thin-films; solvent-engineering of the spray-coated precursor ink to facilitate wetting onto the self-assembled molecules; a spray-coated surface passivation treatment; and the development of a highly-volatile precursor ink to facilitate room-temperature crystallisation of an MAPbI_3 perovskite. Whilst an enormous opportunity exists for PSCs to aid in the global energy transition, commercial feasibility is dictated by the “golden triangle” of solar technologies.^[17] The power conversion efficiency must be high, production should be inexpensive, and the lifespan should be suitable for the deployment purpose. The works presented within this thesis were, therefore, designed with this golden triangle also in mind.

1.2. Thesis Overview

Chapter 2 gives an overview of the underlying physical theory of photovoltaic devices, along with a whistle-stop tour along the development of PSCs over the past decade-and-a-half. Context is provided into state-of-the-art approaches to control the crystalline quality of the perovskite layer, along with methods to boost the performance of PSCs.

Chapter 3 details the fabrication and characterisation techniques used within this thesis. The experimental details are separated by chapter, to allow ease of reference.

Chapter 4 outlines the development of three new key technologies for spray-coated PSCs. Firstly, we demonstrate the spray deposition of an exciting new self-assembled molecule (MeO-2PACz) as a hole-transporting layer for *p-i-n* PSCs.

Secondly, a new gas-assisted spray coating technique is developed to control the crystallisation of spray-coated perovskite films. This method represents a low-cost route to create high quality spray-coated thin-films in a fully roll-to-roll compatible manner.

Thirdly, a more volatile 2-methoxyethanol (2-ME) -based solvent system is explored; these such higher vapour pressure systems (c.f. DMF: DMSO systems) are expected to accelerate the production speed of large-area PSCs. Specifically, this solvent

system facilitates wetting of the perovskite precursor onto the hydrophobic self-assembled molecules.

Combining these developments, we demonstrate record efficiencies for spray-coated PSCs. The use of an air-knife in combination with ultrasonic spray coating has enabled a slew of developments for spray-coated thin films, as discussed within the publication foreword. The work presented in this chapter is published in *Advanced Science* (DOI: 10.1002/advs.202270087.)

Chapter 5 discusses the application of the gas-assisted spray coating technique to a methylammonium-free perovskite composition. This flavour of perovskite is expected to impart enhanced thermal stability compared to methylammonium-containing compositions. Importantly, this chapter also explores the development of a fourth technology: a spray-coated surface-passivating post-treatment for the annealed perovskite layer.

Chapter 6 details the development of a novel, volatile, binary ink system to deposit crystalline MAPbI₃ films without the necessity for a post-deposition annealing treatment. Extending this annealing free approach, a self-assembled molecular hole-selective layer (MeO-2PACz) is deposited without an annealing step, enabling the fabrication of fully annealing free PSCs with reasonable efficiencies. The work presented in this chapter is now published in *Advanced Energy Materials* (DOI: 10.1002/aenm.202203468.)

Chapter 7 summarises the work presented herein, discusses how this work could be improved, and outlines opportunities available to further develop the technologies explored.

1.3. References

- [1] Y. M. Bar-On, R. Phillips, R. Milo, *Proc. Natl. Acad. Sci.* **2018**, *115*, 6506.
- [2] R. E. Zeebe, A. Ridgwell, J. C. Zachos, *Nat. Geosci.* **2016**, *9*, 325.
- [3] M. Hampshire-Waugh, *Climate Change and the Road to Net-Zero*, Crowstone Publishing, **2021**.
- [4] IPCC, *Special Report: Global Warming of 1.5°C*, **2018**.
- [5] IPCC, *Climate Change 2022: Mitigation of Climate Change*, **2022**.
- [6] T. Ameri, N. Li, C. J. Brabec, *Energy Environ. Sci.* **2013**, *6*, 2390.
- [7] International Energy Agency, *Cooling Emissions and Policy Synthesis Report*:

Benefits of Cooling Efficiency and the Kigali Amendment Homes Workplace Medicine Institutions Transport Data Centers Food Cooling Emissions and Policy Synthesis Report, 2020.

- [8] International Renewable Energy Agency, *Renewable Power Generation Costs in 2020, 2020.*
- [9] E. and I. S. Department for Business, *Energy Trends June 2022, 2022.*
- [10] Fraunhofer Institute for Solar Energy, *Photovoltaics Report, 2022.*
- [11] NREL, “Best Research-Cell Efficiency Chart | Photovoltaic Research | NREL,” can be found under <https://www.nrel.gov/pv/cell-efficiency.html>, **2022.** (Accessed August 2022.)
- [12] J. Czochralski, *Zeitschrift für Phys. Chemie* **1918**, *92U*, 219.
- [13] A. Kojima, K. Teshima, Y. Shirai, T. Miyasaka, *J. Am. Chem. Soc.* **2009**, *131*, 6050.
- [14] D. B. Ritzer, T. Abzieher, A. Basibüyük, T. Feeney, F. Laufer, S. Ternes, B. S. Richards, S. Bergfeld, U. W. Paetzold, *Prog. Photovoltaics Res. Appl.* **2022**, *30*, 360.
- [15] M. A. Green, E. D. Dunlop, J. Hohl-Ebinger, M. Yoshita, N. Kopidakis, K. Bothe, D. Hinken, M. Rauer, X. Hao, *Prog. Photovoltaics Res. Appl.* **2022**, *30*, 687.
- [16] N. Rolston, W. J. Scheideler, A. C. Flick, J. P. Chen, H. Elmaraghi, A. Sleugh, O. Zhao, M. Woodhouse, R. H. Dauskardt, *Joule* **2020**, *4*, 2675.
- [17] L. Meng, J. You, Y. Yang, *Nat. Commun.* *2018 91* **2018**, *9*, 1.

Background Theory

2.1. Basic Principles of Solar Cells

Photovoltaic (PV) devices, also referred to as solar cells, convert the energy from light directly into electricity *via* the photovoltaic effect. There are three basic processes which occur during the operation of a PV cell; firstly, light is absorbed and generates charge carriers, which are then separated into free charge carriers of opposite types. Such charge carriers can then be extracted from the cell and deliver electrical power to an external circuit. In this section, the physical principles which govern each of these processes are expanded upon.

2.1.1. Band structures of semiconductors

Semiconducting materials are the core principle of PV technology. Semiconductors are materials with electrical conductivity greater than insulators, but with smaller conductivity than metals. This phenomenon is described by the band theory of solids. Here, the chemical bonds that constitute a crystal lattice are formed as the outer orbitals of the atoms overlap. The overlap of these atomic orbitals forms molecular orbitals, consisting of new bonding and antibonding electronic states. In a densely packed solid, wherein many atoms are brought together, these electronic states form a continuum of energetic levels – known as “bands”.^[1] The highest occupied energetic band is known as the valence band (VB). The upper band, separated from the valence by a band gap, E_g , of forbidden energetic states, is known as the conduction band (CB). For insulating materials, the magnitude of this band gap prevents the excitation of electrons across the gap. Here, electrons are instead immobilized within the bonding orbitals of the crystal. Contrastingly, semiconductors have a smaller band gap, such that electrons may be promoted from the VB into the CB. The electrons promoted into the CB can conduct electricity in the same manner as free electrons in a metal.

2.1.2. The photovoltaic effect

The photovoltaic effect was first reported by Becquerel in 1839,^[2] describing the process wherein a material converts incident light into electricity. The energy, E , of a photon is defined by **Equation 2.1**:

$$E = \frac{hc}{\lambda} = h\nu \quad (\text{Equation 2.1})$$

Here, h is Planck's constant, c is the speed of light, and λ is the wavelength of the incident photon, whilst ν is its frequency. Electrons in the VB of semiconducting materials can absorb photons with energy greater than the bandgap, E_g , of the material. The energy transferred from the incident photon promotes the electron from the VB into the CB, leaving behind a positively charged hole in the VB. The probability of this photon absorption process is greater in direct bandgap materials (such as perovskites) than in indirect bandgap materials (such as silicon), wherein a photon and phonon must combine to satisfy the necessary momentum transfer for excitation. Photons with energy greater than the material bandgap may also be absorbed. Here, the difference in energy between these high-energy photons and the CB minima will be converted into heat *via* thermalisation, rather than into useful energy.

2.1.3. The detailed balance limit

The maximum theoretical efficiency of a solar cell is described by the detailed balance limit.^[3] This limit describes the maximum quantum efficiency (the ratio of incident photons to generated charge carriers) in a single junction material illuminated under a standardised spectrum of solar irradiation.

The Sun's radiation spectrum closely matches that of a black body radiator at ~5,800 K. The Air Mass 1.5 (AM 1.5) spectra corrects for atmospheric losses and is used as the standardised reference spectra for evaluating PV materials. A material with a suitably small E_g could absorb the majority of incident photons, however, as discussed above, energy greater than the E_g would be lost to thermalisation. For materials with a larger bandgap, a smaller proportion of the AM 1.5 spectra would have sufficient energy to excite valence electrons, however, such excited carriers would carry more energy.

Such spectral losses, alongside intrinsic recombination losses within PV materials, places a maximum value on the amount of useable electrical energy that can be extracted per incident photon.

2.1.4. Recombination

The detailed balance limit assumes that the only energetic loss mechanism within a solar cell is radiative recombination. *Radiative* recombination is the process by which excited electrons recombine with holes, emitting a photon which has some probability of being reabsorbed by the semiconductor material. However, electrons may recombine *via* a trap state within the bandgap or at an interface. A photon re-emitted during such processes is therefore below the bandgap of the material, with no possibility of a reabsorption event. Here, the recombination is referred to as *non-radiative*. In ideal materials, all recombination is radiative in order to maximise the quantum efficiency. Photo-generated charge carriers must therefore be efficiently extracted prior to a recombination event.

2.1.5. Charge carrier extraction

The most common configuration of solar cells is the *p-n* (positive-negative) junction. Here, alignment of the fermi levels, E_f , between a *p*-type and *n*-type semiconductor create a built-in field which drives separation of the photo-generated charge carriers. Contrastingly, as perovskites are an intrinsic (*i*) semiconductor the fermi level lies near to the middle of the material bandgap, and the photo-generated electrons and holes experience their own quasi-fermi level, $E_{f,e}$ and $E_{f,h}$, respectively. The splitting between the $E_{f,e}$ and $E_{f,h}$ defines the maximum voltage that may be extracted from the cell. The charge carriers are then extracted by an *n*-type electron-transporting layer or a *p*-type hole-transporting layer. To minimise energetic losses, charge selective layers must have a large bandgap to avoid parasitic absorption, have suitable selectivity (typically through having an energetic barrier to deflect minority carriers), and minimal energetic offset with the quasi-fermi level of the target charge carrier.

2.1.6. Solar cell operation and testing

The solar cell is completed by an anode and cathode contacting the charge-selective layers which sandwich the perovskite layer. The equivalent circuit (**Figure 2.1**) is a simplistic model of a solar cell. Here, a constant current generator is in parallel with an ideal diode. When operated in the dark, the solar cell will act as a diode, with the dark current behaviour described by the Shockley diode equation (**Equation 2.2**):

$$J_{dark}(V) = J_0 \left(e^{\frac{qV}{nk_B T}} - 1 \right) \quad (\text{Equation 2.2})$$

where J_0 is the diode reverse saturation current, k_B is the Boltzmann constant, T is the operating temperature, q is the elementary charge, and V is the applied voltage. n is the diode ideality factor, which describes the type of recombination within the cell. For an ideal diode, $n = 1$.

Under illumination, the J_{dark} opposes the photogenerated current. **Equation 2.3** therefore describes the net current generated under illumination:

$$J(V) = J_{SC} - J_{dark} = J_{SC} - J_0 \left(e^{\frac{qV}{nk_B T}} - 1 \right) \quad (\text{Equation 2.3})$$

Here, J_{SC} is the current density generated by the cell with no applied voltage (short-circuit conditions). The J_{SC} is dependent upon the material's E_g according to its external quantum efficiency (EQE, the flux of extracted electrons per incident photon) at each wavelength, λ , of the incident irradiance, summarised by **Equation 2.4**:

$$J_{SC} = -q \int_{\lambda_2}^{\lambda_1} EQE(\lambda) \phi_{ph,\lambda}^{AM\ 1.5} d\lambda \quad (\text{Equation 2.4})$$

$\phi_{ph,\lambda}^{AM\ 1.5}$ is the spectral photon flux of AM 1.5.

The V_{OC} , the open-circuit voltage is the maximum voltage provided by the cell at the point in which the photogenerated current equally opposes the forward bias diffusion current, i.e., where no net current flows. The V_{OC} is defined by **Equation 2.5**:

$$V_{OC} = \frac{nk_B T}{q} \ln \left(\frac{J_{SC}}{J_0} + 1 \right) \quad (\text{Equation 2.5})$$

Resistive parasitic losses must also be accounted for. The shunt resistance, R_{sh} , accounts for current leakage through unwanted pathways such as through film roughness or pinholes that are formed during fabrication. The series resistance, R_s , opposes extraction of charge from the cell, such as when charge transporting layers are too thick,

or if their energetic alignment with the photoactive layer is non-ideal. To account for these parasitic losses, **Equation 2.3** can be modified to:

$$J(V) = J_{SC} - J_{dark} = J_{SC} - J_0 \left(e^{\frac{q(V+JR_s)}{nk_B T}} - 1 \right) - \frac{V + JR_s}{R_{sh}} \quad (\text{Equation 2.6})$$

The equivalent circuit can also be modified to model the resistive losses, as shown in **Figure 2.2**.

Current-voltage sweeps are performed to evaluate these performance metrics. Here, a source-measure unit measures the current output over a range of applied voltage biases. **Figure 2.3** shows a typical current-voltage (J - V) sweep for a perovskite solar cell, with the J_{SC} and V_{OC} values indicated. The maximum power point (MPP) is the maximum output power generated by the cell (according to $P = V \times I$). The fill factor (FF) of the cell is a measure of the “squareness” of the J - V curve, as can be defined using the MPP of the cell:

$$FF = \frac{J_{MPP} V_{MPP}}{J_{SC} V_{OC}} \quad (\text{Equation 2.7})$$

Shunt and series resistances change the gradient of the curve at J_{SC} and V_{OC} , respectively. The FF is therefore maximised when the series resistance is low, and the shunt resistance is high.

Power conversion efficiency (PCE, or η) is a figure of merit which encompasses all of the above device performance metrics. The PCE defines the ratio of power generated by a cell relative to the power of the incident illumination, P_s , according to the following **Equation 2.8**:

$$PCE = \frac{J_{MPP} V_{MPP}}{P_{in}} = \frac{J_{SC} V_{OC} FF}{P_{in}} \quad (\text{Equation 2.8})$$

Typically, P_{in} , is taken as 1000 W m^{-2} . The J_{SC} , V_{OC} and FF must therefore be carefully optimised to maximise the power generated by a solar cell.

2.2. A Decade (and a bit) of Perovskite Solar Cells

Perovskite is a material generally with an ABX_3 crystal structure, where A and B are cations, with anions occupying the X sites. Perovskites were first discovered in 1839: Gustav Rose discovered naturally forming $CaTiO_3$ and named the structure after friend, Lev Perovski.^[4] Goldschmidt examined the phase stability of the crystal lattice, determining the so-called “Goldschmidt tolerance factor” (**Equation 2.9**):

$$t = \frac{r_A + r_X}{\sqrt{2}(r_B + r_X)} \quad (\text{Equation 2.9})$$

Where r_A , r_B , and r_X are the ionic radii of the A, B and X-site ions. Where $0.8 < t < 1.0$, a stable perovskite structure can form, although deviations from the ideal can lead to distortions in the crystal structure. Here, many combinations of elements can satisfy these conditions and produces a wide compositional space, and perovskites are thereby Earth’s most abundant solid phase.^[5]

Photoactive hybrid lead-halide perovskites typically constitute an organic, monovalent cation in the A site, a divalent metal cation at the B site, and halide anions occupying the X sites. Typical A-site cations include methylammonium, MA, formamidinium, FA, or Cs. The B-site metal is commonly Pb^{2+} or Sn^{2+} . The X-site halides, I^- , Br^- , and Cl^- can form mixed compositions.

Whilst Mitzi described the semiconducting properties of halide perovskites in 1994,^[6] it wasn’t until 2009 when Miyasaka et al. incorporated the material into a dye-sensitized solar cell.^[7] Here, the $MAPbI_3$ -based devices demonstrated PCEs of just 3.9%. However, the organic solvent quickly degraded the perovskite sensitizer in such devices. By improving upon the electrolyte formation and the perovskite deposition technique, Nam-Gyu Park’s group successfully boosted the performance of perovskite-sensitized solar cells to 6.5% in 2011.^[8] In 2012, three publications followed which instead incorporated the perovskite into solid-state cells and triggered the following revolution in the field.^[9,10] The major challenge to the status quo came from the work of Lee et al., who swapped the mesoporous scaffold of TiO_2 for the electrically insulating Al_2O_3 .^[11] Surprisingly, device performances *increased* to 9.7% – the perovskite was able to itself transport charge carriers rather than acting as a simple sensitizer. Thus began the new era of perovskite solar cells. By 2022, single-junction PSCs have reached efficiencies of up to 25.7%, with few signs of slowing down.^[12]

Metal halide perovskites combine a number of ideal properties for solar cell applications. The direct bandgap leads to a high absorption coefficient, with typical metal halide perovskite bandgaps corresponding to excellent absorption across the whole visible spectrum. The direct bandgap itself arises from the hybridisation of the bonding orbitals, from which also emerges the “defect tolerance” of the material. Here, although the formation energy of some defects is relatively low, such defects form as “shallow traps” close to the band edges, rather than as intraband “deep traps”.^[13,14] These halide perovskite materials also combine low exciton binding energies, high carrier mobilities, long carrier diffusion lengths and long charge-carrier lifetimes.^[15–19] These characteristics make perovskite materials highly suitable not only for PV applications, but also in thin film resistors, lasing and lighting applications, and a number of sensing applications.^[20–24]

The enormous compositional parameter space of metal halide perovskites gives exceptional tunability of the material bandgap. By combining wider-bandgap perovskite cells with lower bandgap cells, multijunction devices can be created. Such devices can capture a wider proportion of the solar spectrum, reducing thermalisation losses, with the potential to exceed the thermodynamic efficiency limits of single-junction cells. Perovskite-perovskite tandem cells have now exceeded the state-of-the-art efficiency of single-junction PSCs.^[25] Excitingly, perovskite-silicon tandems have now exceeded the 30% barrier – a long-standing target for the field – this year (2022). Perovskite/CIGS and perovskite/organic tandem architectures are also making impressive progress.^[26–29] Tandem applications can be considered as the closest-to-market approach for commercial perovskite PV. As the balance of systems (BoS) costs – the non-module costs – dominate the cost of PV installation and scale with area, increasing the effected power-per-area output of cells is the best approach towards continuing to drive down the overall cost of PV installation.^[30]

The speed of advancement in PSC research has undoubtedly benefited from the breadth of research into the preceding photovoltaic technologies. However, the understanding and development of the control over perovskite crystallisation has underpinned this progress. It was discovered that tailoring the precursor solution by way of mixed solvents encouraged the formation of intermediate species which led to the formation of higher quality films.^[31,32] Most notably, Jeon et al. discovered that drop-casting toluene as an anti-solvent onto the spinning precursor film enabled the creation

of 16.2% PCE devices, the certified record at the time. This one-step “anti-solvent quench” deposition protocol remains the most commonly used technique to deposit the perovskite for laboratory scale devices. Here, the anti-solvent rapidly drives out the volatile precursor solvents to induce supersaturation uniformly throughout the film, thereby initiating crystallisation.

With a wider toolkit of deposition techniques and solvents available, the field began to make advancements in compositional engineering of the perovskite. Whilst MAPbI_3 remains widely utilised due to its simplicity, the field sought higher performing materials, especially with a view to improve the stability of devices. Building upon the use of mixed cations and halides, Saliba et al. developed the so-called “triple cation” perovskite in 2016.^[33] Here, the incorporation of small amounts of Cs into the mixed MA/FA perovskite composition imparted enhanced device performance, reproducibility, and stability. Due to these characteristics, “triple cation” perovskite has become one of the most widely used compositions. “Quadruple cation” perovskites have also now been demonstrated, also incorporating Rb.^[34,35] More recently, all current state-of-the-art devices incorporate perovskite materials based on FAPbI_3 compositions, due to its lower, more ideal, bandgap. Typically, however, these materials incorporate a small amount of additives to improve the phase stability of the crystal,^[36] suppressing the formation of photoinactive $\delta\text{-FAPbI}_3$.^[37]

The field is now beginning a shift towards eliminating the use of volatile MA, due to its stability issues which will remain a significant barrier to commercialisation.^[38,39] Double cation compositions based on CsFA perovskites have made progress, however lag behind in performance compared to MA-containing counterparts, typically achieving around 21% PCEs.^[40–42] Impressively, Wang et al. have recently demonstrated >24% for a CsFA-based perovskite deposited via vacuum evaporation.^[43] A spray-coated MA-free, CsFA-based perovskite is developed in Chapter 5.

Having arisen from the field of dye-sensitised solar cells, the initial perovskite solar cells were fabricated in a mesoporous architecture, with the n-type extraction layer (electron selective) above the substrate, below the perovskite active layer. This is the so-called mesoporous *n-i-p* architecture. *N-i-p* architectures are also conventionally referred to as “standard architecture devices”. Eventually, the mesoporous scaffold was removed from devices, forming planar architecture cells. Planar *n-i-p* devices have

historically been the more popular architecture choice, likely due to their typically higher device PCEs. However, planar *p-i-n* devices are also possible – the so-called “inverted” architecture device. Here, the perovskite is deposited atop the p-type extraction layer (hole-selective). Despite the device performance of *p-i-n* cells lagging behind those of *n-i-p* counterparts, there are a number of advantages to this cell architecture. Firstly, inverted devices typically employ organic charge-transporting layers, replacing the metal oxides used in regular architecture devices with low-temperature-processable materials. This low-temperature processing makes *p-i-n* cells more suitable for integration with flexible substrates, and in tandem architectures – especially due to their lower parasitic absorption losses.^[44,45] Whilst the first demonstrations of silicon/perovskite tandem cells used *n-i-p* perovskite top cells, leaps in device efficiency were achieved after switching to *p-i-n* devices – up to >29 % PCE today. Furthermore, *p-i-n* devices typically demonstrate enhanced device stability due to the absence of dopants in charge-transporting layers.^[46,47]

Despite these promising qualities, inverted architecture devices rarely demonstrated PCEs approaching 23%. This lagging performance is typically attributed to increased nonradiative losses and reduced current extraction.^[48,49] A particular culprit for such losses are the fullerene-based acceptors typically used as the electron-transporting layers.^[50] Exploration of non-fullerene acceptors as for use in *p-i-n* cells is therefore the subject of intensive research efforts. Similarly has the investigation of strategies to passivate both bulk and interfacial trapping states to improve the photovoltage and fill factor of inverted devices. Synergistic approaches to passivate both the grain boundaries within the perovskite and the perovskite/charge-transport layer interfaces have demonstrated a good level of success, creating devices having efficiencies approaching 24%.^[51,52]

Passivating treatments have become a ubiquitous process for state-of-the-art PSCs. During the perovskite film formation process, it is inevitable that a wide range of defects are formed which restrict device performance *via* nonradiative losses. Typically, passivating treatments applied to the perovskite active layer are classified as either “bulk” or “surface” treatments. For the former, an additive is incorporated directly into the precursor solution. Many solid state additives incorporate multiple functional groups,

which not only assist with modulating the crystallisation process, but also to passivate ionic defects at grain boundaries in the formed perovskite film.^[53] Additives which modulate the crystallisation process typically retard the crystallisation rate by formation of an intermediate, leading to larger, more uniform grain sizes.^[54–56] Surface anchoring ligands and additives have also been explored to promote texture control of the perovskite film to promote efficiency and stability.^[57,58] “Surface” treatments are applied as a post-treatment to the fully formed perovskite thin-film. Lewis acids and Lewis bases can accept and donate a lone pair, respectively. These molecules, therefore, can form coordinate bonds to passivate defect states. Zwitterionic molecules contain both groups and can synchronously passivate positive and negatively charged defect states.^[59,60] The formation of low-dimensional perovskite phases at the perovskite/transport layer interface is a particularly promising surface passivation strategy to boost the efficiency and stability of devices.^[59,61] Treatment of the perovskite film surface with large organic cations which insert into the A-site of the perovskite structure can convert the 3D lattice into a quasi-2D layered structure at the interface. Tuning the chemical structure of the organic cation can control the structural and optoelectronic characteristics of the quasi-2D structure. Chapter 5 demonstrates a spray-coated surface passivating treatment to form such a 2D “capping layer” atop spray-coated perovskite films. This is now one of very few demonstrations in literature of a R2R-compatible surface-passivating treatment.

More recently, *p-i-n* devices having efficiencies of up to 25% have been realised by interfacial functionalisation of the perovskite: hole-transporting layer junction with an organometallic layer.^[62] Here, ferrocenyl-bis-thiophene-2-carboxylate was shown to both reduce interfacial trapping states and accelerate electron transfer through the electron-rich aromatic units of the passivating agent. Most notably, such devices demonstrate a T_{95} lifetime (time required to reach 95% of the initial performance) of >1000 hours under damp heat conditions (85 °C and 85% RH), this successfully qualifying for the main testing focus of the IEC61215:2016 industrial standard for terrestrial flat-plate PV modules.

Moreover, a particularly promising new p-type charge-transporting layer for *p-i-n* devices has recently emerged. Here, a family of carbazole-based self-assembled monolayers have been shown to realise a lossless interface.^[26] In under three years of research, these materials have demonstrated high-performing perovskite^[63] and organic

solar cells^[64]; light-emitting diodes^[65]; in record-breaking tandem cells^[66]; in devices which maintain 100% of their initial efficiency after 1000 hours of aging^[67]; and in devices which passed industrial standard stability tests.^[68] Seemingly, a revolution is afoot for *p-i-n* devices. Chapters 4 and 6 focus on the development of *p-i-n* cells containing these carbazole-based SAMs.

The hole-transporting material free, *n-i-p* mesoscopic device architecture has also made considerable progress over the last decade. Here, TiO₂/SnO₂ and ZrO₂ layers are screen printed and topped with a thick (multiple microns) carbon electrode, into which a perovskite solution, typically MAPbI₃ is infiltrated. Fully screen printed, mesoscopic “carbon-based” cells have now demonstrated 13.11% for a fully-scalable process, and also exhibited over 9000 hours of operational stability.^[69,70]

2.3. Solution Processing of Perovskite Solar Cells

Amongst the properties that make hybrid lead halide perovskites ideal for solar cells, their facile processability is one of the most important. The ability to fabricate high performance cells and modules at a fraction of the cost of incumbent technologies gives PSCs the lowest EPBT of all PV technologies.^[71] Currently, however, state-of-the-art devices (> 25% PCE) are all fabricated at the laboratory level via spin coating. Spin coating is a ubiquitous technique for the fabrication of thin films, dating back as far the 1950s.^[72] Here, a small volume of a solution is uniformly spread over a substrate surface by hydrodynamic and centrifugal forces induced by a high-speed spinning chuck.^[73] The air flow over the spinning substrate drives evaporation of the casting solvent, thinning the wet film. The coating and drying of a thin-film can be accomplished in under a minute. The processing speed, uniformity, and control over the film thickness makes spin coating an invaluable tool for laboratory-scale research.

Spin coating is an inherently non-scalable technique, unsuited to coating large areas and wasting the majority of deposited solutions. As such, a number of so-called “scale up” techniques have now been demonstrated to fabricate PSCs. The most common coating methods are slot-die coating, doctor blading, bar coating, dip coating, screen-printing, inkjet printing, and spray coating. Whilst each technique has achieved notable results, each deposition method has relative drawbacks, as summarised in **Table 2.1**.

Evaporated PSCs have also demonstrated efficiencies >20%, and there is much discourse surrounding the solution processed vs. vacuum processed competition.^[74] Whilst there are many advantages to vacuum processing, it remains that the deposition speed is severely limited such that the commercial cost of vacuum-production of PSCs will remain an enormous barrier to market entry. Thermal and electron beam evaporation are both examples of physical vapour depositions (PVD) protocols. Evaporation is typically conducted within a vacuum chamber, enabling the evaporated material to travel directly to the target surface (unimpeded by particulate collisions), wherein the gaseous particles condense on the surface. The high vacuum level also reduces the energy required to evaporate materials. In thermal evaporation, a high current is passed through a resistive boat (or coiled wire housing a crucible) to heat the source material, causing it to melt and vaporize. In electron beam evaporation, a heated tungsten filament generates electrons, which are directed in a beam (by a magnetic field) at the source material to heat, and eventually vaporize, it. Electron beams can typically reach higher temperatures and therefore allow deposition of a wider range of materials than thermal evaporation.

Table 2.1: A comparison of the common scalable deposition techniques used in the fabrication of perovskite solar.

	Spin Coating	Dip Coating	Slot-die Coating	Doctor Blading	Bar Coating	Inkjet Printing	Spray Coating
Scalability	Not scalable	Limited	Scalable	Scalable	Scalable	Scalable	Scalable
Complexity	Low	Moderate	High	Moderate	Moderate	High	High
Substrates	Small, flat only	Flexible and rigid, flat only	Flexible and rigid, flat only	Flexible and rigid, flat only	Flexible and rigid, flat only	Flexible and rigid, flat only	Flexible and rigid, flat or complex shapes
Solution Wastage	High	High	Low	Moderate	Moderate	Low	Low
Other Drawbacks	Only applicable to laboratory scale	Limited applicability to a R2R process	Complicated deposition procedure	Limited control over film thickness	Limited control over film thickness	Restricted by ink requirements	Very large parameter space for optimisation

2.3.1. Techniques to control crystallisation

The efficiency deficit between small-area, spin-coated PSCs and PSCs deposited *via* scalable techniques is associated with the difficulty in forming high-quality thin-films over large areas. Fine control over the crystallisation and growth kinetics is required for high-quality perovskite film formation; fast nucleation, followed by slow crystallisation is essential.^[75] Whilst anti-solvent treatments are ubiquitous for initiating rapid crystallisation in small-area, spin-coated films, they are challenging to use in scalable, commercial applications, as the large quantity of typically toxic anti-solvent is unsuitable for use in a workplace. Alternatively, physical treatments such as hot-casting, vacuum-quenching, and gas-blowing can be used for the rapid removal of casting solvents in a way which is compatible with scalable deposition technologies and more suitable for commercial applications.

Hot-casting aims to increase the evaporation rate of the casting solvent, either by heating the substrate or the precursor solution itself. This approach is simple to apply. Deng et al. employed a hot-blade-coating method to fabricate devices >20%, with the high substrate temperature encouraging fast evaporation of the casting solvent and direct conversion of the ink into the perovskite film.^[76]

Li et al. introduced the vacuum-flash assisted process (VASP) for large-area perovskite thin-film formation in 2016. Here, the application of a 20 Pa vacuum to the as-cast wet film induced the formation of a DMSO-perovskite intermediate adduct, which upon annealing formed a high-quality perovskite layer.^[77] Utilising this approach, PSCs with certified efficiencies of 19.6% for a 1 cm² active area – a record at the time. Guo et al. demonstrated the application of the VASP treatment for blade-coated perovskite films.^[78] Bishop et al. demonstrated the suitability of this approach to spray-coated PSCs, enabling the formation of high-quality “triple cation” perovskite thin-films.^[79] Although VASP enables the necessary fine control over the crystallisation kinetics to form high-quality perovskite films, the use of a vacuum limits its applicability to a commercial process. The use of vacuum is typically limited to batch-to-batch processing, limiting the overall achievable coating speed and thus the economic viability of the approach.

Gas quenching uses a convective flow of gas (typically air or nitrogen) to induce evaporation of the casting solvents. Gas-quenching avoids the use of any toxic solvents or vacuum treatments and is therefore ideal for a commercial R2R application. Huang et al.

first reported gas-quenching for spin-coated PSCs in 2014.^[80] The solvent composition of the film is a key consideration for the gas-quenching process, due to the difficulty of evaporating high boiling point solvents such as DMSO. The gas flow can itself be heated to further promote solvent evaporation. Since this first report, gas-quenching has been extensively explored for blade-coated and slot-die coated perovskite thin-films.^[81]

In addition to physical process control over crystallisation, additives, including solvents, can be used to modulate the crystallisation process. A wide range of additives including acids, Lewis acids and bases, surfactants, ammonium salts, and excess precursors (typically PbI_2 or methylammonium iodide) have been explored to control the resultant film quality. Lead halides are strong Lewis acids, and therefore readily form intermediate adducts with Lewis bases. Such Lewis bases can either be solid state additives or solvents which contain electron-donating groups such as oxygen, nitrogen, or sulphur. Multidentate ligands have also been explored. The formation of adduct species can increase the solubility of the intermediate species in the casting solvent, retarding supersaturation and, therefore, the rate of nucleation. By tailoring the degree of intermediate formation, the crystallisation kinetics can be tuned to improve the quality of the resulting perovskite thin-film.

2.3.2. Low-temperature and Annealing-free approaches

Some focus is now being directed towards the exploration of volatile precursor solvents. Here, it is considered that the exchange of the typical non-volatile casting solvents with more volatile species would allow circumvention of post-treatments, such as extended quenching and annealing steps.^[82] Here, the volatility of the casting solvents itself would enable near-complete removal of the solvents at room-temperature, facilitating sufficient nucleation and subsequent growth for high-quality perovskite thin-films without further heat treatment. Such innovations could streamline the fabrication process, increasing throughput speed and therefore expected profit margins (to be reinvested in sustainable growth) of commercial PSC production.^[83] This is particularly pertinent considering the deleterious effects of residual, trapped solvents in films – a significant hurdle to improving the stability of solution-processed PSCs.^[84] In Chapter 6, a novel, binary solvent mixture is developed to enable the fabrication of spin-coated PSCs without any post-deposition annealing treatment. **Section 6.2** discusses the previously

reported approaches to “annealing-free” fabrication of PSCs and gives an overview of the volatile solvent systems that have thus far been explored as perovskite precursor solvent systems.

2.3.3. Solvent toxicity

The toxicity of typical perovskite precursor solvents is a key barrier to commercialisation. In a factory environment, the exposure of workers to such toxic solvents must be strictly regulated. The Health and Safety Executive (HSE) is the UK’s national regulator for health and safety in the workplace. HSE have defined Workplace Exposure Limits (WELs) to protect workers from hazardous substances. The long-term exposure limit (defined as an 8-hour time weighted average) of most precursor solvents necessitates non-viable costs for air handling infrastructure. **Table 2.1.** lists the WEL for solvents used within this thesis.^[85] The WEL must, therefore, become a key consideration amongst the field for the development of novel solvent systems in order to move closer to commercialisation of PSCs.

Table 2.1: *The 8-hour time-weighted average Workplace Exposure Limit (WEL) for solvents used within this thesis.*^[85]

Solvent	8-hour TWA (ppm)
DMF	5
NMP	10
Acetonitrile	40
Ethanol	1000
Isopropanol	400
2-methoxyethanol	1
DMSO	-
Tetrahydrofuran	50

2.1.1. Spray coating of PSCs

Typically, spray coating describes the process of forming a mist of droplets from a solution which are then deposited onto a surface and coalesce to form a wet film. The droplet mist can be formed by either air pressure^[86] or an ultrasonic atomizing technique.^[87] Here, ultrasonic spray coating has been used exclusively. The spray coating is performed using a Sonotek Exactacoat system, equipped with an “Impact” head. In this system, a solution is fed into the spray head where a resonating piezoelectric tip shears the solution into highly uniform droplets. This low velocity droplet mist is directed at the substrate surface by a low velocity “shaping gas”, typically operating at around 3 psi. The flat jet air deflector creates a fan-shaped spray pattern, enabling a wide coating width. Using this system, we can comfortably coat the width of our typical substrates in one “spray-pass”. The Sonotek system is housed in an N₂-filled glovebox, enabling processing of perovskite layers under an inert atmosphere.

In contrast to spin coating or meniscus-coating methods, there is no external force applied to encourage the coalescence of the deposited film, or to control the wet film thickness. Instead, the thickness and uniformity of the film is dictated by a delicate balance of the wide parameter space. This includes surface wetting chemistry; solution concentration; solution composition; deposition parameters such as head height, speed, flow rate, and droplet size; and atmospheric conditions. Although challenging to optimise, spray coating does enable deposition over non-planar surfaces and, at present, eclipses the perovskite deposition speeds of all other “scalable” deposition technologies.^[88] Moving forwards, a huge opportunity exists to employ machine learning techniques to accelerate process optimisation, and propel the transition from “lab-to-fab”.^[89]

Since demonstrating the first spray-coated perovskite solar cell in 2014^[90], our lab at the University of Sheffield has primarily focused on developing novel spray deposition technologies for the fabrication of PSCs. The origins of this technique can be traced back to the 1800’s, when Joseph Binks combined a hand-pump, a pressurised paint-containing vessel, and a wand with a nozzle. Binks’ invention debuted on the world stage when he was employed to paint the Chicago buildings hosting the 1893 Columbian Exposition. The so-called “White City” sparkled, spray-painted with whitewash – a mix of oil and white lead. In a nod to this ancestral heritage, spray coating is now a promising technique for depositing lead halide perovskites.

Through careful optimisation of the processing temperature, ink properties, and annealing step to control the quality of the spray-coated perovskite film, device PCEs of 11.1% were demonstrated. Unfortunately, whilst blade coating^[91] and slot die coating^[92] methods have now recently surpassed the 22% PCE milestone, the maximum stabilised PCE for spray-coated cells remained at only 19.4% until 2022.^[93] Due to the complex nature of the spray coating process, it is challenging to optimise and control the uniformity of the deposited film. Spray coating proceeds via four main steps. Firstly, the ink for coating is broken up into small droplets, typically by either pneumatic atomisation^[86] or ultrasonic atomisation. There are a number of benefits to ultrasonic spray coating over airbrush techniques, namely better reproducibility due to the control of the droplet size and uniformity.^[94] Next, the generated droplets are directed to the substrate surface, after which they should coalesce to form a wet film. Finally, the casting solvent is removed to create the target layer.

Clearly, there is an enormous parameter space to optimise for the spray deposition of thin films. The droplet size can be approximated by **Equation 2.10**.^[95] Here, the mean diameter of droplets ($D_{0.5}$) is determined by the surface tension, σ , and the density, ρ , of the ink, as well as the frequency of the vibrating tip, f .

$$D_{0.5} = 0.34 \left(\frac{8\pi\sigma}{\rho f^2} \right)^{\frac{1}{3}} \quad \text{(Equation 2.10)}$$

These atomised droplets are typically guided to the substrate surface by a so-called “shaping gas” which can be controlled to dictate the pattern of the deposited droplet mist. A key consideration, however, is that the increased vapour pressure of the droplets must be considered to prevent premature evaporation of the material, prior to arrival at the substrate surface. The volume of material delivered to the substrate surface is dictated by a wide parameter space, including the concentration of the ink; the flow rate of the solution; the distance between the substrate and the spray-head; the speed of the spray-head as it passes over the surface; the number of spray passes; and the air pressure of the shaping gas. Once the droplet mist arrives at the surface, the wetting should be sufficient to promote coalescence. Again, this process is dependent upon a number of parameters such as the ink density and viscosity, the droplet diameter, the substrate nature, and the surface tension of the ink.^[96] Here, heating the substrate can ameliorate the surface wetting of the ink, so long as the temperature is not excessively high, such that

the casting solvent is evaporated upon droplet contact with the substrate. Surfactants can also be employed to promote the wetting.^[76,97]

Finally, the evaporation rate of the casting solvent must be controlled to allow sufficient time for the coalescence of droplets, but without prolonged drying times which can lead to dewetting and shrinkage effects. This is particularly complicated by the necessity for careful control over the perovskite crystallisation process. As with other scalable techniques, a number of approaches have been demonstrated to control the crystallisation of spray-cast perovskite films. Barrows et al. initially balanced the ink composition with the temperature of the substrate during processing and post-deposition annealing to optimise the resultant film morphology. In 2018, Uličná et al.^[98] adapted an approach that had been pioneered one year earlier by Yang et al.^[99] to sufficiently widen the processing window of spray-coated perovskite films to allow for an anti-solvent treatment. Here, the use of non-volatile *N*-methyl-2-pyrrolidone delayed the drying of the as-cast wet film, allowing the wet film to be dipped into a bath of diethyl ether to extract the casting solvent and enable rapid crystallisation. Spray-coated devices fabricated in this manner demonstrated peak PCEs of up to 17.3%. In 2020, Cai et al. used an anti-solvent bathing approach to demonstrate ultrasonically spray-coated PSCs with efficiencies of up to 20.6%, however no stabilised device efficiencies were reported.^[100] Although effective, the use of such antisolvent bathing methods has limited scalability due to the gradual contamination of the antisolvent bath, which also requires a large volume of typically toxic solvents.

Therefore, to avoid this antisolvent approach, our group explored the use of vacuum-assisted drying approaches. In 2018, the so-called “VASP” (vacuum-assisted solution processing) process was used to fabricate spray-coated, triple cation PSCs having efficiencies of up to 17.8%.^[101] Here, the as-cast wet film was exposed to a low-vacuum to extract the casting solvent and induce nucleation uniformly throughout the film. After further optimisation studies, the VASP technique was used to create spray-coated triple cation devices with PCEs of up to 19.4%.^[93]

Considering the limited application of the VASP technique beyond batch-to-batch processing, there was a necessity to explore R2R-compatible approaches to modulating the film crystallisation. As discussed, the use of gas-quenching has been widely explored in most scalable deposition techniques.^[81] However, this technique had not been

integrated into a spray-deposition process. In Chapter 4, this such process is developed and is implemented to tip the stabilised efficiency of spray-coated PSCs over the 20% benchmark.

The “Perovskite Database Project”, which contains data on PSCs from over 7,400 publications, contains only 18 publications which include an ultrasonically spray-coated perovskite absorber layer, without the use of any spin coating within the process. It should be noted that this data only includes papers published before approximately the beginning of 2020. From this database, it can be seen that 15 of the 18 publications focus on a simple MAPbI_3 composition – only 3 papers explore the formamidinium-containing compounds that are expected to impart greater device performance (**Figure 2.4**). Whilst a handful of papers exploring these other compositions have now been published, it was clear that the spray coating field needed to move towards more exotic perovskite formulations: the median (maximum) PCE achieved by the aforementioned 15 MAPbI_3 -based publications was only 11.6% (17.3%). In Chapter 5, a spray-coated CsFA-based perovskite is therefore developed, demonstrating peak PCEs of up to 20.0%.

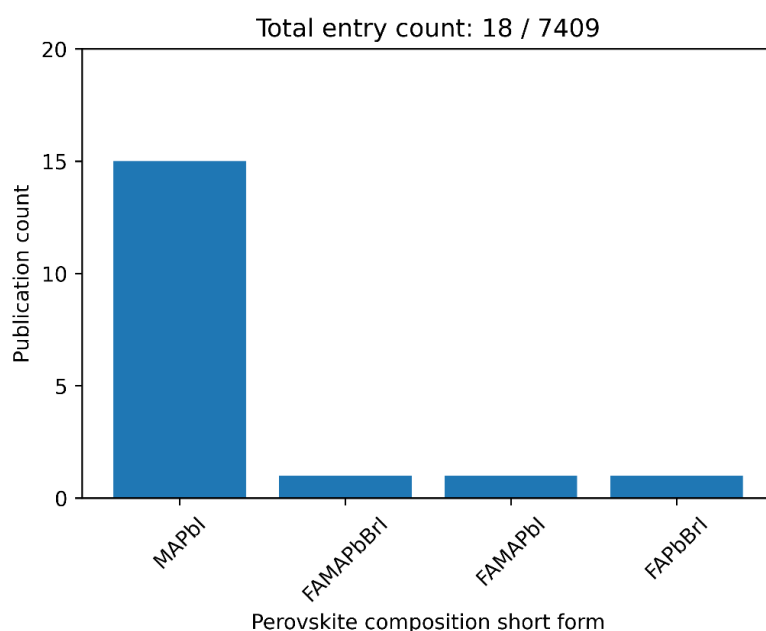


Figure 2.4: Of the 18 publications (out of 7,409) included in the “Perovskite Database Project” which incorporate an “ultrasonically spray-coated” perovskite layer, 15 reports have used a MAPbI_3 composition.

A number of other publications since 2020 have also demonstrated Cs- or formamidinium-containing compositions to create devices having >18% PCEs. In 2020, our

group demonstrated the first spray-coated triple cation composition, fabricated using a vacuum-assisted protocol. These devices, the state-of-the-art at the time, recorded stabilised PCEs of up to 19.4%.^[93] Building on this work, at the end of 2020 Cai et al. deposited a triple cation perovskite using an antisolvent bath technique. Whilst peak efficiencies of up to 20.6% were reported, no stabilised device efficiencies were included in the report.^[100] In 2021, Gao et al. incorporated potassium iodide and L- α -phosphatidylcholine, a surfactant, as additives to create FAMA-based perovskite films via spray coating under ambient conditions.^[102] Such devices achieved peak PCEs of up to 18.2% in a one-step protocol. In late 2020, Rolston et al. pioneered a novel “plasma processing” technique to rapidly fabricate CsFA-based perovskites in ambient conditions.^[88] Here, an N₂ flow delivers plasma to the deposited, wet perovskite film, inducing crystallisation of the perovskite layer. Notably, the plasma treatment circumvented the need for any annealing treatment to the crystallised perovskite layer, enabling the creation of >18% PCE cells at effective throughput speeds of up to 12 m min⁻¹ – an unprecedented speed amongst scalable techniques. Clearly, critical to the deposition speed was the avoidance of extended annealing treatments to the perovskite layer. Radiative annealing and the use of more volatile casting solvents are also promising routes to circumvention of extended annealing steps. However, this methodology must also be applied to the charge-transporting layers in order to achieve high throughput speeds in a commercial PSC manufacturing setting. Reducing the annealing time for metal oxide layers, such as NiO_x or SnO₂, is particularly challenging, although progress has been made to reduce the treatment times to as little as 2 minutes with reasonable device efficiency.^[103] Heating steps can be replaced by UV-ozone treatments, however, the extended timing of these is not practically feasible.^[104] In Chapter 6, a carbazole-based SAM is deposited via an annealing-free route to demonstrate fully-annealing free PSCs. In an ideal commercial R2R process, each layer would be scalably deposited at the same speed, with no/limited annealing steps which would both throttle the effective deposition speeds and increase the energy budget of the fabrication process.

2.4. Materials

Both *p-i-n* and *n-i-p* planar architecture perovskite solar cells have been fabricated within this thesis. SnO₂ is a particularly appealing ETL to replace TiO₂, due to a number of properties^[105] including the possibility of low-temperature processing^[106] and rapid processing^[103]; high optical transparency; high stability under light, heat and moisture; and minimal photoactivity.^[107] SnO₂-based PSCs now demonstrate PCEs of up to 25.5%.^[36,108,109] Such state-of-the-art *n-i-p* PSCs typically employ spiro-OMeTAD as the HTL, first developed for dye-sensitised solar cells.^[9] Typically, spiro-OMeTAD is heavily doped to enhance the electrical properties of the material, due to the low conductivity and hole mobility of the pristine material. However, there are a number of drawbacks associated with this material. The doping required leads to a high degree of instability within a PSC, especially at elevated temperatures^[110]; the molecule is extremely expensive to synthesise and therefore not a candidate for practical manufacturing purposes^[111]; and a high degree of parasitic absorption renders this material unsuitable for tandem applications.^[112]

In *p-i-n* architecture, a self-assembled molecule ([2-(3,6-Dimethoxy-9H-carbazol-9-yl)ethyl]phosphonic acid, MeO-2PACz) is employed as the HTL, with a C₆₀ ETL. A bathocuproine (BCP) hole-blocking layer is used on top of the C₆₀, due to the shallow valence band of the fullerene.

Self-assembled monolayers (SAMs) are ordered arrays of small organic molecules formed by the spontaneous adsorption of an anchoring group onto a surface. This reaction is self-limiting, as once all available surface binding sites are occupied no more molecules may bind; this forms a molecular monolayer. By modifying the anchoring, spacer, and head group of the molecule, it is possible to encode the functionality of bulk layers into a single molecular monolayer. A number of such SAMs have now been integrated into PSCs to enhance device performance.^[113] Recently, a new class of carbazole-based SAMs have been developed by researchers at Helmholtz-Zentrum Berlin and Kaunas University of Technology.^[26,114] These SAMs, namely MeO-2PACz, 2-PACz ([2-(9H-carbazol-9-yl)ethyl]phosphonic acid), and Me-4PACz ([4-(3,6-dimethyl-9H-carbazol-9-yl)butyl]phosphonic acid) have now been utilised in world record tandem devices, on both rigid^[66] and flexible substrates^[115]; devices which have passed the damp heat test^[68]; and devices which retain 100% of their initial performance after 1000 hours of

operation.^[67] Combining low-costs, facile synthesis and deposition, stability, and high efficiency, these SAMs are one of the most promising hole-transporting materials demonstrated in the field thus far.

Whilst such carbazole-based SAMs can form a practically lossless interface with the perovskite, the typically used fullerene-based ETLs for *p-i-n* devices are severely limited by non-radiative recombination at the perovskite / ETL interface.^[50] Although C₆₀ is the dominant ETL for state-of-the-art *p-i-n* devices, reducing such non-radiative losses associated with this material remains one of the most critical challenges to improve *p-i-n* device performance. Because of this, *p-i-n* devices have not rivalled the > 25% PCEs demonstrated by *n-i-p* PSCs until extremely recently: Li et al. have now demonstrated an organometallic-functionalised perovskite / C₆₀ interface to realise *p-i-n* devices having efficiencies of up to 25.0% and which pass the international stability standards for silicon solar cells (IEC61215).^[62]

The chemical structures of the organic charge-transporting layers are shown in **Figure 2.1(a)-(d)**.

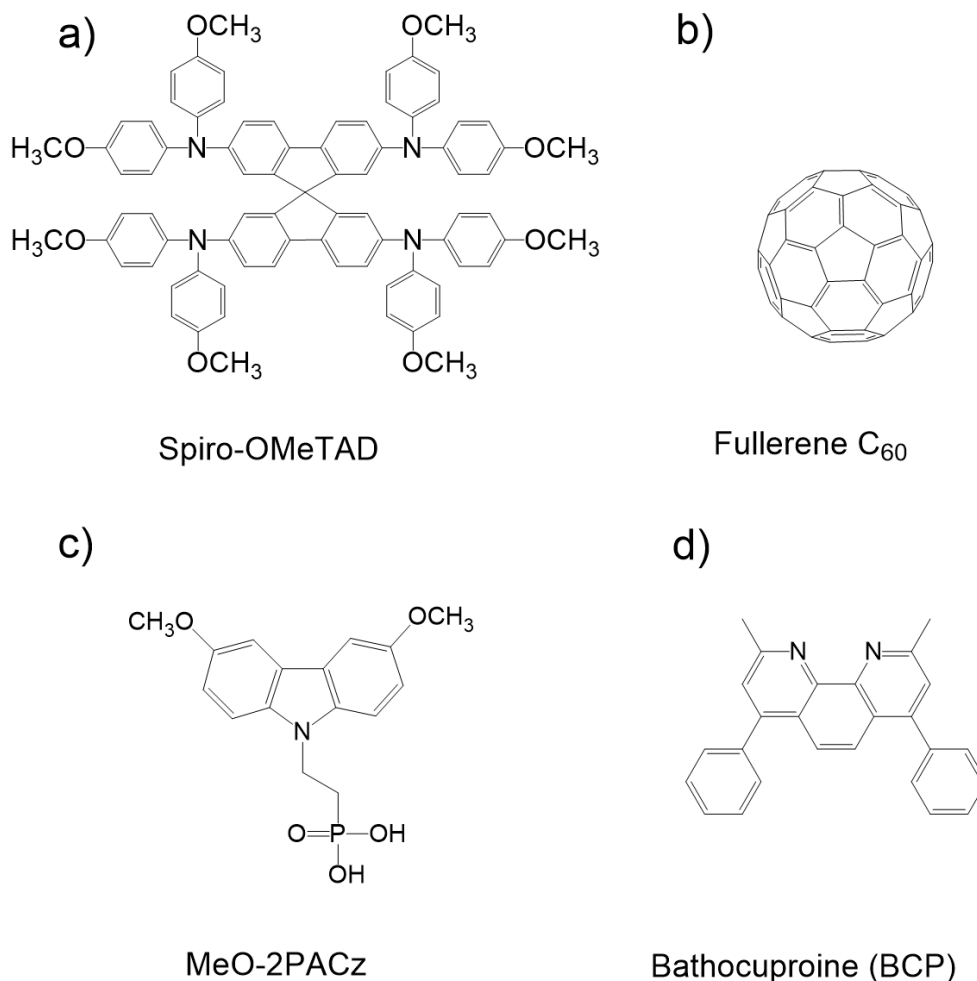


Figure 2.1: The chemical structure of (a) Spiro-OMeTAD, (b) C₆₀, (c) MeO-2PACz, and (d) bathocuproine (BCP).

2.5. Anti-reflective coatings

To maximise the performance of solar technologies, as much incoming light as possible should be directed into the active layer. One of the simplest light management strategies is the use of anti-reflective coatings (ARCs.) ARCs reduce the light lost to reflection as a result of the mismatch of refractive indices at an interface. The simplest form of ARC is a single-layer interference coating. To reduce the reflection arising from the mismatch between air (n_0) and the glass substrate (n_s) a layer with optimal refractive index $n_1 = \sqrt{n_0 n_s}$ is applied to the glass surface. The layer thickness should be finely controlled to be one quarter of the incoming light to ensure destructive interference of the reflected light. The optimal thickness of the single-layer ARC is therefore $d = \frac{\lambda}{4n_1}$. For

the air: soda lime glass interface, a refractive index of $n \approx 1.23$ is ideal, however, few materials have this refractive index. Instead, MgF_2 ($n = 1.38$) or LiF ($n = 1.39$) are typically used due to facile deposition *via* evaporation.

Single-layer ARCs are, therefore, targeted at a specific wavelength of maximum reflection. The reflection can remain large at other wavelengths. Here, multilayer coatings can instead be used to reduce reflection over a wider spectral band. Alternative layers of high- and low- refractive index material can be used in such a multilayer ARC but can be complex to deposit. In Chapter 4, a single layer ARC (LiF) is used to reduce the reflective losses arising from illumination through the glass substrate.

2.6. Characterisation Techniques

2.6.1. External Quantum Efficiency

External quantum efficiency (EQE) measurements are a vital tool for photovoltaic device characterisation. This is a measure of the generated photocurrent in a device versus the rate of incident photons, as a function of wavelength. As such, the EQE of a device is sometimes referred to as the “incident photon-to-current efficiency” (IPCE). From the EQE, the optical band gap of the material can be derived, and the spectral shape can reveal information about loss mechanisms within the device stack. An estimate of the J_{SC} of the cell can be calculated from the integral of this spectral response curve in combination with the AM1.5 spectrum. The EQE spectrum is now an expected provision for publication of results for PSCs,^[116] demonstrating good agreement between the J_{SC} from the J - V measurement and the integrated J_{SC} from the EQE spectra. Typically, up to a 10% mismatch between these values is viewed as acceptable, with this mismatch arising from a number of factors.^[117,118]

Here, a Newport QuantX-300 Quantum Efficiency Measurement System is used to record the EQE response of the PSCs. A 100 W xenon arc lamp, chopped at 25 Hz, is focused through a monochromator (Oriel Monochromator, CS130B). Before each set of measurements, the system was referenced to a Newport-calibrated silicon and germanium reference detector.

2.6.2. X-ray Diffraction

Repeating crystallographic structures interact with electromagnetic waves where the interatomic distances are comparable to the wavelength, with the 3D crystal acting as

a diffraction grating to produce interference effects.^[119] Constructive interference of the diffracted waves occurs according to the Bragg equation (**Equation 3.1**):

$$2d\sin\theta = n\lambda \quad (\text{Equation 3.1})$$

where λ is the incident wavelength, n is an integer multiple of the wavelength, d is the interatomic distance, and θ is the angle of incidence. With a known wavelength, the interatomic distances within a crystal structure can therefore be derived.

The two common data collection geometries for XRD are the Bragg-Brentano and Debye-Scherrer geometries. The Bragg-Brentano geometry is most commonly used, wherein x-rays incident upon a flat sample at an angle θ are diffracted from the sample surface at the same angle. This process is analogous to specular reflection; thus the Bragg-Brentano geometry is commonly referred to as the “reflection” geometry.

XRD-based techniques are an incredibly powerful tool to characterize perovskite structures, providing information on crystal structure, phase purity, crystallite size and orientation, and micro strain. Moreover, laboratory-based x-ray diffractometers are fairly commonplace, easy to operate, and can probe a large structural area (*c.f.* atomic-force microscopy (AFM), scanning-electron microscopy (SEM) etc.), and can be performed under a range of sample environments and processing conditions.^[120]

Here, X-ray diffraction (XRD) patterns were collected at room temperature using a PANalytical X'Pert Pro system equipped with a Copper Line Focus X-ray tube run at 45 kV with a tube current of 40 mA. The diffractometer operated in Bragg–Brentano geometry to record diffraction patterns from 5° to $100^\circ 2\theta$.

2.6.3. Grazing Incidence Wide-Angle X-ray Scattering

Where the XRD measurements described above provide a 1D diffraction pattern from the probed material, additional information can be obtained using wide-angle X-ray scattering techniques. Grazing incidence wide-angle x-ray scattering (GIWAXS) uses a 2D detector to collect scattering data over a typical q range of $0.1 - 3 \text{ \AA}^{-1}$, corresponding to the atomic-level regime according to **Equation 3.2**:

$$d = \frac{2\pi}{q} \quad (\text{Equation 3.2})$$

where q is the scattering vector and d is the interatomic distance, as above. Here, the use of a 2D detector provides information on the degree of texture (preferred crystallite orientation) in a film. GIWAXS is therefore a powerful tool to study perovskite

thin films, providing detailed structural information – including depth-dependent information – and the potential for extremely fast data collection when measured using synchrotron radiation, enabling *in situ* observations of crystallisation dynamics.^[120,121] Such *in situ* measurements can be performed under a variety of sample environments.

2.6.4. Scanning Electron Microscopy

Scanning electron microscopes produce images of a sample by rastering electrons across the sample surface. The wavelength of electrons enables far superior resolutions than optical microscopy, down to the nm scale. Here, electrons (generated by a field emission gun within this thesis) are directed and focused by magnetic lenses onto the sample surface. Such measurements are performed under vacuum conditions to prevent molecular interactions with the electron beam. The interaction of the electrons with the sample generates secondary electrons, which are collected by a detector and provide an image of the sample surface. This technique is used within this thesis to characterise the morphology of the deposited perovskite film, either as a “top-down” image of the sample surface, or as a cross-sectional image probing a cleaved sample. The samples were cleaved by freezing in liquid nitrogen before being snapped.

2.7. References

- [1] M. Fox, *Optical Properties of Solids*, Oxford University Press, **2010**.
- [2] A. E. Becquerel, *Comptes Rendus L'Academie des Sci.* **1839**, *9*, 145.
- [3] W. Shockley, H. J. Queisser, *J. Appl. Phys.* **2004**, *32*, 510.
- [4] G. Rose, *Ann. Phys.* **1840**, *126*, 652.
- [5] O. Tschauner, M. Chi, J. R. Beckett, C. Prescher, V. B. Prakapenka, G. R. Rossman, *Science (80-.)*. **2014**, *346*, 1100.
- [6] D. B. Mitzi, C. A. Feild, W. T. A. Harrison, A. M. Guloy, *Nat. 1994 3696480* **1994**, *369*, 467.
- [7] A. Kojima, K. Teshima, Y. Shirai, T. Miyasaka, *J. Am. Chem. Soc.* **2009**, *131*, 6050.
- [8] J. H. Im, C. R. Lee, J. W. Lee, S. W. Park, N. G. Park, *Nanoscale* **2011**, *3*, 4088.
- [9] U. Bach, D. Lupo, P. Comte, J. E. Moser, F. Weissörtel, J. Salbeck, H. Spreitzer, M. Grätzel, *Nat. 1998 3956702* **1998**, *395*, 583.
- [10] I. Chung, B. Lee, J. He, R. P. H. Chang, M. G. Kanatzidis, *Nature* **2012**, *485*, 486.
- [11] M. M. Lee, J. Teuscher, T. Miyasaka, T. N. Murakami, H. J. Snaith, *Science (80-.)*. **2012**, *338*, 643.
- [12] NREL, "Best Research-Cell Efficiency Chart | Photovoltaic Research | NREL," can be found under <https://www.nrel.gov/pv/cell-efficiency.html>, **2022**.
- [13] K. X. Steirer, P. Schulz, G. Teeter, V. Stevanovic, M. Yang, K. Zhu, J. J. Berry, *ACS Energy Lett.* **2016**, *1*, 360.
- [14] W. J. Yin, T. Shi, Y. Yan, *Appl. Phys. Lett.* **2014**, *104*, 063903.
- [15] S. D. Stranks, G. E. Eperon, G. Grancini, C. Menelaou, M. J. P. Alcocer, T. Leijtens, L. M. Herz, A. Petrozza, H. J. Snaith, *Science (80-.)*. **2013**, *342*, 341.
- [16] C. Wehrenfennig, G. E. Eperon, M. B. Johnston, H. J. Snaith, L. M. Herz, C. Wehrenfennig, G. E. Eperon, M. B. Johnston, H. J. Snaith, L. M. Herz, *Adv. Mater.* **2014**, *26*, 1584.
- [17] A. Miyata, A. Mitioglu, P. Plochocka, O. Portugall, J. T. W. Wang, S. D. Stranks, H. J. Snaith, R. J. Nicholas, *Nat. Phys.* **2015**, *11*, 582.
- [18] D. W. DeQuilettes, S. M. Vorpahl, S. D. Stranks, H. Nagaoka, G. E. Eperon, M. E. Ziffer, H. J. Snaith, D. S. Ginger, *Science (80-.)*. **2015**, *348*, 683.
- [19] G. Xing, N. Mathews, S. Sun, S. S. Lim, Y. M. Lam, M. Graetzel, S. Mhaisalkar, T. C. Sum, *Science (80-.)*. **2013**, *342*, 344.

- [20] G. Xing, N. Mathews, S. S. Lim, N. Yantara, X. Liu, D. Sabba, M. Grätzel, S. Mhaisalkar, T. C. Sum, *Nat. Mater.* **2014**, *13*, 476.
- [21] Z. K. Tan, R. S. Moghaddam, M. L. Lai, P. Docampo, R. Higler, F. Deschler, M. Price, A. Sadhanala, L. M. Pazos, D. Credgington, F. Hanusch, T. Bein, H. J. Snaith, R. H. Friend, *Nat. Nanotechnol.* **2014**, *9*, 687.
- [22] H.-H. Fang, S. Adjokatse, H. Wei, J. Yang, G. R. Blake, J. Huang, J. Even, M. A. Loi, *Sci. Adv.* **2016**, *2*, 2375.
- [23] S. Yakunin, D. N. Dirin, Y. Shynkarenko, V. Morad, I. Cherniukh, O. Nazarenko, D. Kreil, T. Nauser, M. V. Kovalenko, *Nat. Photonics* **2016**, *10*, 585.
- [24] H. Wei, Y. Fang, P. Mulligan, W. Chuirazzi, H. H. Fang, C. Wang, B. R. Ecker, Y. Gao, M. A. Loi, L. Cao, J. Huang, *Nat. Photonics* **2016**, *10*, 333.
- [25] R. Lin, J. Xu, M. Wei, Y. Wang, Z. Qin, Z. Liu, J. Wu, K. Xiao, B. Chen, S. M. Park, G. Chen, H. R. Atapattu, K. R. Graham, J. Xu, J. Zhu, L. Li, C. Zhang, E. H. Sargent, H. Tan, *Nat.* **2022**, *6037899* **2022**, *603*, 73.
- [26] A. Al-Ashouri, A. Magomedov, M. Roß, M. Jošt, M. Talaikis, G. Chistiakova, T. Bertram, J. A. Márquez, E. Köhnen, E. Kasparavičius, S. Levenco, L. Gil-Escrig, C. J. Hages, R. Schlatmann, B. Rech, T. Malinauskas, T. Unold, C. A. Kaufmann, L. Korte, G. Niaura, V. Getautis, S. Albrecht, *Energy Environ. Sci.* **2019**, *12*, 3356.
- [27] Z. Zhang, C. Cueto, Y. Ding, L. Yu, T. P. Russell, T. Emrick, Y. Liu, *ACS Appl. Mater. Interfaces* **2022**, *14*, 29896.
- [28] M. Jošt, E. Köhnen, A. Al-Ashouri, T. Bertram, Š. Tomšič, A. Magomedov, E. Kasparavičius, T. Kodalle, B. Lipovšek, V. Getautis, R. Schlatmann, C. A. Kaufmann, S. Albrecht, M. Topič, *ACS Energy Lett.* **2022**, *7*, 1298.
- [29] K. O. Brinkmann, T. Becker, F. Zimmermann, C. Kreusel, T. Gahlmann, M. Theisen, T. Haeger, S. Olthof, C. Tückmantel, M. Günster, T. Maschwitz, F. Göbelsmann, C. Koch, D. Hertel, P. Caprioglio, F. Peña-Camargo, L. Perdigón-Toro, A. Al-Ashouri, L. Merten, A. Hinderhofer, L. Gomell, S. Zhang, F. Schreiber, S. Albrecht, K. Meerholz, D. Neher, M. Stolterfoht, T. Riedl, *Nat.* **2022**, *6047905* **2022**, *604*, 280.
- [30] H. Li, W. Zhang, *Chem. Rev.* **2020**, *120*, 9835.
- [31] N. J. Jeon, J. H. Noh, Y. C. Kim, W. S. Yang, S. Ryu, S. Il Seok, *Nat. Mater.* **2014**, *13*, 897.
- [32] N. Ahn, D. Y. Son, I. H. Jang, S. M. Kang, M. Choi, N. G. Park, *J. Am. Chem. Soc.* **2015**,

137, 8696.

- [33] M. Saliba, T. Matsui, J. Y. Seo, K. Domanski, J. P. Correa-Baena, M. K. Nazeeruddin, S. M. Zakeeruddin, W. Tress, A. Abate, A. Hagfeldt, M. Grätzel, *Energy Environ. Sci.* **2016**, *9*, 1989.
- [34] M. Saliba, T. Matsui, K. Domanski, J. Y. Seo, A. Ummadisingu, S. M. Zakeeruddin, J. P. Correa-Baena, W. R. Tress, A. Abate, A. Hagfeldt, M. Grätzel, *Science (80-.)*. **2016**, *354*, 206.
- [35] M. Zhang, J. S. Yun, Q. Ma, J. Zheng, C. F. J. Lau, X. Deng, J. Kim, D. Kim, J. Seidel, M. A. Green, S. Huang, A. W. Y. Ho-Baillie, *ACS Energy Lett.* **2017**, *2*, 438.
- [36] J. J. Yoo, G. Seo, M. R. Chua, T. G. Park, Y. Lu, F. Rotermund, Y. K. Kim, C. S. Moon, N. J. Jeon, J. P. Correa-Baena, V. Bulović, S. S. Shin, M. G. Bawendi, J. Seo, *Nature* **2021**, *590*, 587.
- [37] Y. Huang, X. Lei, T. He, Y. Jiang, M. Yuan, *Adv. Energy Mater.* **2021**, 2100690.
- [38] S.-H. Turren-Cruz, A. Hagfeldt, M. Saliba, *Science (80-.)*. **2018**, *362*, 449.
- [39] R. D. J. Oliver, P. Caprioglio, F. Peña-Camargo, L. R. V Buizza, F. Zu, A. J. Ramadan, S. G. Motti, S. Mahesh, M. M. McCarthy, J. H. Warby, Y.-H. Lin, N. Koch, S. Albrecht, L. M. Herz, M. B. Johnston, D. Neher, M. Stollerfoht, H. J. Snaith, *Energy Environ. Sci.* **2022**, *15*, 714.
- [40] D. Li, Y. Huang, G. Wang, Q. Lian, R. Shi, L. Zhang, X. Wang, F. Gao, W. Kong, B. Xu, C. Cheng, S. Li, *J. Mater. Chem. A* **2021**, *9*, 12746.
- [41] J. Feng, Y. Jiao, H. Wang, X. Zhu, Y. Sun, M. Du, Y. Cao, D. Yang, S. F. Liu, *Energy Environ. Sci.* **2021**, *14*, 3035.
- [42] L. E. Mundt, F. Zhang, A. F. Palmstrom, J. Xu, R. Tirawat, L. L. Kelly, K. H. Stone, K. Zhu, J. J. Berry, M. F. Toney, L. T. Schelhas, *ACS Energy Lett.* **2022**, *7*, 471.
- [43] S. Wang, L. Tan, J. Zhou, M. Li, X. Zhao, H. Li, W. Tress, L. Ding, M. Graetzel, C. Yi (易陈谊), *Joule* **2022**, *6*, 1344.
- [44] K. A. Bush, A. F. Palmstrom, Z. J. Yu, M. Boccard, R. Cheacharoen, J. P. Mailoa, D. P. McMeekin, R. L. Z. Z. Hoye, C. D. Bailie, T. Leijtens, I. M. Peters, M. C. Minichetti, N. Rolston, R. Prasanna, S. Sofia, D. Harwood, W. Ma, F. Moghadam, H. J. Snaith, T. Buonassisi, Z. C. Holman, S. F. Bent, M. D. McGehee, *Nat. Energy* **2017**, *2*, 17009.
- [45] K. Jäger, L. Korte, B. Rech, S. Albrecht, *Opt. Express* **2017**, *25*, A473.

- [46] F. Lamberti, T. Gatti, E. Cescon, M. Meneghetti, A. Petrozza, L. Franco, R. Sorrentino, A. Rizzo, E. Menna, G. Meneghesso, *Chem* **2019**, *5*, 1806.
- [47] E. Kasparavicius, A. Magomedov, T. Malinauskas, V. Getautis, *Chem. - A Eur. J.* **2018**, *24*, 9910.
- [48] X. Lin, D. Cui, X. Luo, C. Zhang, Q. Han, Y. Wang, L. Han, *Energy Environ. Sci* **2020**, *13*, 3823.
- [49] M. Stolterfoht, P. Caprioglio, C. M. Wolff, J. A. Márquez, J. Nordmann, S. Zhang, D. Rothhardt, U. Hörmann, Y. Amir, A. Redinger, L. Kegelman, F. Zu, S. Albrecht, N. Koch, T. Kirchartz, M. Saliba, T. Unold, D. Neher, *Energy Environ. Sci.* **2019**, *12*, 2778.
- [50] J. Warby, F. Zu, S. Zeiske, E. Gutierrez-Partida, L. Frohloff, S. Kahmann, K. Frohna, E. Mosconi, E. Radicchi, F. Lang, S. Shah, F. Peña-Camargo, H. Hempel, T. Unold, N. Koch, A. Armin, F. De Angelis, S. D. Stranks, D. Neher, M. Stolterfoht, *Adv. Energy Mater.* **2022**, *12*, 2103567.
- [51] M. Degani, Q. An, M. Albaladejo-Siguan, Y. J. Hofstetter, C. Cho, F. Paulus, G. Grancini, Y. Vaynzof, *Sci. Adv.* **2021**, *7*, 7930.
- [52] S. Gharibzadeh, P. Fassel, I. M. Hossain, P. Rohrbeck, M. Frericks, M. Schmidt, T. Duong, M. R. Khan, T. Abzieher, B. A. Nejad, F. Schackmar, O. Almora, T. Feeney, R. Singh, D. Fuchs, U. Lemmer, J. P. Hofmann, S. A. L. Weber, U. W. Paetzold, *Energy Environ. Sci.* **2021**, *14*, 5875.
- [53] S. Tang, Y. Peng, Z. Zhu, J. Zong, L. Zhao, L. Yu, R. Chen, M. Li, *J. Phys. Chem. Lett.* **2022**, *2022*, 5116.
- [54] X. Dai, Y. Deng, C. H. Van Brackle, S. Chen, P. N. Rudd, X. Xiao, Y. Lin, B. Chen, J. Huang, *Adv. Energy Mater.* **2020**, *10*, 1903108.
- [55] S. S. Mali, J. V Patil, H. Kim, H. Kim, C. Kook Hong, S. S. Mali, J. V Patil, H. J. Kim, H. H. Kim, C. K. Hong, *Adv. Funct. Mater.* **2019**, *29*, 1807420.
- [56] Y. Yang, H. Peng, C. Liu, Z. Arain, Y. Ding, S. Ma, X. Liu, T. Hayat, A. Alsaedi, S. Dai, *J. Mater. Chem. A* **2019**, *7*, 6450.
- [57] X. Zheng, Y. Hou, C. Bao, J. Yin, F. Yuan, Z. Huang, K. Song, J. Liu, J. Troughton, N. Gasparini, C. Zhou, Y. Lin, D. J. Xue, B. Chen, A. K. Johnston, N. Wei, M. N. Hedhili, M. Wei, A. Y. Alsalloum, P. Maity, B. Turedi, C. Yang, D. Baran, T. D. Anthopoulos, Y. Han, Z. H. Lu, O. F. Mohammed, F. Gao, E. H. Sargent, O. M. Bakr, *Nat. Energy* **2020**, *5*, 131.
- [58] C. Ma, F. T. Eickemeyer, S. H. Lee, D. H. Kang, S. J. Kwon, M. Grätzel, N. G. Park,

Science (80-.). **2023**, 379, 173.

- [59] G. Wu, R. Liang, M. Ge, G. Sun, Y. Zhang, G. Xing, *Adv. Mater.* **2022**, 34, 2105635.
- [60] X. Zheng, B. Chen, J. Dai, Y. Fang, Y. Bai, Y. Lin, H. Wei, X. C. Zeng, J. Huang, *Nat. Energy* 2017 27 **2017**, 2, 1.
- [61] E. Elahi, G. Dastgeer, A. S. Siddiqui, S. A. Patil, M. W. Iqbal, P. R. Sharma, *Dalt. Trans.* **2022**, 51, 797.
- [62] Z. Li, B. Li, X. Wu, S. A. Sheppard, S. Zhang, D. Gao, N. J. Long, Z. Zhu, *Science (80-.).* **2022**, 376, 416.
- [63] J. Li, J. Dagar, O. Shargaieva, M. A. Flatken, H. Köbler, M. Fenske, C. Schultz, B. Stegemann, J. Just, D. M. Többens, A. Abate, R. Munir, E. Unger, *Adv. Energy Mater.* **2021**, 11, 2003460.
- [64] Y. Lin, Y. Firdaus, F. H. Isikgor, M. I. Nugraha, E. Yengel, G. T. Harrison, R. Hallani, A. El-Labban, H. Faber, C. Ma, X. Zheng, A. Subbiah, C. T. Howells, O. M. Bakr, I. McCulloch, S. De Wolf, L. Tsetseris, T. D. Anthopoulos, *ACS Energy Lett.* **2020**, 5, 2935.
- [65] M. Gedda, D. Gkeka, M. I. Nugraha, A. D. Scaccabarozzi, E. Yengel, J. I. Khan, I. Hamilton, Y. Lin, M. Deconinck, Y. Vaynzof, F. Laquai, D. D. C. Bradley, T. D. Anthopoulos, *Adv. Energy Mater.* **2022**, 2201396.
- [66] A. Al-Ashouri, E. Köhnen, B. Li, A. Magomedov, H. Hempel, P. Caprioglio, J. A. Márquez, A. B. Morales Vilches, E. Kasparavicius, J. A. Smith, N. Phung, D. Menzel, M. Grischek, L. Kegelmann, D. Skroblin, C. Gollwitzer, T. Malinauskas, M. Jošt, G. Matič, B. Rech, R. Schlatmann, M. Topič, L. Korte, A. Abate, B. Stannowski, D. Neher, M. Stollerfoht, T. Unold, V. Getautis, S. Albrecht, *Science (80-.).* **2020**, 370, 1300.
- [67] M. Roß, S. Severin, M. B. Stutz, P. Wagner, H. Köbler, M. Favin-Lévêque, A. Al-Ashouri, P. Korb, P. Tockhorn, A. Abate, B. Stannowski, B. Rech, S. Albrecht, *Adv. Energy Mater.* **2021**, 11, 2101460.
- [68] R. Azmi, E. Ugur, A. Seitkhan, F. Aljamaan, A. S. Subbiah, J. Liu, G. T. Harrison, M. I. Nugraha, M. K. Eswaran, M. Babics, Y. Chen, F. Xu, T. G. Allen, A. ur Rehman, C.-L. Wang, T. D. Anthopoulos, U. Schwingenschlögl, M. De Bastiani, E. Aydin, S. De Wolf, *Science (80-.).* **2022**, 376, 73.
- [69] A. Mei, Y. Sheng, Y. Ming, Y. Hu, Y. Rong, W. Zhang, S. Luo, G. Na, C. Tian, X. Hou, Y. Xiong, Z. Zhang, S. Liu, S. Uchida, T. W. Kim, Y. Yuan, L. Zhang, Y. Zhou, H. Han, *Joule*

- 2020**, 4, 2646.
- [70] D. Raptis, C. A. Worsley, S. M. P. Meroni, A. Pockett, M. Carnie, T. Watson, *Sol. 2022*, Vol. 2, Pages 293-304 **2022**, 2, 293.
- [71] J. Gong, S. B. Darling Bc, F. You, *Cite this Energy Environ. Sci* **2015**, 8, 1953.
- [72] R. G. Larson, T. J. Rehg, *Liq. Film Coat.* **1997**, 709.
- [73] J. Danglad-Flores, S. Eickelmann, H. Riegler, *Chem. Eng. Sci.* **2018**, 179, 257.
- [74] Y. Vaynzof, Y. Vaynzof, *Adv. Energy Mater.* **2020**, 10, 2003073.
- [75] C. Liu, Y. B. Cheng, Z. Ge, *Chem. Soc. Rev.* **2020**, 49, 1653.
- [76] Y. Deng, X. Zheng, Y. Bai, Q. Wang, J. Zhao, J. Huang, *Nat. Energy* **2018**, 3, 560.
- [77] X. Li, D. Bi, C. Yi, J. D. Décoppet, J. Luo, S. M. Zakeeruddin, A. Hagfeldt, M. Grätzel, *Science (80-.)*. **2016**, 353, 58.
- [78] F. Guo, S. Qiu, J. Hu, H. Wang, B. Cai, J. Li, X. Yuan, X. Liu, K. Forberich, C. J. Brabec, Y. Mai, F. Guo, S. Qiu, J. Hu, J. Li, Y. Mai, H. Wang, B. Cai, X. Yuan, X. Liu, K. Forberich, C. J. Brabec, *Adv. Sci.* **2019**, 6, 1901067.
- [79] J. E. Bishop, J. A. Smith, C. Greenland, V. Kumar, N. Vaenas, O. S. Game, T. J. Routledge, M. Wong-Stringer, C. Rodenburg, D. G. Lidzey, *ACS Appl. Mater. Interfaces* **2018**, 10, 39428.
- [80] F. Huang, Y. Dkhissi, W. Huang, M. Xiao, I. Benesperi, S. Rubanov, Y. Zhu, X. Lin, L. Jiang, Y. Zhou, A. Gray-Weale, J. Etheridge, C. R. McNeill, R. A. Caruso, U. Bach, L. Spiccia, Y.-B. Cheng, *Nano Energy* **2014**, 10, 10.
- [81] Y. Yu, F. Zhang, T. Hou, X. Sun, H. Yu, M. Zhang, *Sol. RRL* **2021**, 2100386.
- [82] C. Wu, K. Wang, J. Li, Z. Liang, J. Li, W. Li, L. Zhao, B. Chi, S. Wang, *Matter* **2021**, 4, 775.
- [83] K. Bruening, B. Dou, J. Simonaitis, Y. Y. Lin, M. F. A. M. van Hest, C. J. Tassone, *Joule* **2018**, 2, 2464.
- [84] Y. Zhou, A. Najar, J. Zhang, J. Feng, Y. Cao, Z. Li, X. Zhu, D. Yang, S. F. Liu, *Cite This ACS Appl. Mater. Interfaces* **2022**, 14, 28729.
- [85] Health and Safety Executive, *List of Workplace Exposure Limits (WELS) (Fourth Edition 2020)*, **2020**.
- [86] S. Tobiska, P. Kleinebudde, *Pharm. Dev. Technol.* **2003**, 8, 39.
- [87] R. J. Lang, *Cit. J. Acoust. Soc. Am.* **1962**, 34, 6.
- [88] N. Rolston, W. J. Scheideler, A. C. Flick, J. P. Chen, H. Elmaraghi, A. Sleugh, O. Zhao, M. Woodhouse, R. H. Dauskardt, *Joule* **2020**, 4, 2675.

- [89] Z. Liu, N. Rolston, A. C. Flick, T. W. Colburn, Z. Ren, R. H. Dauskardt, T. Buonassisi, *Joule* **2022**, *6*, 834.
- [90] A. T. Barrows, A. J. Pearson, C. K. Kwak, A. D. F. Dunbar, A. R. Buckley, D. G. Lidzey, *Energy Environ. Sci.* **2014**, *7*, 2944.
- [91] Q. Liang, K. Liu, M. Sun, Z. Ren, P. W. K. Fong, J. Huang, M. Qin, Z. Wu, D. Shen, C. S. Lee, J. Hao, X. Lu, B. Huang, G. Li, *Adv. Mater.* **2022**, *34*, 2200276.
- [92] M. Du, X. Zhu, L. Wang, H. Wang, J. Feng, X. Jiang, Y. Cao, Y. Sun, L. Duan, Y. Jiao, K. Wang, X. Ren, Z. Yan, S. Pang, S. (Frank) Liu, *Adv. Mater.* **2020**, *32*, 2004979.
- [93] J. E. Bishop, C. D. Read, J. A. Smith, T. J. Routledge, D. G. Lidzey, *Sci. Rep.* **2020**, *10*, 6610.
- [94] S. Bose, S. S. Keller, T. S. Alstrøm, A. Boisen, K. Almdal, *Langmuir* **2013**, *29*, 6911.
- [95] M. Majumder, C. Rendall, M. Li, N. Behabtu, J. A. Eukel, R. H. Hauge, H. K. Schmidt, M. Pasquali, *Chem. Eng. Sci.* **2010**, *65*, 2000.
- [96] J. E. Bishop, T. J. Routledge, D. G. Lidzey, *J. Phys. Chem. Lett.* **2018**, *9*, 1977.
- [97] K. Liu, Q. Liang, M. Qin, D. Shen, H. Yin, Z. Ren, Y. Zhang, H. Zhang, P. W. K. Fong, Z. Wu, J. Huang, J. Hao, Z. Zheng, S. K. So, C. Lee, X. Lu, G. Li, *Joule* **2020**, *4*, 2404.
- [98] S. Ulična, B. Dou, D. H. Kim, K. Zhu, J. M. Walls, J. W. Bowers, M. F. A. M. Van Hest, *ACS Appl. Energy Mater.* **2018**, *1*, 1853.
- [99] M. Yang, Z. Li, M. O. Reese, O. G. Reid, D. H. Kim, S. Siol, T. R. Klein, Y. Yan, J. J. Berry, M. F. A. M. Van Hest, K. Zhu, *Nat. Energy* **2017**, *2*, 1.
- [100] H. Cai, X. Liang, X. Ye, J. Su, J. Guan, J. Yang, Y. Liu, X. Zhou, R. Han, J. Ni, J. Li, J. Zhang, *ACS Appl. Energy Mater.* **2020**, *3*, 9696.
- [101] J. E. Bishop, J. A. Smith, C. Greenland, V. Kumar, N. Vaenas, O. S. Game, T. J. Routledge, M. Wong-Stringer, C. Rodenburg, D. G. Lidzey, *ACS Appl. Mater. Interfaces* **2018**, *10*, 39428.
- [102] C. Gao, P. Wang, H. Wang, C. Yu, B. Du, H. Zhang, T. Li, D. Liu, T. Wang, *ACS Appl. Energy Mater.* **2021**, *4*, 11496.
- [103] J. A. Smith, O. S. Game, J. E. Bishop, E. L. K. K. Spooner, R. C. Kilbride, C. Greenland, R. Jayaprakash, T. I. Alanazi, T. I. Alanazi, E. J. Cassella, A. Tejada, A. Tejada, G. Chistiakova, M. Wong-Stringer, T. J. Routledge, A. J. Parnell, D. B. Hammond, D. G. Lidzey, *ACS Appl. Energy Mater.* **2020**, *3*, 5552.
- [104] A. Pang, J. Li, X. F. Wei, Z. W. Ruan, M. Yang, Z. N. Chen, *Nanoscale Adv.* **2020**, *2*, 4062.

- [105] P. Wu, S. Wang, X. Li, F. Zhang, *J. Mater. Chem. A* **2021**, *9*, 19554.
- [106] D. Blackburn, T. J. Routledge, M. O’Kane, E. J. Cassella, O. S. Game, T. E. Catley, C. J. Wood, T. McArdle, D. G. Lidzey, *Sol. RRL* **2022**, *6*, 2200263.
- [107] S. Lin, B. Yang, X. Qiu, J. Yan, J. Shi, Y. Yuan, W. Tan, X. Liu, H. Huang, Y. Gao, C. Zhou, *Org. Electron.* **2018**, *53*, 235.
- [108] H. Min, D. Y. Lee, J. Kim, G. Kim, K. S. Lee, J. Kim, M. J. Paik, Y. K. Kim, K. S. Kim, M. G. Kim, T. J. Shin, S. Il Seok, *Nat. 2021 5987881* **2021**, *598*, 444.
- [109] M. Kim, J. Jeong, H. Lu, T. K. Lee, F. T. Eickemeyer, Y. Liu, I. W. Choi, S. J. Choi, Y. Jo, H. B. Kim, S. I. Mo, Y. K. Kim, H. Lee, N. G. An, S. Cho, W. R. Tress, S. M. Zakeeruddin, A. Hagfeldt, J. Y. Kim, M. Grätzel, D. S. Kim, *Science (80-.)*. **2022**, *375*, 302.
- [110] G. Tumen-Ulzii, C. Qin, T. Matsushima, M. R. Leyden, U. Balijipalli, D. Klotz, C. Adachi, *Sol. RRL* **2020**, *4*, 2000305.
- [111] H. D. Pham, Z. Wu, L. K. Ono, S. Manzhos, K. Feron, N. Motta, Y. Qi, P. Sonar, *Adv. Electron. Mater.* **2017**, *3*, 1700139.
- [112] A. J. Bett, K. M. Winkler, M. Bivour, L. Cojocar, Ö. Kabakli, P. S. C. Schulze, G. Siefer, L. Tutsch, M. Hermle, S. W. Glunz, J. C. Goldschmidt, *ACS Appl. Mater. Interfaces* **2019**, *11*, 45796.
- [113] F. Ali, C. Roldán-Carmona, M. Sohail, M. K. Nazeeruddin, *Adv. Energy Mater.* **2020**, *10*, 2002989.
- [114] A. Magomedov, A. Al-Ashouri, E. Kasparavičius, S. Strazdaite, G. Niaura, M. Jošt, T. Malinauskas, S. Albrecht, V. Getautis, *Adv. Energy Mater.* **2018**, *8*, 1801892.
- [115] L. Li, Y. Wang, X. Wang, R. Lin, X. Luo, Z. Liu, K. Zhou, S. Xiong, Q. Bao, G. Chen, Y. Tian, Y. Deng, K. Xiao, J. Wu, M. I. Saidaminov, H. Lin, C. Ma, Z. Zhao, Y. Wu, L. Zhang, H. Tan, *Nat. Energy* **2022**, DOI 10.1038/s41560-022-01045-2.
- [116] O. Almora, D. Baran, G. C. Bazan, C. Berger, C. I. Cabrera, K. R. Catchpole, S. Erten-Ela, F. Guo, J. Hauch, A. W. Y. Ho-Baillie, T. J. Jacobsson, R. A. J. Janssen, T. Kirchartz, N. Kopidakis, Y. Li, M. A. Loi, R. R. Lunt, X. Mathew, M. D. McGehee, J. Min, D. B. Mitzi, M. K. Nazeeruddin, J. Nelson, A. F. Nogueira, U. W. Paetzold, N. Park, B. P. Rand, U. Rau, H. J. Snaith, E. Unger, L. Vaillant-Roca, H. Yip, C. J. Brabec, *Adv. Energy Mater.* **2021**, *11*, 2002774.
- [117] M. Saliba, L. Etgar, *ACS Energy Lett.* **2020**, *5*, 2886.
- [118] S. Ravishankar, C. Aranda, P. P. Boix, J. A. Anta, J. Bisquert, G. Garcia-Belmonte, *J.*

Phys. Chem. Lett. **2018**, *9*, 3099.

[119] H. Stanjek, W. Häusler, *Hyperfine Interact.* **2004**, *154*, 107.

[120] W. L. Tan, C. R. McNeill, *Appl. Phys. Rev.* **2022**, *9*, 021310.

[121] C. Wang, C. Zuo, Q. Chen, L. Ding, *J. Semicond.* **2021**, *42*, 060201.

Experimental Methods

3.1 Introduction

This chapter thoroughly details the fabrication and characterisation techniques used throughout this thesis.

3.1.1 Materials

All materials and solvents were used as received without any further purification. MeO-2PACz (>98%), 2PACz (>98%) and PbI₂ (99.99% trace metals basis) were purchased from TCI Chemicals. Methylammonium iodide (MAI, >99.9%), 20 mm x 15 mm ITO (~20 Ω/□), TEC10 FTO (11-13 Ω/□), 2,2',7,7'-Tetrakis[N,N-di(4-methoxyphenyl)amino]-9,9'-spirobifluorene (Spiro-OMeTAD, >99.5% purity), Formamidinium Iodide (FAI, >99.5% purity), and iso-butylammonium bromide (i-BABr, > 98%) were purchased from Ossila. All solvents and remaining materials including C₆₀ (sublimed, 99.99 %), bathocuproine (BCP, sublimed, 99.99 %), PbCl₂ (99.999% trace metals basis) and CsI (99.999% trace metals basis), were purchased from Sigma Aldrich unless otherwise stated.

Pre-patterned 20 mm x 15 mm ITO-coated glass substrates (~20 Ω/□) were purchased from Ossila. Where non-patterned ITO-coated substrates were used, zinc and acid (4 M, HCl) etch was used to selectively pattern the ITO. A schematic and corresponding image of the device structure and “8-pixel” layout are shown in **Figure 3.1**. All substrates were then cleaned by subsequent ultrasonication in diluted Helmanex solution, boiling deionized water, acetone, and IPA consecutively. Substrates were then dried under a flow of N₂, and UV ozone treated for at least 15 minutes immediately prior to further processing. All perovskite solutions were filtered into a clean, glass vial through a 0.2 μm PTFE filter prior to deposition.

Note that we observed a small increase in device performance over the first few days of testing. All device PCEs are reported at their highest point, typically 3 days after fabrication of the perovskite layer.

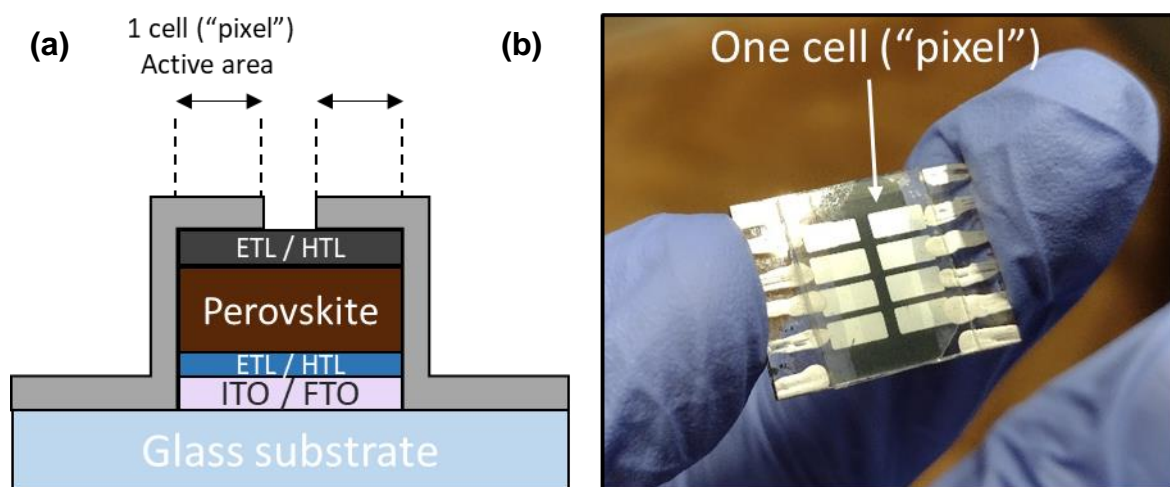


Figure 3.1: (a) Side-view schematic of a coated substrate illustrating two individual cells, where ETL is an electron-transporting layer and HTL is a hole-transporting layer. (b) A photograph of a fabricated device, where 8 individual cells (or “pixels”) are defined per substrate.

3.1.2 Device Fabrication

3.1.2.1 Chapter Four

Hole-transport layer:

Spin coating: A stock solution of the SAM (1 mmol in ethanol) was prepared and stored under N₂, with a small amount decanted for use as necessary. Solutions were vortex mixed for ~30 s immediately prior to usage. 60 μ L of the SAM solution was spin-coated for 30 s at 3000 rpm in a N₂-filled glovebox, followed by annealing at 100 °C for 10 minutes. No subsequent rinsing steps were applied.

Dip coating: SAM solutions (0.1 mmol in ethanol) were prepared by diluting a quantity of the stock solution. Dip coating was conducted in a polypropylene beaker to minimize usage of material. Cleaned substrates were immersed in the solution overnight under ambient conditions, with the beaker sealed using Parafilm. After deposition, the excess solution was removed with an N₂ gun. Substrates were then moved into the glovebox and annealed at 100 °C for 10 minutes. After annealing, dip-coated substrates were rinsed three times by successive submersion in ethanol and then dried using an N₂ flow.

Spray coating: SAM solutions (0.1 mmol in ethanol) were prepared by diluting the stock solution. Spray coating was performed using a Sonotek Exactacoat system mounted with an Impact spray head. The SAM solution was delivered through a vibrating piezoelectric tip at a flow rate of 1.5 ml min⁻¹. The spray head was moved in three passes over the substrate surface at a separation of around 3 cm at a speed of 40 mm s⁻¹. Optimized performance was achieved by subjecting spray-coated substrates to a single rinse performed immediately after the deposition of the SAM by submersion in ethanol whilst the film was still wet. Substrates were then dried under an N₂ flow and annealed at 100 °C for 10 minutes. After annealing, the substrates were rinsed three times by successive submersion in ethanol and then dried with a N₂ flow.

Airbrush coating: SAM solutions (0.1 mmol in ethanol) were prepared by diluting the stock solution. Solutions were loaded into an airbrush pen located in a N₂ filled glovebox. Substrates were spray-coated until a uniform, wet film was created. They were then annealed at 100 °C for 10 minutes. After annealing, the airbrush-coated substrates were rinsed three times by successive submersion in ethanol and then dried with a N₂ flow.

Perovskite:

Spin coating: A MAPbI₃ (1 M) precursor in 2-methoxy ethanol (2-ME) was prepared and deposited according to a previously reported protocol.^[20] Briefly, PbI₂ (461 mg ml⁻¹) and MAI (159 mg ml⁻¹) were dissolved in 2-ME by combination of vortex mixing and stirring. Dimethyl-sulfoxide (DMSO) was introduced as an additive at a concentration of ~11.77 mol%. 60 µl of the precursor solution was dropped onto the centre of the substrate before it was spun at 800 rpm s⁻¹ for 5 s, followed by 4000 rpm for 35 s. An N₂ flow of around 20 psi was directed at the substrate starting 6 s after the beginning of the spin program. The MAPbI₃ films were then annealed at 100 °C for 10 minutes.

Spray coating: 2-ME MAPbI₃ (0.5 M – 1 M) precursor solutions were deposited using a Sonotek Exactacoat System. The solution was delivered at a flow rate of 1.5 ml min⁻¹ to the Impact head which operated at 2 W. During coating, the spray head moved over the substrate at a distance of around 3 cm at a speed of 80 mm s⁻¹. No heating was applied to the substrate during deposition. After deposition of the perovskite precursor, an automated gantry passed an air knife (Meech A8 80 mm Air Knife, RS Components) over the substrate at a speed of 3 mm s⁻¹ and a distance of around 2 cm from the surface. This

delivered an N₂ flow at 20 psi to the surface at an angle of 45° from the substrate normal. This process occurred after a delay time of between 5 and 60 s after spray coating, with a delay of 30 s corresponding to the optimized process. **Figure 3.2** shows the equipment setup used for the spray coating processes. Perovskite films were then annealed at 100 °C for 10 minutes.

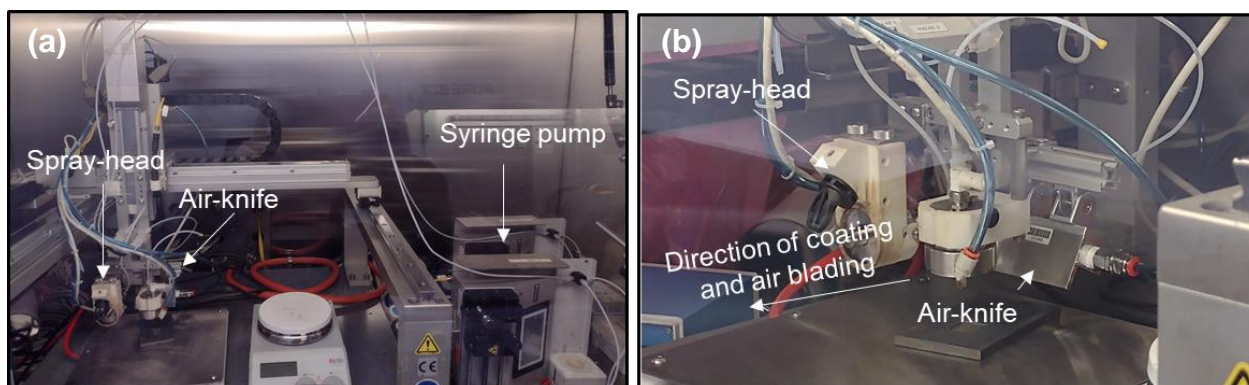


Figure 3.2: (a) A perovskite precursor solution is fed to the spray-head by a syringe pump. The head moves forward in one-pass over an underlying substrate. After a short delay time, the air knife is passed over the substrate in the same direction as the spray-head pass. (b) A close-up image of the spray-head and air-knife, indicating the direction of gantry movement over a substrate.

Electron-transport layer and cathode:

The substrates were transferred to a thermal evaporator (Angstrom Engineering). BCP (8 nm), C₆₀ (23 nm) and silver (100 nm) were deposited sequentially through shadow masks without breaking vacuum. During evaporation, the chamber base pressure was maintained at $< 2.4 \times 10^{-6}$ mbar. BCP and C₆₀ were deposited using RADAK sources at a constant rate of 0.1 \AA s^{-1} . It was found that the C₆₀ became discoloured after each evaporation run and was therefore replaced with fresh material each time. Silver pellets (Lesker) were deposited from resistive sources at a rate of $0.1 - 1.0 \text{ \AA s}^{-1}$. Following evaporation, devices were encapsulated using an epoxy pen (Bluefixx Blue LED Repair Pen, CPC UK) and glass encapsulation coverslips (Ossila). For some devices, an anti-reflective coating of LiF (Lithium Fluoride, 100nm) was applied to the substrate back-surface by thermally evaporating at 1 \AA s^{-1} at a base pressure of at least 4×10^{-6} mbar.

3.1.2.2 Chapter Five

Spin-coated layers: To deposit nanoparticle-SnO₂ electron transport layers, a colloidal SnO₂ solution (15 wt% in H₂O, Alfa Aesar) diluted 1:4 in deionized water was

statically spin coated at 3000 rpm, prior to annealing at 150 °C for 30 minutes and then UV ozone treated for a further 15 minutes. A 2 M $\text{Cs}_{0.15}\text{FA}_{0.75}\text{PbI}_{2.85}\text{Cl}_{0.15}$ precursor ink was prepared according to previously reported procedures.^[22] Briefly, 1 ml of the precursor solution contained 285.5 mg FAI, 922 mg PbI_2 , 55.6 mg of PbCl_2 and 88.3 mg CsI dissolved in 1 ml of DMF, with 192.9 μL of NMP added. We found that the purity of the FAI was critical to device performances (see **Figure S2**). The precursor solution was spin-coated onto SnO_2 -coated substrates in a N_2 -filled glovebox at 5000 rpm for 50 s, before annealing at 70 °C for 5 minutes inside the glovebox and then at 150 °C for ten minutes in a ~50 %RH ambient cleanroom. Spin-passivated substrates had 50 μl of a 15 mM solution of i-BABr in IPA statically deposited and subsequently spun at 4000 rpm for 20 seconds, before being annealed on a hot plate at 100 °C for 5 minutes. Spiro-OMeTAD (86 mg ml^{-1}) was dissolved in chlorobenzene, then doped with 34 $\mu\text{l ml}^{-1}$ 4-tert-butyl-pyridine, 20 $\mu\text{l ml}^{-1}$ of a lithium bis(trifluoromethanesulfonyl)imide solution (500 mg ml^{-1} in acetonitrile) and 11 μl of FK209 solution (FK209 Co(II) PF_6 salt, 300 mg ml^{-1} in acetonitrile). The solution was thoroughly vortex mixed and filtered through a 0.2 μm PTFE filter before spin coating dynamically at 4000 rpm 20 seconds. The Spiro-OMeTAD-coated devices were left to oxidize overnight in a dry box.

Spray-coated layers: A 1.1 M $\text{Cs}_{0.15}\text{FA}_{0.75}\text{PbI}_{2.85}\text{Cl}_{0.15}$ precursor ink was prepared by dilution from a 2 M precursor ink. The 1.1 M ink was spray-coated in a nitrogen-filled glovebox using a Sonotek Exactacoat system. The substrate was held at 30 °C in the optimized protocol described in the main text. A motorized-gantry moved the spray head over the substrate surface at a speed of 80 mm s^{-1} and a tip-surface separation of around 10 cm. The precursor ink was delivered at a flow rate of 1 ml min^{-1} through a tip driven at 2 W and directed to the substrate surface by a N_2 gas flow at a pressure of 3 psi. After a short delay time (25 seconds for optimized devices), an air knife (Meech A8 80 mm Air Knife, RS Components) was passed over the substrate surface at a speed of 3 mm s^{-1} and distance of around 2 cm, blowing ambient-temperature N_2 at a pressure of 20 psi and an angle of 45 ° from the surface normal. The perovskite films were subsequently annealed at 70 °C for 5 minutes in the glovebox, and then at 150 °C in ambient conditions in a ~50 %RH cleanroom. Spray-passivation was then performed within an N_2 -filled glovebox. For spray-passivated films, an i-BABr solution (either 7.5 mM or 15 mM in IPA) was delivered to the spray-head at a flow rate of 1.5 ml min^{-1} . A piezoelectric tip operated at 1W formed

a droplet mist which was directed at the substrate by a flow of N₂ at a pressure of 3 psi. In our optimized process, the spray-head passed once over the substrate held at room temperature at a speed of 40 mm s⁻¹. The spray-passivated films were then annealed at 100 °C for 5 minutes.

Evaporated layers and contacts: Device layers were patterned using a razorblade before evaporation of an Au (Cooksongold, 80 nm) back contact through a shadow-mask at 0.1-1.0 Å s⁻¹.

3.1.2.3 Chapter Six

A stock solution of the MeO-2PACz (1 mmol in ethanol) was prepared and stored under N₂, with a small amount decanted for use as necessary. We have so far found this stock solution to be stable (no difference in resulting device performance) over a period of 18 months. 60 µL of MeO-2PACz solution was statically spin-coated onto the substrate for 30 s at 3000 rpm in an N₂-filled glovebox. Where the MeO-2PACz was annealed, the as-spun films were transferred to a hotplate at 100 °C for 10 min. No subsequent rinsing steps were applied.

A MAPbI₃ precursor ink (0.5 M) was prepared in different compositions of tetrahydrofuran (THF): 2-methoxyethanol (2-ME). Stoichiometric quantities of MAI and PbI₂ (i.e., 79.5 mg ml⁻¹ and 230.5 mg ml⁻¹, respectively) were dissolved in the appropriate ratio of the two solvents and dissolved by stirring overnight. The best-performing binary composition investigated here was based on a 1: 9 ratio of THF: 2-ME. The precursor inks were spin-coated at 800 rpm s⁻¹ for 5 s, then 4000 rpm for 35 s. At 6 s into the spinning, a “gas-quench” was employed wherein an N₂ flow of ~20 psi was directed at the spinning substrate, immediately inducing a colour change from yellow to dark brown.

The C₆₀/BCP electron-transporting layer was thermally evaporated (Angstrom Engineering) at a chamber base pressure of at least 2.4 × 10⁻⁶ mbar from alumina crucible sources (RADAK, Luxel Corp.) at a constant rate of 0.1 Å s⁻¹. Silver pellets (Lesker) were deposited from a resistive boat source at a ramped rate of 0.1–1.0 Å s⁻¹ through a shadow mask to form the Ag back-electrode. Devices were then encapsulated using an epoxy pen (Bluefixx Blue LED Repair Pen, Combined Precision Components) and glass encapsulation coverslips (Ossila).

3.2 Device Characterisation

Current-voltage Measurements: JV measurements were recorded under ambient conditions using a Newport 92251A-1000 solar simulator. No preconditioning of devices was carried out. Prior to testing, the AM1.5 spectrum was adjusted to 100 mW cm⁻² at the substrate holder location using an NREL certified silicon reference cell. The active measurement area was defined using metal aperture masks with a calibrated area of 2.5 mm². A Keithley 237 source-measure unit swept devices between -0.1 V and 1.2 V at 100 mV s⁻¹. Stabilized power output (SPO) measurements were performed by holding the device at a bias defined by the average voltage at maximum power (V_{mpp}) determined from the forward and reverse sweeps. Note that an increase in device PCE was frequently observed over the first few days after fabrication.

Profilometry: A Bruker DekTak XT surface profilometer was used to investigate large-area morphology of the thin films deposited. A stylus (12.5 μm radius tip) was raster scanned over the surface (1000 μm lines each separated by 1 μm) using a stylus force of 3 mg. The resultant line scans were stitched together to form a large-area topographical 'map'. Map profiles were processed using Gwyddion software to remove artificial curvature and step line correct in both the x and y axis. Roughness measurements were extracted using the same software. Film thickness measurements were collected using this system. A razor blade was used to scratch the perovskite thin films prepared as described above. The profilometer tip (12.5 μm diameter) was scanned 1000 μm across this "scratch" in the film surface at a stylus force of 3 mg. Vison64 software (Bruker) was used to level the 1D line scan and extract a step height from the film to the scratched valley.

External quantum efficiency: External quantum efficiency measurements were recorded over a 325-900 nm range using a Newport QuantX-300 Quantum Efficiency Measurement System. The system was equipped with a 100 W Xenon arc lamp focused through an Oriel Monochromator (CS130B) and chopped at 25 Hz.

X-ray diffraction (XRD): XRD data was recorded at room temperature using a PANalytical X'Pert Pro system equipped with a Copper Line Focus X-ray tube run at 45 kV with a tube current of 40 mA. The diffractometer operated in Bragg-Brentano geometry to record diffraction patterns from 5° to 99.99° 2θ.

Scanning electron microscopy (SEM): SEM top-down images of the perovskite surface for Chapter Four were recorded using an FEG-Raith SEM at a working distance of ~4.5 mm and beam energy of 1.5 kV. Grain size analysis was performed using ImageJ software. SEM images for Chapters Five and Six were recorded using an FEI Nova Nano450 SEM operating at a beam energy of 1.5 kV at a working distance of 4–5 mm, with an in-lens detector used to collect backscattered electrons.

Atomic Force Microscopy (AFM): The samples were imaged using Atomic Force Microscopy (Veeco Dimension 3100) in Intermittent Contact (Tapping) Mode with a NuNano Scout 350 cantilever (nominal spring constant 42 N/m, resonant frequency 350 kHz). Each sample was scanned over two 10x10 μm areas with a resolution of 512x512 pixels.

Grazing incidence wide-angle X-ray scattering (GIWAXS): GIWAXS measurements were performed using a Xenocs Xeuss 2.0 beamline system equipped with a liquid Ga X-ray source (Excillum MetalJet) and a Dectris Pilatus 1M pixel detector. The beam was directed at the surface at an angle of incidence of 0.3°. Perovskite films for GIWAXS were prepared as for devices, being deposited on top of SnO₂-coated ITO substrates.

Steady-state Photoluminescence: Steady state photoluminescence (SSPL) measurements were performed using a homemade setup consisting of a 400 nm excitation wavelength laser and a VIS-NIR fibre-optic spectrometer (Ocean Insight Flame) with an integration time of 100 ms. Unless otherwise stated, samples were prepared directly on clean quartz substrates (Ossila) by the same deposition methods as for device fabrication.

Absorbance: Ultraviolet-Visible (UV-Vis) absorption measurements were performed using a home-made set up consisting of an Ocean Optics light source (DH-2000-BAL) and an Ocean Optics spectrometer (HR2000+ES). Measurements were recorded in transmission mode and referenced to a blank substrate (quartz). UV-Visible transmission measurements for Chapter Six were recorded using a Fluoromax-4 fluorometer (Horiba), with corresponding absorbance values calculated according to the logarithmic relationship $A = -\log_{10} T$. Precursor inks were diluted to 0.05 M to prevent saturation of the detector and referenced to the empty quartz cuvette used for measurements. UV-Vis measurements for the precursor inks were recorded over the spectral range 250 – 500 nm. Perovskite films for UV-Vis measurements were prepared

following the device procedure described above on cleaned quartz glass. Spectra were recorded over the wavelength range 600 – 800 nm and referenced to plain, quartz glass.

X-ray Photoelectron Spectroscopy (XPS): ITO-coated glass substrates were mounted onto the sample holder with double sided carbon tape, and then copper alloy bars were screwed into the sample holder in such a way that they overlapped slightly the top and bottom edges of each sample in order to ensure the treated surface was not electrically isolated. Charge neutralisation was also used to prevent surface charge build-up. The analyses were carried out using a Kratos Supra instrument with a monochromated aluminium source, and two analysis points per sample, of area 700 μm by 300 μm . Survey scans were collected between 1200 to 0 eV binding energy, at 160 eV pass energy, 1 eV intervals, and 300 seconds/sweep with one sweep being collected. High-resolution O 1s, C 1s, In 3d, N 1s and P 2p XPS spectra were also collected at 20 eV pass energy and 0.1 eV intervals for each analysis point over an appropriate energy range, with one 300 second sweep for all spectra except N 1s and P 2p for which two sweeps were collected. The data collected was calibrated in intensity using a transmission function characteristic of the instrument to make the values instrument independent. The data can then be quantified using theoretical Schofield relative sensitivity factors modified to account for instrument geometry, variation in penetration depth with energy and the angular distribution of the photoelectrons. The binding energy scale was calibrated for all samples by fixing In 3d_{5/2} at 444.57 eV. This In 3d_{5/2} value puts the main C 1s peak for the ITO samples at 285.0 eV, consistent with the assumption it is carbonaceous contamination.

Contact angle measurements of droplets on thin-films were performed using a contact angle goniometer (Ossila). A small droplet of water was deposited onto the substrate surface and recorded at 20 fps. The Ossila contact angle software was then used to extract the angle between the droplet and the sample surface at the point of initial contact.

Optical Microscope images were recorded using a Nikon Eclipse ME600 microscope at 50x magnification.

Gas-Assisted Spray Coating of Perovskite Solar Cells Incorporating Sprayed Self-Assembled Monolayers

4.1. Publication Foreword

Whilst spray-coated PSCs had finally surpassed 20 % PCE in 2020, the techniques employed to induce crystallization – namely anti-solvent baths, or vacuum-based processes – posed difficulties for upscaling, particularly into a R2R process. Gas-quenching, wherein a gas-flow promotes solvent evaporation and induces nucleation, had become a mature technology in most other scalable PSC processing techniques. A clear “gap in the market” therefore existed to combine this technology with a spray-coating process to demonstrate fully R2R-compatible PSC fabrication.

Around the same time, towards the end of 2019, a promising new class of hole-selective self-assembled molecules (SAMs) were developed by researchers at Helmholtz-Zentrum Berlin and Kaunas University of Technology, Lithuania. This class of SAMs has now been used in an NREL certified world-record 29.15% monolithic perovskite/Si tandem solar cell, and demonstrated exceptional stability in planar devices, retaining 100% of the initial device efficiency after 1000 hours of illumination. Promising stability, versatility, low-cost, *and* performance, these SAMs were an opportunity not to be missed.

We therefore developed protocols to both spray coat the SAM as a hole-selective layer in *p-i-n* PSCs, and to spray coat and gas-quench (using an “air-knife”) a perovskite active layer on top. Using this approach, we created state-of-the-art spray-coated devices achieving PCEs of up to 20.8%. This publication was accepted into the journal “Advanced Science” and published as the front cover article.

The air-knife has since facilitated a number of novel spray coating approaches within our lab, including controlling the drying (and resultant morphology) of spray-coated organic solar cells, and depositing PSCs over non-planar substrates.

4.2. Author Contributions

E.J. Cassella conceptualised the project; fabricated all samples; performed all data analysis and created figures; wrote the original draft manuscript and completed further edits. **E.L.K. Spooner** assisted with data analysis and manuscript writing. **T. Thornber** recorded XRD patterns. **M.E. O’Kane** recorded SEM images. **T.E. Catley** provided AFM measurements. **J.E. Bishop** provided initial assistance with the spray coating equipment. **J.A. Smith** and **O.S. Game** assisted with editing the draft manuscript. **D.G. Lidzey** provided funding, and equipment, and assisted with editing the draft manuscript.

4.3. Publication Main Text

Gas-Assisted Spray Coating of Perovskite Solar Cells Incorporating Sprayed Self-Assembled Monolayers

DOI: 10.1002/adv.202270087

*Elena J. Cassella, Emma L.K. Spooner, Timothy Thornber, Mary E. O’Kane, Thomas E. Catley, James E. Bishop, Joel A. Smith, Onkar S. Game, David G. Lidzey**

E.J. Cassella, E.L.K. Spooner, T. Thornber, M.E. O’Kane, T.E. Catley, Dr. J.E. Bishop, Dr. O.S. Game, Prof. D.G. Lidzey

Department of Physics and Astronomy, University of Sheffield, Hicks Building, Hounsfield Road, Sheffield, S3 7RH, United Kingdom

E-mail: d.g.lidzey@sheffield.ac.uk

Dr. J.A. Smith

Department of Physics, University of Oxford, Clarendon Laboratory, Parks Road, Oxford, OX1 3PU, United Kingdom

4.3.1. Abstract

Self-assembled monolayers (SAMs) are becoming widely utilized as hole-selective layers in high-performance p-i-n architecture perovskite solar cells. In this work, we demonstrate ultrasonic spray coating and airbrush coating as effective methods to deposit MeO-2PACz; a carbazole-based SAM. We overcome potential dewetting of hybrid perovskite precursor solutions from this layer using optimized solvent rinsing protocols. We then explore the use of air-knife gas-quenching to rapidly remove the volatile solvent from a MAPbI₃ precursor film spray-coated onto a MeO-2PACz SAM, allowing us to fabricate p-i-n devices with power conversion efficiencies in excess of 20%, with all other layers thermally evaporated. This combination of deposition techniques is consistent with a rapid, roll-to-roll manufacturing process for the fabrication of large-area solar cells.

4.3.2. Introduction

Organic-inorganic metal halide perovskite photo-absorbers have enabled the development of single-junction perovskite solar cells (PSCs) with power conversion efficiencies (PCEs) of up to 25.5%.^[1] Further gains in device efficiency (towards the theoretical thermodynamic efficiency limit) are anticipated via the further suppression of nonradiative recombination pathways within PSCs, both within the bulk perovskite material and at the transport layer interfaces.^[2–4] Losses at such interfaces have generally limited the efficiency of p-i-n ('inverted') architectures compared to n-i-p PSCs. However, p-i-n devices offer promising operational stability, competitive large-area performances and compatibility with silicon bottom cells in perovskite/Si tandem devices.^[5–8] For this reason, the development of surface passivation and interface management strategies have been the focus of recent efforts to enhance p-i-n PSC device performance.^[9,10] One material system of particular interest are self-assembled monolayers (SAMs) that comprise carbazole moieties and phosphonic acid tail groups, with such materials capable of creating practically lossless hole-transport interfaces.^[11,12] SAMs, therefore, represent a simple and low-cost PSC technology, with state-of-the-art inverted devices demonstrating PCEs approaching 23%^[13] and perovskite/Si tandems surpassing 29%.^[14]

To drive PSC technology towards commercialization, it is increasingly important to develop new perovskite and charge-transporting materials that combine high-performance, enhanced operational stability, low-cost and the ability to be deposited

using scalable techniques.^[15] In n-i-p PSCs, the widely-used hole-transport layer (HTL) spiro-OMeTAD has been a bottleneck to the development of large-area devices due to a combination of thermal and dopant instability and high materials cost.^[16,17] Other commonly used p-i-n HTLs also have drawbacks; for example the conjugated polymers PTAA and poly-TPD require costly synthesis. NiOx has been used to create spray-based minimodules,^[18] however, it typically requires high-temperature sintering steps, which limits its end-use applications. The polymer blend HTL PEDOT: PSS is known to be hygroscopic and can cause device instability.^[19] Recently, carbazole-based SAMs have emerged as a new class of HTLs for PSCs. These materials present an exciting new opportunity to combine scalability and stability with significantly reduced materials cost compared to the current state-of-the-art devices. In particular, devices based on the SAMs MeO-2PACz (([2-(3,6-dimethoxy-9H-carbazol-9-yl)ethyl]phosphonic acid) and 2PACz ([2-(9H-carbazol-9-yl)ethyl]phosphonic acid) have been fabricated by both spin- and dip coating, with 2PACz also used in PSCs fabricated via slot-die coating and used to create minimodules.^[20]

The development of appropriate high-throughput PSC fabrication processes will require deposition technologies that can be used to fabricate thin films at high volume and high speed, with this being a critical component of a practical commercialization process.^[21] Here, spray coating enables both unparalleled linear deposition speeds of up to 12 m min⁻¹,^[22] and also permits deposition over non-planar surfaces.^[23–26] This has driven a growing interest in the utilization of spray coating to deposit all active layers in PSC devices. However, the performance of spray-fabricated PSCs and modules has not yet matched those prepared by other scalable techniques.^[27,28] For example, state-of-the-art spray-cast PSCs presently exhibit PCEs of only around 20% and have required post-deposition treatments which may limit their potential for roll-to-roll (R2R) processing, such as submersion into an anti-solvent bath^[29] or exposure to a vacuum to induce supersaturation.^[30] Furthermore, dewetting effects can occur during spray-deposition, which generate morphological defects and limit the performance of large-area spray-coated PSCs.^[31] Such effects can be pronounced when using hydrophobic transport layers typical in *p-i-n* devices. Here, we note that perovskite crystallization dynamics can be controlled using gas-assisted techniques in which a high-pressure gas-jet from an air-knife is directed across a drying film. This technique (first explored in 2014 by Huang et

al.^[32]) was first used to dry spin-coated MAPbI₃ films (achieving peak PCEs of 17%) and then applied to other perovskite compositions.^[33] Following this, gas-assisted crystallization has quickly gained interest and has been utilized in films that are drop-cast,^[34,35] bar,^[36–38] blade,^[39–47] and inkjet-printed,^[48] and has been used to create slot-die PSCs and modules,^[20,49–55] tandem-devices^[56] and LEDs.^[57] Recently, gas-assisted, spin-coated, passivated FA_{0.80}MA_{0.15}Cs_{0.05}PbI_{2.55}Br_{0.45} devices have been fabricated with a record PCE of 23.6%.^[58] Therefore, it is clear that the use of gas-quenching represents a potentially robust post-treatment in a practical PSC manufacturing process.

In this paper, we combine three key technologies described above, namely high-performing SAM hole-transport layers, ultrasonic spray coating, and gas-assisted quenching to fabricate high-efficiency p-i-n PSCs. We firstly deposit a MeO-2PACz SAM transport layer using an ultrasonic spray-deposition route which is combined with a spin-coated MAPbI₃ layer, realizing devices with an efficiency of over 20%. We then develop a novel gas-assisted spray processing (GASP) protocol to spray-cast highly crystalline and uniform MAPbI₃ perovskite films on top of a hydrophobic MeO-2PACz SAM transport layer. Finally, we spray-coat both the SAM HTL and the MAPbI₃ perovskite, realizing devices with a stabilized efficiency of 20.5%. We believe this work further demonstrates the promise of spray coating as an industrially viable, scalable deposition technique for low-cost PSC manufacture.

4.3.3. Results and Discussion

4.3.3.1. Methodology

All devices were fabricated on a pixelated indium-doped tin oxide (ITO) anode unless otherwise stated. As we describe below, we explored airbrush-, spray-, dip-, and spin-coated MeO-2PACz SAM transport layers. A MAPbI₃ perovskite precursor solution was then deposited on top of the SAM HTL using either spin coating or gas-assisted spray coating, with all spray and spin deposition processes performed in a nitrogen-filled glovebox. Finally, devices were completed by the thermal evaporation of a BCP / C₆₀ / silver cathode. **Figure 4.1(a)** shows a schematic of the resultant p-i-n device stack. Full details of all materials, fabrication techniques and processes used are described in the Experimental Methods.

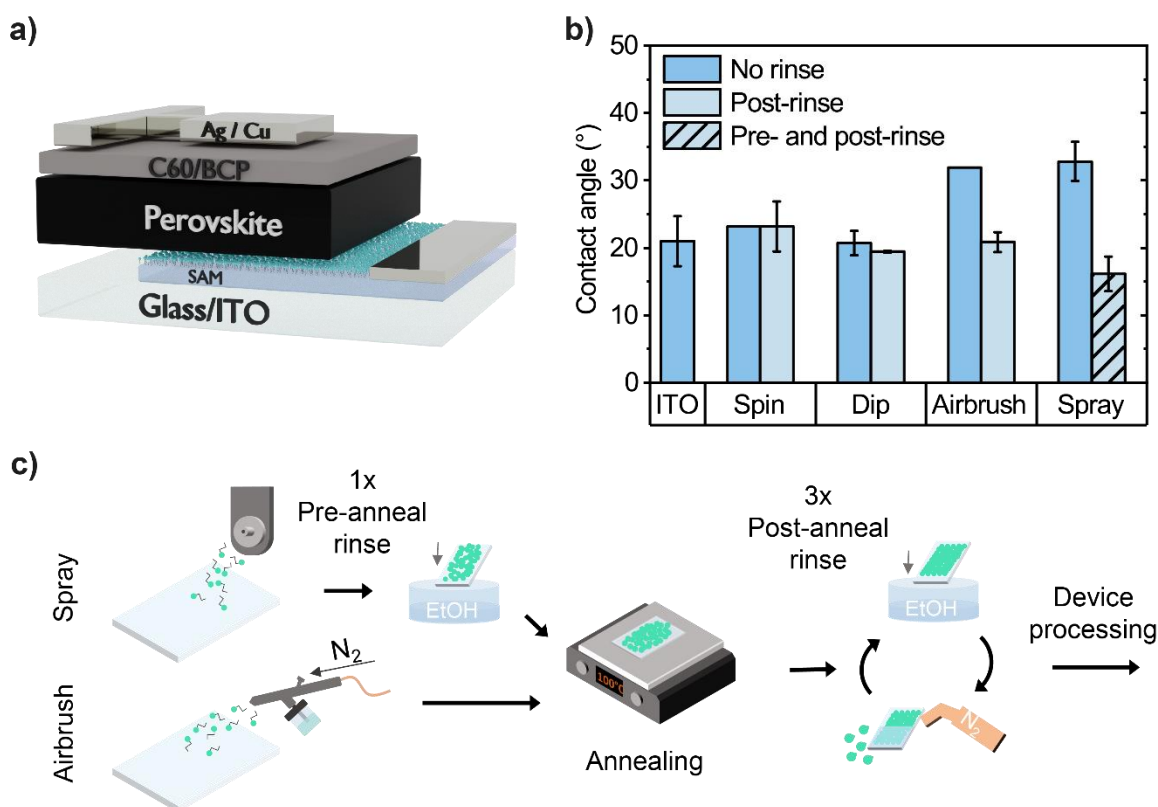


Figure 4.1: (a) Illustration of the *p-i-n* device structure used. (b) Initial contact angle for 2-methoxy ethanol (2-ME) on clean ITO and MeO-2PACz films deposited on ITO via each technique without rinsing (darker-blue) and for post-rinsed films (lighter-blue). For spray-coated MeO-2PACz, we found that an additional pre-rinse, together with a post-rinse significantly improved the 2-ME contact angle (hatched-area). (c) A schematic of the optimized rinsing procedures for spray- and airbrush-coated MeO-2PACz.

4.3.3.2. Developing spray-coated self-assembled monolayers

We have investigated two scalable deposition techniques to deposit a SAM HTL layer, namely ultrasonic spray coating (referred to henceforth as ‘spray’) and spray coating with an airbrush pen (denoted here as ‘airbrush’). Spray coating is a relatively sophisticated technique that typically requires careful control of parameter space to facilitate the deposition of high-quality layers.^[59] In contrast, airbrush pen spray coating is a more straightforward and widely accessible process that is ideally suited to deposit a SAM. Here, it is simply necessary to ensure that all parts of a surface become coated with the SAM material, with the phosphonic acid component of each molecule forming (upon annealing) a covalent bond with oxide vacancies at the substrate surface.^[60]

We firstly discuss the optimization of the deposition of the MeO-2PACz SAM HTL. Here, we compare the fabrication of films and the performance of devices in which the SAM was deposited using spray- and airbrush deposition, with those in which it was

deposited by spin coating or dip coating from a 1 mmol or 0.1 mmol ethanol solution respectively, with the substrate held at room temperature in all cases.^[12] The SAMs were then annealed at 100 °C for 10 minutes. Our initial experiments demonstrated that to produce a uniform wet film across a substrate, it was necessary to make three sequential spray passes using an ultrasonic spray-coater, with minimal solvent evaporation observed between each pass. Initial experiments indicated that if fewer spray-passes or reduced solvent flow rates were used, then the performance of the resultant devices was widely distributed, indicating that the SAM did not uniformly coat the surface (see **Figure 4.2**).

It is known that the SAMs used are hydrophobic (having a high contact angle) and can cause the de-wetting of subsequently deposited layers. Indeed, the formation of a SAM on an ITO surface is known to be self-limiting; once all molecular surface binding sites are occupied, additional molecules do not attach to the ITO but instead remain as unbound material. Here, additional unbound molecules result in a MeO-2PACz film having a larger contact angle due to exposed phosphonic acid groups.^[61] We can therefore use contact angle measurements as a probe to explore the degree to which a complete SAM layer is formed without problems resulting from excess unbound materials. In our device studies, we deposited the MAPbI₃ perovskite precursor from a 2-methoxy ethanol solution (2-ME) which has previously been shown to create efficient PSCs when used with a 2PACz hole-extracting contact.^[20]

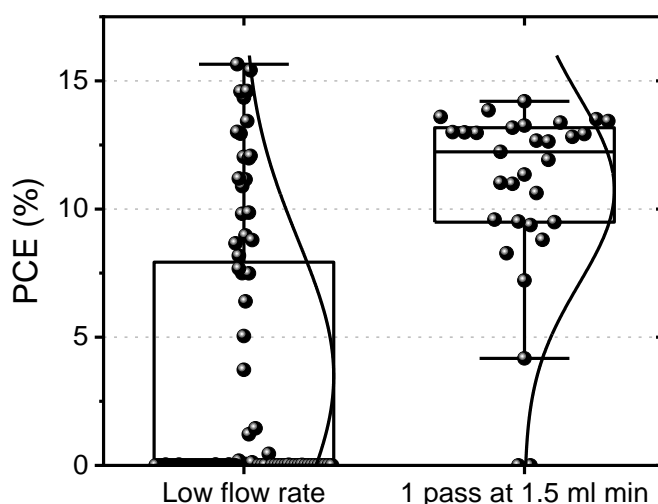


Figure 4.2: Device performance metrics for sprayed MeO-2PACz films at low flow rate (1 ml min^{-1}), at which a wet film is not achieved and at 1.5 ml min^{-1} with only a single pass of the spray head, where a wet film is realized. Both cases yield lower, more widely distributed device performance than spin coated MeO-2PACz devices.

Figure 4.1(b) shows the contact angle of a drop of 2-ME solvent on top of annealed SAM films prepared via spin coating, dip coating, airbrush coating and spray coating. The figure also records the contact angle of 2-ME on a clean ITO surface for reference. Interestingly, we find that the initial contact angle of the spray and airbrush-coated MeO-2PACz films were much higher for than for dip- or spin-coated layers, being 32.8° and 31.9° versus 20.7° and 23.2°, respectively. In all cases, the contact angle of the SAM films was similar or larger than that of the clean ITO/glass control (21.0°). We also find a similar trend for contact angle measurements performed using a dimethylformamide: dimethyl sulfoxide (DMF: DMSO) solvent blend and deionized water (see **Figure 4.3(a-b)**). We interpret this result in terms of an excess of MeO-2PACz on the ITO surface when they are deposited using spray and airbrush techniques.

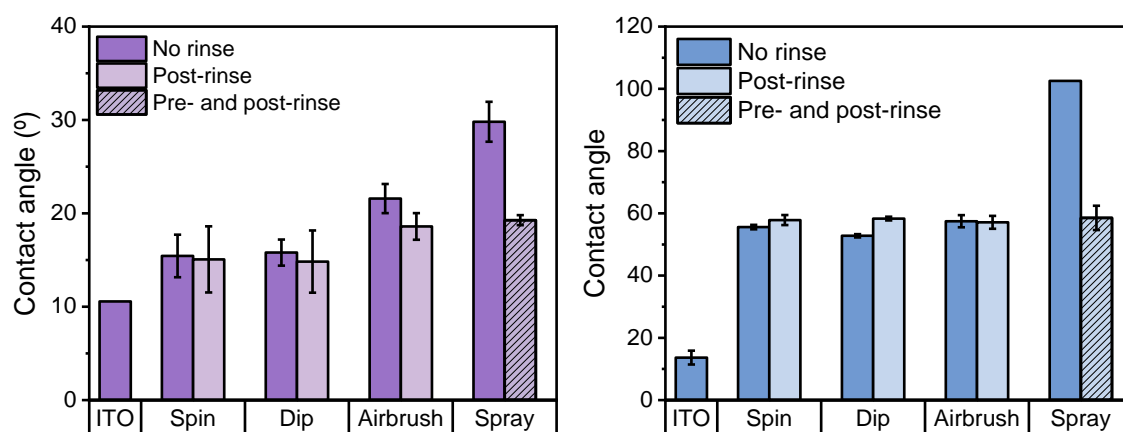


Figure 4.3: The initial contact angles of (a) a 4:1 DMF: DMSO solution and (b) deionized water on non-rinsed (darker) and post-anneal rinsed (lighter) or pre- and post-rinsed (hatched) films of MeO-2PACz fabricated by either spin, dip, airbrush, or spray coating. The optimized dip-rinsing protocols used here successfully reduce the contact angle of both solutions on spray and airbrushed MeO-2PACz to a similar level as those for spin coated control films.

We found that dewetting of the perovskite precursor arising from this excess of MeO-2PACz severely impacted device performance (see **Figure 4.4**). Previous research has described the removal of excess SAM material via rinsing, washing, or sonicating in the deposition solvent.^[62–64] Such rinsing processes are typically applied after thermal annealing (referred to henceforth as a “post-rinse”), as they result in the formation of stronger, covalent bonds that attach the monolayer material to the surface, and thereby prevent the monolayer being unintentionally stripped from the surface. In our

experiments, we ‘dip-rinsed’ the annealed SAM films in ethanol and then dried them under a flow of nitrogen, with this process performed three times. However, an additional process was also found to be needed as rinsing spray-coated SAMs post-annealing was alone not sufficient to fully alleviate wetting issues (see **Figure 4.4(a)**). This was because it was observed that without any rinsing, or with only a post-rinse, spray-coated perovskite precursor inks would not coalesce to form a continuous film. We therefore also explored rinsing films before they were annealed in order to remove a greater degree of material from the (still wet) film; an approach recently established to remove aggregates and multilayers of spray-coated gemini perfluorinated phosphonic acid SAMs deposited on top of ITO.^[65]

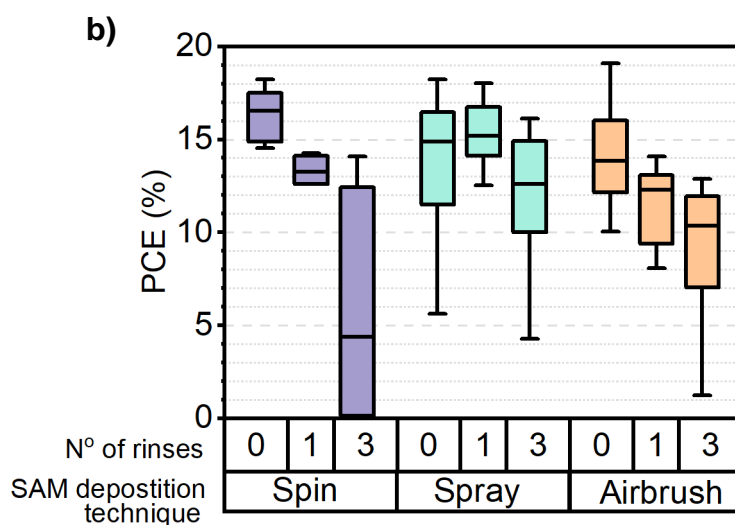
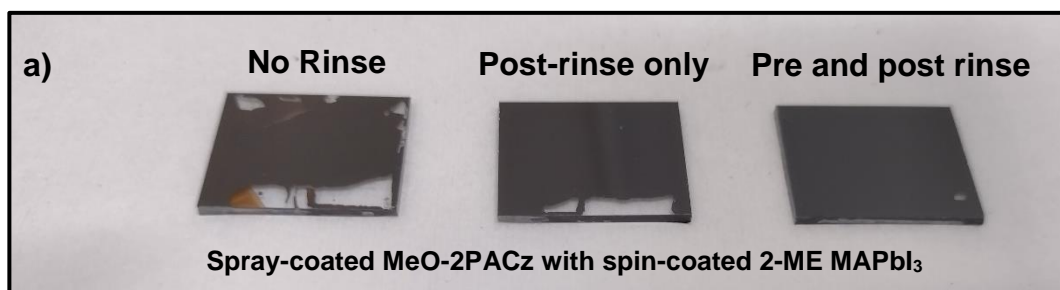


Figure 4.4: (a) Photographs of MAPbI_3 films spun from 2-methoxy ethanol on spray-coated MeO-2PACz with (left) no rinsing, (middle) post-anneal rinsing only, and (right) with both pre- and post-anneal rinsing. It can be seen the wetting behaviour of the spin-coated 2-methoxyethanol ink mostly overcomes the dewetting effects arising from the excess sprayed material.

(b) The PCE of spin- (purple) spray- (green) and airbrush- (orange) coated MeO-2PACz with 0, 1 and 3 repeated pre-rinse steps. In all cases, the MAPbI_3 perovskite was spin-coated. For all conditions, the application of 3 pre-rinses were detrimental to device performance.

In our experiments, we therefore explored the use of various numbers of “pre-rinse” steps, with this study guided by device optimization (**Figure 4.4(b)**) with the optimized rinse / pre-rinse protocol developed in **Figure 4.1(c)**. As can be seen in **Figure 4.4(b)**, when no rinses are applied to the spray-coated SAM, we see a slight drop in device performance compared to devices that utilize a spin-coated SAM that have also not been rinsed. Devices made on unrinsed, spray-cast SAMs also have a larger statistical spread in their efficiency. Devices fabricated using spin-cast perovskite films on the un-rinsed spray-cast SAM layer still have high performance despite a noticeable degree of dewetting observed in the perovskite films (see left-hand image in **Figure 4.4(a)**).

When only the post-annealing rinse protocol is applied (middle image, **Figure 4.4(a)**), some slight dewetting is seen. Applying a single pre-rinsing step to the spray-cast SAM alone significantly reduces this spread in device performance (see **Figure 4.4(b)**), but the median device efficiency is lower than spin-coated, unrinsed control devices due to some residual dewetting effects. We note that for techniques such as spray coating, where there are no additional forces to encourage coalescence of the wet as-deposited film, these dewetting effects on spray-coated MeO-2PACz without any rinsing, or with only post-annealing rinsing, prevent the 2-methoxy ethanol precursor from forming a continuous film and devices *cannot* be fabricated. This therefore necessitates additional rinsing steps, further to either single pre-rinsing, or post-rinsing alone.

Any pre-anneal rinsing applied to spin- or airbrush- coated SAMs (see **Figure 4.4(b)**) reduces device performance, likely from over-removing material and resulting in contact between the perovskite and ITO surface.

It was therefore found that a single pre-rinse, in combination with a post-rinse, was beneficial when applied to films that had been spray-cast, but instead was detrimental when applied to devices made from films deposited using an airbrush or spin coating. When spray-coating SAMs, we believe that unbound excess material is removed by the first pre-rinse. This both improves wetting behaviour, but also likely improves the charge transport at the perovskite: HTL interface by removing any material accumulated there that would otherwise hinder charge transfer. This initial pre-rinse results in a PCE increase likely due to improved extraction of charge carriers. With subsequent pre-annealing rinses however, we speculate that we begin to remove loosely bound material at the ITO surface (i.e., having lower denticity^[66]). This causes a decrease in PCE due to

the removal of regions of the monolayer leading to contact between the perovskite and the ITO, resulting in a poorly rectifying junction. For airbrush-coated MeO-2PACz, a smaller volume of deposited material results in a lower quantity of excess material and thus the pre-rinsing step immediately begins rinsing away regions of the loosely-bound monolayer, leading to a drop in PCE. We suspect that the relative amounts of excess unbound or loosely-bound material will vary between sample types (being dependent on the deposition conditions) and explains the different effects of rinsing that we see.

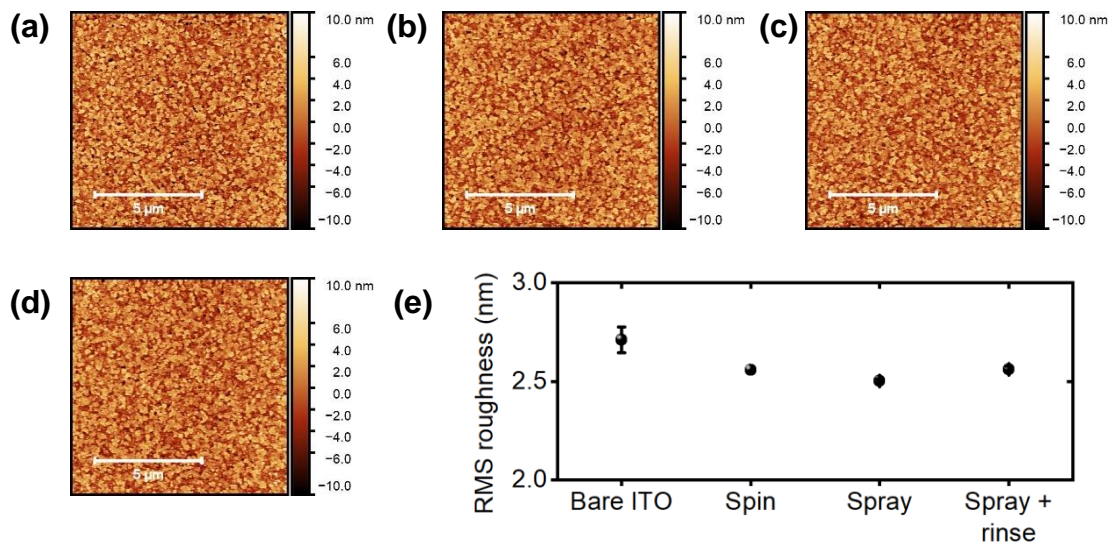


Figure 4.5: 10 μm x 10 μm AFM-scans of (a) bare ITO, (b) ITO with spin-coated MeO-2PACz and (c) ITO with spray-coated MeO-2PACz, and (d) ITO with spray-coated MeO-2PACz both pre- and post-rinsed. The plot in (e) shows the average ($n=2$) root-mean-square roughness (R_q) of each sample. It can be seen that there is very little visual difference between samples. We observe a small trend in roughness reduction in the MeO-2PACz coated samples with the R_q of the bare ITO being slightly greater than that of ITO coated with MeO-2PACz (2.71 and 2.50 nm respectively). However, we do not believe such an observation has statistical significance. We conclude that the thin MeO-2PACz layers conformally coat the ITO surface, with the AFM being unable to resolve significant changes in roughness from the polycrystalline ITO below.

The effect of the rinsing processes on contact angle can be seen in **Figure 4.1(b)**. Here, it is evident that the contact angle of 2-ME on the spray- and airbrush-coated MeO-2PACz films is reduced by the rinsing procedures to 16.2° and 20.8° respectively, with this value being comparable to, or lower than similar rinsed MeO-2PACz films prepared by spin or dip coating. We attribute the greater reduction in contact angle upon rinsing for spray- and airbrush-deposited layers as resulting from a larger degree of excess material being present at the surface which is then removed. We have attempted to explore

changes in film roughness using atomic force microscopy (AFM) imaging as a result of coating with MeO-2PACz films and the effect of the rinsing process on such coated films (**Figure 4.5**). We find however that such effects are small (statistically insignificant), and we conclude that the thin MeO-2PACz layers conformally coat the ITO surface,^[67] with the AFM being unable to resolve significant changes in roughness due to the polycrystalline nature of the ITO surface on which it is deposited.

Table 4.1: A summary of the optimized rinsing protocol developed for each MeO-2PACz film fabrication technique.

MeO-2PACz deposition technique	Pre-anneal rinse	Post-anneal rinse
Spin	None	None
Dip	None	3x
Airbrush	None	3x
Spray	1x	3x

We have used the MeO-2PACz SAM layers prepared using the optimized rinsing techniques described above (see **Figure 4.1(c)** and summarized in **Table 4.1**) to fabricate PSC devices. Here, our reference (control) devices included a MAPbI₃ active layer that was deposited using a gas-assisted spin coating protocol as described in the Experimental Methods. The spread of device PCEs prepared via the different deposition routes is shown in **Figure 4.6(a)**. Similar performances were realized for spin-coated MAPbI₃ devices incorporating an airbrush or spray-coated MeO-2PACz layer and the spin-cast SAM controls. Here, the champion spray- and airbrush-coated MeO-2PACz devices achieved a PCE of 20.2% (20.3% stabilized) and 19.9% (19.8% stabilized) respectively (see *JV* curves and EQE data in **Figure 4.6(b-f)**). We note that a small mismatch observed between the J_{sc-EQE} and J_{sc-JV} (1 mA cm⁻²) falls within acceptable limits as discussed previously.^[68,69] All average and champion performance metrics are tabulated in **Tables 4.2(a-b)**.

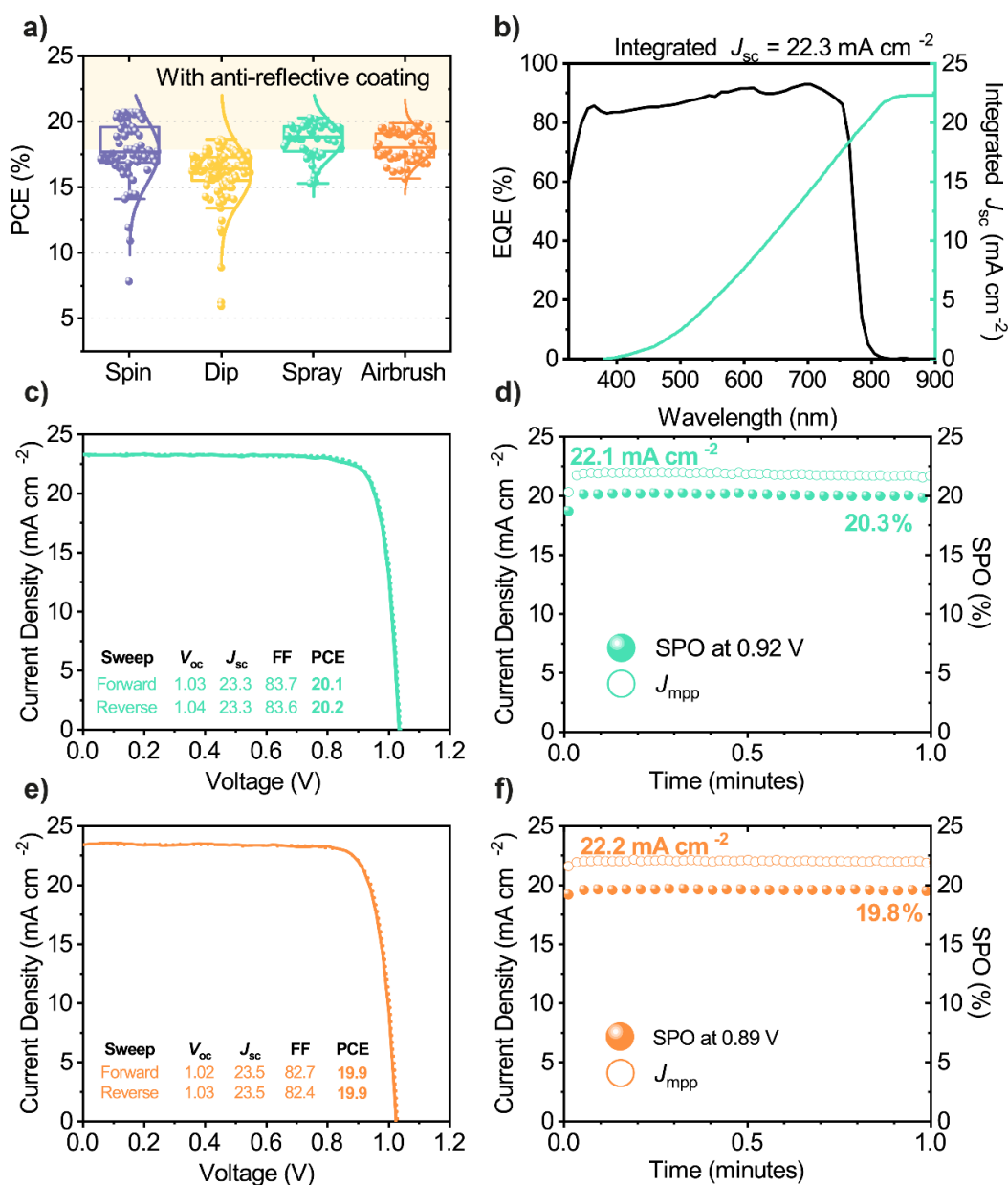


Figure 4.6: (a) Device PCE for spin-coated MAPbI₃ devices fabricated on ITO substrates with a spin- (unrinsed, purple), dip- (post-anneal rinsed only, yellow), spray- (pre- and post-rinsed, green), and airbrush- (post-rinsed only, orange) deposited MeO-2PACz hole-selective transport layer prepared as described in the text. (b) External quantum efficiency, (c) JV curve, and (d) stabilized power output (SPO) for the best-performing spray-coated MeO-2PACz device. (e) JV curve and (f) SPO for the best-performing airbrush-coated MeO-2PACz device. Both champion devices incorporate an anti-reflective coating.

Table 4.2a: A summary of PSC performance metrics (including both forward and reverse JV sweeps, and data for devices **without anti-reflective coatings on ITO**) for spin coated MAPbI₃ perovskite on MeO-2PACz deposited via each deposition technique. Bold font data represents champion performance metrics, while averages and standard deviations are shown in parentheses.

SAM					
deposition technique	J_{sc} [mA cm ⁻²]	V_{oc} [V]	FF [%]	PCE [%]	N_{cells}
Spin	23.8 (22.7 ± 0.8)	1.06 (1.01 ± 0.05)	76.3 (70.0 ± 6.2)	18.2 (16.2 ± 2.2)	18
Dip	23.9 (21.7 ± 1.2)	1.04 (1.01 ± 0.04)	77.5 (72.6 ± 7.0)	18.6 (15.9 ± 2.1)	25
Spray	23.5 (23.0 ± 0.4)	1.04 (1.01 ± 0.02)	77.1 (75.6 ± 1.6)	18.4 (17.6 ± 0.6)	6
Airbrush	23.0 (22.9 ± 0.3)	1.03 (1.02 ± 0.01)	76.7 (73.6 ± 2.0)	18.1 (17.3 ± 0.6)	7

Table 4.2b: A summary of PSC performance metrics (including both forward and reverse JV sweeps, and data for devices **with anti-reflective coatings on ITO**) for spin coated MAPbI₃ perovskite on MeO-2PACz deposited via each deposition technique. Bold font data represents champion performance metrics, while averages and standard deviations are shown in parentheses.

SAM					
deposition technique	J_{sc} [mA cm ⁻²]	V_{oc} [V]	FF [%]	PCE [%]	N_{cells}
Spin	24.6 (24.0 ± 0.5)	1.05 (1.03 ± 0.02)	83.8 (81.5 ± 1.9)	20.7 (20.1 ± 0.9)	9
Spray	23.6 (23.0 ± 0.4)	1.04 (1.00 ± 0.05)	84.3 (81.8 ± 2.7)	20.3 (18.6 ± 1.3)	22
Airbrush	23.5 (22.9 ± 0.6)	1.03 (1.00 ± 0.02)	83.0 (80.6 ± 2.4)	19.9 (18.4 ± 1.1)	18

4.3.3.3. Developing an air-knife gas-quenching process for perovskites deposited on spin-coated SAMs

This section discusses the deposition and optimization of MAPbI₃ perovskite films and PSCs using a gas-assisted spray-process (GASP). Here, such films are deposited on spin-coated MeO-2PACz SAMs on ITO substrates without any anti-reflective coating applied.

It is well understood that the performance of a PSC is a function of the quality of the crystalline perovskite layer. This is highly dependent on the nucleation and growth of crystal grains, with such nucleation triggered by the supersaturation of the precursor. Typically, this involves the use of an anti-solvent during spin coating.^[70] However, to trigger nucleation during or after spray coating, researchers have also used an anti-solvent bath method,^[29,71] although the scalability of this processes is limited by the use of significant quantities of solvent that becomes gradually “contaminated” during any device run. Alternative approaches to induce supersaturation include thermal annealing,^[72] vacuum-assisted solution processing (VASP),^[73] hot-air blowing,^[74] and plasma-treatments.^[22] Here, we investigate a gas-assisted spray processing (GASP) protocol in which an ambient temperature nitrogen gas-jet from an air-knife is blown at a surface that has been spray-cast with a perovskite precursor solution, with the evaporation of the volatile casting-solvent inducing supersaturation. For further information on gas-quenching techniques we direct the reader to a recent review.^[75]

In the GASP process developed, an ultrasonic spray-head was moved linearly across the substrate surface, uniformly depositing a MAPbI₃ precursor solution from a 2-ME solvent. This highly volatile precursor system has previously been used to deposit MAPbI₃ thin films,^[76] and has been used with 2PACz SAM layers to realize MAPbI₃ devices with a PCE of 20.8%.^[20] In our process a short delay was included to allow the precursor droplets to coalesce (30 s), after which an air-knife (blowing ambient temperature nitrogen at a pressure of 20 psi) was moved across the substrate. During this process, the distance between the surface and the air-knife was maintained at around 2 cm. It was found that the application of the gas-jet induced a rapid color change of the precursor film from yellow to dark brown. The entire process was performed inside a nitrogen-filled glovebox at room temperature, with the films produced being annealed at 100 °C for 10

minutes. We illustrate the GASP procedure in **Figure 4.7(a-c)**. Here, both the spray head and air knife move from the back of the substrate to the front.



Figure 4.7: (a) The gantry moves the spray head linearly over the (unheated) substrate surface. The focusing gas directs the wet droplets to the substrate surface. (b) After a short delay – to enable coalescence of the deposited droplets – the gantry moves the air knife over the surface, blowing room temperature nitrogen at 45° to the normal over the wet film. (c) The films are then annealed at 100 °C for 10 minutes.

As part of our optimization process, we have explored the effect of the molarity of the spray-cast precursor solution on device performance. We find that when the precursor was spray-cast at a molarity of 1 M, the top surface of the film appeared highly crystalline however the quality of the bottom interface was extremely poor. We reach this conclusion from the cloudy appearance of such films (see **Figure 4.8(a)**) which suggest poor contact with the underlying substrate caused by the presence of voids in the film. We believe that when the gas-jet is applied to films spray-cast from high concentration precursors, the evaporation of solvent proceeds more quickly than the solvent molecules can diffuse through the ‘wet’ film. As a result, a uniform composition does not establish throughout the depth of the wet film, with regions closer to the surface becoming supersaturated and therefore undergoing rapid crystallization.^[77] This most likely results in dendritic crystal growth from the film surface, (a top-down crystallization mechanism^[78]) that is exacerbated by the application of the gas-jet. This process has been previously explored in detail in films cast from DMSO-containing precursors – with a solvent-trapping phenomenon identified that leads to the formation voids in the film as the trapped solvent escapes upon annealing.^[53,79] The results of this effect are illustrated practically in **Figure 4.9(a)**, where it can be seen that device PCE increases as the precursor molarity is reduced.

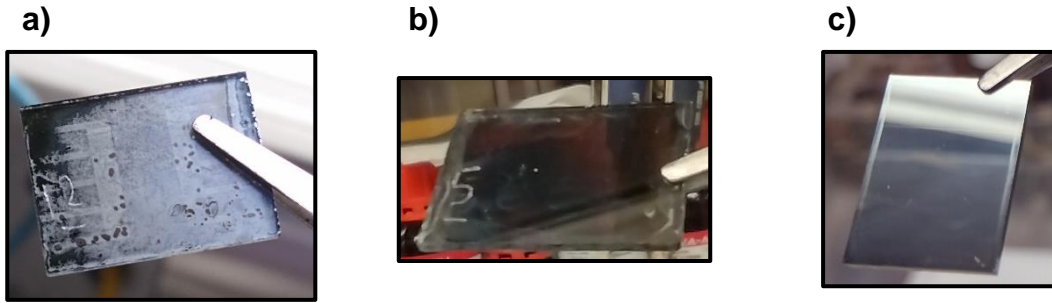


Figure 4.8: Photographs of (a) the rear side of an ITO substrate coated with spin-coated MeO-2PACz and GASP MAPbI₃ at 1 M concentration, wherein the cloudy appearance is indicative of voids between the perovskite and the glass surface. (b) The rear side of an ITO substrate coated with spin-coated MeO-2PACz and GASP MAPbI₃ at 0.5 M concentration without any noticeable voids, and (c) the top surface of the same substrate, showing a highly specular surface.

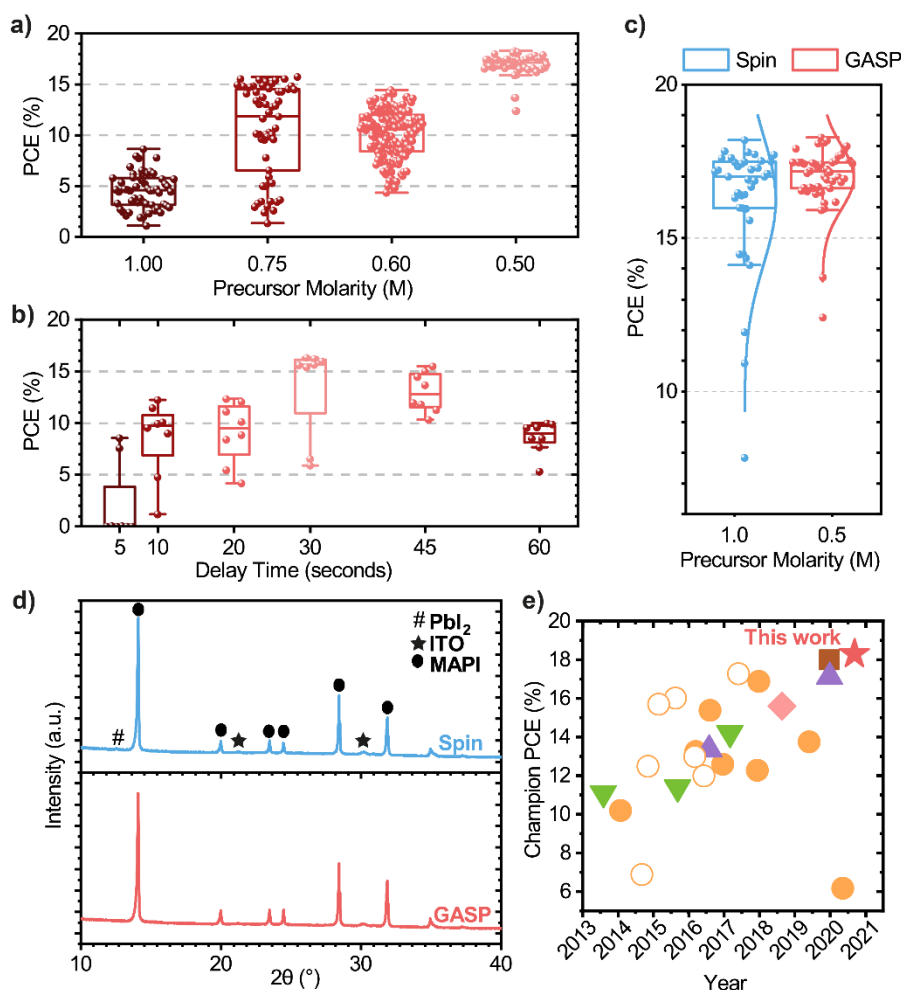


Figure 4.9: All devices are fabricated on ITO and do not include an anti-reflective coating. (a) Photovoltaic performance of gas-assisted spray-processed (GASP) MAPbI₃ devices as a function of the molarity of the 2-methoxy ethanol precursor ink. (b) Photovoltaic performance of GASP devices fabricated from a 0.5 M precursor ink with increasing delay time between deposition of the ink and application of a N₂ gas-jet. (c) Photovoltaic device efficiency of MAPbI₃ devices prepared using GASP under optimized conditions (0.5 M, 30 s delay, red) vs. spin-coated control devices (blue). (d) X-ray diffraction patterns for spin-coated (blue) and GASP MAPbI₃ (red) films. (e) The development of spray-cast p-i-n and n-i-p MAPbI₃ devices over time; p-i-n (filled orange circles) and n-i-p (outlined orange circles) MAPbI₃, p-i-n MAPbI_{3-x}Cl_x (inverted green triangles), MAPbI_{3-x}Br_x, Cs_xFA_{1-x}PbI₃, (brown square) and mixed cation (pink diamond). This work (pink star) demonstrates the highest power conversion efficiency for spray-coated MAPbI₃ perovskite solar cells achieved to date (more details can be found in Table S4).

As part of our optimisation studies, we have explored the effect of the “delay time” between spray-coating the perovskite precursor solution and the application of the N₂ gas-jet. This is shown in **Figure 4.9(b)** where it can be seen that device efficiency is apparently optimised when deposited from a solution having a molarity of 0.5 M, where a delay of around 30 s is included between spray-casting and the application of the gas-jet.

We discuss this effect in more detail below. **Figure 4.9(c)** summarizes the efficiency of MAPbI₃ devices prepared using GASP under optimised conditions (0.5 M, 30 s delay). This is compared with control devices created using a gas-assisted spin coating protocol in which a jet of N₂ at around 20 psi was directed at the spinning substrate 6 s after the deposition of the perovskite precursor solution. Here, we find the champion efficiency of GASP and control devices to be 18.3% (17.0 ± 1.0%) and 18.2% (16.2 ± 2.1%) respectively. The close similarity in device efficiency between different processes indicates the broad utility of the GASP process. For completeness, we plot full device metrics in **Table 4.3** together with representative *JV* and a 1-minute stabilized power output (SPO) measurement in **Figure 4.10(a-b)**.

Table 4.3: Device statistics for devices (without anti-reflective coatings on ITO) fabricated with spin-coated MeO-2PACz and MAPbI₃ (19 cells) vs. spin-coated MeO-2PACz and GASP MAPbI₃ (23 cells). Champion performance data is in boldface type, with mean and standard deviations parenthesized.

MAPbI₃ deposition technique	<i>J</i>_{sc} [mA cm⁻²]	<i>V</i>_{oc} [V]	FF [%]	PCE [%]
Spin	23.8 (22.7 ± 0.9)	1.06 (1.02 ± 0.06)	76.3 (70.1 ± 6.0)	18.2 (16.2 ± 2.1)
GASP	23.0 (22.1 ± 0.4)	1.07 (1.05 ± 0.03)	76.1 (72.4 ± 2.8)	18.3 (17.0 ± 1.0)

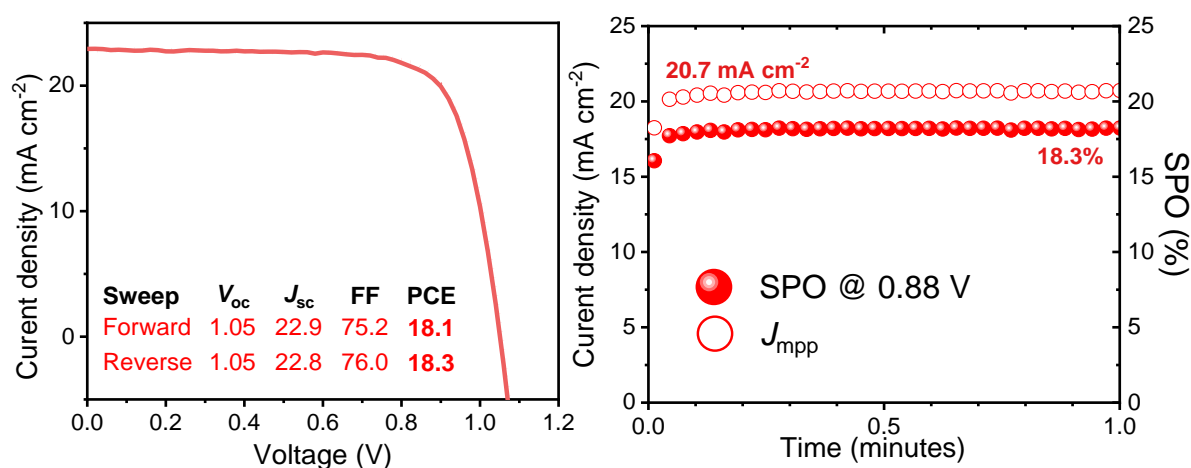


Figure 4.10: (a) JV curve and (b) stabilized power output (SPO) for the best-performing gas-assisted spray-processed (GASP) MAPbI₃ on spin-coated MeO-2PACz without an anti-reflective coating on ITO substrates.

To investigate the morphology and structure of MAPbI₃ films fabricated by GASP, we have performed X-ray diffraction (XRD) and scanning electron microscopy (SEM) measurements. **Figure 4.9(d)** presents diffraction patterns recorded from a gas-quenched spin-control and GASP-prepared film. The near-identical patterns confirm that the N₂ flow post-treatment fully converts the precursor solution into a highly crystalline MAPbI₃ film with no undesirable secondary phases present. SEM images indicate a similar average grain size distribution in GASP films (30 s delay) and spin-cast films (375 nm vs. 386 nm respectively). In contrast, the GASP films prepared using a delay time of 45 s between spray-casting and application of the gas-jet have a reduced average grain-size of around 261 nm (see **Figure 4.11 (a-d)**). Such differences in grain size formed as a function of delay time most likely originate from the evaporation of the volatile casting solvent; here we suspect that after a 45 second delay time, the precursor solution is closer to its supersaturation point with the gas-jet then generating a greater density of nuclei which lead to a film characterized by smaller grain sizes. Using surface profilometry, we also find that over larger areas (1 mm²) there is little difference in the RMS roughness of the spin-cast (10.85 nm) and GASP films (10.15 nm) (see **Figure 4.12**), although in both techniques we observe morphological features arising from solvent flow.

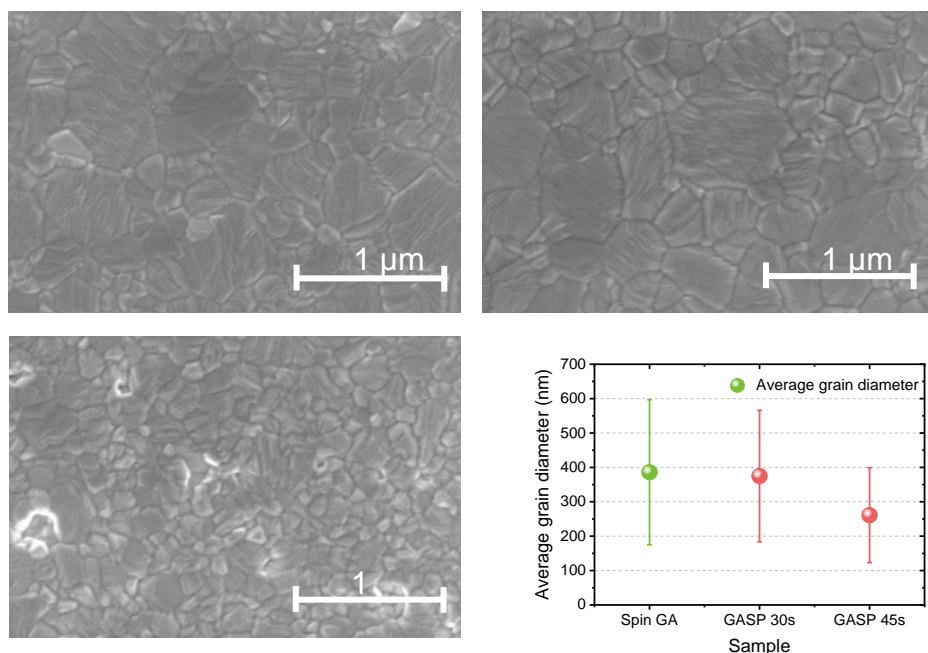


Figure 4.11: Scanning electron microscope (SEM) images of (a) gas-assisted spin-coated MAPbI₃, (b) GASP MAPbI₃ with 30 s delay between deposition and airflow, and (c) GASP MAPbI₃ with 45 s delay between deposition and airflow. 1 μm scale bar inset. (d) The mean and standard deviation of grain sizes for each sample, extracted with Image J software. The grain structure for 30 s delay GASP films is similar to spin controls, however at a delay time of 45 s, there is a greater number of smaller grains.

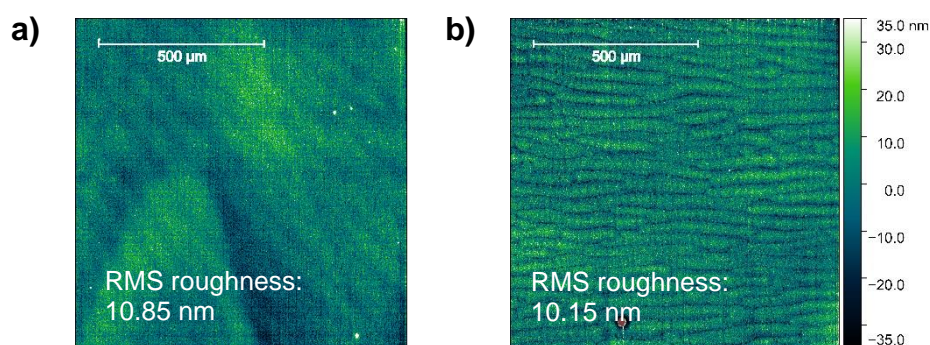


Figure 4.12: 1 mm x 1 mm profilometer mapping scans of (a) gas-assisted spin-coated MAPbI₃ and (b) GASP (30 s delay) MAPbI₃ films with 500 μm scale bar inset. There is little disparity in the root-mean-square (RMS) roughness between the films.

In **Figure 4.9(e)**, we compare the efficiency of a champion GASP-treated MAPbI₃ device (without any anti-reflective coating) with literature values for p-i-n and n-i-p architecture devices incorporating a spray-cast active layer (data also tabulated in **Table 4.4**). To our knowledge, this work represents the highest performance spray-coated MAPbI₃ PSC and spray-coated p-i-n architecture PSC device reported to date.

Table 4.4: State-of-the-art spray coated inverted and n-i-p MAPbI₃ PSCs.a) 10.4 cm² minimodule

Year	PCE [%]	J _{sc} [mA cm ⁻²]	V _{oc} [V]	FF [%]	Config.	Stack	Ref
2014	11.1	16.8	0.92	72	p-i-n	ITO/PEDOT:PSS/MAPbI ₃ - _x Cl _x /PCBM/Ca/Al	[81]
2015	10.2	17.3	0.93	0.63	p-i-n	ITO/PEDOT:PSS/MAPbI ₃ /C ₆₀ /BCP/Al	[82]
2015	6.93	23.01	0.69	43.4	n-i-p	FTO/TiO ₂ /MAPbI ₃ /Au	[83]
2015	12.5	19.1	0.94	69	n-i-p	FTO/c-TiO ₂ /mp-TiO ₂ /MAPbI ₃ /spiro-OMeTAD/Ag	[84]
2016	15.7	22.5	0.95	73	n-i-p	ITO/TiO ₂ /MAPbI _{3-x} Br _x /Spiro-OMeTAD/Au	[85]
2016	16.03	20.27	1.047	75.5	n-i-p	FTO/c-TiO ₂ /mp-TiO ₂ /MAPbI ₃ /spiro-OMeTAD/Au	[86]
2016	11.4	17.6	0.92	74	p-i-n	ITO/PEDOT:PSS/MAPbI ₃ - _x Cl _x /PCBM/LiF/Al	[87]
2017	13	19	0.99	69	n-i-p	FTO/c-TiO ₂ /np-TiO ₂ /MAPbI ₃ /spiro-MeOTAD/Au	[88]
2017	13.27	17.79	0.98	74.7	p-i-n	ITO/PEDOT:PSS/MAPbI ₃ /C ₆₀ /BCP/LiF/Al	[89]
2017	12.01	22.4	1.03	52	n-i-p	FTO/c-TiO ₂ /mp-TiO ₂ /MAPbI ₃ /spiro-OMeTAD/Au	[90]
2017	13.35	20.8	0.87	73.6	p-i-n	FTO/PEDOT:PSS/MAPbI ₃ - _x Br _x /PCBM/BCP/Ag	[91]
2017	15.4	21	0.96	76	p-i-n	ITO/PEDOT:PSS/MAPbI ₃ /C ₆₀ /PCBM/Al	[23]
2017	12.6	22.5	0.87	63.4	p-i-n	ITO/PEDOT:PSS/MAPbI ₃ /PCBM/Ag	[92]
2018	14.2	22.4	0.92	69	p-i-n	ITO/PEDOT:PSS/MAPbI ₃ - _x Cl _x /PCBM/PEIE/Ag	[93]
2018	17.3	21.70	1.033	73	n-i-p	FTO/SnO ₂ /MAPbI ₃ /Spiro-OMeTAD/MoO _x /Al	[71]
2018	12.3	21.94	0.83	67.6	p-i-n	ITO/PEDOT:PSS/MAPbI ₃ /C ₆₀ /Ag	[94]
2018	16.9	21.6	1.03	76	p-i-n	ITO/PEDOT:PSS/MAPbI ₃ /C ₆₀ /BCP/Cu	[95]
2019	15.61	22.27	1.00	70.3	p-i-n	FTO/NiO _x /FA _{0.25} MA _{0.75} PbI ₃ /C ₆₀ /BCP/Ag	[96]
2020	13.76	22.31	0.98	62.9	p-i-n	ITO/NiO _x /MAPbI ₃ /C ₆₀ /PCBM:PNDI(20D)T2/Ag	[97]
2020	18	-	-	-	p-i-n	ITO/NiO _x /(Cs _{0.17} FA _{0.83})PbI ₃ /C ₆₀ /BCP/Ag	[22]
2020	17.11	21.81	1.03	76	p-i-n	ITO/NiO _x /MAPbI _{3-x} Br _x /C ₆₀ /BCP/Ag	[98]
2021	6.18 ^{a)}	2.91	37.2	59.4	p-i-n	ITO/NiO _x /MAPbI ₃ /C ₆₀ /BCP/Ag	[18]
2021	18.3	22.8	1.05	76	p-i-n	ITO/MeO-2PACz/MAPbI₃/C₆₀/BCP/Ag	This work

4.3.3.4. Combining GASP perovskite and spray-coated SAMs for p-i-n PSCs

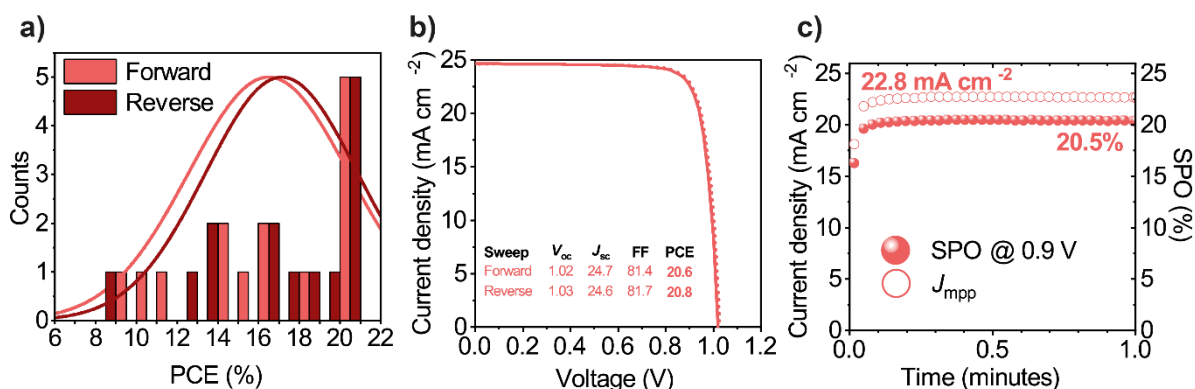


Figure 4.13: (a) A histogram of device PCE for 14 cells prepared using both a spray-coated MeO-2PACz hole-transporting layer and a gas-assisted spray-processed (GASP) MAPbI₃ active layer, with an anti-reflective coating on FTO substrates. (b) JV curve and (c) stabilized power output (SPO) measurement for the best-performing device.

In this section we describe the development of devices based on spray-coated MeO-2PACz (utilizing the optimized pre- and post-rinsing protocol discussed above) and GASP MAPbI₃. Again, such p-i-n devices utilized a thermally evaporated C60/BCP/Ag cathode. **Figure 4.13(a-c)** plots a histogram of device performance, together with the JV curve and SPO of the best-performing device. These devices include an anti-reflective layer. In order to maximize device performance, these devices were fabricated on a fluorine-doped tin oxide (FTO) anode as we have observed an enhancement in the J_{sc} for devices with an anti-reflective coating on FTO, rather than on ITO (see **Figure 4.14**). Although we measure a greater spread in device performance when both the HTL and active layers are spray-coated, high efficiency PSCs are often realized, with the champion PSC having a PCE of 20.8% (20.5% stabilized). A summary of performance metrics prepared using such ‘fully scalable’ techniques is presented in **Table 4.5**.

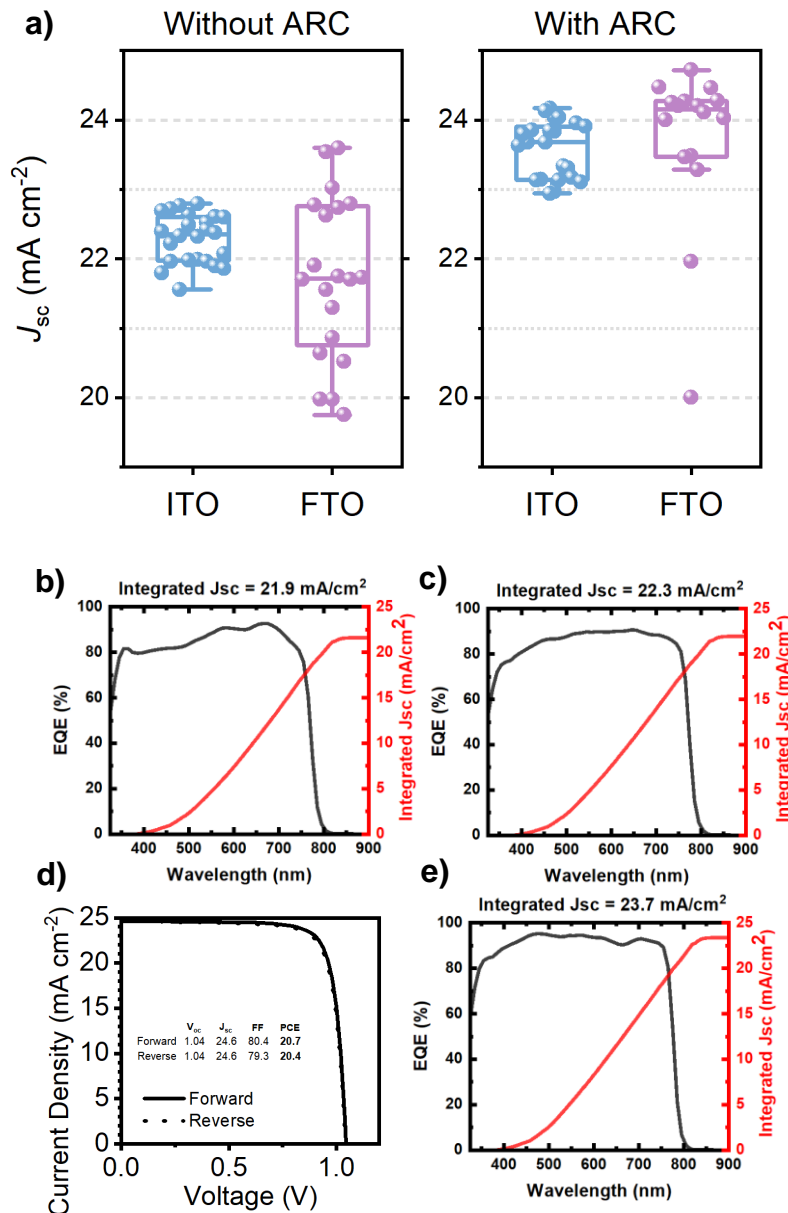


Figure 4.14: (a) The J_{sc} of MAPbI₃ devices on both ITO and FTO without (left) and with (right) an anti-reflective coating applied to the substrate surface. The FTO-based devices have a higher J_{sc} than ITO-based devices after application of the coating. We find that the EQE of the ITO substrates (b) has a lower contribution to charge generation in the 400 to 600 nm region than the FTO substrates (c). (d) and (e) present the J-V curve and EQE spectra of a best-performing spin-coated control device on FTO substrate with the anti-reflective coating applied.

Table 4.5: Photovoltaic performance metrics for 14 cells comprising a spray-coated MeO-2PACz hole-transporting layer and gas-assisted spray-processed MAPbI₃ active layer. Here all devices are prepared on an FTO substrates and include an anti-reflective coating. Champion performance metrics are presented in bold, whilst the mean and standard deviation values are shown in parenthesis.

Device	J_{sc} [mA cm ⁻²]	V_{oc} [V]	FF [%]	PCE [%]
Spray MeO-2PACz with GASP MAPbI ₃	24.9 (24.1 ± 0.6)	1.03 (0.95 ± 0.09)	82.8 (73.0 ± 10.6)	20.8 (16.9 ± 3.6)

We note however that our process is not under full control and there still remains a degree of variation from device to device as a result of the dip-rinsing process (which is done by hand) which will impact on the amount of excess SAM material that is removed from the surface. We therefore attribute the distribution in device performance to partial dewetting effects of the perovskite precursor ink from the spray-coated SAM layer, resulting in film thickness variations which likely exacerbate solvent trapping effects and leads to the formation of voids at the perovskite/glass interface.^[53] We anticipate that it will be possible to mitigate such effects through the use of surfactants^[80] or higher boiling-point additives^[38,79] to stabilize the interface and enable more reproducible device performance. We speculate that improvements in our process will also come by using a second spray-head to deposit a rinse solvent and using an air-knife to shear off the excess material.

4.3.4 Conclusion

We have developed two new protocols to fabricate MeO-2PACz hole-transporting layers; namely ultrasonic spray coating and airbrush pen coating, with both techniques realizing PSC devices having comparable performance to spin-coated controls. Here, the use of an airbrush represents a widely accessible, high-throughput technique to rapidly deposit carbazole-SAM hole-transporting materials. We then demonstrate the application of a gas-jet quenching method to spray-coated perovskite precursor films, creating high-quality perovskite layers. We optimize the gas-assisted spray processing (GASP) process by control of the solid concentration in the precursor solution and the delay time between deposition of the precursor and application of the gas-jet. Finally, we combine ultrasonic spray coating / gas-assisted processing of both the MeO-2PACz and MAPbI₃ layers, creating devices having a peak PCE of 20.8% (20.5% SPO); a value that represents the highest reported stabilized efficiency for spray-coated PSCs to date. We summarize the champion device efficiencies achieved via each processing route in **Table 4.6**. The deposition techniques developed are ideally suited to high-speed roll-to-roll fabrication of PSCs and are thus directly relevant for practical manufacture and device scale-up.

Table 4.6: A summary of best-performing devices for each case presented within this work alongside corresponding control device performance.

MeO-2PACz deposition technique	Spin	Spin	Spray (with pre- and post-rinse)	Spin	Spray (with pre- and post-rinse)
MAPbI₃ deposition technique	Spin	Spin	Spin	GASP	GASP
Manuscript Section	2.2 and 2.3	2.4	2.2	2.3	2.4
Substrate	ITO	FTO	ITO	ITO	FTO
Anti-reflective coating	X (✓)	✓	X (✓)	X	✓
PCE (%)	18.2 (20.7)	20.7	18.4 (20.2)	18.3	20.8

4.3.5 Acknowledgments

This work was funded by the Engineering and Physical Sciences Research Council (EPSRC) grant EP/S009213/1 (The integration of photovoltaic devices with carbon-fiber composites). E.J.C., J.A.S. and E.L.K.S. thank the EPSRC for a PhD studentship from the Centre for Doctoral Training in New and Sustainable PV, (EP/L01551X/1). M.E.O’K. thanks the EPSRC for a PhD studentship from the Centre for Doctoral Training in Polymers and Colloids, EP/ (EP/L016281/1). T.T. and T.E.C thank the faculty of Science, University of Sheffield for a studentship.

4.3.6 Conflicts of Interest

D.G.L. is a director of the materials science company Ossila that retails materials and equipment for thin film fabrication, including for research and development of perovskite photovoltaics.

4.3.7 References

- [1] NREL, "Best Research-Cell Efficiencies," **2021**. (Accessed: August 2021)
- [2] J. Diekmann, P. Caprioglio, M. H. Futscher, V. M. Le Corre, S. Reichert, F. Jaiser, M. Arvind, L. P. Toro, E. Gutierrez-Partida, F. Peña-Camargo, C. Deibel, B. Ehrler, T. Unold, T. Kirchartz, D. Neher, M. Stollerfoht, *Sol. RRL* **2021**, *5*, 2100219.
- [3] M. Stollerfoht, C. M. Wolff, J. A. Márquez, S. Zhang, C. J. Hages, D. Rothhardt, S. Albrecht, P. L. Burn, P. Meredith, T. Unold, D. Neher, *Nat. Energy* **2018**, *3*, 847.
- [4] C. A. R. Perini, T. A. S. Doherty, S. D. Stranks, J. P. Correa-Baena, R. L. Z. Hoyer, *Joule* **2021**, *5*, 1024.
- [5] K. A. Bush, A. F. Palmstrom, Z. J. Yu, M. Boccard, R. Cheacharoen, J. P. Mailoa, D. P. McMeekin, R. L. Z. Z. Hoyer, C. D. Bailie, T. Leijtens, I. M. Peters, M. C. Minichetti, N. Rolston, R. Prasanna, S. Sofia, D. Harwood, W. Ma, F. Moghadam, H. J. Snaith, T. Buonassisi, Z. C. Holman, S. F. Bent, M. D. McGehee, *Nat. Energy* **2017**, *2*, 17009.
- [6] Y. Deng, S. Xu, S. Chen, X. Xiao, J. Zhao, J. Huang, *Nat. Energy* **2021**, *6*, 633.
- [7] Y. Deng, C. H. Van Brackle, X. Dai, J. Zhao, B. Chen, J. Huang, *Sci. Adv.* **2019**, *5*, eaax7537.
- [8] M. Wong-Stringer, O. S. Game, J. A. Smith, T. J. Routledge, B. A. Alqurashy, B. G. Freestone, A. J. Parnell, N. Vaenas, V. Kumar, M. O. A. Alawad, A. Iraqi, C. Rodenburg, D. G. Lidzey, *Adv. Energy Mater.* **2018**, *8*, 1.
- [9] B. Li, Y. Xiang, K. D. G. I. Jayawardena, D. Luo, Z. Wang, X. Yang, J. F. Watts, S. Hinder, M. T. Sajjad, T. Webb, H. Luo, I. Marko, H. Li, S. A. J. Thomson, R. Zhu, G. Shao, S. J. Sweeney, S. R. P. Silva, W. Zhang, *Nano Energy* **2020**, *78*, 105249.
- [10] Q. Cao, Y. Li, H. Zhang, J. Yang, J. Han, T. Xu, S. Wang, Z. Wang, B. Gao, J. Zhao, X. Li, X. Ma, S. M. Zakeeruddin, W. E. I. Sha, X. Li, M. Grätzel, *Sci. Adv.* **2021**, *7*, eabg0633.
- [11] A. Magomedov, A. Al-Ashouri, E. Kasparavičius, S. Strazdaite, G. Niaura, M. Jošt, T. Malinauskas, S. Albrecht, V. Getautis, *Adv. Energy Mater.* **2018**, *8*, 1801892.
- [12] A. Al-Ashouri, A. Magomedov, M. Roß, M. Jošt, M. Talaikis, G. Chistiakova, T. Bertram, J. A. Márquez, E. Köhnen, E. Kasparavičius, S. Levenco, L. Gil-Escrig, C. J. Hages, R. Schlatmann, B. Rech, T. Malinauskas, T. Unold, C. A. Kaufmann, L. Korte, G. Niaura, V. Getautis, S. Albrecht, *Energy Environ. Sci.* **2019**, *12*, 3356.
- [13] S. Gharibzadeh, P. Fassel, I. M. Hossain, P. Rohrbeck, M. Frericks, M. Schmidt, T. Duong, M. R. Khan, T. Abzieher, B. A. Nejad, F. Schackmar, O. Almora, T. Feeney, R. Singh,

- D. Fuchs, U. Lemmer, J. P. Hofmann, S. A. L. Weber, U. W. Paetzold, *Energy Environ. Sci.* **2021**, *14*, 5875-5893
- [14] A. Al-Ashouri, E. Köhnen, B. Li, A. Magomedov, H. Hempel, P. Caprioglio, J. A. Márquez, A. B. Morales Vilches, E. Kasparavicius, J. A. Smith, N. Phung, D. Menzel, M. Grischek, L. Kegelman, D. Skroblin, C. Gollwitzer, T. Malinauskas, M. Jošt, G. Matič, B. Rech, R. Schlatmann, M. Topič, L. Korte, A. Abate, B. Stannowski, D. Neher, M. Stolterfoht, T. Unold, V. Getautis, S. Albrecht, *Science (80-.)*. **2020**, *370*, 1300.
- [15] F. Yang, D. Jang, L. Dong, S. Qiu, A. Distler, N. Li, C. J. Brabec, H. Egelhaaf, *Adv. Energy Mater.* **2021**, *11*, 2101973.
- [16] Z. Wu, W. Li, Y. Ye, X. Li, H. Lin, *Sustain. Energy Fuels* **2021**, *5*, 1926.
- [17] Z. Li, C. Xiao, Y. Yang, S. P. Harvey, D. H. Kim, J. A. Christians, M. Yang, P. Schulz, S. U. Nanayakkara, C. S. Jiang, J. M. Luther, J. J. Berry, M. C. Beard, M. M. Al-Jassim, K. Zhu, *Energy Environ. Sci.* **2017**, *10*, 1234.
- [18] L. H. Chou, Y. T. Yu, I. Osaka, X. F. Wang, C. L. Liu, *J. Power Sources* **2021**, *491*, 229586.
- [19] C. Bracher, B. G. Freestone, D. K. Mohamad, J. A. Smith, D. G. Lidzey, *Energy Sci. Eng.* **2018**, *6*, 35.
- [20] J. Li, J. Dagar, O. Shargaieva, M. A. Flatken, H. Köbler, M. Fenske, C. Schultz, B. Stegemann, J. Just, D. M. Többens, A. Abate, R. Munir, E. Unger, *Adv. Energy Mater.* **2021**, *11*, 2003460.
- [21] K. Bruening, B. Dou, J. Simonaitis, Y. Y. Lin, M. F. A. M. van Hest, C. J. Tassone, *Joule* **2018**, *2*, 2464.
- [22] N. Rolston, W. J. Scheideler, A. C. Flick, J. P. Chen, H. Elmaraghi, A. Sleugh, O. Zhao, M. Woodhouse, R. H. Dauskardt, *Joule* **2020**, *4*, 2675.
- [23] S. Bag, J. R. Deneault, M. F. Durstock, *Adv. Energy Mater.* **2017**, *7*, 1.
- [24] T. Carey, C. Jones, F. Le Moal, D. Deganello, F. Torrisi, *ACS Appl. Mater. Interfaces* **2018**, *10*, 19948.
- [25] S. Sansoni, M. De Bastiani, E. Aydin, E. Ugur, F. H. Isikgor, A. Al-Zahrani, F. Lamberti, F. Laquai, M. Meneghetti, S. De Wolf, *Adv. Mater. Technol.* **2020**, *5*, 1901009.
- [26] I. J. Kramer, G. Moreno-Bautista, J. C. Minor, D. Kopilovic, E. H. Sargent, *Appl. Phys. Lett.* **2014**, *105*, 183105.
- [27] Z. Yang, Z. Liu, V. Ahmadi, W. Chen, Y. Qi, *Sol. RRL* **2021**, *6*, 2100458.
- [28] N.-G. G. Park, K. Zhu, *Nat. Rev. Mater.* **2020**, *5*, 333.

- [29] H. Cai, X. Liang, X. Ye, J. Su, J. Guan, J. Yang, Y. Liu, X. Zhou, R. Han, J. Ni, J. Li, J. Zhang, *ACS Appl. Energy Mater.* **2020**, *3*, 9696.
- [30] J. E. Bishop, C. D. Read, J. A. Smith, T. J. Routledge, D. G. Lidzey, *Sci. Rep.* **2020**, *10*, 6610.
- [31] J. E. Bishop, J. A. Smith, D. G. Lidzey, *ACS Appl. Mater. Interfaces* **2020**, *12*, 48237.
- [32] F. Huang, Y. Dkhissi, W. Huang, M. Xiao, I. Benesperi, S. Rubanov, Y. Zhu, X. Lin, L. Jiang, Y. Zhou, A. Gray-Weale, J. Etheridge, C. R. McNeill, R. A. Caruso, U. Bach, L. Spiccia, Y.-B. Cheng, *Nano Energy* **2014**, *10*, 10.
- [33] B. Conings, A. Babayigit, M. T. Klug, S. Bai, N. Gauquelin, N. Sakai, J. T.-W. Wang, J. Verbeeck, H.-G. Boyen, H. J. Snaith, *Adv. Mater.* **2016**, *28*, 10701.
- [34] J. Ding, Q. Han, Q. Q. Ge, D. J. Xue, J. Y. Ma, B. Y. Zhao, Y. X. Chen, J. Liu, D. B. Mitzi, J. S. Hu, *Joule* **2019**, *3*, 402.
- [35] J. Zheng, M. Zhang, C. F. J. Lau, X. Deng, J. Kim, Q. Ma, C. Chen, M. A. Green, S. Huang, A. W. Y. Ho-Baillie, *Sol. Energy Mater. Sol. Cells* **2017**, *168*, 165.
- [36] D.-K. Lee, D.-N. Jeong, T. K. Ahn, N.-G. Park, *ACS Energy Lett.* **2019**, *4*, 2393.
- [37] D.-K. Lee, K.-S. Lim, J.-W. Lee, N.-G. Park, *J. Mater. Chem. A* **2021**, *9*, 3018.
- [38] J. W. Yoo, J. Jang, U. Kim, Y. Lee, S.-G. Ji, E. Noh, S. Hong, M. Choi, S. Il Seok, *Joule* **2021**, *5*, 2420.
- [39] L.-L. Gao, C.-X. Li, C.-J. Li, G.-J. Yang, *J. Mater. Chem. A* **2017**, *5*, 1548.
- [40] M. Kohlstädt, M. A. Yakoob, U. Würfel, *Phys. status solidi* **2018**, *215*, 1800419.
- [41] H. Hu, Z. Ren, P. W. K. K. Fong, M. Qin, D. Liu, D. Lei, X. Lu, G. Li, *Adv. Funct. Mater.* **2019**, *29*, 1.
- [42] B. Chen, Z. J. Z. Yu, S. Manzoor, S. Wang, W. Weigand, Z. J. Z. Yu, G. Yang, Z. Ni, X. Dai, Z. C. Holman, J. Huang, *Joule* **2020**, *4*, 850.
- [43] Z. Ouyang, M. Yang, J. B. Whitaker, D. Li, M. F. A. M. van Hest, *ACS Appl. Energy Mater.* **2020**, *3*, 3714.
- [44] J. Küffner, T. Wahl, M. Schultes, J. Hanisch, J. Zillner, E. Ahlswede, M. Powalla, *ACS Appl. Mater. Interfaces* **2020**, *12*, 52678.
- [45] K. Liu, Q. Liang, M. Qin, D. Shen, H. Yin, Z. Ren, Y. Zhang, H. Zhang, P. W. K. Fong, Z. Wu, J. Huang, J. Hao, Z. Zheng, S. K. So, C. Lee, X. Lu, G. Li, *Joule* **2020**, *4*, 1.
- [46] H. Li, T. Bu, J. Li, Z. Lin, J. Pan, Q. Li, X.-L. Zhang, Z. Ku, Y.-B. Cheng, F. Huang, *ACS Appl. Mater. Interfaces* **2021**, *13*, 18724.

- [47] P. W. Fong, H. Hu, Z. Ren, K. Liu, L. Cui, T. Bi, Q. Liang, Z. Wu, J. Hao, G. Li, *Adv. Sci.* **2021**, *8*, 2003359.
- [48] F. Mathies, E. R. Nandayapa, G. Paramasivam, M. F. Al Rayes, V. R. F. Schröder, C. Rehermann, E. J. W. List-Kratochvil, E. L. Unger, *Mater. Adv.* **2021**, *2*, 5365.
- [49] G. Cotella, J. Baker, D. Worsley, F. De Rossi, C. Pleydell-Pearce, M. Carnie, T. Watson, *Sol. Energy Mater. Sol. Cells* **2017**, *159*, 362.
- [50] Y.-J. Heo, J.-E. Kim, H. Weerasinghe, D. Angmo, T. Qin, K. Sears, K. Hwang, Y.-S. Jung, J. Subbiah, D. J. Jones, M. Gao, D.-Y. Kim, D. Vak, *Nano Energy* **2017**, *41*, 443.
- [51] J.-E. Kim, Y.-S. Jung, Y.-J. Heo, K. Hwang, T. Qin, D.-Y. Kim, D. Vak, *Sol. Energy Mater. Sol. Cells* **2018**, *179*, 80.
- [52] D. Burkitt, R. Swartwout, J. McGettrick, P. Greenwood, D. Beynon, R. Brenes, V. Bulović, T. Watson, *RSC Adv.* **2019**, *9*, 37415.
- [53] X. Dai, Y. Deng, C. H. Van Brackle, S. Chen, P. N. Rudd, X. Xiao, Y. Lin, B. Chen, J. Huang, *Adv. Energy Mater.* **2020**, *10*, 1903108.
- [54] M. Du, X. Zhu, L. Wang, H. Wang, J. Feng, X. Jiang, Y. Cao, Y. Sun, L. Duan, Y. Jiao, K. Wang, X. Ren, Z. Yan, S. Pang, S. (Frank) Liu, *Adv. Mater.* **2020**, *32*, 2004979.
- [55] C. Gong, S. Tong, K. Huang, H. Li, H. Huang, J. Zhang, J. Yang, *Sol. RRL* **2020**, *4*, 1900204.
- [56] A. S. Subbiah, F. H. Isikgor, C. T. Howells, M. De Bastiani, J. Liu, E. Aydin, F. Furlan, T. G. Allen, F. Xu, S. Zhumagali, S. Hoogland, E. H. Sargent, I. McCulloch, S. De Wolf, *ACS Energy Lett.* **2020**, *5*, 3034.
- [57] V. Prakasam, D. Tordera, F. Di Giacomo, R. Abbel, A. Langen, G. Gelinck, H. J. Bolink, *J. Mater. Chem. C* **2019**, *7*, 3795.
- [58] S. Tang, J. Bing, J. Zheng, J. Tang, Y. Li, M. Mayyas, Y. Cho, T. W. Jones, T. C.-J. Yang, L. Yuan, M. Tebyetekerwa, H. T. Nguyen, M. P. Nielsen, N. J. Ekins-Daukes, K. Kalantar-Zadeh, G. J. Wilson, D. R. McKenzie, S. Huang, A. W. Y. Ho-Baillie, *Cell Reports Phys. Sci.* **2021**, 100511.
- [59] M. Eslamian, *Coatings* **2014**, *4*, 60.
- [60] S. A. Paniagua, A. J. Giordano, O. L. Smith, S. Barlow, H. Li, N. R. Armstrong, J. E. Pemberton, J.-L. Brédas, D. Ginger, S. R. Marder, *Chem. Rev.* **2016**, *116*, 7117.
- [61] M. Roß, S. Severin, M. B. Stutz, P. Wagner, H. Köbler, M. Favin-Lévêque, A. Al-Ashouri, P. Korb, P. Tockhorn, A. Abate, B. Stannowski, B. Rech, S. Albrecht, *Adv. Energy Mater.* **2021**,

2101460.

- [62] D. K. Schwartz, *Annu. Rev. Phys. Chem.* **2001**, *52*, 107.
- [63] A. Bulusu, S. A. Paniagua, B. A. MacLeod, A. K. Sigdel, J. J. Berry, D. C. Olson, S. R. Marder, S. Graham, *Langmuir* **2013**, *29*, 3935.
- [64] E. B. Troughton, C. D. Bain, G. M. Whitesides, R. G. Nuzzo, D. L. Allara, M. D. Porter, *Langmuir* **1988**, *4*, 365.
- [65] G. A. L. Andreatta, N. Blondiaux, J. Gay, S. Unterhofer, A. Lachowicz, A. Faes, *Thin Solid Films* **2021**, *732*, 138783.
- [66] P. J. Hotchkiss, S. C. Jones, S. A. Paniagua, A. Sharma, B. Kippelen, N. R. Armstrong, S. R. Marder, *Acc. Chem. Res.* **2012**, *45*, 337.
- [67] N. Phung, M. Verheijen, A. Todinova, K. Datta, M. Verhage, A. Al-Ashouri, H. Köbler, X. Li, A. Abate, S. Albrecht, M. Creatore, *ACS Appl. Mater. Interfaces* **2022**, *14*, 2166.
- [68] O. Almora, D. Baran, G. C. Bazan, C. Berger, C. I. Cabrera, K. R. Catchpole, S. Erten-Ela, F. Guo, J. Hauch, A. W. Y. Ho-Baillie, T. J. Jacobsson, R. A. J. Janssen, T. Kirchartz, N. Kopidakis, Y. Li, M. A. Loi, R. R. Lunt, X. Mathew, M. D. McGehee, J. Min, D. B. Mitzi, M. K. Nazeeruddin, J. Nelson, A. F. Nogueira, U. W. Paetzold, N. Park, B. P. Rand, U. Rau, H. J. Snaith, E. Unger, L. Vaillant-Roca, H. Yip, C. J. Brabec, *Adv. Energy Mater.* **2021**, *11*, 2002774.
- [69] M. Saliba, L. Etgar, *ACS Energy Lett.* **2020**, *5*, 2886.
- [70] S. Paek, P. Schouwink, E. N. Athanasopoulou, K. T. Cho, G. Grancini, Y. Lee, Y. Zhang, F. Stellacci, M. K. Nazeeruddin, P. Gao, *Chem. Mater.* **2017**, *29*, 3490.
- [71] S. Ulična, B. Dou, D. H. Kim, K. Zhu, J. M. Walls, J. W. Bowers, M. F. A. M. Van Hest, *ACS Appl. Energy Mater.* **2018**, *1*, 1853.
- [72] C. Gao, P. Wang, H. Wang, C. Yu, B. Du, H. Zhang, T. Li, D. Liu, T. Wang, *ACS Appl. Energy Mater.* **2021**, *4*, 11496.
- [73] J. E. Bishop, J. A. Smith, C. Greenland, V. Kumar, N. Vaenas, O. S. Game, T. J. Routledge, M. Wong-Stringer, C. Rodenburg, D. G. Lidzey, *ACS Appl. Mater. Interfaces* **2018**, *10*, 39428.
- [74] J. Su, H. Cai, X. Ye, X. Zhou, J. Yang, D. Wang, J. Ni, J. Li, J. Zhang, *ACS Appl. Mater. Interfaces* **2019**, *11*, 10689.
- [75] Y. Yu, F. Zhang, T. Hou, X. Sun, H. Yu, M. Zhang, *Sol. RRL* **2021**, 2100386.
- [76] K. H. Hendriks, J. J. van Franeker, B. J. Bruijnaers, J. A. Anta, M. M. Wienk, R. A. J. Janssen, *J. Mater. Chem. A* **2017**, *5*, 2346.

- [77] O. Shargaieva, H. Näsström, J. A. Smith, D. Többens, R. Munir, E. Unger, *Mater. Adv.* **2020**, *1*, 3314.
- [78] S. Chen, X. Xiao, B. Chen, L. L. Kelly, J. Zhao, Y. Lin, M. F. Toney, J. Huang, *Sci. Adv.* **2021**, *7*, 26.
- [79] S. Chen, X. Dai, S. Xu, H. Jiao, L. Zhao, J. Huang, *Science (80-.)*. **2021**, *373*, 902.
- [80] Y. Deng, X. Zheng, Y. Bai, Q. Wang, J. Zhao, J. Huang, *Nat. Energy* **2018**, *3*, 560.
- [81] A. T. Barrows, A. J. Pearson, C. K. Kwak, A. D. F. Dunbar, A. R. Buckley, D. G. Lidzey, *Energy Environ. Sci.* **2014**, *7*, 2944.
- [82] M. Ramesh, K. M. Boopathi, T. Y. Huang, Y. C. Huang, C. S. Tsao, C. W. Chu, *ACS Appl. Mater. Interfaces* **2015**, *7*, 2359.
- [83] S. Gamliel, A. Dymshits, S. Aharon, E. Terkieltaub, L. Etgar, *J. Phys. Chem. C* **2015**, *119*, 19722.
- [84] F. Li, C. Bao, H. Gao, W. Zhu, T. Yu, J. Yang, G. Fu, X. Zhou, Z. Zou, *Mater. Lett.* **2015**, *157*, 38.
- [85] J. G. Tait, S. Manghooli, W. Qiu, L. Rakocevic, L. Kootstra, M. Jaysankar, C. A. Masse De La Huerta, U. W. Paetzold, R. Gehlhaar, D. Cheyns, P. Heremans, J. Poortmans, *J. Mater. Chem. A* **2016**, *4*, 3792.
- [86] H. Huang, J. Shi, L. Zhu, D. Li, Y. Luo, Q. Meng, *Nano Energy* **2016**, *27*, 352.
- [87] D. K. Mohamad, J. Griffin, C. Bracher, A. T. Barrows, D. G. Lidzey, *Adv. Energy Mater.* **2016**, *6*, 1.
- [88] M. Remeika, S. R. Raga, S. Zhang, Y. Qi, *J. Mater. Chem. A* **2017**, *5*, 5709.
- [89] S. C. Hong, G. Lee, K. Ha, J. Yoon, N. Ahn, W. Cho, M. Park, M. Choi, *ACS Appl. Mater. Interfaces* **2017**, *9*, 7879.
- [90] S. Kavadiya, D. M. Niedzwiedzki, S. Huang, P. Biswas, *Adv. Energy Mater.* **2017**, *7*, 1.
- [91] G. Chai, S. Luo, H. Zhou, W. A. Daoud, *Mater. Des.* **2017**, *125*, 222.
- [92] J. Yao, L. Yang, F. Cai, Y. Yan, R. S. Gurney, D. Liu, T. Wang, *Sustain. Energy Fuels* **2018**, *2*, 436.
- [93] S. Han, H. Kim, S. Lee, C. Kim, *ACS Appl. Mater. Interfaces*, **2018**, *10*, 7281.
- [94] L. H. Chou, X. F. Wang, I. Osaka, C. G. Wu, C. L. Liu, *ACS Appl. Mater. Interfaces* **2018**, *10*, 38042.
- [95] M. Park, W. Cho, G. Lee, S. C. Hong, M. cheol Kim, J. Yoon, N. Ahn, M. Choi, *Small* **2019**, *15*, 1.

- [96] Y. S. Chou, L. H. Chou, A. Z. Guo, X. F. Wang, I. Osaka, C. G. Wu, C. L. Liu, ACS Sustain. Chem. Eng. **2019**, 7, 14217.
- [97] L. H. Chou, Y. T. Yu, X. F. Wang, I. Osaka, C. G. Wu, C. L. Liu, Energy Technol. **2020**, 8, 1.
- [98] A. Z. Guo, L. H. Chou, S. H. Yang, D. Wang, X. F. Wang, I. Osaka, H. W. Lin, C. L. Liu, Adv. Mater. Interfaces **2021**, 8, 1.

Spray Deposition of an Alkyl-Ammonium Halide Passivating Agents for Spray-Coated, Methylammonium-Free Perovskite Solar Cells

5.1 Publication Foreword

Whilst the GASP technique developed in Chapter Four enabled the creation of state-of-the-art spray-coated solar cells, MAPbI₃-based perovskite compositions are only a “fruit fly” of PSC research. Although such methylammonium-containing compositions are the most studied hybrid perovskite materials, they are expected to be far too unstable to be a suitable candidate for long-term stability, and thus commercialisation. In this chapter, we have therefore investigated the GASP-deposition of a methylammonium-free perovskite composition. To mitigate the high-degree of hysteresis recorded in such devices, a spray-cast, surface-passivating post-treatment is also developed. Such surface-passivation strategies have attracted increasing attention as a technique to impart enhanced robustness to the perovskite absorber layer. Accordingly, a roll-to-roll compatible surface passivating technique is expected to be of significant interest to the research community. The manuscript presented below as Chapter Five is planned for submission to the journal “Advanced Materials”.

5.2 Author Contributions

E.J. Cassella conceptualised the project and developed the methodology; prepared samples; performed all data analysis and created all figures; wrote the original draft and completed all further revisions. **T. Thornber** prepared samples and performed XRD. **E.L.K. Spooner** assisted with sample preparation, UV-Vis measurements, and writing the original draft. **M.E. O’Kane** assisted with sample preparation and performed SEM measurements. **R.C. Kilbride** performed GIWAXS measurements. **O.S. Game** advised on the methodology and assisted with manuscript revision. **D.G. Lidzey** provided funding and equipment and assisted with revisions to the original manuscript.

5.3 Publication Main Text

Spray Deposition of an Alkyl-Ammonium Halide Passivating Agent for Spray-Coated, Methylammonium-Free Perovskite Solar Cells

Elena J. Cassella^{}, Timothy Thornber, Mary E. O’Kane, Emma L.K. Spooner, Rachel C. Kilbride, Onkar S. Game, David G. Lidzey^{*}*

E.J. Cassella, T. Thornber, Dr. M.E. O’Kane, Dr. E.L.K. Spooner, Dr. R.C. Kilbride, Dr. O.S. Game, Prof. D.G. Lidzey^{*}

Department of Physics and Astronomy, University of Sheffield, Hicks Building, Hounsfield Road, Sheffield, S3 7RH, United Kingdom

^{*}E-mail: d.g.lidzey@sheffield.ac.uk

5.3.1 Abstract

Methylammonium-free (MA-free) perovskite compositions are a preferential composition for perovskite solar cells (PSCs) due to their intrinsically higher thermostability. However, MA-free compositions suffer from greater energetic losses typically attributed to a high density of defects due to poor crystalline quality. Here, we deposit a $\text{Cs}_{0.15}\text{FA}_{0.75}\text{PbI}_{2.85}\text{Cl}_{0.15}$ perovskite active layer using gas-assisted spray coating. In combination with spin-coated tin oxide and spiro-OMeTAD as electron- and hole-selective contacts respectively, we fabricate *n-i-p* PSCs having power conversion efficiencies (PCEs) of up to 18.6%. A high degree of hysteresis, however, results in devices having a stabilized efficiency of 16.6%. Suppression of interfacial recombination through post-annealing treatments of perovskite is now a ubiquitous approach for device efficiency optimization. We have therefore explored the use of a spray-coated post-deposition treatment to reduce non-radiative recombination at the perovskite/hole-transporting layer (HTL) interface. Here, an iso-butylammonium bromide (i-BABr) solution was deposited onto the perovskite surface by ultrasonic spray coating, forming a quasi-2D perovskite. Devices created in this manner demonstrate PCEs of up to 19.8% (19.4% stabilized); a value that is highly comparable with spin-passivated reference devices (20.0%). This work represents the first demonstration of a spray-coated passivation treatment which is compatible with roll-to-roll processing.

5.3.2 Introduction

Organic-inorganic metal halide perovskite photovoltaics (PV) have become the focus of much research attention due to unprecedented developments in power conversion efficiencies (PCE), increasing from 3.8% up to 25.7% in little over a decade.^[1] In order to drive this technology towards commercialization, perovskite PV must simultaneously meet requirements for high efficiency, long lifetime and low cost.^[2] Whilst Levelized Cost of Energy (LCOE) requirements are relatively insensitive to the absorber material – so long as lifetime and efficiency requirements are met – the capital expenditure (capex) for module production must be sufficiently low to enable sustainable growth of manufacturing output capabilities.^[3] Here, solution-processable technologies (such as perovskites) capable of high-throughput manufacturing can significantly lower

the capex of upscaling module production (by orders of magnitude) compared to existing silicon and cadmium telluride technologies.

Spray coating has already been used to fabricate devices at throughput speeds of up to 12 m min^{-1} ; a rate that exceeds all other roll-to-roll (R2R) deposition techniques.^[4] As such, spray coating is particularly promising for cost-effective, sustainable production of PSCs. Furthermore, spray coating is a non-contact deposition method, potentially enabling devices to be fabricated over non-planar surfaces and rigid substrates.^[5]

The PCEs of spray-coated perovskite solar cells (PSCs) have not yet matched those of other R2R compatible technologies, such as blade or slot-die coating.^[6] Here, poor-quality films are often created without fine control over the spray deposition and crystallization processes.^[7] However, a number of advances using “one-step” techniques to obtain high-quality films, including; hot air blowing^[8]; plasma processing^[4]; additive engineering^[9]; anti-solvent bath treatments^[10,11]; vacuum flash-assisted solution processing^[12]; and more recently, gas-assisted spray processing (GASP) which demonstrated PCEs approaching 21% for lab-scale devices.^[13] As a result of the use of such techniques and developments, top-performing devices already reach the determined PCE values necessary to compete with ubiquitous c-Si PV technologies.^[14,15] They also offer the promise of proportionally lower-costs due to high throughput speed. Indeed, as the LCOE is more dependent on module lifetime, rather than device efficiency, it appears that improving device stability is now a highly pertinent issue for spray-coated PSCs.^[4]

Despite this progress, there are relatively few demonstrations of spray-coated PSCs that avoid the use of thermally unstable methylammonium (MA) molecules in their formulation.^[7,16] Furthermore, polycrystalline perovskite thin-films by nature contain a large number of defects which are mostly concentrated at grain boundaries and other interfaces.^[17] Such defects significantly contribute to non-radiative recombination losses, hinder charge transport, and reduce the electrical stability of the perovskite.^[18] State-of-the-art PSCs are therefore typically limited by their open-circuit voltage (V_{OC}), with this being particularly true for MA-free compositions. Further progress towards the radiative efficiency limit of such devices is expected via reducing nonradiative recombination losses, with such losses being particularly important at the interface with charge-transporting layers.^[19,20] Developing approaches to passivate the bulk and surface defects of the perovskite have therefore been the subject of intensive research efforts.^[21,22] It is

important, therefore, to develop R2R-compatible strategies that reduce interfacial energetic losses in devices fabricated using high-throughput processing techniques.

In this paper, we adapt the work of Bu et al.^[23] in which they reported a solvent-engineered DMF: NMP precursor ink to form an NMP-based intermediate adduct that templated the formation of highly-crystalline FACs-containing perovskite films. We use this precursor formulation along with our developed gas-assisted spray processing (GASP) protocol, to fabricate spray-coated PSCs with a $\text{Cs}_{0.15}\text{FA}_{0.75}\text{PbI}_{2.85}\text{Cl}_{0.15}$ active layer (where FA is formamidinium), with devices created having PCEs of up to 18.6%. Here, the stoichiometry of the perovskite composition refers to the stoichiometry of the precursor solution. To further enhance device performance, we develop a spray coating process to passivate the top surface of the perovskite film using iso-butylammonium bromide (i-BABr). This alkyl-ammonium cation is found to form a 2D perovskite phase at film surface, a finding in agreement with previous reports. We believe that this represents the first demonstration of a spray-cast, surface-passivating post-treatment. Using this approach, we improve the median PCE of spray-coated devices by up to 2.1 absolute %. This allows us to create small-area, proof-of-concept spray-passivated devices having PCE values of up to 19.8%. Critically, the spray-coated passivation technique is found to match the benefits achieved using a comparable spin-coated passivation treatment.

5.3.3 Results and Discussion

5.3.3.1 Developing the GASP protocol for spray-coated CsFA-based perovskite thin-films

Figure 5.1(a) schematically illustrates the *n-i-p* architecture of the fabricated devices. Small-area devices were deposited onto indium-doped tin oxide- (ITO) coated glass substrates (20 mm x 15 mm). An electron-transporting layer (ETL) deposited via a colloidal nanoparticle tin oxide (np-SnO_2) solution was first spin-coated onto the ITO under ambient conditions.

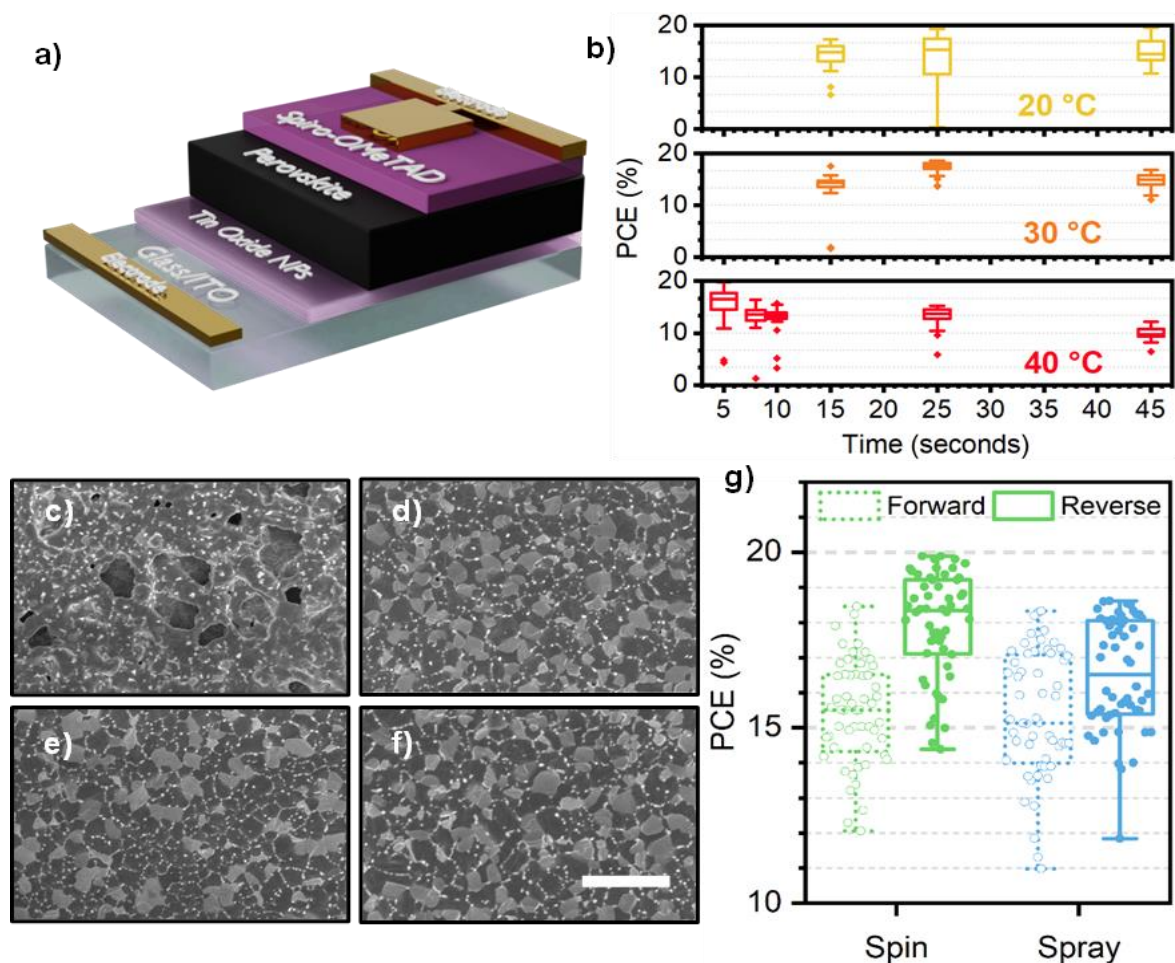


Figure 5.1: (a) A schematic of the ITO/nanoparticle-SnO₂/perovskite/spiro-OMeTAD/Au perovskite solar cell architecture used. (b) A comparison of the resultant device performance as a function of air-knife delay time and temperature of the substrate during deposition. Lower temperatures extend the processing window; however, a greater degree of performance variation is found for devices spray-cast at 20 °C. Scanning electron microscopy images of spray-coated perovskite films deposited onto substrates held at (c) 20 °C, (d) 30 °C, and (e) 40 °C s, and (f) spin-coated control devices. Scale bar inset is 2 μm. (g) Box plot of device PCE for devices cast on substrates at 30 °C with a 25 second delay time (the optimum deposition conditions) vs. spin-coated control devices. Sprayed devices demonstrate fairly comparable performance to spin-coated control devices.

A perovskite active layer was then spray-coated using an ultrasonic Sonotek Exactacoat system housed within an N₂-filled glovebox. The spray head (controlled by a motorized gantry) was moved linearly across the substrate at a speed of 80 mm s⁻¹, depositing material in a single pass at a flow rate of 1 ml min⁻¹, with such conditions based upon our previously established protocols.^[24] Here, the piezoelectric tip of the spray coater was driven at power of 2 W. In the GASP technique, an “air-knife” – controlled by the same motorized gantry – was held at 45 ° to the substrate normal and passed over the

substrate surface at a relative separation of around 2 cm, blowing ambient-temperature N₂ onto the surface at a pressure of 20 psi. This “gas-quench” step was applied after a short delay time to allow solution droplet coalescence and slight drying of the spray-deposited material. A spiro-OMeTAD hole-transporting layer (HTL) was also spin-coated onto the perovskite films within an N₂-filled glovebox. Full details can be found in the Experimental Methods (Chapter 3).

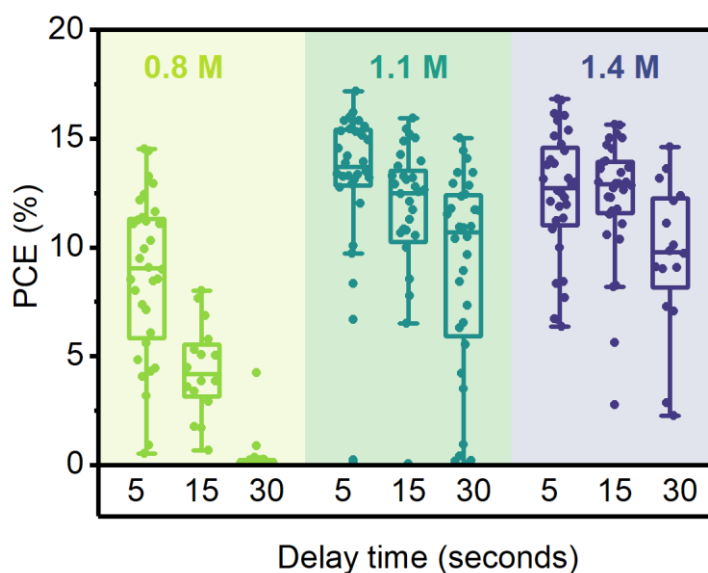


Figure 5.2: The resulting device PCE from perovskite absorber layers spray-cast from 0.8M (light green), 1.1 M (dark green), and 1.4 M (blue) precursor solutions with a delay time or either 5, 15 or 30 seconds between the ink deposition and application of the air-knife. In all cases, the substrate was held at 40 °C during spray casting of the precursor ink.

Previously, we have found it necessary to hold the substrate at an elevated temperature during deposition to facilitate surface wetting of the precursor solution.^[12] In our initial experiments, the substrate was therefore held at 40 °C during coating. However, it is known that the GASP process is sensitive to the molarity of the precursor ink.^[13] All spin-coated devices were fabricated from a 2 M perovskite solution. We therefore explored a series of reduced molarity inks for the spray-coated devices, including 0.8 M, 1.1 M, and 1.4 M solutions. A range of delay times between the spray deposition and gas-quench were also explored. **Figure 5.2** demonstrates that the resultant device PCE was maximized when using 1.1 M precursor inks. Note that device efficiency was similar for devices made from 1.4 M inks, however, a lower ink

concentration would reduce materials costs in a commercial process, and so all further experiments utilized a 1.1 M ink.

Figure 5.2 shows the effect of “delay time” between deposition of the wet film and application of the air knife gas-jet. This can be seen to have a significant effect on device PCE, a finding in line with previous reports. This delay must be carefully timed as the spray-cast droplets require time to coalesce into a wet film, with the gas-jet then applied prior to ambient evaporation-induced supersaturation of the film. Without application of the gas-jet, we find that the resultant films contain a low density of crystalline nuclei which consequently results in the formation of poor quality thin-films.^[25] Whilst holding the substrate at 40 °C during deposition created highly specular films with correspondingly high device performance, we found that the processing window between deposition of the film and application of the gas-jet was extremely short (5 seconds). For delay times more than 5 seconds, we found device PCEs were reduced for substrates held at 40 °C. This effect is illustrated in **Figure 5.1(b)**, where we plot device performance as a function of temperature and delay time when cast from the 1.1 M precursor ink. Importantly, we found that the processing window was greatly extended by reducing the substrate temperature to room temperature (labelled here as “20 °C”), or 30 °C. However, whilst best-performing devices fabricated at 20 °C were comparable with best-performing devices cast at 30 °C and 40 °C, we find a much greater degree of statistical variation in all device performance metrics (**Figure 5.3**).

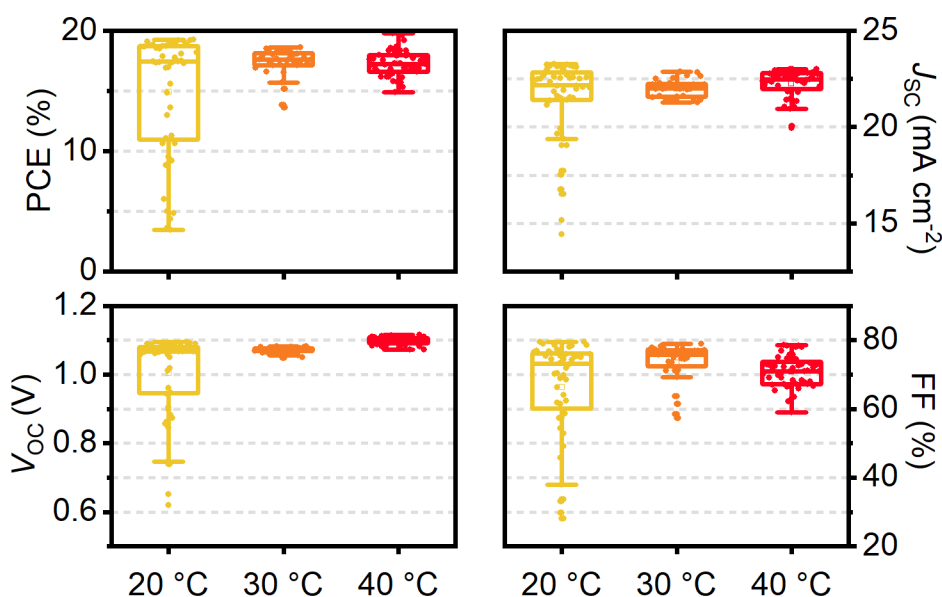


Figure 5.3: Solar cell performance metrics corresponding to devices presented in Figure 1(b).

To investigate this effect, we have recorded scanning electron microscopy (SEM) images of spray-coated perovskite films fabricated at an optimal delay time (corresponding to maximum device performance) for substrates held at each temperature during perovskite deposition; namely 25 s / 20 °C, 25 s / 30 °C, and 5s / 40 °C. These images are presented in **Figure 5.1(c-e)** alongside an SEM image of a spin-coated control film (**Figure 5.1(f)**). The film spray-cast at 20 °C contains many “voids” that have a lateral scale of up to 1 μm which are visible at the top surface. We speculate that such defects form due to an insufficient removal of solvent from the wet film during the gas-quench. These films are then thermally annealed firstly at 70 °C and then at 150 °C, with the subsequent removal of solvent leaving voids distributed throughout the perovskite film. In addition to reducing surface coverage, such defects act as significant electrical shunts, increasing leakage currents and reducing the open-circuit voltage (V_{oc}), short-circuit current (J_{sc}), and fill factor (FF). Interestingly, we also see “tracks” formed in the perovskite surface for films cast at 20 °C (see **Figure 5.4**). Here, we suspect that air flow over the still-wet film surface generates solvent flow, resulting in recrystallization in affected regions. This is indicated by the large reduction in apparent grain size in the area surrounding the solvent-flow “tracks”.

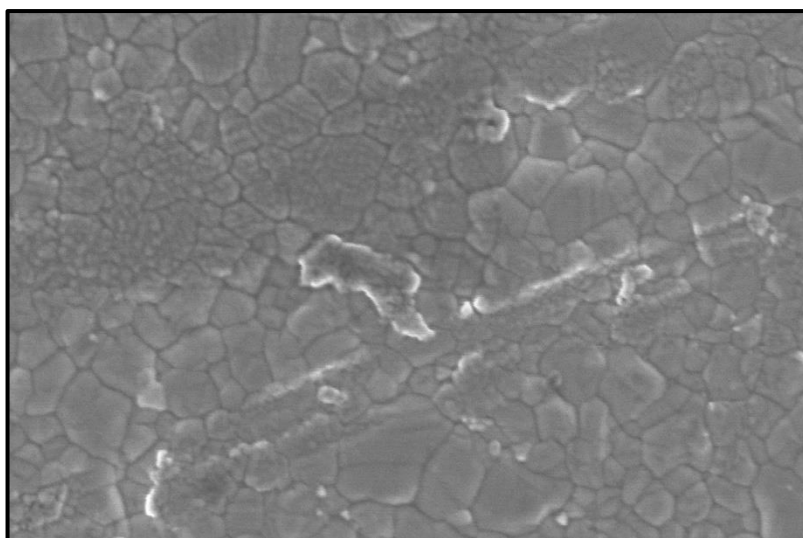


Figure 5.4: Scanning electron microscope (SEM) image of a 1.1 M film spray-cast onto a substrate held at 20 °C with a delay time of 25 s. 500 nm scale bar inset.

In all SEM images, several small, bright crystallites are apparent, concentrated at the grain boundaries. These are likely PbI_2 crystallites formed as a by-product of the substitution of chlorine moieties with I^- or I^- interstitials. Such PbI_2 regions are expected to passivate the perovskite film and enhance the PCE of the resulting devices.^[26–32] In general, the SEM images of the perovskite deposited onto substrates held at 30 °C and 40 °C are visually similar to those of the spin control film. However, the average perovskite grain size is marginally smaller in films cast at 30 °C and 40 °C, compared to the spin controls (480 ± 170 nm and 480 ± 150 nm compared to 570 ± 150 nm, respectively). We speculate that this small difference in grain size arises from a greater density of nuclei formed when the precursor ink is deposited onto a heated substrate. We find that the perovskite grains are much larger than the PbI_2 crystallites, with a high proportion of the perovskite grains having a “lighter” shade than others. Such lighter regions are likely to be lead rich, whilst the darker grains are closer to a stoichiometric composition^[33]; an effect typically observed in lead-excess precursor solutions.

X-ray diffraction (XRD) patterns (see **Figure 5.5**) corroborate the presence of large quantities of PbI_2 in the films, with a high intensity signal observed at $12.8^\circ 2\theta$ corresponding to the PbI_2 . All diffraction patterns are seen to have a well-defined perovskite {110} peak at 14.2° . The intensity of this signal is slightly reduced in the spray-coated perovskite films with respect to that of the spin-coated films, with this being most apparent in films cast at 20 °C (**Figure 5.5** (inset)). This suggests that films cast onto substrates held at room-temperature are less-crystalline in nature. For this reason, our

optimized process is based on substrates being held at 30 °C with a delay time of 25 s is used in all further device fabrication. This process condition also has an extended processing window and produces films having improved quality and more repeatable device performance.

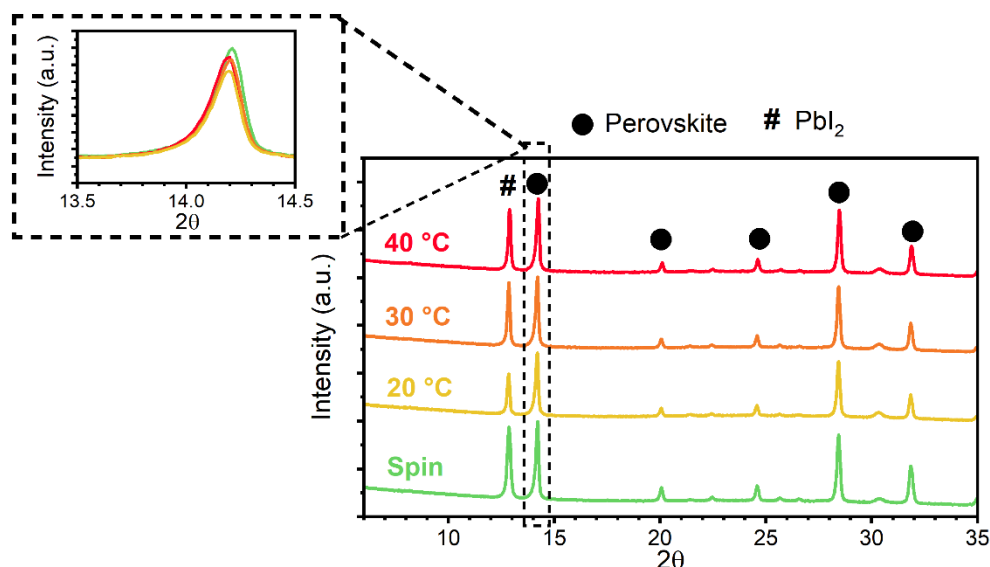


Figure 5.5: X-ray diffraction (XRD) patterns of perovskite absorber layers spray-cast from a 1.1M precursor ink onto a substrate held at 20 °C (yellow), 30 °C (orange), or 40 °C (red). A spin-coated reference film (from a 2 M precursor ink) is also shown (green). The enhanced region (inset) corresponds to a perovskite diffraction peak at $\sim 14.2^\circ 2\theta$.

Table 5.1: Summarised solar cell performance metrics for spin-coated 2 M $\text{Cs}_{0.15}\text{FA}_{0.75}\text{PbI}_{2.85}\text{Cl}_{0.15}$, and GASP-treated 1.1 M $\text{Cs}_{0.15}\text{FA}_{0.75}\text{PbI}_{2.85}\text{Cl}_{0.15}$ devices (substrate held at 30 °C with a delay time of 25 seconds), as presented in **Figure 1(g)**. Champion performance metrics are presented in bold, with mean ± 1 standard deviation values in parentheses.

Device	J_{sc} [mA cm^{-2}]	V_{oc} [V]	FF [%]	PCE [%]	N_{cells}
Spin	23.5	1.07	79.5	19.9	40
Control	(22.3 \pm 1.3)	(1.01 \pm 0.14)	(69.7 \pm 9.6)	(16.0 \pm 3.2)	
Spray	23.5	1.08	79.0	18.6	64
Control	(21.0 \pm 1.7)	(1.03 \pm 0.10)	(69.4 \pm 8.9)	(15.3 \pm 2.8)	

To further verify the quality of the GASP perovskite layer, we compare the PCE of devices having a spray-coated perovskite absorber layer with reference devices having a spin-coated perovskite layer. The results of this experiment are shown in a boxplot in **Figure 5.1(g)**. For completeness, all device metrics together with standard deviations are summarized in **Table 5.1**. It can be seen that the PCE of devices fabricated by the two processes have roughly comparable performance when measured using the forward-direction current-voltage (J - V) sweep. In contrast, the median device PCE for the reverse sweep of the spray-coated cells is noticeably reduced in comparison to the reverse-sweep of the spin-coated reference cell. Specifically, best-performing devices demonstrate 19.9% and 18.6% PCE on the reverse J - V sweep for spin and spray devices respectively. Despite this, the median value of the combined forward- and reverse-sweep device PCEs is 16.5 % vs. 15.9 % for spin-coated and spray-coated PSCs, respectively. Here, we identify reduced J_{SC} as the main factor contributing to the slightly lower performance of the spray-cast devices (21.0 ± 1.7 vs. 22.3 ± 1.3 mA cm⁻² for spray- and spin-coated cells, respectively). This effect likely arises from a slightly reduced active layer thickness of spray-coated active layers, being 457 ± 39 nm vs. 496 ± 19 nm for spray- and spin-cast layers, respectively (depicted in **Figure 5.6**). Regardless of this, we find that the GASP technique allows us to spray-coat high-quality, MA-free perovskite layers and construct devices having comparable device efficiencies to spin-coated references.

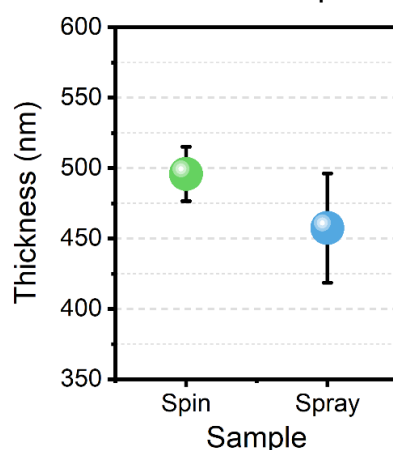


Figure 5.6: The measured thickness of the perovskite absorber layer deposited from a spin-coated, 2 M precursor ink (green), and a spray-cast 1.1 M precursor ink deposited onto a substrate held at 30 °C with a delay time of 25 s.

We observe a high degree of hysteresis between the forward and reverse J - V sweeps in most devices made by either spin- or spray-casting. Indeed, the stabilized power output (SPO) for the best-performing spray-coated perovskite device was only 16.6%. This PCE value lies 2 % (absolute) lower than the initial reverse J - V sweep (see **Figure 5.7(a-b)**). Although Bu et al incorporated KPF_6 into the perovskite precursor solution to reduce device hysteresis,^[23] we found this to have little or no effect in either reducing hysteresis or improving device performance (see **Figure 5.8**). We assign this effect to the fact that the np- SnO_2 ETL contains a KOH stabilizing additive which serves as an intrinsic source of K^+ ions and already partially passivate the SnO_2 /perovskite interface. As a result, addition of the excess KPF_6 into the precursor solution actually reduces device performance; an effect that we have observed in other perovskite compositions.^[34] We have therefore explored a surface passivating post-treatment strategy to improve device performance and reduce hysteresis, whilst retaining compatibility with a R2R manufacturing process.

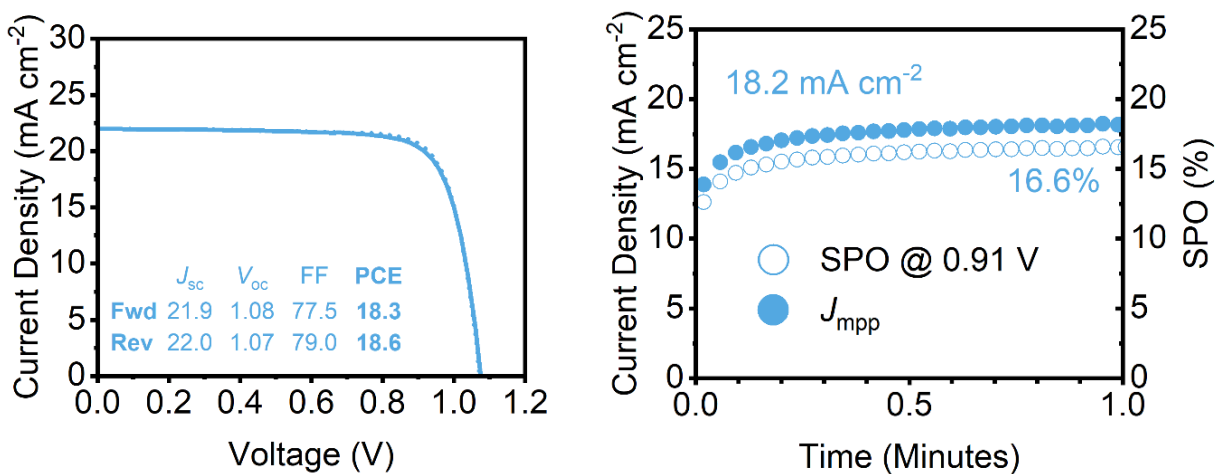


Figure 5.7: J - V curve (left) and stabilised power output (right) corresponding to the best-performing spray-cast cell (1.1 M precursor ink, 25 s delay time, 30 °C substrate).

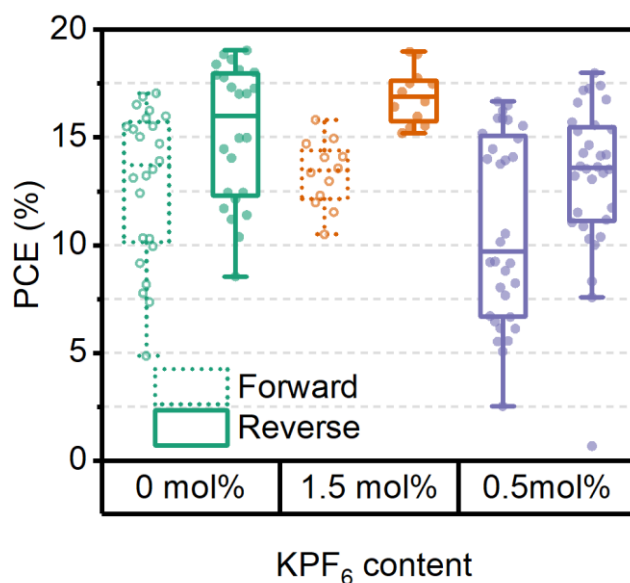


Figure 5.8: Device PCE for spin-coated cells incorporating 0 mol % (green), 1.5 mol % (orange), or 0.5 mol % (purple) of a KPF_6 additive in the precursor ink.

5.3.3.2 Developing a protocol for spray deposition of i-BABr

Long-chain alkyl-ammonium moieties can undergo exchange with cations at the surface of a perovskite film, forming an *in situ* 2D, or quasi-2D, capping layer on top of the bulk 3D perovskite.^[35] We note that some molecules may instead simply form a surface layer, although the underlying mechanisms to distinguish which of the two processes occurs is under some debate.^[36] This 2D capping layer is expected to impart both improved device stability and improved device efficiency by reducing nonradiative recombination losses at the film surface.^[37] The hydrophobic nature of such 2D capping layers is also proposed to improve their environmental stability.^[38,39] In addition, the overlap of the blue-shifted emission from the 2D perovskite with the absorption of the 3D perovskite is believed to lead to a “heterogeneous photon recycling” effect.^[40] A large number of such 2D/3D passivation strategies have now been explored and are thoroughly reviewed elsewhere.^[41,42] Whilst n-butylammonium iodide (BAI) and n-butylammonium bromide^[43] (BABr) have been used to demonstrate effective passivation of perovskite films through formation of a mixed 3D/2D perovskite,^[44,45] Liu et al. have demonstrated superior performance for iso-BAI than for n-BAI when applied to a $FAPbI_3$ perovskite.^[46] Here, the branched-chain molecule was found to form an $n = 2$ overlayer, with larger n values expected to provide better orbital overlap and, consequently, hole extraction. To passivate the top-surface of the spray-coated perovskite films, we have therefore

explored the use of iso-butylammonium bromide (i-BABr),^[23] with the deposition of this material explored using R2R-compatible techniques.

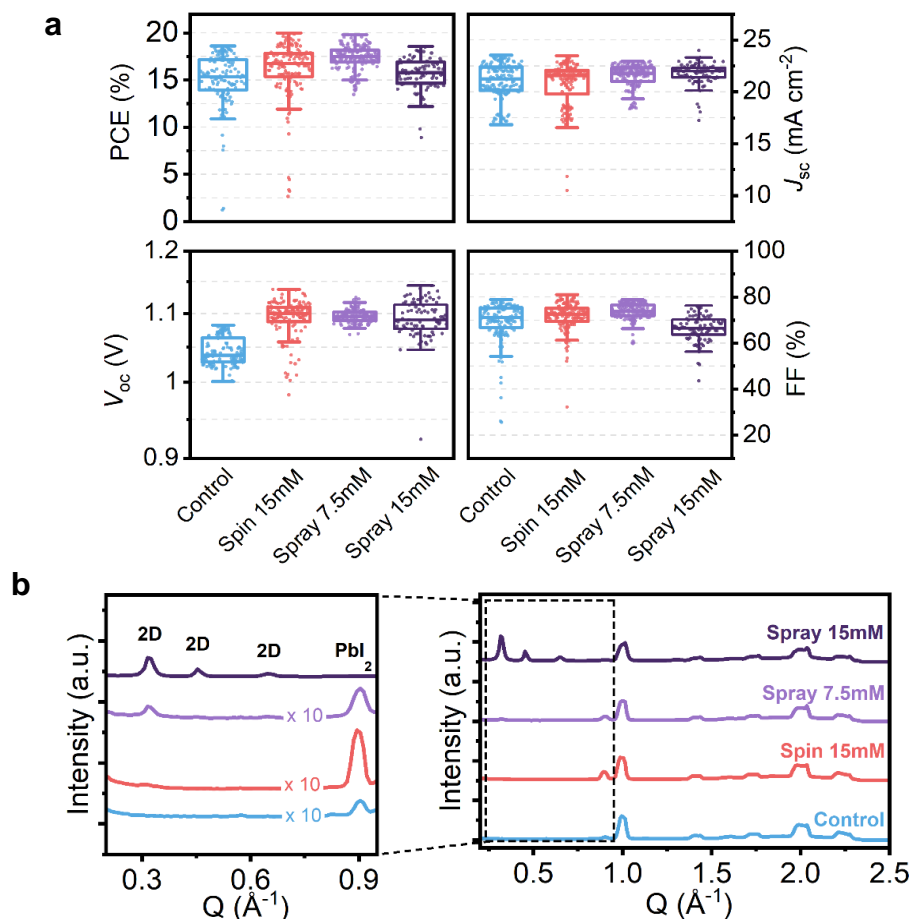


Figure 5.9: (a) Device performance metrics for a spray-coated $CS_{0.15}FA_{0.75}PbI_{2.85}Cl_{0.15}$ (blue), spray-coated perovskite with a spin-coated i-BABr passivating treatment (red), spray-coated perovskite with a spray-coated 7.5 mM i-BABr treatment (light purple), and spray-coated perovskite with a spray-coated 15 mM i-BABr treatment (dark purple). At 7.5 mM, the spray-coated passivation treatment results in comparable device performance to the spin-passivated cells. (b) 1D azimuthal integrations of the grazing incidence wide-angle scattering (GIWAXS) patterns of each of the above cases. (left) enhanced region of interest corresponding to the expected location of scattering intensities from 2D perovskite phases at low Q . Here, the scale is enhanced 10 x for the spray-coated 7.5 mM, spin-coated 7.5 mM, and unpassivated control diffraction patterns to highlight low-intensity signals.

Table 5.2: Summarised solar cell performance metrics for devices presented in **Figure 5.9(a)**. Champion performance metrics are presented in bold, with mean ± 1 standard deviation values in parentheses.

Device	J_{sc} [mA cm ⁻²]	V_{oc} [V]	FF [%]	PCE [%]	N_{cells}
Spray Control	23.5 (21.0 \pm 1.7)	1.08 (1.03 \pm 0.10)	79.0 (69.4 \pm 8.9)	18.6 (15.3 \pm 2.8)	64
Spin 15 mM	23.5 (20.8 \pm 2.2)	1.14 (1.07 \pm 0.13)	81.0 (71.5 \pm 6.3)	20.0 (16.1 \pm 3.1)	70
Spray 7.5 mM	23.0 (21.5 \pm 1.2)	1.13 (1.10 \pm 0.01)	78.9 (73.6 \pm 3.7)	19.8 (17.4 \pm 1.3)	70
Spray 15 mM	24.0 (21.7 \pm 1.1)	1.14 (1.09 \pm 0.03)	76.3 (66.3 \pm 5.7)	18.6 (15.7 \pm 1.8)	41

In this section, all perovskite active layers are deposited via spray coating. We have explored control (unpassivated) devices, and devices having an i-BABr solution applied to the perovskite surface by either spin or spray coating (passivated). Such passivating treatments were applied after the perovskite layer had been annealed and left to cool to room temperature. The optimization of the spray-coated passivation process was guided by PSC device performance. **Figure 5.9(a)** presents all device metrics for such studies, with device metrics also tabulated in **Table 5.2**. Here, the “control” devices – unpassivated, spray-coated perovskite – were fabricated as described above. For devices with a spin-coated passivation treatment (“spin 15 mM”), 50 μ l of a 15 mM i-BABr solution (\sim 2 mg ml⁻¹ in IPA) was spin-coated at 4000 rpm for 20 s onto the spray-cast and annealed perovskite film. This film was then then annealed at 100 $^{\circ}$ C for 5 minutes. This spin-coated passivation process results in a mean V_{oc} boost of 40 mV, and maximum V_{oc} values of up to 1.14 V vs. 1.08 V for the unpassivated “control” cells. Such devices have maximum PCE values up to 20.0% – an absolute increase of 1.4%. Notably, however, we observe a high degree of variation in the V_{oc} for spin-passivated devices. This most probably results from an unintentional variation in contact-time between the statically deposited i-BABr solution and the perovskite film. Here, 2D perovskite phases are known to have anisotropic charge

conductivity due to the relatively high resistance organic interlayer between the adjacent inorganic perovskite “slabs”.^[35] If excess 2D-material is generated, it results in “over-passivation” of the perovskite, with an insulating barrier formed at the perovskite surface. This insulating barrier layer will clearly reduce device PCE. Furthermore, the polar nature of the IPA carrier-solvent can dissolve the organic cation components within the perovskite lattice.^[47] During the spin coating process, the dissolved organic components are likely to be carried away from the film surface in the IPA solvent, leaving behind an organic deficient, lead excess film composition. We discuss this effect further below.

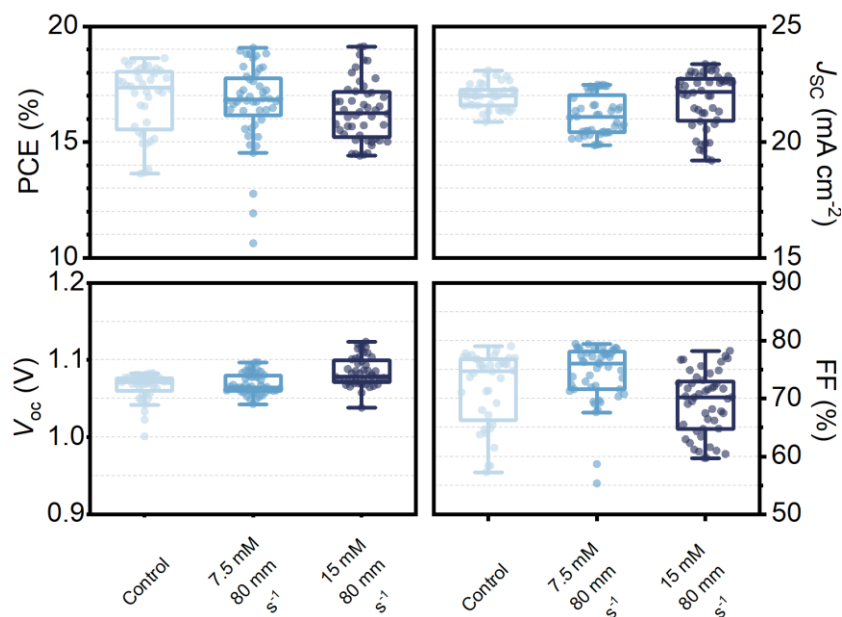


Figure 5.10: Solar cell metrics for PSCs with a spray-cast perovskite absorber layer (control), a spray-cast absorber layer with a 7.5 mM *i*-BABr treatment deposited at 80 mm s⁻¹ (7.5 mM, 80 mm s⁻¹), and a spray-cast absorber layer with a 15 mM *i*-BABr treatment deposited at 80 mm s⁻¹ (15 mM, 80 mm s⁻¹).

To spray-passivate films, the spray-head (operated at a power of 1 W) was passed once over the perovskite surface, depositing the *i*-BABr/IPA solution. Here, the substrate was held at room temperature during this deposition. The as-cast, wet film was then observed to dry by evaporation over a period of a few seconds. Spray-treated films were also then annealed at 100 °C for 5 minutes. We anticipate a longer contact-time between the spray-coated *i*-BABr solution and the perovskite compared with the spin-coated *i*-BABr film. Here, solvent evaporation is driven by the volatility of the IPA, rather than by air-flow effects induced during spin coating. For this reason, we reduced the concentration of the spray-coated *i*-BABr to 7.5 mM (from 15 mM). Based on extensive

device optimization, we find that spray coating a 7.5 mM solution of i-BABr at a spray-head speed of 40 mm s^{-1} resulted in highest-performing devices. By increasing the spray-head velocity over the substrate to 80 mm s^{-1} , we observed no apparent improvement in the median device V_{OC} (see **Figure 5.10**). We attribute this to the deposition of an insufficient quantity of material. At optimal deposition conditions, (40 mm s^{-1} , 7.5 mM i-BABr solution, “spray 7.5 mM”), we find that the average V_{OC} is improved by 70 mV with respect to control devices realizing a maximum value of 1.13 V (see **Figure 5.9(a)** and **Table 5.2**). This increase, alongside a reduction in the average FF, can be attributed to a thicker capping layer formed via spray coating vs. spin coating the i-BABr. This finding is consistent with the enhanced contact-time between the i-BABr solution and the perovskite film. Despite the thicker capping layer, champion spray 7.5 mM-passivated devices demonstrate a PCE of 19.8%, a value that is comparable to the maximum PCE values demonstrated via the use of a spin-cast passivation protocol (20.0%).

We have also confirmed that spray coating a higher concentration i-BABr solution at 40 mm s^{-1} (15 mM, “spray 15 mM”) is detrimental to the efficiency of the resulting devices. Specifically, we find that although peak V_{OC} values of up to 1.14 V are realized, the FF of devices is reduced from 74% to an average of 66% vs. “spray 7.5 mM” devices. This reduction in FF reduces the maximum PCE to around 18.6% – a value comparable to the unpassivated control devices. Indeed, even at a higher head-speed of 80 mm s^{-1} , the spray-coated 15 mM i-BABr solution has a detrimental effect on the median device PCE (**Figure 5.10**). We again determine a reduced FF which indicates an “over-passivation” of the perovskite films when i-BABr is sprayed at too high concentrations.

To confirm that the sprayed i-BABr passivation layer indeed forms a 2D perovskite layer, we here used grazing-incidence wide-angle X-ray scattering (GIWAXS) measurements. We show 1D azimuthal integrations of the 2D scattering intensity patterns in **Figure 5.9(b)** for the “control”, “spin 15 mM”, “spray 7.5 mM” (40 mm s^{-1}), and “spray 15 mM” (40 mm s^{-1}) films. See **Figure 5.11** for the corresponding 2D GIWAXS patterns. For “spray 15 mM” films, GIWAXS peaks are evident at $Q = 0.32, 0.45, 0.65 \text{ \AA}^{-1}$, with these being reflected in prominent and periodic diffraction peaks in the corresponding XRD patterns (**Figure 5.12**). Based upon previous reports, we attributed such features to multilayer stacked 2D perovskites.^[43] A clear 2D perovskite diffraction peak at $Q = 0.32 \text{ \AA}^{-1}$ is also apparent for spray 7.5mM-treated films. This 2D perovskite peak appears with extremely

low intensity in the spin-passivated films (**Figure 5.13**). Similarly, no 2D perovskite diffraction peaks are present in the XRD pattern of spin-passivated films. This presumably reflects the limited surface sensitivity of these measurements combined with the limited thickness of the capping layer. This result supports our assertion that the 2D capping layer is significantly thinner in spin-passivated films than in spray-passivated films, a finding in agreement with the observed trends in device V_{oc} and FF discussed above.

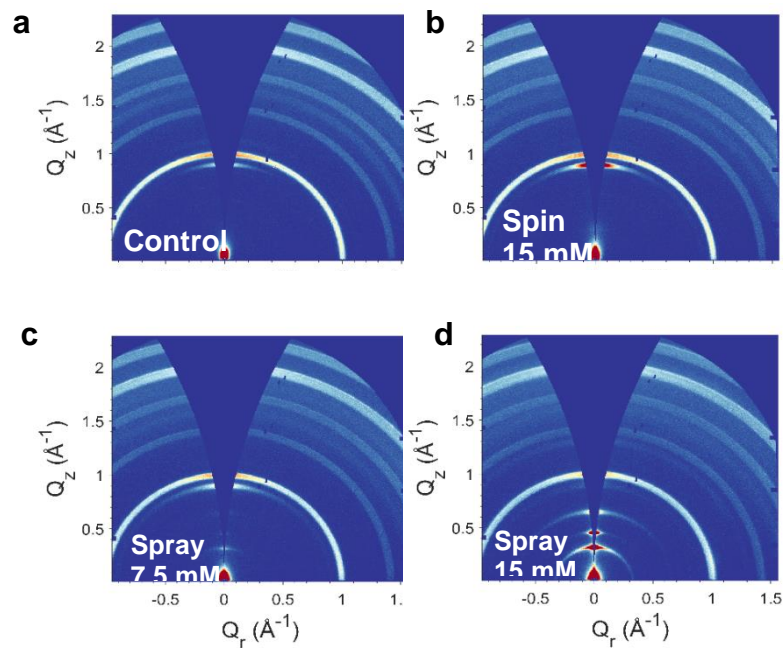


Figure 5.11: 2D Grazing-Incidence Wide-Angle X-ray Scattering (GIWAXS) patterns of (a) a spray-cast $\text{Cs}_{0.15}\text{FA}_{0.75}\text{PbI}_{2.85}\text{Cl}_{0.15}$ perovskite absorber layer, (b) the spray-cast perovskite layer with a spin-coated, 15 mM *i*-BABr treatment, (c) the spray-cast perovskite layer with a spray-cast, 7.5 mM *i*-BABr treatment, and (d) the spray-cast perovskite layer with a spray-cast, 15 mM *i*-BABr treatment.

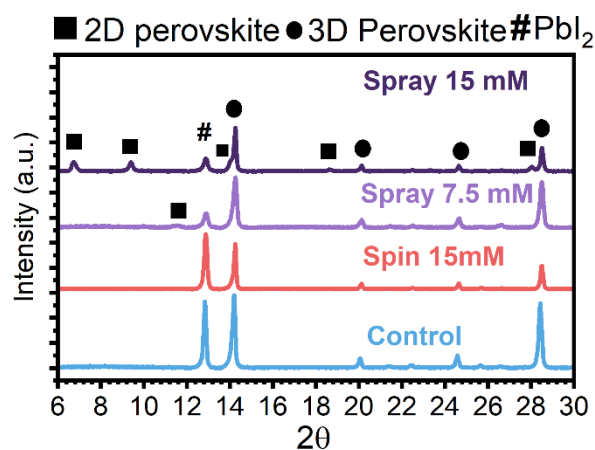


Figure 5.12: X-ray diffraction (XRD) patterns of a spray-cast $Cs_{0.15}FA_{0.75}PbI_{2.85}Cl_{0.15}$ absorber layer (control, blue), the spray-cast absorber layer with a spin-coated, 15 mM *i*-BABr treatment (spin 15 mM, red), the spray-cast absorber layer with a spray-cast, 7.5 mM *i*-BABr treatment (spray 7.5 mM, purple), and the spray-cast absorber layer with a spray-cast, 15 mM *i*-BABr treatment (spray 15 mM, dark purple).

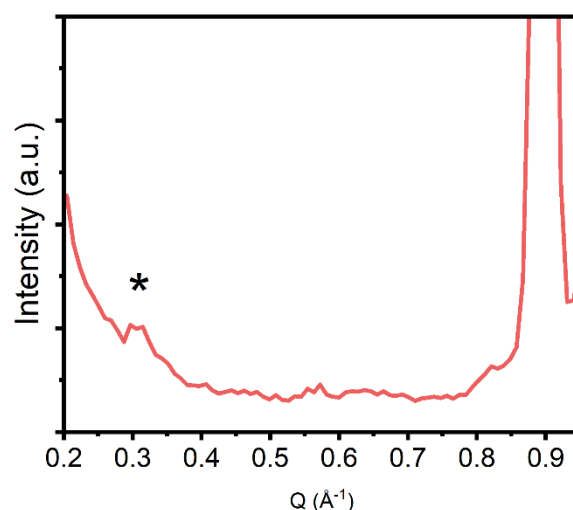


Figure 5.13: The enhanced intensity $0.20 < Q < 0.95 \text{ \AA}^{-1}$ region of the 1D azimuthal integration of the 2D scattering pattern of the spin-passivated perovskite film. Here, a signal corresponding to a 2D perovskite phase is detected at low intensity.

Notably, we observe a shift of the perovskite {100} peak at $\sim 14.2^\circ$ and $Q = 1.0 \text{ \AA}^{-1}$ towards higher $2\theta / Q$ in *i*-BABr-treated films, with a greater degree of shift observed for spray 15 mM films (**Figure 5.14**). Here, a substitution of I^- into the perovskite lattice by the Br^- counterions from the *i*-BABr molecule results in a lattice contraction.^[48] This effect is expected to be enhanced when a greater concentration of *i*-BABr is deposited, as is the

case for spray-passivated films. Indeed, a slight blue-shift of both the steady-state photoluminescence (PL) emission maxima and absorption onset are also observed (**Figure 5.15(a-b)**), a finding in agreement with the incorporation of Br⁻ into the perovskite lattice.^[49] We observe an enhancement in the PL intensity (with respect to control films) for both spin- and spray-passivated perovskite films deposited onto quartz. This observation is consistent with a reduction in nonradiative Shockley-Read-Hall recombination expected as a result of the surface passivation treatment.

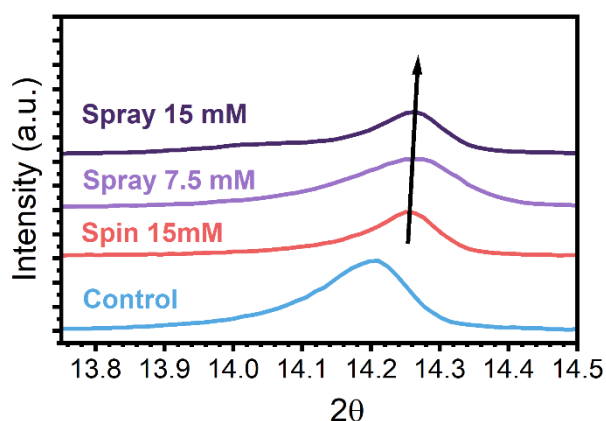


Figure 5.14: X-ray diffraction (XRD) patterns corresponding to control (blue), spin 15 mM-treated (red), spray 7.5 mM-treated (purple), and spray 15 mM-treated (dark purple) perovskite films.

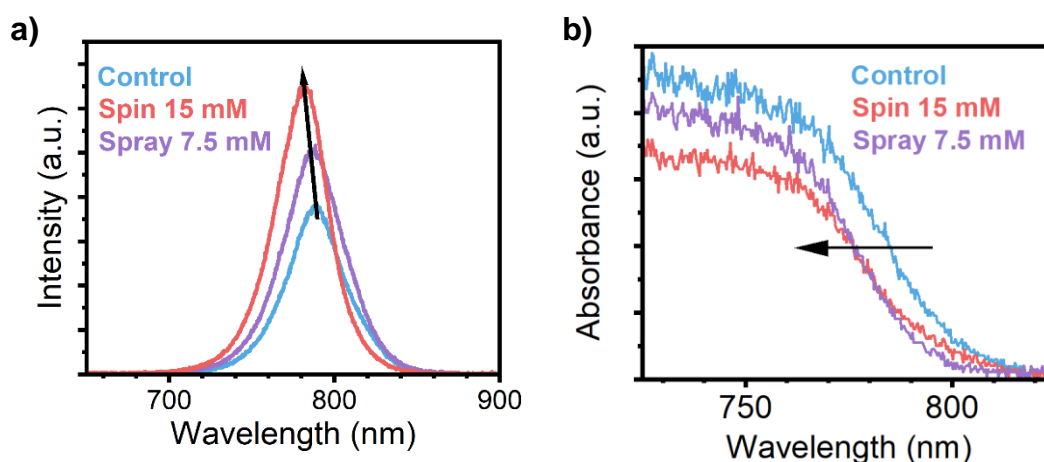


Figure 5.15: (a) Steady-state photoluminescence and (b) absorbance responses of a spray-cast $\text{Cs}_{0.15}\text{FA}_{0.75}\text{PbI}_{2.85}\text{Cl}_{0.15}$ layer (control, blue), the spray-cast perovskite with a spin-coated *i*-BABr passivating treatment (spin 15 mM, red), and the spray-cast perovskite with a spray-cast *i*-BABr passivating treatment (spray 7.5 mM, purple).

The effect of the variation in surface contact time for spin-passivated devices is shown in **Figure 5.16**. We find that when the i-BABr solution sits on the surface of the perovskite for 5-6 seconds rather than 2-3 seconds, a clear signal appears in the GIWAXS pattern corresponding to the formation of a 2D perovskite. When the contact time is reduced to 2-3 seconds, the thickness of the quasi-2D perovskite falls below the detection limits of the GIWAXS measurement technique and no 2D-perovskite scattering signal is observed. These results illustrate the variability of the spin-coated passivation treatment. Importantly, we find that passivation via spray-coating i-BABr to be a much more repeatable process. Here, we find a mean V_{OC} value of 1.07 ± 0.13 V for the spin-coated passivation, compared with 1.13 ± 0.01 V for the spray-coated treatment. This significant reduction in the spread of the V_{OC} values represents an order of magnitude reduction in device performance variability.

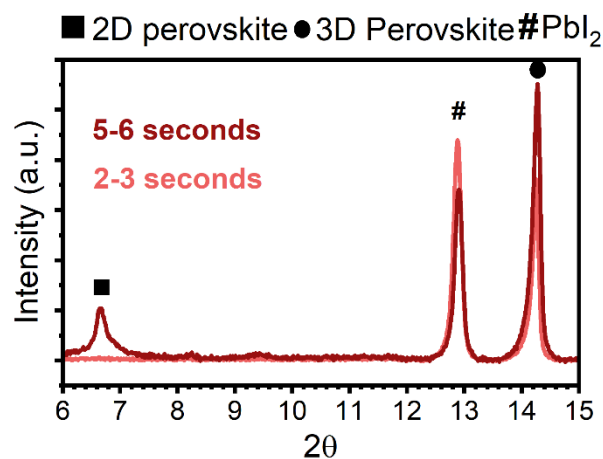


Figure 5.16: X-ray diffraction (XRD) patterns of the perovskite absorber layer treated with a spin-coated i-BABr solution left in contact with the substrate surface for 2-3 seconds (light red) or 5-6 seconds (dark red) before beginning the spin programme.

We find that the best-performing spray-passivated device demonstrated a PCE of 19.8 %, with **Figure 5.17(a)** showing the J - V curve for this “champion” cell. Clearly, a degree of hysteresis remains between the forward and reverse J - V sweep. This observation is in agreement with previous reports in which only interface passivation was used and the bulk perovskite remained unpassivated. Importantly, the SPO of this cell was 19.4%, a value that is a significant improvement on 16.6% demonstrated for the best-performing unpassivated, spray-coated cell. The corresponding EQE spectra for this device is presented in **Figure 5.17(c)**. Here, the integrated J_{SC-EQE} value (20.8 mA cm^{-2}) is in good agreement (within 10%)^[50,51] of the measured J_{SC-JV} (22.8 mA cm^{-2}). Most notably, the PCE of this champion spray-passivated cell is commensurate with the best-performing spin-passivated devices (19.8% vs. 20.0%, respectively).

To summarize, we find that post-treatment of the perovskite films with i-BABr forms a 2D capping layer at the perovskite: HTL interface, in accordance with previous reports.^[23,43] The formation of the 2D layer reduces nonradiative recombination, enhancing the V_{oc} of devices. The V_{oc} of spray-passivated devices is enhanced to a greater degree than is observed in spin-passivated devices (compared to unpassivated control cells). Furthermore, we find that the standard deviation in the V_{oc} of passivated devices

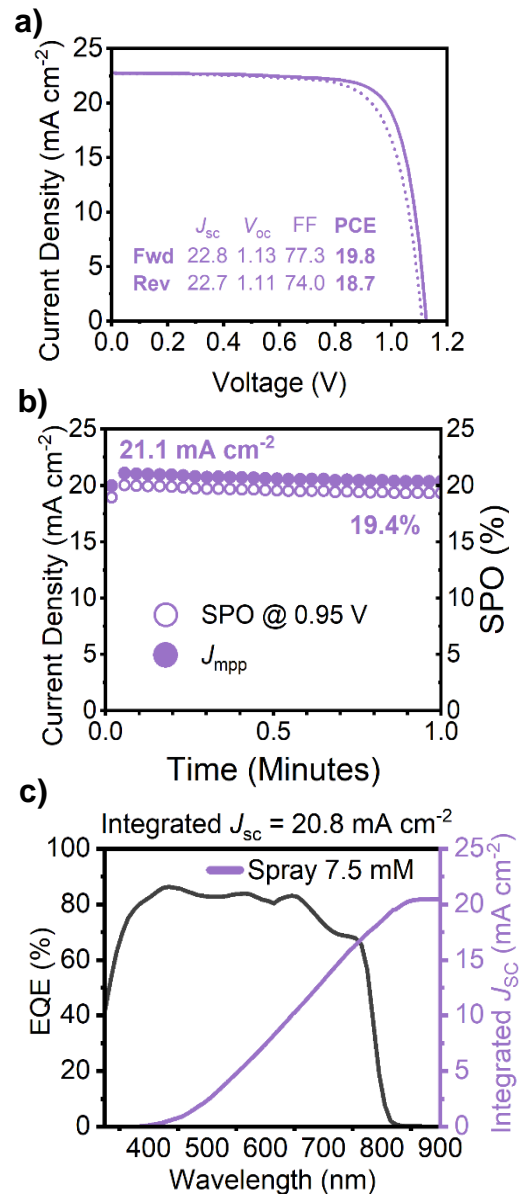


Figure 5.17: (a) J - V curve for the best-performing spray-passivated cell and (b) corresponding stabilized measurement, and (c) EQE curve with integrated J_{sc} value.

to be an order of magnitude smaller in spray-passivated cells than for spin-passivated cells. This effect is attributed to the enhanced repeatability of the spray coating process.

For perovskite films treated with a spray-coated 15 mM solution of i-BABr, a periodic diffraction pattern characteristic of multilayers of 2D material are seen in both GIWAXS and XRD patterns. This observation is accompanied with a reduction in the FF of corresponding devices, a finding that is indicative of a much thicker 2D capping layer formed when a higher concentration i-BABr solution is spray-deposited, with such a process “over-passivating” the perovskite surface.

At the optimal spray-deposition conditions (a 7.5 mM solution of i-BABr in IPA, sprayed at 40 mm s^{-1} onto an unheated substrate), spray-passivated PSCs achieve comparable PCEs to spin-passivated devices (19.8% versus 20.0%, respectively). Notably, the “champion” spray-passivated cell had a stabilized device efficiency of 19.4%. This is a significant enhancement compared to the stabilized efficiency of 16.6% observed in the best-performing unpassivated, spray-coated cell.

As can be seen in **Figure 5.17(a)**, we still observe a degree of hysteresis in the spray-passivated PSCs. We anticipate that further improvements in PCE will arise by combining surface passivation and bulk-perovskite passivating approaches. Such “dual passivation” techniques have realized devices whose performance reach the state-of-the-art in both *p-i-n* and *n-i-p* PSCs.^[52,53] Furthermore, the detrimental effects of the polar IPA casting-solvent should be avoided by using non-polar solvents such as chloroform.^[47] Here, we note that the higher volatility of chloroform might pose processing challenges as the droplet must may dry before it reaches the substrate surface. Clearly, there is still a large parameter space to fully optimize this process.

5.3.4 Conclusion

We have optimized a gas-assisted spray processing (GASP) technique to spray coat a $\text{Cs}_{0.15}\text{FA}_{0.75}\text{PbI}_{2.85}\text{Cl}_{0.15}$ perovskite absorber layer. We create *n-i-p* devices with a spray-coated active layer having comparable performance to reference cells with a spin-coated perovskite. We found that although such devices demonstrated reasonable efficiencies, a high degree of hysteresis was found between forward and reverse *J-V* sweeps. As a result, the best-performing spray-coated device demonstrated a stabilized power output of only 16.6%, despite having a reverse-sweep efficiency of 18.6%.

To reduce hysteresis in such devices, and improve device performance, we developed a spray-coated surface treatment to passivate the perovskite/ spiro-OMeTAD interface. Here, an i-BABr solution was ultrasonically spray-coated onto an annealed perovskite thin-film. This surface treatment resulted in the formation of a 2D capping layer on top of the 3D perovskite film. By suppressing nonradiative recombination losses, the average V_{oc} of spray-passivated devices increased by 70 mV with respect to cells based on an untreated, spray-coated perovskite active layer. Although this capping layer was found to have greater thickness in spray-passivated perovskite films compared to those that were spin-passivated, the resultant device performance was similar in both cases.

Using this approach, we have enhanced the mean device efficiency of spray-coated PSCs by an absolute value of 2.1%. Importantly, best-performing devices achieved a PCE of up to 19.8% (19.4% SPO), compared to 18.6% (16.6% SPO) for the devices that were based on an unpassivated, spray-coated perovskite active layer.

A degree of hysteresis remains in the i-BABr-passivated devices. We anticipate that further device efficiency improvements will be achieved by exploration of bulk-perovskite passivating agents which are unaffected by the K-content of the np-SnO₂ ETL used here. Furthermore, as the polar, protic IPA used to solubilize the passivating agent can dissolve the organic components of the perovskite lattice, the i-BABr casting solvent should be exchanged for a nonpolar solvent, such as chloroform, to avoid destabilizing the underlying perovskite.

These results pave the way for the scale up of PSCs by spray coating, a technique that combines high deposition-speed, excellent device performance, and improved device stability; three key ingredients for the cost-effective commercialization of PSCs.

5.3.5 Acknowledgements

This work was funded by the Engineering and Physical Sciences Research Council (EPSRC) grant EP/S009213/1 (The integration of photovoltaic devices with carbon-fiber composites). E.J.C. and E.L.K.S. thank the EPSRC for a PhD studentship from the Centre for Doctoral Training in New and Sustainable PV, (EP/L01551X/1). T.T. thanks the Faculty of Science, University of Sheffield for a studentship. M.E.O'K. thanks the EPSRC for a PhD

studentship from the Centre for Doctoral Training in Polymers and Colloids, EP/ (EP/L016281/1).

5.3.6 References

- [1] NREL, “Best Research Cell Efficiencies,” can be found under <https://www.nrel.gov/pv/cell-efficiency.html>, **2022**.
- [2] F. Yang, D. Jang, L. Dong, S. Qiu, A. Distler, N. Li, C. J. Brabec, H. Egelhaaf, *Adv. Energy Mater.* **2021**, *11*, 2101973.
- [3] K. Bruening, B. Dou, J. Simonaitis, Y. Y. Lin, M. F. A. M. van Hest, C. J. Tassone, *Joule* **2018**, *2*, 2464.
- [4] N. Rolston, W. J. Scheideler, A. C. Flick, J. P. Chen, H. Elmaraghi, A. Sleugh, O. Zhao, M. Woodhouse, R. H. Dauskardt, *Joule* **2020**, *4*, 2675.
- [5] T. Thornber, O. S. Game, E. J. Cassella, M. E. O’Kane, J. E. Bishop, T. J. Routledge, T. I. Alanazi, M. Togay, P. J. M. Isherwood, L. C. Infante-Ortega, D. B. Hammond, J. M. Walls, D. G. Lidzey, *ACS Appl. Mater. Interfaces* **2022**, *14*, 37587.
- [6] Z. Yang, Z. Liu, V. Ahmadi, W. Chen, Y. Qi, *Sol. RRL* **2022**, *6*, 2100458.
- [7] J. E. Bishop, J. A. Smith, D. G. Lidzey, *ACS Appl. Mater. Interfaces* **2020**, *12*, 48237.
- [8] J. Su, H. Cai, X. Ye, X. Zhou, J. Yang, D. Wang, J. Ni, J. Li, J. Zhang, *ACS Appl. Mater. Interfaces* **2019**, *11*, 10689.
- [9] C. Gao, P. Wang, H. Wang, C. Yu, B. Du, H. Zhang, T. Li, D. Liu, T. Wang, *ACS Appl. Energy Mater.* **2021**, *4*, 11496.
- [10] H. Cai, X. Liang, X. Ye, J. Su, J. Guan, J. Yang, Y. Liu, X. Zhou, R. Han, J. Ni, J. Li, J. Zhang, *ACS Appl. Energy Mater.* **2020**, *3*, 9696.
- [11] S. Ulična, B. Dou, D. H. Kim, K. Zhu, J. M. Walls, J. W. Bowers, M. F. A. M. Van Hest, *ACS Appl. Energy Mater.* **2018**, *1*, 1853.
- [12] J. E. Bishop, J. A. Smith, C. Greenland, V. Kumar, N. Vaenas, O. S. Game, T. J. Routledge, M. Wong-Stringer, C. Rodenburg, D. G. Lidzey, *ACS Appl. Mater. Interfaces* **2018**, *10*, 39428.
- [13] E. J. Cassella, E. L. K. Spooner, T. Thornber, M. E. O’Kane, T. E. Catley, J. E. Bishop, J. A. Smith, O. S. Game, D. G. Lidzey, *Adv. Sci.* **2022**, *9*, 2104848.
- [14] L. Meng, J. You, Y. Yang, *Nat. Commun.* **2018**, *9*, 1.
- [15] Z. Song, C. L. McElvany, A. B. Phillips, I. Celik, P. W. Krantz, S. C. Watthage, G. K.

- Liyanage, D. Apul, M. J. Heben, *Energy Environ. Sci.* **2017**, *10*, 1297.
- [16] S.-H. Turren-Cruz, A. Hagfeldt, M. Saliba, *Science (80-.)*. **2018**, *362*, 449.
- [17] S. Bera, A. Saha, S. Mondal, A. Biswas, S. Mallick, R. Chatterjee, S. Roy, *Mater. Adv.* **2022**, *3*, 5234.
- [18] J. M. Ball, A. Petrozza, *Nat. Energy* **2016**, *1*, 16149.
- [19] C. M. Wolff, P. Caprioglio, M. Stolterfoht, D. Neher, *Adv. Mater.* **2019**, *31*, 1902762.
- [20] P. Caprioglio, M. Stolterfoht, C. M. Wolff, T. Unold, B. Rech, S. Albrecht, D. Neher, *Adv. Energy Mater.* **2019**, *9*, 1901631.
- [21] P. Zhao, B. J. Kim, H. S. Jung, *Mater. Today Energy* **2018**, *7*, 267.
- [22] F. Gao, Y. Zhao, X. Zhang, J. You, *Adv. Energy Mater.* **2020**, *10*, 1902650.
- [23] T. Bu, J. Li, H. Li, C. Tian, J. Su, G. Tong, L. K. Ono, C. Wang, Z. Lin, N. Chai, X.-L. Zhang, J. Chang, J. Lu, J. Zhong, W. Huang, Y. Qi, Y.-B. Cheng, F. Huang, *Science (80-.)*. **2021**, *372*, 1327.
- [24] J. E. Bishop, C. D. Read, J. A. Smith, T. J. Routledge, D. G. Lidzey, *Sci. Rep.* **2020**, *10*, 6610.
- [25] M. Abbas, L. Zeng, F. Guo, M. Rauf, X. C. Yuan, B. Cai, *Materials (Basel)*. **2020**, *13*, 1.
- [26] A. Ren, H. Lai, X. Hao, Z. Tang, H. Xu, B. M. F. Yu Jeco, K. Watanabe, L. Wu, J. Zhang, M. Sugiyama, J. Wu, D. Zhao, *Joule* **2020**, *4*, 1263.
- [27] M. I. Saidaminov, J. Kim, A. Jain, R. Quintero-Bermudez, H. Tan, G. Long, F. Tan, A. Johnston, Y. Zhao, O. Voznyy, E. H. Sargent, *Nat. Energy* **2018**, *3*, 648.
- [28] Q. Jiang, L. Zhang, H. Wang, X. Yang, J. Meng, H. Liu, Z. Yin, J. Wu, X. Zhang, J. You, *Nat. Energy* **2017**, *2*, 16177.
- [29] B.-W. Park, N. Kedem, M. Kulbak, D. Y. Lee, W. S. Yang, N. J. Jeon, J. Seo, G. Kim, K. J. Kim, T. J. Shin, G. Hodes, D. Cahen, S. Il Seok, *Nat. Commun.* **2018**, *9*, 3301.
- [30] T. J. Jacobsson, J.-P. Correa-Baena, E. Halvani Anaraki, B. Philippe, S. D. Stranks, M. E. F. Bouduban, W. Tress, K. Schenk, J. Teuscher, J.-E. Moser, H. Rensmo, A. Hagfeldt, *J. Am. Chem. Soc.* **2016**, *138*, 10331.
- [31] Q. Chen, H. Zhou, T. Bin Song, S. Luo, Z. Hong, H. S. Duan, L. Dou, Y. Liu, Y. Yang, *Nano Lett.* **2014**, *14*, 4158.
- [32] L. Wang, C. McCleese, A. Kovalsky, Y. Zhao, C. Burda, *J. Am. Chem. Soc.* **2014**, *136*, 12205.
- [33] O. S. Game, J. A. Smith, T. I. Alanazi, M. Wong-Stringer, V. Kumar, C. Rodenburg, N. J.

- Terrill, D. G. Lidzey, *J. Mater. Chem. A* **2020**, *8*, 10943.
- [34] T. I. Alanazi, O. S. Game, J. A. Smith, R. C. Kilbride, C. Greenland, R. Jayaprakash, K. Georgiou, N. J. Terrill, D. G. Lidzey, *RSC Adv.* **2020**, *10*, 40341.
- [35] F. Zhang, H. Lu, J. Tong, J. J. Berry, M. C. Beard, K. Zhu, *Energy Environ. Sci.* **2020**, *13*, 1154.
- [36] S. Akin, B. Dong, L. Pfeifer, Y. Liu, M. Graetzel, A. Hagfeldt, *Adv. Sci.* **2021**, *8*, 2004593.
- [37] Y. Cho, A. M. Soufiani, J. S. Yun, J. Kim, D. S. Lee, J. Seidel, X. Deng, M. A. Green, S. Huang, A. W. Y. Ho-Baillie, *Adv. Energy Mater.* **2018**, *8*, 1703392.
- [38] I. C. Smith, E. T. Hoke, D. Solis-Ibarra, M. D. McGehee, H. I. Karunadasa, *Angew. Chemie Int. Ed.* **2014**, *53*, 11232.
- [39] T. M. Koh, V. Shanmugam, X. Guo, S. S. Lim, O. Filonik, E. M. Herzig, P. Müller-Buschbaum, V. Swamy, S. T. Chien, S. G. Mhaisalkar, N. Mathews, *J. Mater. Chem. A* **2018**, *6*, 2122.
- [40] S. G. Motti, T. Crothers, R. Yang, Y. Cao, R. Li, M. B. Johnston, J. Wang, L. M. Herz, *Nano Lett* **2019**, *19*, 3960.
- [41] G. Wu, R. Liang, M. Ge, G. Sun, Y. Zhang, G. Xing, *Adv. Mater.* **2022**, *34*, 2105635.
- [42] J. Kim, A. Ho-Baillie, S. Huang, *Sol. RRL* **2019**, *3*, 1800302.
- [43] S. Gharibzadeh, B. Abdollahi Nejad, M. Jakoby, T. Abzieher, D. Hauschild, S. Moghadamzadeh, J. A. Schwenzler, P. Brenner, R. Schmager, A. A. Haghighirad, L. Weinhardt, U. Lemmer, B. S. Richards, I. A. Howard, U. W. Paetzold, *Adv. Energy Mater.* **2019**, *9*, 1803699.
- [44] G. Yang, Z. Ren, K. Liu, M. Qin, W. Deng, H. Zhang, H. Wang, J. Liang, F. Ye, Q. Liang, H. Yin, Y. Chen, Y. Zhuang, S. Li, B. Gao, J. Wang, T. Shi, X. Wang, X. Lu, H. Wu, J. Hou, D. Lei, S. K. So, Y. Yang, G. Fang, G. Li, *Nat. Photonics* **2021**, *15*, 681.
- [45] Y. Hu, J. Schlipf, M. Wussler, M. L. Petrus, W. Jaegermann, T. Bein, P. Müller-Buschbaum, P. Docampo, *ACS Nano* **2016**, *10*, 5999.
- [46] Y. Liu, S. Akin, A. Hinderhofer, F. T. Eickemeyer, H. Zhu, J. Seo, J. Zhang, F. Schreiber, H. Zhang, S. M. Zakeeruddin, A. Hagfeldt, M. I. Dar, M. Grätzel, *Angew. Chemie* **2020**, *132*, 15818.
- [47] J. J. Yoo, S. Wieghold, M. C. Sponseller, M. R. Chua, S. N. Bertram, N. Titan Putri Hartono, J. S. Tresback, E. C. Hansen, J.-P. Correa-Baena, V. Bulovic, T. Buonassisi, S. Sik Shin, M. G. Bawendi, *2192 | Energy Environ. Sci* **2019**, *12*, 2192.

- [48] J. H. Noh, S. H. Im, J. H. Heo, T. N. Mandal, S. Il Seok, *Nano Lett.* **2013**, *13*, 1764.
- [49] T. Jesper Jacobsson, J.-P. Correa-Baena, M. Pazoki, M. Saliba, K. Schenk, M. Grätzel, A. Hagfeldt, *Energy Environ. Sci.* **2016**, *9*, 1706.
- [50] O. Almora, D. Baran, G. C. Bazan, C. Berger, C. I. Cabrera, K. R. Catchpole, S. Erten-Ela, F. Guo, J. Hauch, A. W. Y. Ho-Baillie, T. J. Jacobsson, R. A. J. Janssen, T. Kirchartz, N. Kopidakis, Y. Li, M. A. Loi, R. R. Lunt, X. Mathew, M. D. McGehee, J. Min, D. B. Mitzi, M. K. Nazeeruddin, J. Nelson, A. F. Nogueira, U. W. Paetzold, N. Park, B. P. Rand, U. Rau, H. J. Snaith, E. Unger, L. Vaillant-Roca, H. Yip, C. J. Brabec, *Adv. Energy Mater.* **2021**, *11*, 2002774.
- [51] M. Saliba, L. Etgar, *ACS Energy Lett.* **2020**, *5*, 2886.
- [52] S. Tang, J. Bing, J. Zheng, J. Tang, Y. Li, M. Mayyas, Y. Cho, T. W. Jones, T. C.-J. Yang, L. Yuan, M. Tebyetekerwa, H. T. Nguyen, M. P. Nielsen, N. J. Ekins-Daukes, K. Kalantar-Zadeh, G. J. Wilson, D. R. McKenzie, S. Huang, A. W. Y. Ho-Baillie, *Cell Reports Phys. Sci.* **2021**, *2*, 100511.
- [53] S. Gharibzadeh, P. Fassel, I. M. Hossain, P. Rohrbeck, M. Frericks, M. Schmidt, T. Duong, M. R. Khan, T. Abzieher, B. A. Nejand, F. Schackmar, O. Almora, T. Feeney, R. Singh, D. Fuchs, U. Lemmer, J. P. Hofmann, S. A. L. Weber, U. W. Paetzold, *Energy Environ. Sci.* **2021**, *14*, 5875.

A Binary Solvent System Used to Fabricate Fully Annealing-Free Perovskite Solar Cells

6.1 Publication Foreword

The GASP process developed and expanded upon in Chapters Four and Five enables the roll-to-roll deposition and crystallisation of high-quality perovskite thin films. Such roll-to-roll deposition could permit high-speed, high-volume manufacturing of PSCs; however, the necessity for lengthy annealing post-deposition treatments severely limits the maximum throughput speed. Annealing treatments are a ubiquitous practice for both the perovskite absorber layer *and* most charge-transporting layers. Therefore, in this chapter a route to fabricate fully annealing-free PSCs is explored. By solvent engineering a high volatility, low-coordinating solvent system, spin-coated devices with an annealing-free MAPbI₃ absorber layer realise device power conversion efficiencies in excess of 18%. This process is then combined with an annealing-free approach to spin-cast an MeO-2PACz hole-extracting layer, creating devices having efficiencies in excess of 17%. The theoretical throughput speed of manufacturing such fully annealing-free devices is therefore limited by coating speed alone. Importantly, this work is of specific interest to the field of flexible photovoltaics, wherein the thermal tolerance of plastic substrates is a key consideration.

Here, MAPbI₃ is explored (rather than a CsFA-based perovskite) for two key reasons: firstly, due to the simplicity of crystallisation for the single cation system, and also due to the limited solubility of Cs-salts in 2-methoxyethanol.

The manuscript presented within Chapter Six has now been accepted for publication in the journal “Advanced Energy Materials.”

6.2 Author Contributions

E.J. Cassella conceptualised the project and developed the methodology; prepared all samples; performed data analysis (except the GIWAXS and XPS data) and created all figures except GIWAXS figures; wrote the original draft and completed all further revisions. **E.L.K. Spooner** assisted with sample preparation, UV-Vis measurements, writing the original draft, and assisted with further revisions. **J.A. Smith** recorded *in-situ* GIWAXS data, performed analysis of the scattering patterns and created the corresponding figures. **T. Thornber** record XRD patterns. **M.E. O’Kane** performed SEM measurements. **S. Choudhary** assisted with *in-situ* GIWAXS experiments. **C.J. Wood** advised on the methodology and assisted with manuscript revision. **D.B. Hammond** performed XPS measurements, provided analysis of the resulting data, and assisted with revisions to the original manuscript. **H.J. Snaith** provided funding and assisted with revisions to the original manuscript. **D.G. Lidzey** provided funding and equipment and assisted with revisions to the original manuscript.

6.3 Publication Main Text

A Binary Solvent System Used to Fabricate Fully Annealing-Free Perovskite Solar Cells

DOI: 10.1002/aenm.202203468

Elena J. Cassella, Emma L.K. Spooner, Joel A. Smith, Timothy Thornber, Mary E. O’Kane, Saqlain Choudhary, Christopher J. Wood, Deborah B. Hammond, Henry J. Snaith, David G. Lidzey**
E.J. Cassella, Dr. E.L.K. Spooner, T. Thornber, M.E. O’Kane, Prof. D.G. Lidzey*

Department of Physics and Astronomy, University of Sheffield, Sheffield, S3 7RH, United Kingdom

*E-mail: e.j.cassella@sheffield.ac.uk, d.g.lidzey@sheffield.ac.uk

Dr. J.A. Smith, S. Choudhary, Prof. H.J. Snaith

Department of Physics, University of Oxford, Clarendon Laboratory, Parks Road, Oxford, OX1 3PU, United Kingdom

Dr. C.J. Wood

Power Roll Limited, Unit 5 Jade Business Park, Spring Road, Seaham, SR7 9DR, United Kingdom

Dr. D.B. Hammond

Department of Chemistry, University of Sheffield, Sheffield, S3 7HF, United Kingdom

6.3.1 Abstract

High temperature post-deposition annealing of hybrid lead halide perovskite thin films – typically lasting at least ten minutes – dramatically limits the maximum roll-to-roll coating speed which determines solar module manufacturing costs. Whilst a number of approaches for “annealing-free” perovskite solar cells (PSCs) have been demonstrated, many are of limited feasibility for scalable fabrication. Here, we have solvent-engineered a high vapor pressure solvent mixture of 2-methoxy ethanol (2-ME) and tetrahydrofuran (THF) to deposit highly crystalline perovskite films at room temperature with gas-quenching used to remove the volatile solvents. Using this approach, we demonstrate *p-i-n* devices with an annealing-free MAPbI₃ perovskite layer achieving stabilized power conversion efficiencies (PCEs) of up to 18.0%, compared to 18.4% for devices containing an annealed perovskite layer. We then explore the deposition of self-assembled molecules as the hole-transporting layer without annealing. We finally combine our methods to create fully annealing-free devices having stabilized PCEs of up to 17.1%. This represents the state-of-the-art for annealing-free fabrication of PSCs with a process fully compatible with roll-to-roll manufacture.

6.3.2 Introduction

Organic-inorganic metal halide perovskites are rapidly approaching state-of-the-art silicon solar cells, with best-performing devices now reaching power conversion efficiencies (PCEs) of 25.7%.^[1] Although stability remains a challenge for perovskite solar cells (PSCs), their solution-processability represents a major advantage. Techniques such as blade coating,^[2] slot-die coating,^[3] and spray coating^[4] are compatible with roll-to-roll (R2R) processing, which – in principle – should allow much higher throughput speeds than existing silicon solar technologies. However, the lengthy annealing times used to crystallize the perovskite active layer reduce the maximum theoretical web speeds that could be achieved in a practical manufacture process.

In 2020, Rolston et al. demonstrated the highest coating speeds of any scalable PSC processing technologies, achieving production speeds of $>12 \text{ m min}^{-1}$.^[5] Here, spray coating was combined with an atmospheric plasma post-processing route^[6], creating PSC devices and modules with a PCE of 18% and 15.5%, respectively. Critically, these were fabricated without annealing the perovskite layer. At these speeds, the module cost is

expected to be fully competitive with Si.^[7] This is compared with a calculated throughput rate for spin-coated PSCs incorporating a 10-minute anneal of just 0.017 m min^{-1} ; a rate prohibitive for commercialization. Furthermore, high temperature processing steps increase device manufacturing costs through increased utility costs and reduced throughput.^[8] High process temperatures are also incompatible with sensitive flexible (polymeric) substrates that are expected to be important in “Internet of Things” applications.^[9,10] This growing market is expected to reduce the initial investment and barrier to market entry for perovskites by an order of magnitude.^[11]

Many approaches to create “annealing-free” PSCs have been demonstrated. For example, thermal evaporation of the perovskite layer without any post-annealing treatments can be used to realize devices having reasonable efficiencies.^[12,13] Zhou et al. demonstrated devices with a PCE of 15.7% for MAPbI_3 (where MA is methylammonium) films grown via electrochemical fabrication.^[14] The use of anti-solvent treatments is an effective way to rapidly remove highly coordinating solvents, such as DMF, DMSO, NMP, and DMAc, and crystallize the perovskite at room temperature.^[15–20] Although efficiencies of up to 20.1% have been achieved^[21] using such processes, anti-solvent treatments are difficult to utilize at scale due to the large volume of mostly toxic washing solvents that become increasingly contaminated. Ultrasonic vibration-based post-treatments have also been used in conjunction with high-boiling point (low vapor pressure) solvents.^[22] Notably, $(\text{FAPbI}_3)_{0.85}(\text{MAPbBr}_3)_{0.15}$ compositions can be created at room temperature via this route.^[23,24] Perovskite crystallization has also been generated by exposing two-step, spin-coated MAPbI_3 films to humid air, with devices having a PCE of >15% demonstrated, however this process required an exposure time of an hour.^[25] Dubey et al. adapted this process,^[26] to make spin-coated perovskite films from a low vapor pressure mix of GBL and DMSO which were then exposed to an anti-solvent wash followed by exposure to humid air. This approach created devices with efficiencies of up to 16.8% after 5 hours of air-exposure. The use of volatile solvent systems has been identified as an extremely promising alternative route for the scalable fabrication of PSCs. Such processes can eliminate complex post-deposition treatments to remove highly coordinating, non-volatile solvents.^[27] The use of high vapor pressure, low boiling point solvents enables rapid evaporation of the casting solvent, and significantly reduces the time required to induce a high degree of supersaturation and crystal nucleation. A

number of volatile solvents have now been explored for post-treatment-free fabrication of PSCs, including DMF,^[28] ACN^[29], mixtures of methylamine in THF or EtOH in combination with a secondary solvent (ACN,^[30] or THF^[31]), and 2-methoxyethanol^[32] (2-ME). We note that 2-ME has recently emerged^[33] as an excellent solvent for PSC fabrication due to its low boiling point. High-performance PSCs have now been fabricated from 2-ME using a number of techniques, including blade coating,^[34,35] bar coating^[36,37], slot-die coating^[38], and spray coating.^[39]

Here, we use a mixture of 2-methoxy ethanol (2-ME) with tetrahydrofuran (THF) as a route to deposit highly crystalline MAPbI₃ perovskite films without the requirement for any post-treatment heating steps. The process developed uses gas-quenching to accelerate the evaporation of the volatile casting solvents to induce a high degree of nucleation, with dense, pinhole-free perovskite films created. Devices fabricated in this manner demonstrate PCEs of up to 18%. We then demonstrate that a carbazole-based self-assembled molecule (SAM) can also be deposited and used as a hole-transporting layer without the necessity for annealing. Using these approaches, we create fully “annealing-free” PSCs achieving stabilized PCEs of up to 17.1%. To our knowledge, this number represents the highest literature value for a fully annealing-free PSC device having no additional post-processing steps, making our process compatible with high-throughput R2R coating. We expect that such a fully R2R-compatible processes will have a high degree of industrial-relevance, eliminating energy-expensive, time-consuming heating steps which will limit manufacturing throughput. Our process also avoids the use of any toxic anti-solvents which are difficult to utilize at scale.

6.3.3 Results and Discussion

6.3.3.1 Optimisation of the casting precursor solution composition for high device efficiency

We have explored the use of THF as a high vapor pressure additive in a 2-ME MAPbI₃ precursor ink to facilitate fast solvent drying and formation of a crystalline perovskite at room temperature. According to Raoult's law, the total vapor pressure of a system is a function of the partial vapor pressures of the components in a mixture.^[40] For ideal mixtures, the total vapor pressure of a mixture will linearly increase (decrease) upon the addition of a higher (lower) vapor pressure component. In reality, however, non-ideal

behavior will arise from interactions between molecules in solution, resulting in a deviation from ideal, linear behavior. The vapor pressures of THF and 2-ME are 162 mm Hg and 9.5 mm Hg at 25 °C, respectively.^[41,42] Assuming negligible molecular interactions, we might expect the rapid evaporation of the volatile THF solvent to accelerate the saturation of a precursor film, which in turn results in the onset of crystallization. Here, the rapid drying of such a wet film should produce compact layers which are comprised of smaller crystals. Such high-quality perovskite thin-films would ideally not contain residual any solvent and would not need annealing. Here, we note that Zhang et al. recently employed THF as a co-solvent in a DMF: DMSO precursor ink to fabricate annealed PSC devices with PCEs of up to 24%.^[43]

In our experiments, we screened 11 compositions of THF and 2-ME from 0 vol % to 100 vol % of THF co-solvent in steps of 10 vol %. For simplicity, we use a naming convention that refers to the solvent ratio of THF: 2-ME, i.e., 0: 10 for a 0 vol % THF composition. Images of MAPbI₃ solutions with a molarity of 0.5 M for each composition are shown in **Figure 6.1**. It can be seen that for compositions >70 vol % THF, the precursor materials were not solubilized, instead black MAPbI₃ was precipitated. Such precipitated solutions were not studied further.

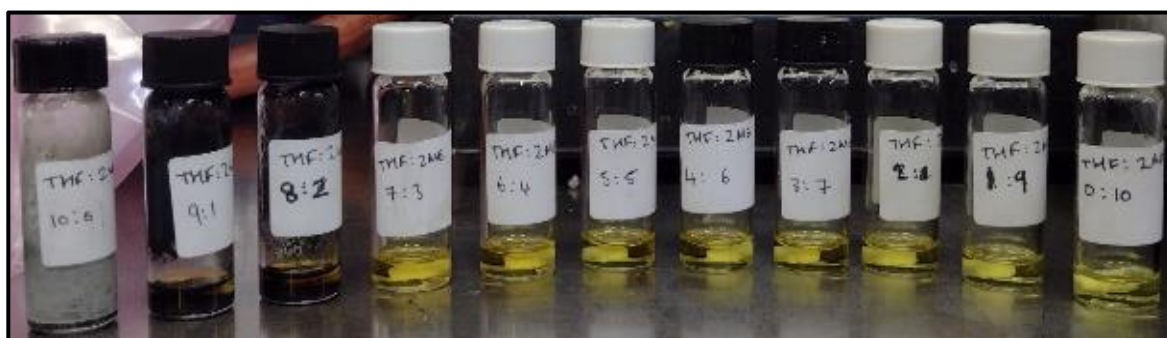


Figure 6.1: 0.5 M MAPbI₃ solutions with increasing tetrahydrofuran: 2-methoxyethanol concentrations from right to left.

The solubility limit is indicative of reduced coordination between the THF and the Pb²⁺ and I⁻ moieties in solution. In a MAPbI₃ solution, an equilibrium mixture of solvent molecules and I⁻ ligands will be reached that will depend on the affinity between the solvents and each ion (MA⁺, I⁻, Pb²⁺), in the Pb²⁺ first coordination sphere. The resulting Pbl_x^{2-x+} polyiodide plumbate complexes have characteristic absorption bands, so I⁻ and Pb²⁺ interactions can be used to understand the competing interactions between the

solvents and the solvated ions. To do this, we have measured the ultraviolet (UV)-visible transmittance of dilute (0.05 M) inks having different THF: 2-ME compositions. The corresponding absorbances over the wavelength range 250 – 500 nm are shown in **Figure 6.2(a)**. Here, the Pbl^+ , Pbl_2 , Pbl_3^- , and Pbl_4^{2-} labels correspond to decreasing numbers of coordinated solvent ligands, i.e., $\text{Pbl}^+\text{Solv}_5$, $\text{Pbl}_2\text{Solv}_4$, $\text{Pbl}_3^-\text{Solv}_3$ and $\text{Pbl}_4^{2-}\text{Solv}_2$, respectively.^[44,45] Upon addition of THF, there is a clear increase in absorbance by higher-order iodoplumbate species than occurs in pure 2-ME solutions. Indeed, solutions based on a 2-ME solvent exhibit absorption peaks corresponding to $\text{Pbl}^+\text{Solv}_5$ (~ 270 nm) and $\text{Pbl}_2\text{Solv}_4$ (326 nm) alone. Conversely, the addition of THF results in the formation of $\text{Pbl}_3^-\text{Solv}_3$ (365 nm), and $\text{Pbl}_4^{2-}\text{Solv}_2$ (420 nm) species at > 50 vol% of THF.

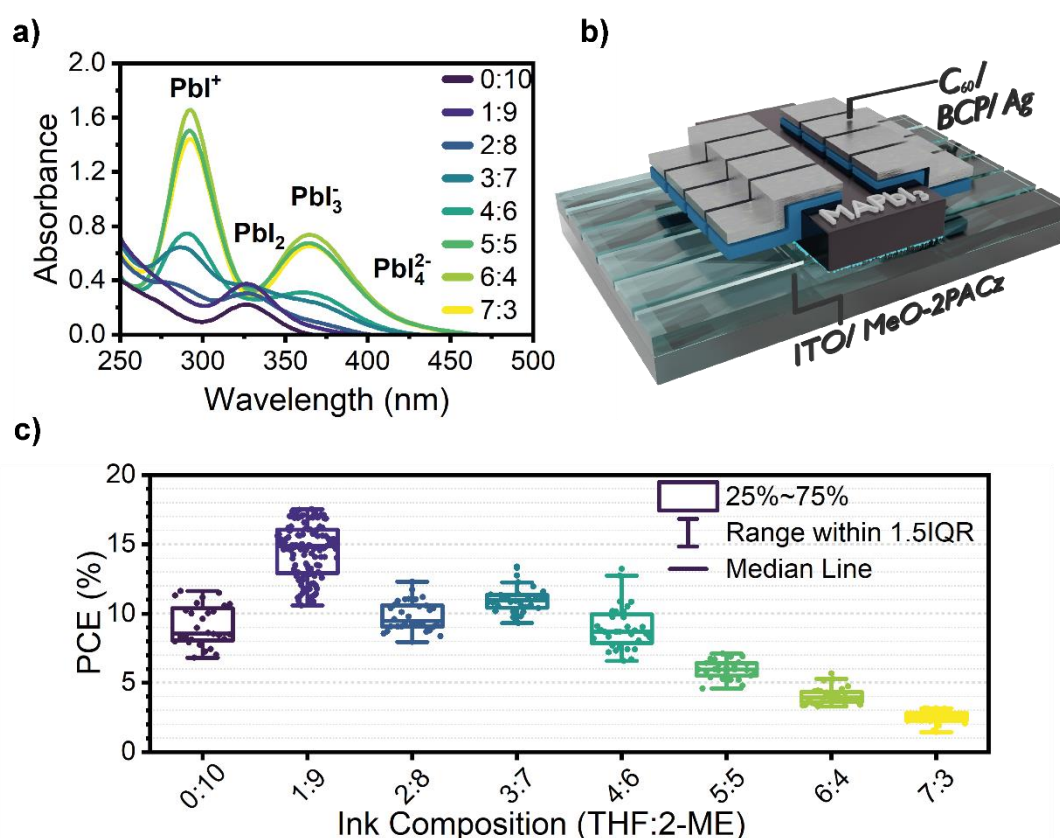


Figure 6.2: (a) The absorbance spectra of MAPbI₃ in each of the tetrahydrofuran: 2-methoxy ethanol precursor ink compositions. (b) An illustrative schematic of the p-i-n device architecture used. (c) The corresponding device power conversion efficiency (PCE) of cells containing an absorber layer fabricated from each ink composition.

Interestingly, the observed trend does not follow that predicted by the donor numbers, D_N , of 2-ME and THF. Here, D_N describes the strength of the interaction between

a Lewis-basic solvent and soft Lewis-acidic Pb^{2+} centers. In solvents with low D_N , the I^- to Pb^{2+} ligand interaction dominates rather than solvent coordination, shifting the equilibrium towards higher order PbI_x^{2-x+} complexes.^[46] The D_N values for THF and 2-ME are very similar, being 20.0^[47] and 19.7,^[48] respectively. Despite the nominally identical affinity to Pb^{2+} ions, we instead attribute the formation of higher-order polyiodide plumbates in THF to reduced hydrogen bonding interactions. Indeed, the greater the Hansen hydrogen-bonding parameter, δ_{HB} , the stronger the interaction between the solvent and organic cations and halide anions in solution.^[49] The δ_{HB} values for THF and 2-ME are 8.0 and 16.4, respectively.^[50] This suggests therefore, that the 2-ME (THF) should solvate the methylammonium and iodide species to a greater (lesser) extent, precluding (facilitating) coordination of I^- to the Pb^{2+} ions.

It has been speculated that higher order iodoplumbate complexes, meaning more highly halide coordinated Pb, promote the transformation of the precursor to the perovskite phase, such as through the formation of larger and more oriented perovskite crystals.^[44,51,52] Indeed, the relatively weak coordination of both 2-ME and THF to Pb^{2+} is expected to suppress the formation of solvent-coordinated intermediates which would require thermal annealing for solvent dissociation.

To evaluate the performance of the various precursor inks, we fabricated a series of photovoltaic devices. All devices were fabricated on cleaned, patterned indium tin-oxide (ITO) coated glass substrates, with all processing performed within an N_2 -filled glovebox. An MeO-2PACz ([2-(3,6-dimethoxy-9H-carbazol-9-yl)ethyl]phosphonic acid)^[53] hole-transporting layer (HTL) was first spin-coated and annealed at 100 °C for 10 minutes. The MAPbI_3 perovskite precursor inks were then spin-coated and “gas-quenched” by directing a flow of N_2 at the spinning substrate to promote evaporation of the volatile solvents. Gas-quenching is a facile, low-cost technique that has been demonstrated to have excellent potential for large-area PSC fabrication.^[54] An immediate color change from yellow to dark brown was observed upon application of the gas-jet for all ink compositions. The converted perovskite films were not annealed. The substrates were then transferred to an evaporation chamber for deposition of a C_{60} /BCP electron-transporting layer (ETL) and an Ag cathode. **Figure 6.2(b)** shows a schematic of the *p-i-*

n device architecture used. All processes and techniques are described fully in the Experimental Methods.

Figure 6.2(c) shows a boxplot of the resulting device PCEs for the range of compositions of THF: 2-ME from 0: 10 to 7: 3. Despite all converted films looking visually similar, it can be seen that there is a significant variation in device performance. Here, it is found that devices fabricated from 10 vol % THF have a median PCE of 14.9 %. This compares to devices made from a pure 2-ME solution, which have a PCE of 8.6 %. Devices made from 20 vol % $< V_{\text{THF}} < 40$ vol % solutions have a very similar efficiency compared to the pure 2-ME precursor devices. At > 50 vol % THF, device performance is significantly reduced. This trend is similar for other device metrics (short-circuit current density (J_{sc}), open-circuit voltage (V_{oc}), and fill factor (FF)) as shown in **Figure 6.3**.

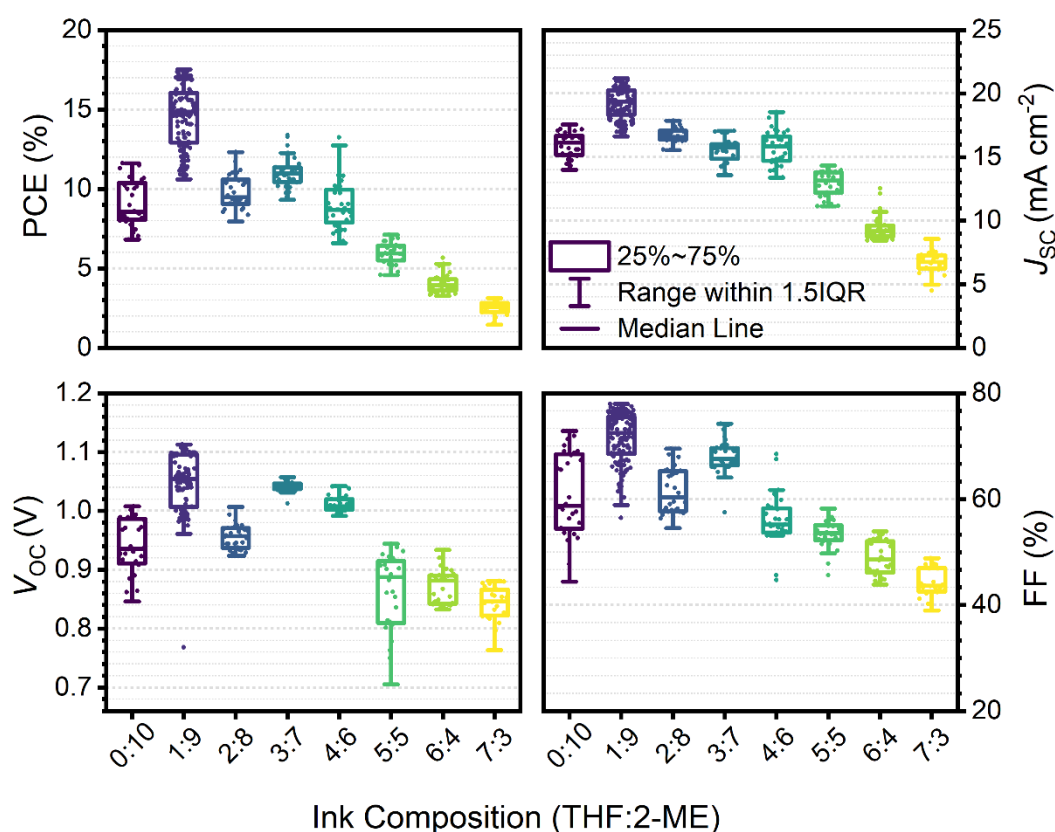


Figure 6.3: Power conversion efficiency (PCE), short-circuit current density (J_{sc}), open-circuit voltage (V_{oc}), and fill factor (FF) of devices fabricated from each precursor ink composition.

Using the optimum 1:9 THF: 2-ME composition, we demonstrate devices having stabilized PCEs of up to 18.0%. The current-density (J - V) curve, 2-minutes stabilized power output (SPO), and corresponding external quantum efficiency (EQE) graph are

presented in **Figure 6.4(a)-(c)**. This champion device displays negligible hysteresis and has a J_{SC} of 20.8 mA cm^{-2} , a V_{OC} of 1.11 V , a FF of 75.4% , and PCE of 17.5% determined from the reverse sweep. An integrated J_{SC} of 20.5 mA cm^{-2} determined from the EQE curve (J_{SC-EQE}) is also in good agreement with the measured J_{SC-JV} .^[55] Note that we determine a positive light-soaking effect, resulting in a SPO of 18.0% . This value compares extremely favorably with the state-of-the-art annealing-free devices, and occurs without the use of any anti-solvents, pre-purification of any precursor materials, or pre-heating of the substrate or solution.

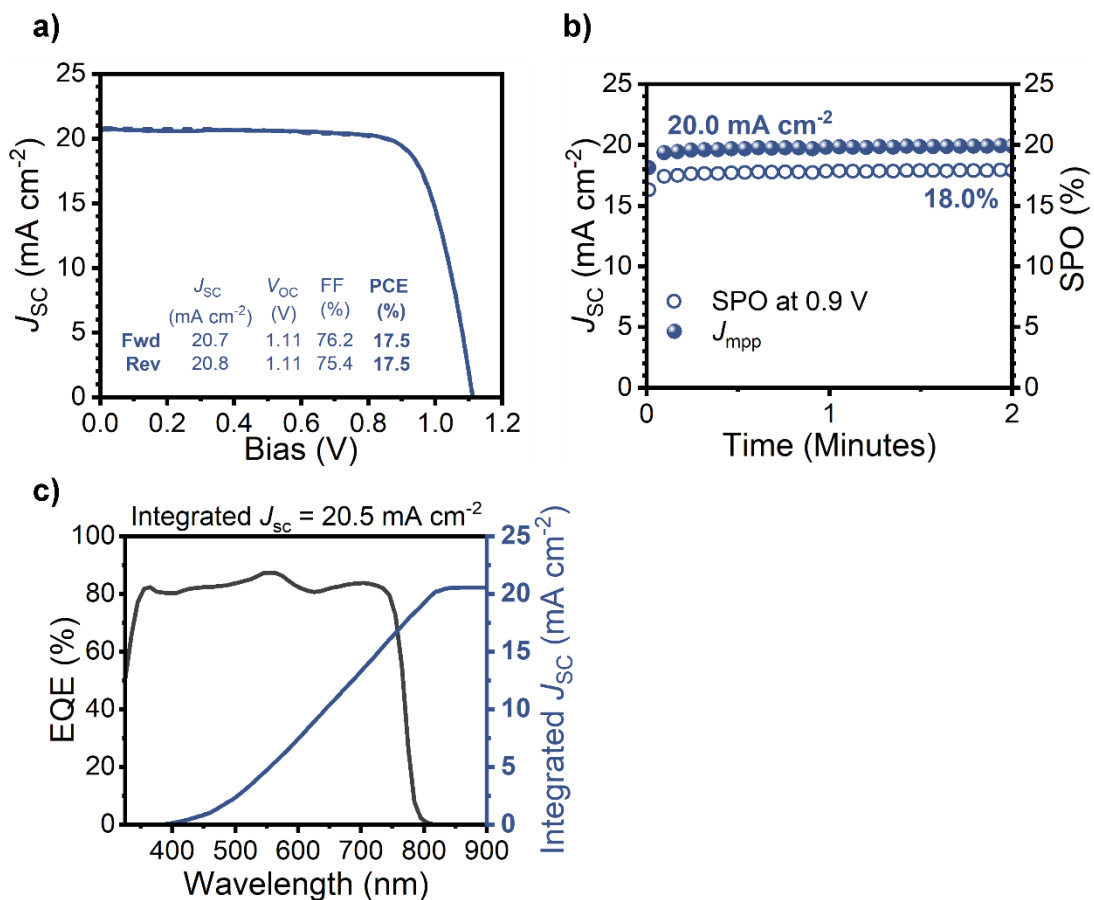


Figure 6.4: (a) J - V curve, (b) stabilized power output, and (c) external quantum efficiency (EQE) of the best-performing cell with an annealing-free perovskite absorber layer fabricated from the 1: 9 ink composition.

To investigate the beneficial effect of incorporating 10 vol % THF, we have conducted a number of characterization studies. Firstly, to characterize the morphological impact of films cast from THF: 2-ME, we recorded X-ray diffractograms (XRD) of films of each composition (see **Figure 6.5(a)**). It can be seen that films cast from all compositions display the characteristic peaks of MAPbI_3 .^[56] Only compositions 3: 7 and 4: 6 have an additional peak at $12.7^\circ 2\theta$, corresponding to the presence of a small amount

of PbI_2 . Importantly, we do not observe any crystalline intermediate residues in the diffraction patterns. This implies that the gas-quench successfully converts the precursor into a highly crystalline film for all compositions of THF: 2-ME. **Figure 6.5(b)** shows the full width at half-maximum (FWHM) of the (110)/ (002) perovskite peak at $\sim 14.2^\circ$. Here, it can be seen that the linewidth broadens with increasing proportion of THF. The linewidth can be used as a marker for crystallite size,^[57] suggesting therefore, that smaller crystallites are formed from inks containing an increasing proportion of THF. This finding is consistent with a greater density of nuclei being formed in precursor films containing a higher vapor pressure, less-coordinating precursor solvent.

We have measured the thickness of the spin-coated films fabricated from each ink composition, as shown in **Figure 6.5(c)**. Here, a large increase in both the film thickness and spread of the data is observed, going from $276 \text{ nm} \pm 14.0 \text{ nm}$ (standard deviation, $n = 5$) for films cast from the 0: 10 ink, to $586 \text{ nm} \pm 101 \text{ nm}$ for the films cast from the 7: 3 precursor. To determine whether such apparent variations in film thickness were a real effect, or instead were created by the presence of voids at the interface with the underlying substrate, we have recorded both optical microscope images and scanning electron microscope (SEM) images. Here, it is known that voids can form within films due to the solidification of the top surface induced by a gas-jet. Such rapid solvent evaporation is expected to be exacerbated by high proportions of the more volatile THF component. This effect has been reported previously in perovskite films fabricated from volatile precursors.^[34] Voids in the perovskite films reduce the working area of the device, reducing initial performance, act as regions of high recombination, and have been identified as regions from which degradation of the perovskite film is initiated.^[35] **Figure 6.6(a)-(h)** shows optical microscope images of the series of films cast from the different precursor solutions. Here, it can be seen that there is an increase in roughness with increased THF. Indeed, the film fabricated from the 7: 3 ink is characterized by a number of large voids visible in the top surface of the film.

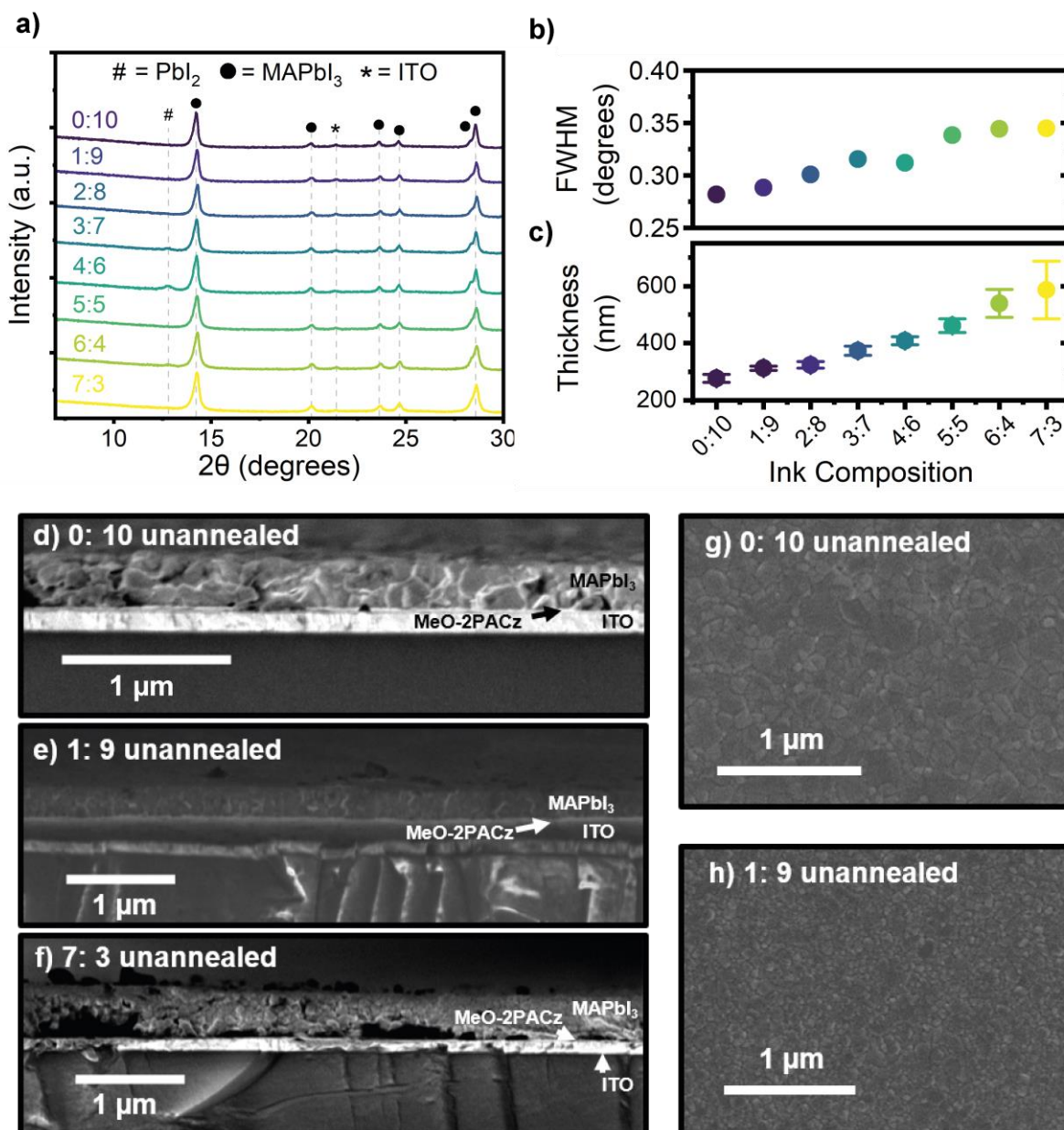


Figure 6.5: a) X-ray diffraction (XRD) patterns of perovskite films fabricated from each ink composition. b) The extracted full-width-at-half-maximum of the perovskite diffraction peak at $\approx 14.2^\circ 2\theta$. c) The thickness of the perovskite absorber layer fabricated from each ink composition. Cross-sectional scanning electron microscope (SEM) images of perovskite films fabricated from the d) 0:10 precursor, e) 1:9 precursor, and f) 7:3 precursor ink. Top-down SEM images of perovskite films fabricated from g) 0:10 precursor ink and h) 1:9 precursor ink.

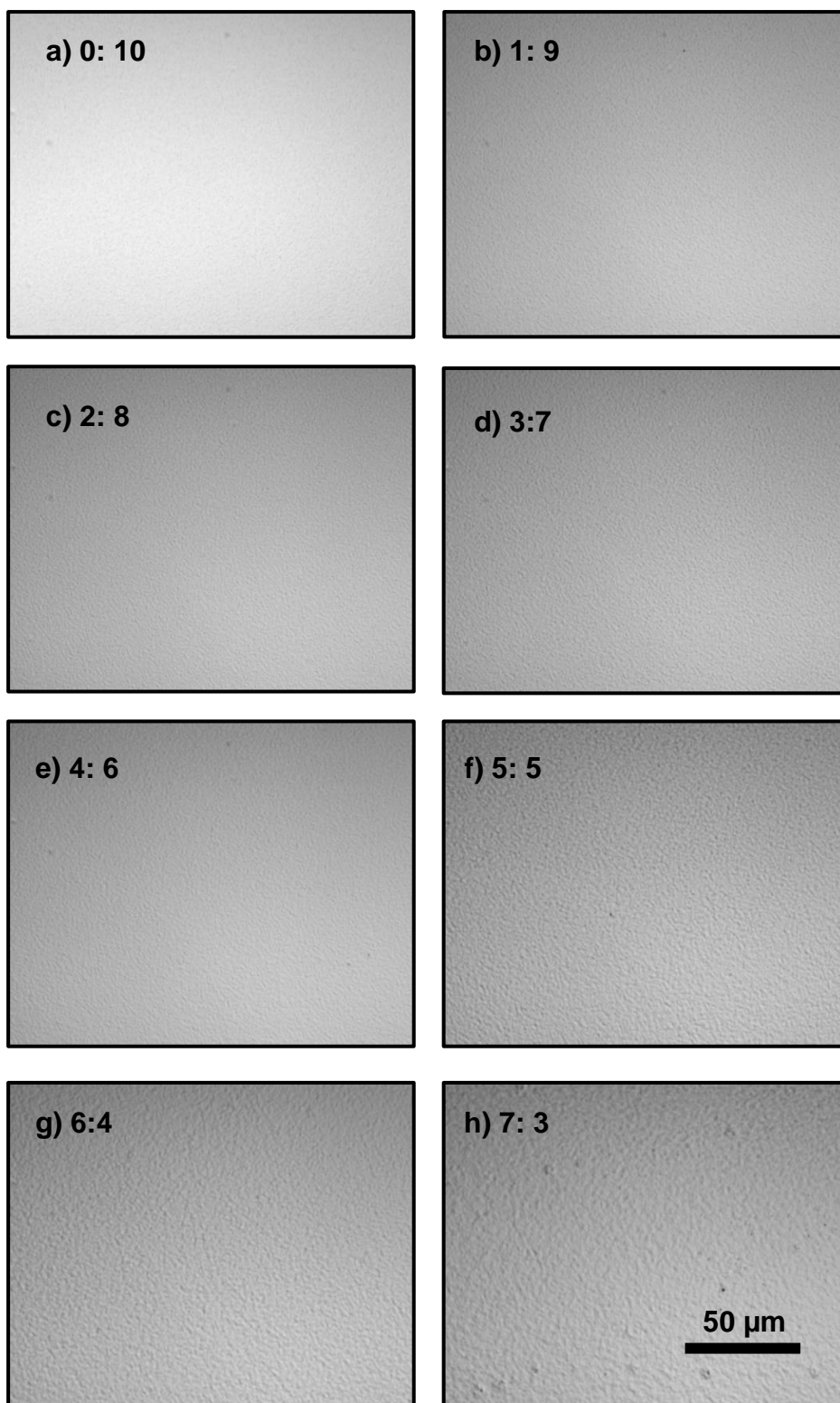


Figure 6.6: Optical microscope images of MAPbI_3 perovskite films spun from a 0.5 M precursor ink consisting of tetrahydrofuran: 2-methoxy ethanol in ratios of (a) 0:10 (b) 1:9 (c) 2:8 (d) 3:7 (e) 4:6 (f) 5:5 (g) 6:4 and (h) 7:3. The film roughness appears to increase along with increasing proportions of THF in the precursor ink, with obvious voids present in the 7:3 film. 50 μm scale bar inset.

In **Figure 6.5(d)-(f)** we present cross-sectional SEM images of films fabricated from the 0:10, 1:9 (champion), and 7:3 inks. Here, it is clear that there a number of voids between the perovskite crystal grains within the film cast from pure 2-ME (0:10, see **Figure 6.5(d)**). We speculate that these result from regions of trapped solvent caused by the high boiling point of pure 2-ME. Upon annealing, this trapped solvent is expected to rapidly escape through the top surface of the film, creating pinholes throughout the perovskite layer; a finding consistent with previous reports.^[38] For films cast from the 1:9 ink – which resulted in the highest device PCEs – these voids appear largely absent, with good contact made between the perovskite layer and the substrate surface (see **Figure 6.5(e)**). In contrast, at 70 vol % THF, we observe large voids at the perovskite: substrate interface (see **Figure 6.5(f)**). The perovskite film thicknesses determined from the SEM cross-sectional images correspond well to those presented in **Figure 6.5(c)** which were measured using surface profilometry. It can be seen that the interfacial voids in the films cast from solutions containing a higher concentration of THF contribute to the enhanced film “thickness” as measured between the upper surface of the perovskite film and the underlying ITO interface.

Our SEM images of the top-surface of films cast from 0: 10 and 1: 9 precursor solutions indicate that there is a reduction in the grain size upon addition of THF to the precursor (see **Figure 6.5(g)-(h)**, with the full images presented in **Figure 6.7(a)-(b)**). Whilst a number of pinholes are observed in the top-surface of the film cast from the 0: 10 ink, only one such defect is seen in the top-surface of the film cast from the 1: 9 solution. Our results suggest, therefore, that 10 vol % THF in the 2-ME precursor solution allows the creation of a compact film of small MAPbI₃ crystallites without pinholes and with excellent contact to the underlying substrate. At higher THF concentrations, increased ink volatility and reduced co-ordination of the precursor solvents accelerates nucleation at the top-surface, induced by the gas-jet. This results in the formation of a solidified “crust” at the film surface and the formation of voids throughout the bulk of the film. The voids observed between grains in the 0:10 films, and the interfacial voids within films prepared from solutions at higher THF concentrations account for the reduced device efficiency

compared to those prepared from the “champion” 1: 9 composition. This finding is evidenced by a reduction in all device metrics.

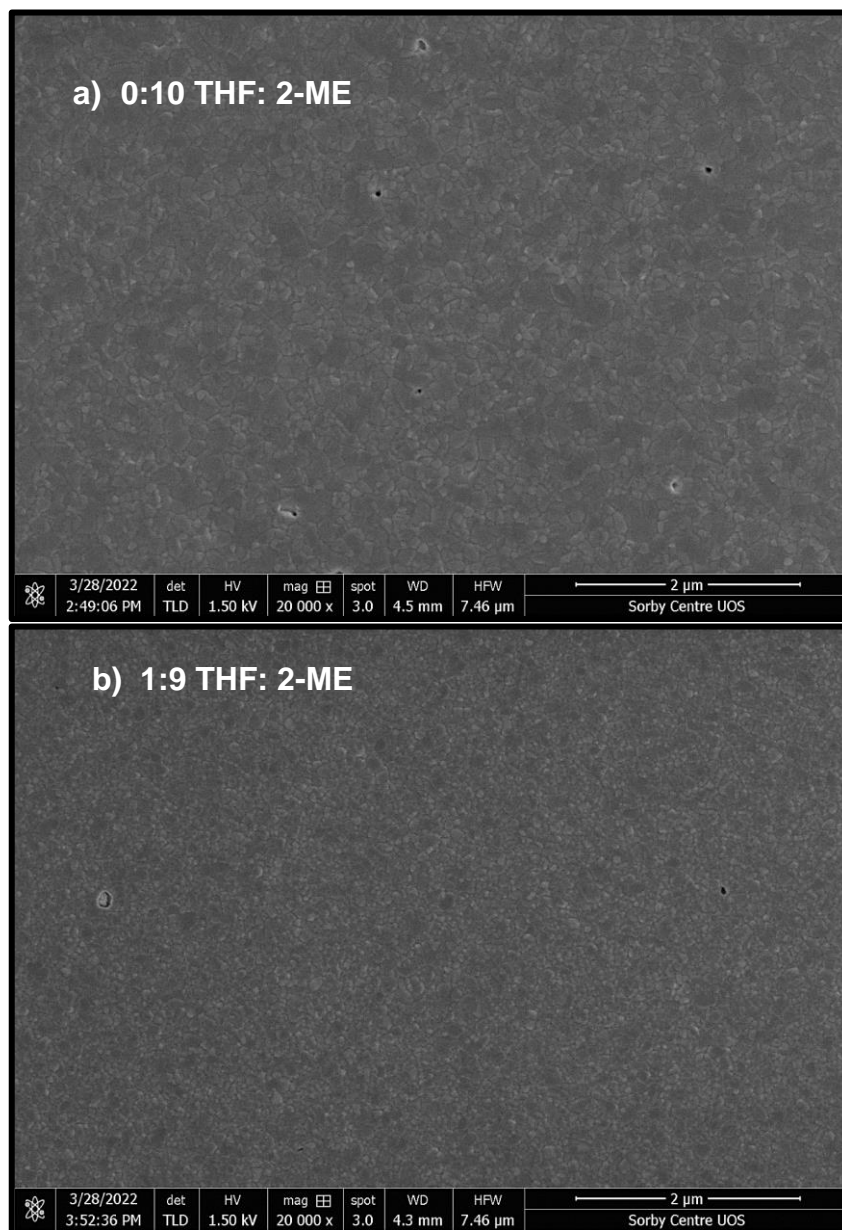


Figure 6.7: Top-down scanning electron microscope (SEM) images of perovskite films spin-cast from an (a) 0: 10 and (b) 1: 9 precursor ink.

To further probe the formation of functional films from the 1:9 THF: 2-ME solvent system, we performed *in situ* grazing incidence wide-angle X-ray scattering (GIWAXS) measurements on solutions deposited via blade coating (see schematic shown in **Figure 6.8**, full methods are available in the Experimental Methods).

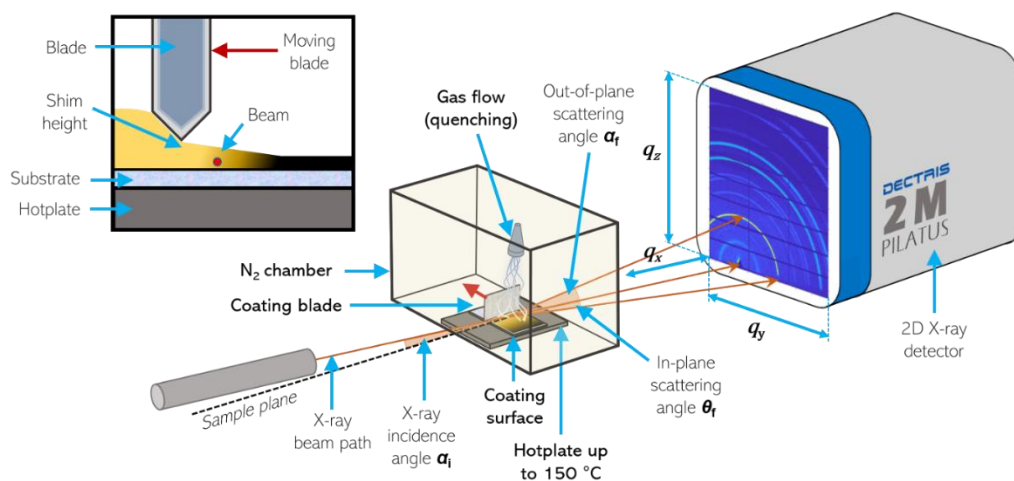


Figure 6.8: Illustration of GIWAXS experimental setup incorporating an in-situ blade coater (moving orthogonal to the synchrotron beam), N₂ flow for gas quenching and an integrated hotplate for the annealing experiment. Scattering from the sample is collected with a 2D detector. Further details are given in the Experimental Methods.

To mirror the spin-coating protocol, films were continuously gas-quenched after deposition, with coating performed in an N₂ atmosphere. We observed that the as-deposited film exhibits amorphous scattering, which is typical for a disordered solvate phase (**Figure 6.9(a)**). Immediately after gas-quenching, however, we observed the presence of two distinct intermediate phases during the crystallization process. The first is characterized by an oriented intermediate phase (**1**) with characteristic reflections at $Q = 0.42 \text{ \AA}^{-1}$ and 0.84 \AA^{-1} ($2\theta = 5.9^\circ$ and 11.9°), see **Figure 6.10(a)**. This rapidly (~ 1 s) evolved into a second highly textured phase (**2**, see **Figure 6.10(b)**) with a broad peak at $Q = 0.59 \text{ \AA}^{-1}$ ($2\theta = 8.2^\circ$), which gradually diminished in intensity over the course of the measurement (see **Figure 6.9(b)-(c)**). The appearance of phase **2** is concurrent with the emergence of peaks corresponding to tetragonal MAPbI₃^[56] which grow as a function of time (see **Figure 6.10(c)**). Azimuthal integrations of the scattering pattern of each phase are given in **Figure 6.11**. Here, we evidence peaks which possibly correspond to a 2H polytype phase that has been theoretically proposed for MAPbI₃^[58] but was not observed when simply spin coating such films. We suspect this observation may result somehow from the fact that the GIWAXS blade coating studies explored a relatively thicker film, with the nature of the coating procedure perhaps also being significant. Importantly, neither intermediate phase **1** nor phase **2** were detected in the XRD patterns of the fabricated films (see **Figure 6.3(a)**). This result indicates that the intermediate phases that form during the initial crystallization process are readily converted to a perovskite phase

at room temperature, most likely due to the weak coordinating ability of the two solvents. This is not the case for MAPbI₃ intermediate phases formed using typical solvents such as DMF and DMSO, which are generally stable at room temperature.^[59,60]

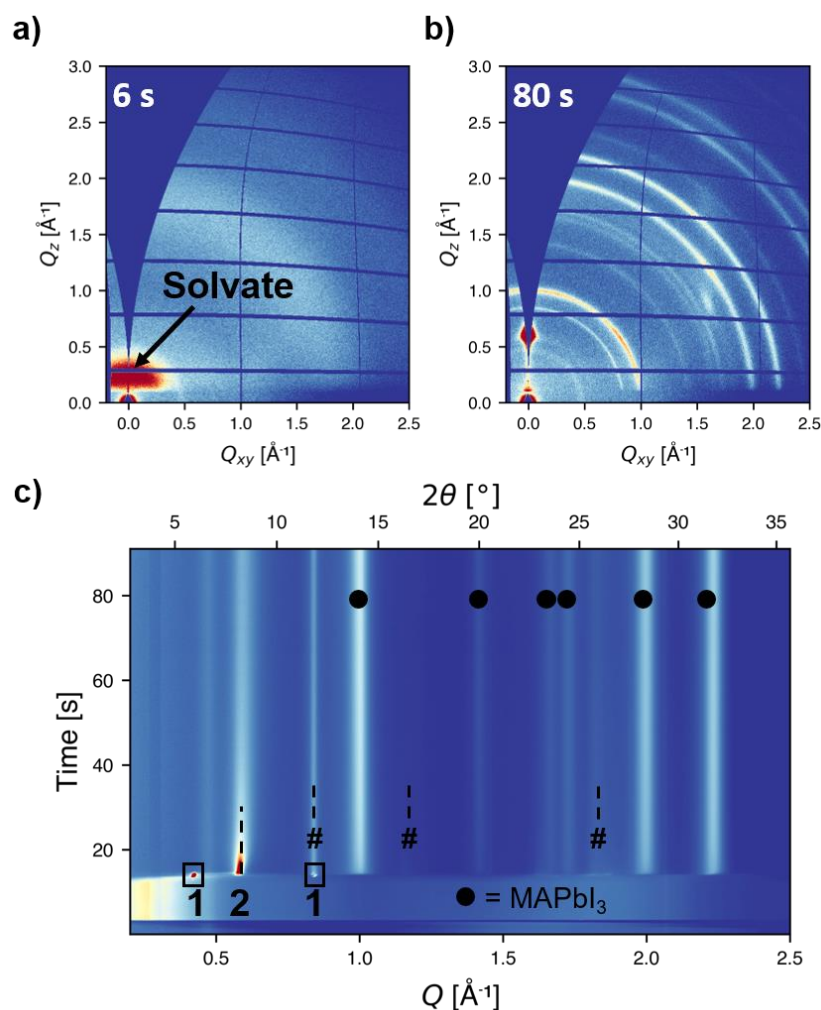


Figure 6.9: 2D GIWAXS of a) scattering from a solvate phase present prior to the crystallisation of phase 1 and b) scattering at 80 s into the coating experiment with the film primarily composed of MAPbI₃ with some phase 2 present. c) 1D integrated scattering spectra recorded over the whole experiment, highlighting all the phases present. Here, # denotes peaks possibly associated with a 2H polytype, which was not present in XRD of completed films and so is thought to form from differences between the coating regime employed here compared to those commonly used to prepare these perovskite films.

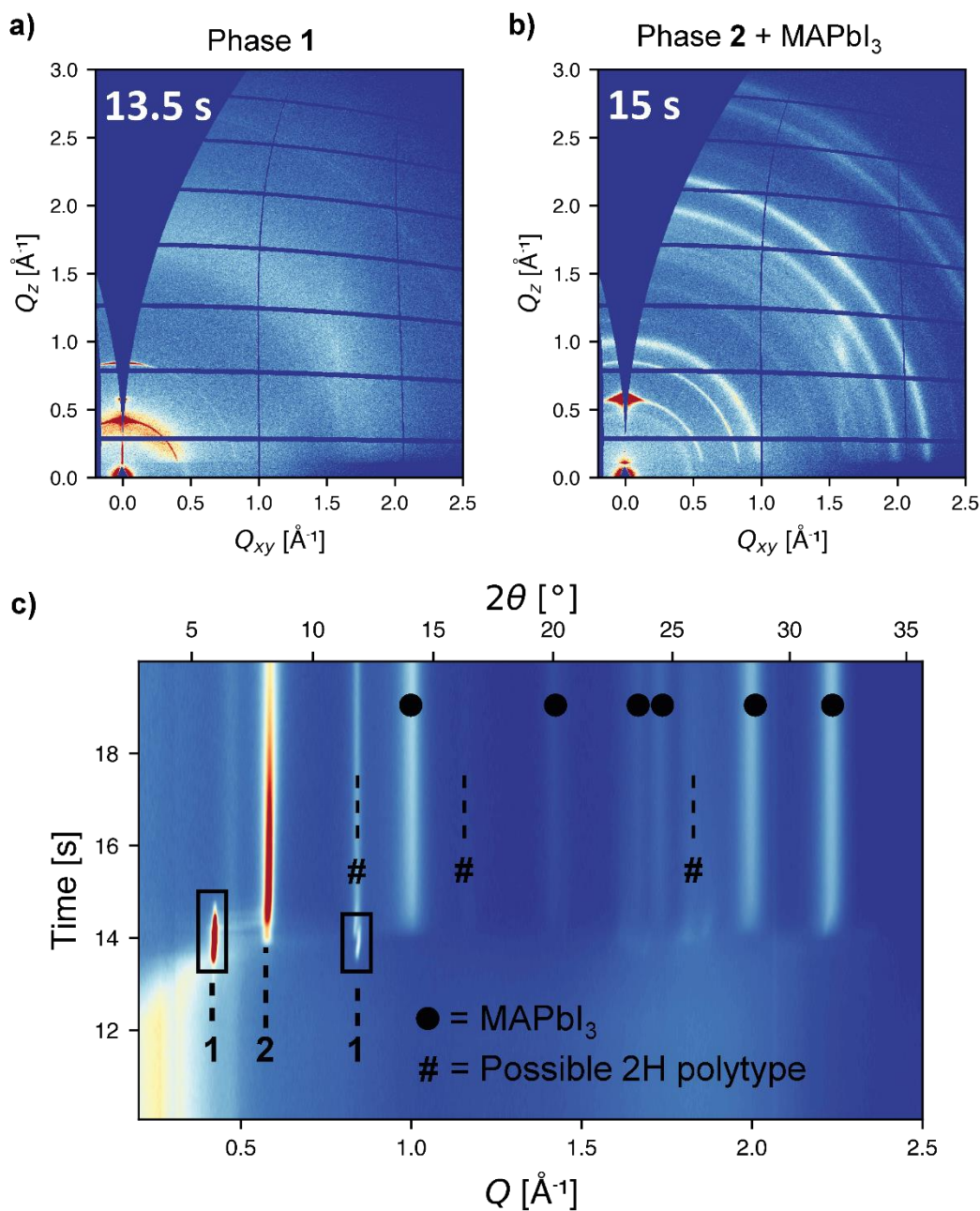


Figure 6.10: GIWAXS of (a) phase 1 at 13.5 s and (b) phase 2 and MAPbI₃ at 15 s. (c) 1D integrated in situ GIWAXS highlighting the 10-20 s time period following blade coating. At around 13 s, the solvate phase shifts to higher angles as solvent is removed, followed by the crystallization of phase 1, which rapidly converts to phase 2 at ~14 s, which rapidly reduces in intensity over a period of ~5 seconds, with MAPbI₃ then becoming the dominant material phase.

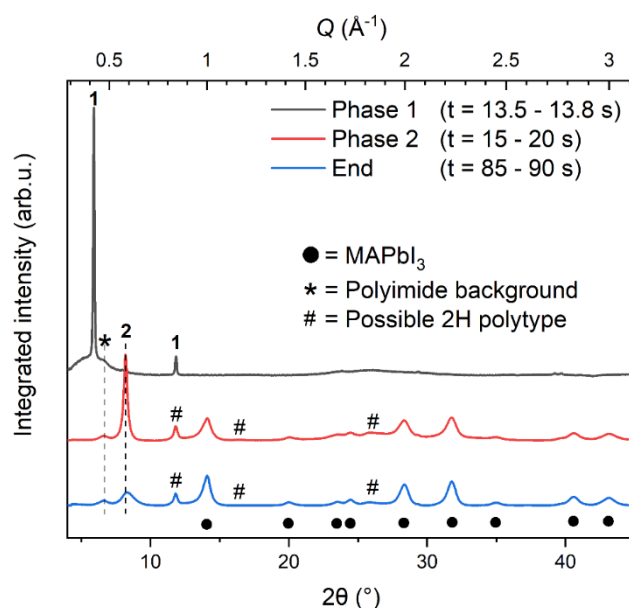


Figure 6.11: 1D azimuthally integrated GIWAXS patterns at key time points (averaged over the indicated time periods) highlighting diffraction peaks from the identified intermediate, MAPbI₃ and possible 2H polytype phases.

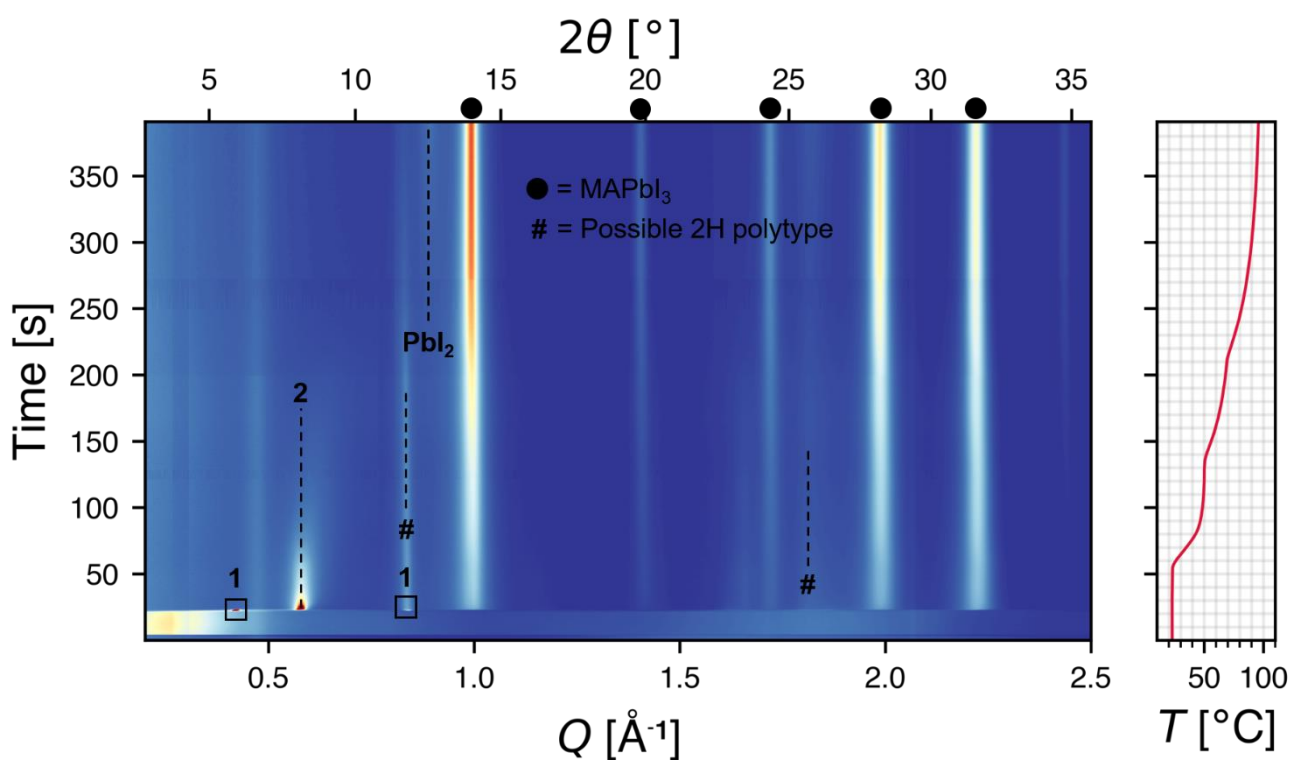


Figure 6.12: In situ GIWAXS acquired on a similarly coated film as Figure 4 but subsequently annealed gradually in situ.

We have also explored thermally annealing such blade-coated films while recording GIWAXS spectra as shown in **Figure 6.12**. Here, we find that intermediate phase **2** was completely removed at around 70 °C, and that heating the film above 50 °C improved the crystallinity of MAPbI₃. We speculate that this may explain the observed performance enhancement upon light-soaking of annealing free devices. Indeed, we suspect that the *in operando* heating of annealing-free devices may improve the crystallinity of devices during testing.

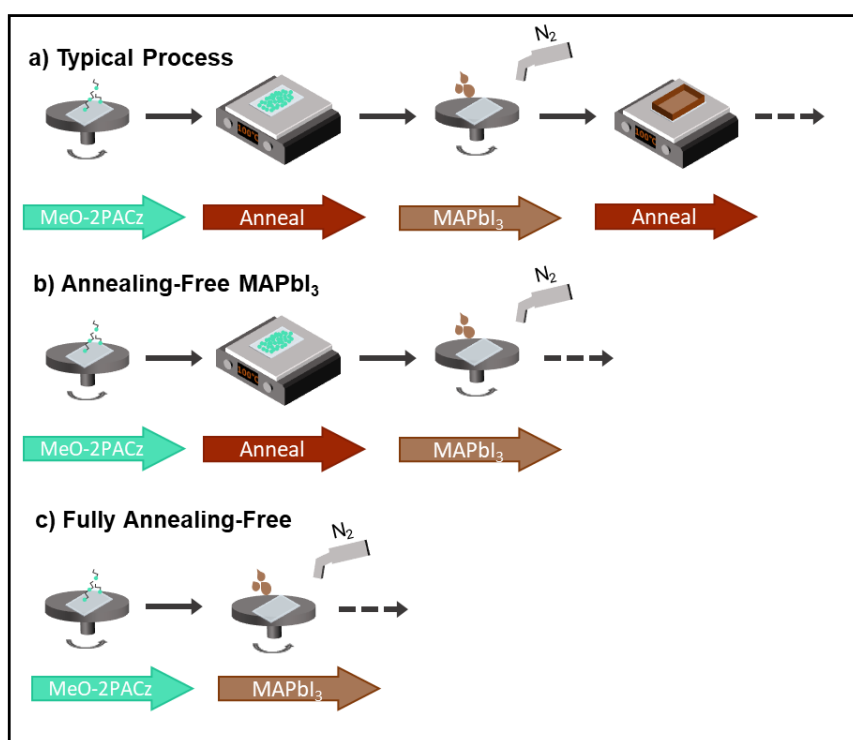


Figure 6.13: (a) The prototypical fabrication process for the MeO-2PACz hole-transporting layer and MAPbI₃ active layer. Here, each layer is annealed for 10 minutes after spin-deposition. (b) The fabrication process for the annealing-free perovskite layer only. Here, the MeO-2PACz layer is annealed post-deposition, whereas the MAPbI₃ layer is simply spin-coated prior to further processing. (c) The fabrication process for fully annealing-free devices. Here, both the MeO-2PACz and MAPbI₃ layer are simply spin-coated without any further post-deposition treatment steps.

To further evaluate the utility of our annealing-free approach, we compare our device performance to that of conventionally annealed devices. Again, the same *p-i-n* architecture was used, but the perovskite film (fabricated from the 1:9 THF: 2-ME composition) was annealed at 100 °C for 10 minutes. For clarity, this process versus an “annealing-free MAPbI₃” process is schematically illustrated in **Figure 6.13(a)-(b)**. We find that although the median device PCE is improved from 14.9% to 16.0% upon annealing the perovskite, this median value falls within the interquartile range (IQR) of the annealing-

free devices. For this reason, we conclude that there is only a slight statistical improvement in device performance upon annealing. If we compare the EQE spectra of the champion annealing-free MAPbI₃ device against that of the best-performing annealed-MAPbI₃ device (see **Figure 6.14(a)**), we observe only a small increase in the EQE of the annealed device over the wavelength range 600 – 800 nm. We attribute this increase upon annealing to improved charge carrier collection which in turn results from an increase in grain size and morphology during the annealing treatment.^[61,62] This can be evidenced by the XRD patterns and SEM images presented in **Figure 6.14(b)** and **Figure 6.14(c)-(d)**, respectively. Here, a significant enlargement of the perovskite grain size and an enhancement in the crystallinity of the perovskite film upon annealing can be clearly seen. We also observe a reduced splitting of the tetragonal (220)/ (004) diffraction peaks at 28.3° and 28.6° 2θ, which may indicate a change in the unit cell geometry upon annealing.

We therefore ascribe the overall increase in device performance upon annealing to an increase in J_{SC} arising from enhanced charge carrier extraction, with both the FF and V_{OC} of annealed devices remaining statistically similar to that of devices containing an annealing-free active layer. Here, we note that interfacial voids are observed in the cross-sectional SEM image of the annealed perovskite film (see **Figure 6.15**). Such voids presumably arise due to strain effects during the crystalline growth process and may limit the overall PCE of the annealed devices. The corresponding $J-V$ curve, EQE with integrated current density, and SPO of the champion annealed MAPbI₃ device are plotted in **Figure 6.16(a)-(c)**. Here, the champion stabilized PCE of 18.4% for this annealed device compares extremely favorably to the champion anneal-free MAPbI₃ device (18.0% stabilized). We conclude, therefore, that the 1:9 THF: 2-ME solvent system facilitates the fabrication of annealing-free MAPbI₃ films with excellent crystalline, optical, and optoelectronic properties.

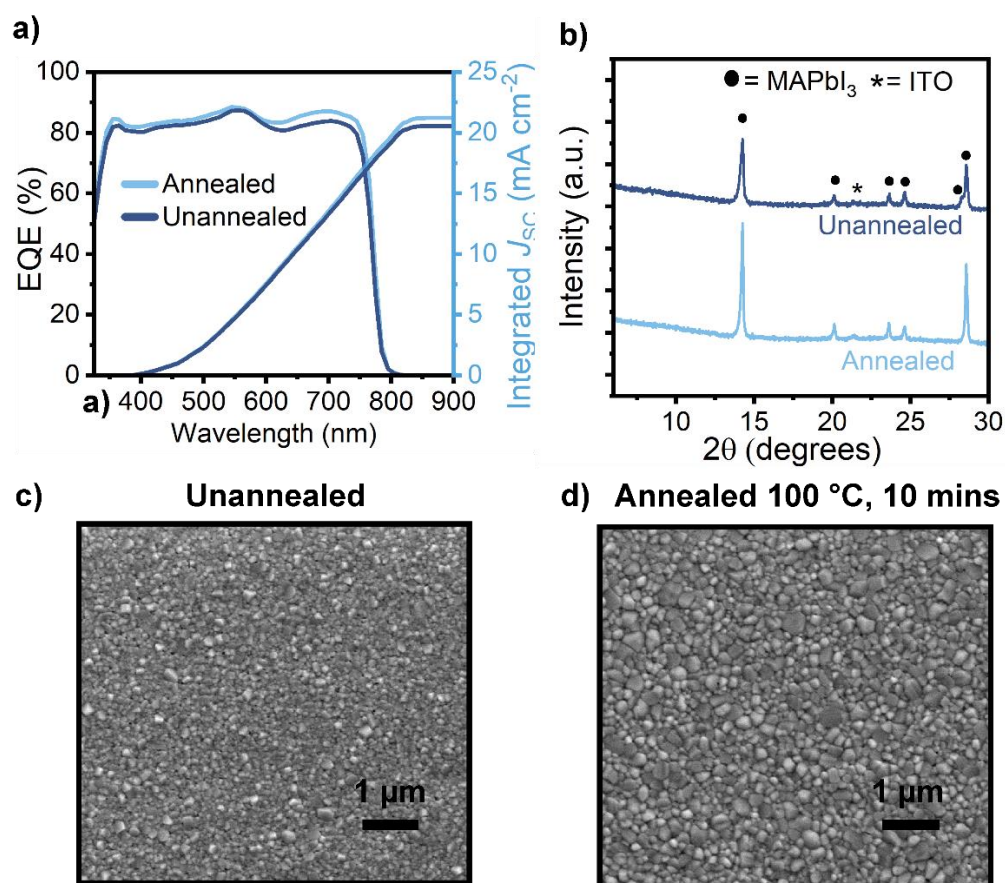


Figure 6.14: (a) External quantum efficiencies of cells with an unannealed or annealed (100 °C for 10 minutes) active layer. (b) X-ray diffraction (XRD) patterns of annealed and unannealed perovskite film cast from the 1: 9 precursor ink. Scanning electron microscope (SEM) images of the surface of the perovskite absorber layer fabricated from a 1: 9 THF: 2-ME precursor ink (c) without annealing and (d) with an annealing treatment (100 °C, 10 minutes).

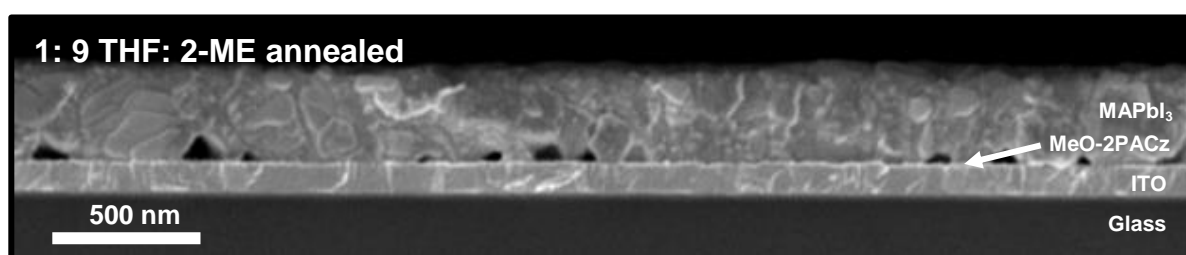


Figure 6.15: Cross-sectional scanning electron microscope (SEM) image of a MAPbI_3 film spin-cast from a 1: 9 tetrahydrofuran: 2-methoxyethanol precursor ink and annealed at 100 °C for 10 minutes.

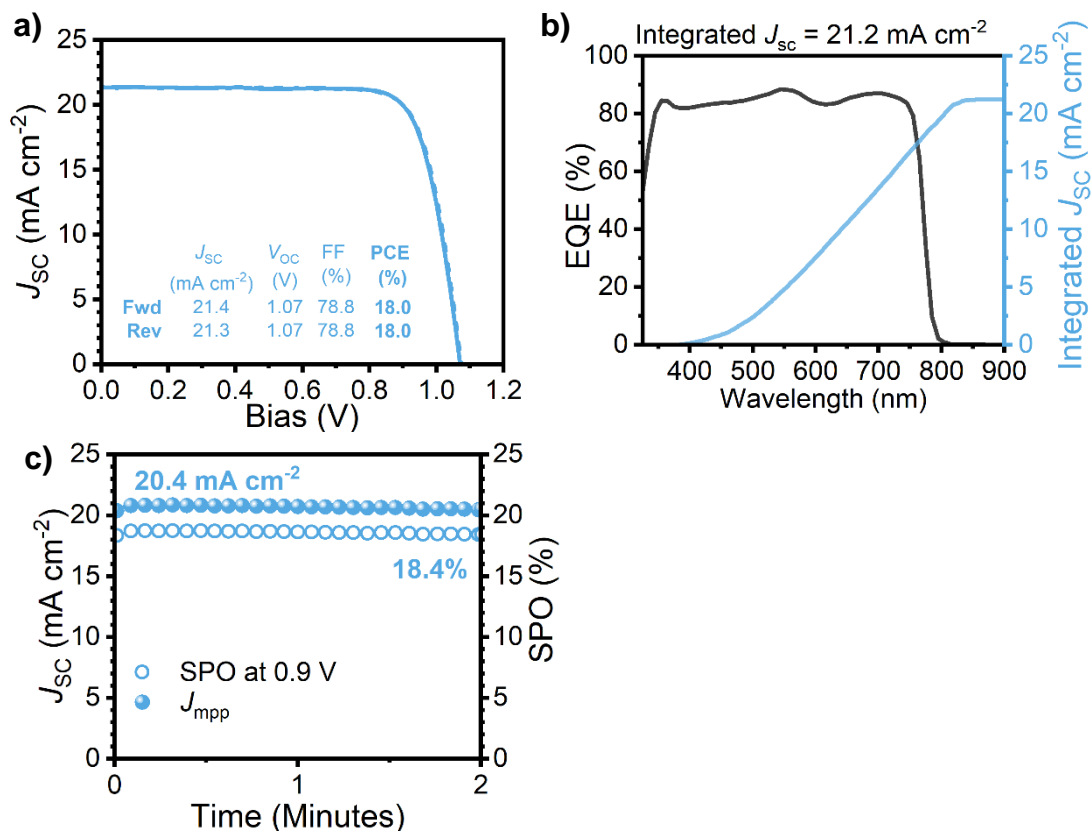


Figure 6.16: (a) J - V curve, (b) external quantum efficiency (EQE), and (c) stabilised power output of the best-performing device fabricated with an annealed perovskite active layer spin-cast from a 1: 9 precursor ink.

6.3.3.2 Stability of ink and devices

To examine the stability of our annealing-free devices, we have periodically recorded J - V characteristics of devices stored in a glovebox, under N₂ and in the dark. All J - V measurements were conducted in air. This stability testing protocol is, however, not a rigorous test. Accelerated aging tests involving maximum power point tracking, light soaking, and environmental stressors are far more representative of the “in-deployment” stability of PSCs. Here, a simplified stress-test was applied to remove the influence of external stressors and instead investigate the intrinsic chemical stability of the annealing-free perovskite thin-films.

Figure 6.17(a) shows the mean \pm minimum/maximum of device PCEs for 16 cells (including both forward and reverse J - V sweep) as a function of storage time. We observe a slight increase in the mean PCE of the devices as they age. Indeed, after 15 days, we observe a 1 % absolute increase in the mean value of device PCE. This spontaneous

enhancement of the performance of the dark-stored PCE has previously been attributed to a reduction in trap-assisted non-radiative recombination, likely caused by a reduction in film strain.^[63] We have applied a linear regression model ($y = 15.23 - 0.007 * x$) to determine whether the shelf-age of the devices can be used to predict the device performance upon retesting. The model results indicate that shelf-age of the device was not a significant predictor of device performance, with the slope coefficient not significantly different from zero ($F(1, 156), p = 0.177, R^2 = 0.012$). This 9-week shelf-life of devices indicates a promising level of intrinsic stability. From this, we infer that annealing-free films are not likely to contain residual, trapped solvent which would be expected to induce intrinsic instability by slowly corroding or otherwise degrading the perovskite thin films. We note, however, that the application of vacuum during the electrode deposition steps is likely to remove trapped solvents.

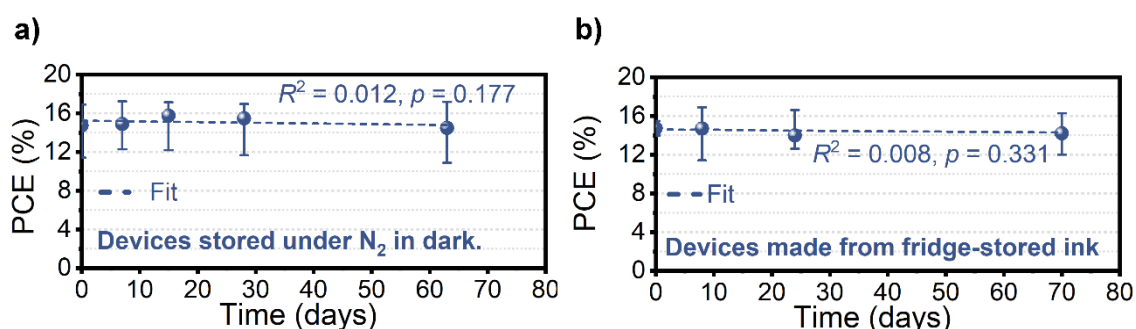


Figure 6.17: (a) The PCE of devices containing an annealing-free perovskite absorber layer stored in a glovebox in the dark and retested periodically over two months. (b) The PCE of cells periodically fabricated from the 1: 9 ink stored in the fridge.

It is important that any perovskite precursor inks should demonstrate a high degree of intrinsic stability, as this will make them compatible with a practical manufacturing process. We have previously demonstrated that storing precursor inks at low-temperature can extend their shelf life, however solvent choice is known to have a significant impact on solution stability.^[64] We therefore investigated the shelf-life of the 1: 9 THF: 2-ME MAPbI₃ precursor ink when stored at low temperature ($\sim 4^\circ\text{C}$). To do this, devices were periodically fabricated from a single batch of a fridge-stored ink. **Figure 6.17(b)** shows the resulting device PCEs over a period of 10 weeks ink storage-time, plotted as the mean \pm minimum/maximum device PCE for both the forward and reverse *J-V* sweep of at least 16 cells per time point. Again, a linear regression was used to test whether the ink age (storage time) significantly predicted the resultant device PCE. The

fitted regression model was ($y = 14.5 - 0.005 * x$) and the slope was again not significantly significant from zero ($F(1, 118), p = 0.331, R^2 = 0.008$). We therefore found no statistical difference in the device PCEs over this storage timeframe. This negligible deterioration demonstrates excellent solution stability for the THF: 2-ME mixture containing MAPbI₃ precursor materials.



Previous work has shown that methylamine – either introduced directly as a precursor solvent^[65] or formed via degradation of methylammonium – accelerates the degradation of formamidinium (FA)-containing perovskite precursor inks. Here, the methylamine participates in a series of addition-elimination reactions, forming further secondary reaction products which result in the formation of non-perovskite polytype phases in the resultant perovskite thin-film.^[66] Here, we avoid the use of methylamine as a solvent. We therefore speculate that a THF: 2-ME binary solvent system is also likely to have a high degree of stability when used with FA-based perovskite precursors.







6.3.3.3 Fully annealing-free fabrication of perovskite solar cells

To make a fully annealing-free PSC, the charge transporting layers must also be fabricated without annealing steps in a high-speed R2R process. To date, there are very few demonstrations of annealing-free perovskite layers combined with annealing-free transport layers. Many reports use ZnO, TiO₂ or SnO₂ ETLs which require high temperature sintering steps. UV-ozone treatments can be used to replace the annealing of SnO₂.^[20] but such treatments can take upwards of 30 minutes, thus eliminating any benefit to manufacturing throughput. Notably, Jiang et al. fabricated an Nb₂O₅-TiO₂ ETL at room temperature but this required the application of a time-consuming 15-minute UV-ozone treatment prior to deposition of the perovskite.^[19] Such methods also required the use of anti-solvent treatments to fabricate the annealing-free perovskite layer. The HTL poly(3,4-ethylenedioxythiophene) polystyrene sulfonate (PEDOT: PSS) can be deposited without any requirement for thermal annealing, however, it is known to be hygroscopic and typically needs annealing treatments to remove residual water to prevent device instability.^[67] Wang et al. successfully created fully annealing-free PSCs having efficiencies of up to 16.40% using a room temperature dried PEDOT: PSS HTL.^[68] We note, however, that the 60-minute water vapor annealing treatment used is incompatible with a high

speed R2R process. In 2015, Su et al. developed HTL-free, annealing-free PSCs by thermal evaporation, demonstrating PCEs of up to 8.37%.^[12] In 2016, Zhao et al. thermally deposited fully annealing-free PSCs having efficiencies of up to 15.7% (14.6% stabilized).^[13]

To create fully annealing-free PSCs, we have investigated the performance of devices based on the HTL MeO-2PACz without the application of a heating treatment. Although annealing of self-assembled molecules after deposition is a ubiquitous process – and is expected to strengthen the bonding between the SAM and the underlying substrate^[69] – we demonstrate that sufficient binding occurs spontaneously during deposition of MeO-2PACz to create efficient PSCs without the necessity of annealing. In our experiments, we spin coat the MeO-2PACz and 1: 9 MAPbI₃ precursor as described above, without using an annealing step for either layer (see **Figure 6.13(c)** for schematic). Again, devices were completed with a thermally evaporated C₆₀/BCP/Ag cathode to realize fully annealing-free cells. In **Figure 6.18(a)** we show boxplots that compare such fully annealing-free devices against devices with an annealed MeO-2PACz HTL and an unannealed MAPbI₃ active layer. Notably, we find very little statistically significant difference between such devices. For completeness, **Table 6.1** summarizes the performance of devices made from the three combinations of annealed/unannealed MeO-2PACz and MAPbI₃ layers that are discussed above.

Table 6.1: A summary of PSC performance metrics (including both forward and reverse J-V sweeps) for all devices presented in this work. Bold font data represents the champion performance metric, with median \pm standard deviation values presented in parentheses.  is annealed,  is unannealed.

MeO-2PACz	MAPbI ₃	J_{sc} (mA cm ⁻²)	V_{oc} (V)	FF (%)	PCE (%)	n_{cells}
		(21.1 \pm 0.8) 22.4	(1.06 \pm 0.03) 1.08	(75.3 \pm 6.2) 80.3	(15.9 \pm 1.7) 18.0	24
		(19.4 \pm 1.2) 21.2	(1.05 \pm 0.05) 1.11	(72.5 \pm 4.7) 78.0	(14.9 \pm 1.9) 17.5	62
		(19.2 \pm 0.5) 20.4	(1.08 \pm 0.05) 1.09	(72.4 \pm 5.6) 76.6	(14.8 \pm 1.6) 16.6	16

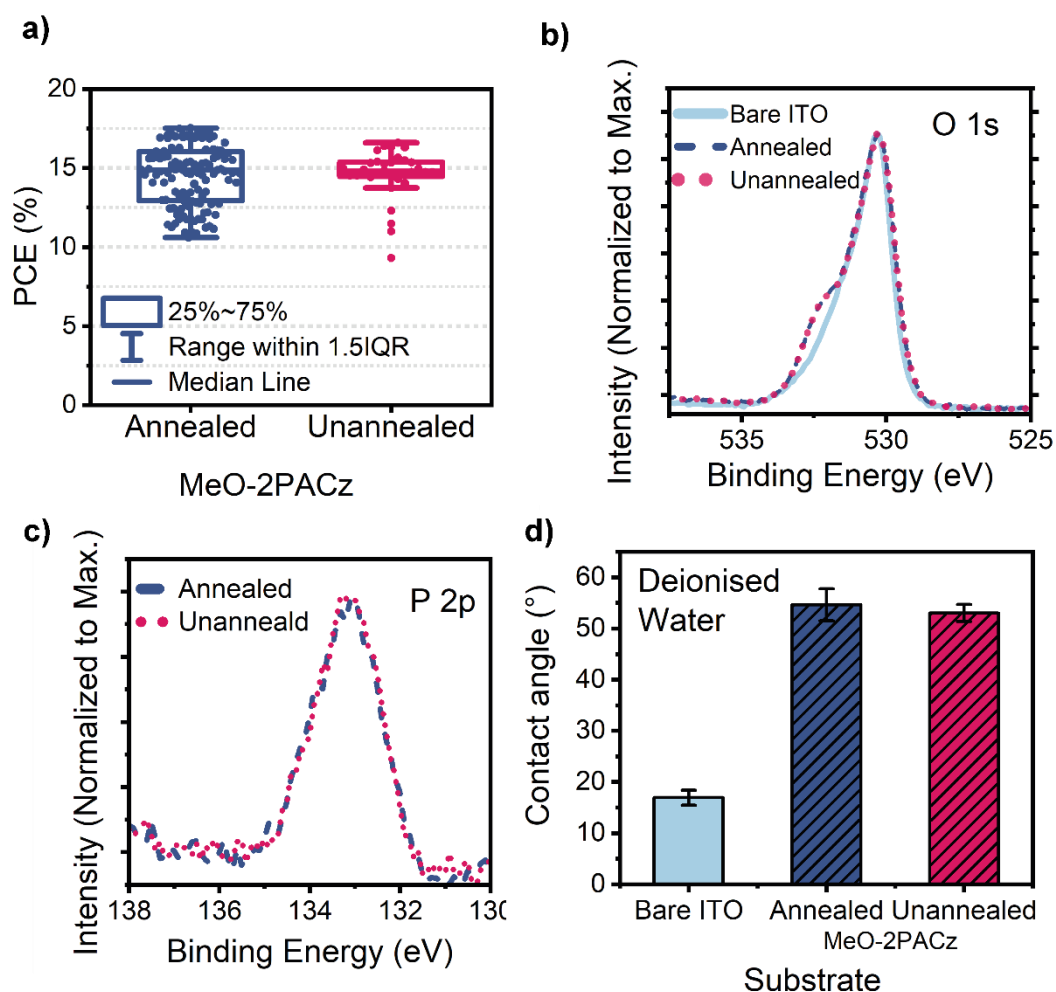


Figure 6.18: (a) A boxplot comparing the PCE of devices containing an annealing-free perovskite absorber layer with an annealed MeO-2PACz hole-transporting layer (blue) and an unannealed MeO-2PACz hole-transporting layer (green). High-resolution X-ray photoelectron spectroscopy (XPS) spectra of the (b) O 1s and (c) P 2p regions of bare ITO-coated glass (light blue, solid), ITO with spin-coated and annealed MeO-2PACz (dark blue, dashed), and ITO with spin-coated, unannealed MeO-2PACz (green, dotted). (d) The contact angle of a water droplet on bare ITO-coated glass (light blue), an annealed MeO-2PACz film (dark blue), and an unannealed MeO-2PACz film (green).

To further explore the quality of the unannealed MeO-2PACz layer, we conducted X-ray photoelectron spectroscopy (XPS) analysis to compare the surface chemistry of annealed and unannealed MeO-2PACz layers (**Figure 6.18(b-c)**). Here, we recorded high-resolution O 1s and P 2p spectra in order to investigate the binding of the phosphonic acid tail group to the ITO substrate, as demonstrated previously.^[70] This phosphonic acid group contains three oxygen atoms capable of covalently binding to ITO surface oxides, with a large number of different binding modes available.^[71] Typically, an annealing treatment has been used to promote such covalent binding. Whilst we find that there is a clear difference in the O 1s spectra between the bare ITO-coated glass substrate and the

MeO-2PACz coated samples, there is no difference in either the O 1s or P 2p environments of the MeO-2PACz as a consequence of the annealing treatment. Similarly, we find no significant difference in the contact angle of a water droplet on the surface of the annealed vs. unannealed MeO-2PACz ($54.6 \pm 3.1^\circ$ vs. $53.0 \pm 1.7^\circ$, respectively, see **Figure 6.18(d)**).

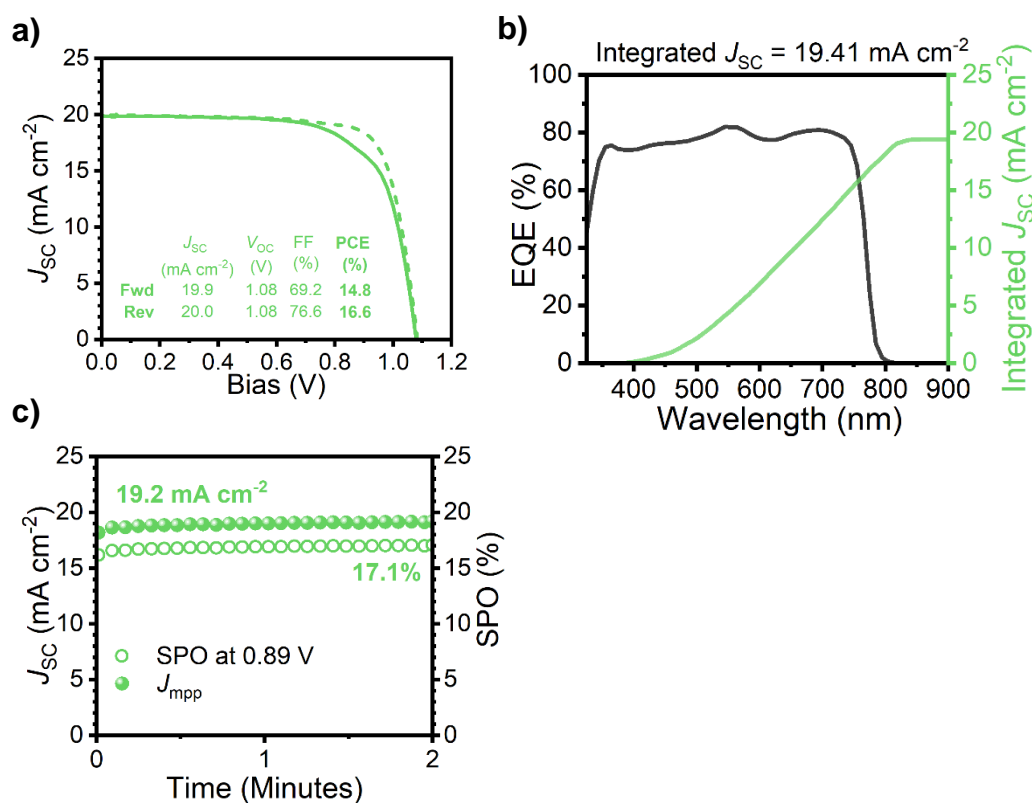


Figure 6.19: (a) J - V curve, (b) external quantum efficiency (EQE), and (c) stabilised power output of the best-performing fully annealing free device.

We therefore find that annealing the deposited MeO-2PACz layer is not necessary for the formation of a high-quality hole-transporting layer. Using this approach, we have fabricated fully annealing-free PSCs with a champion stabilized efficiency of 17.1% (**Figure S6.19** (a)-(c)), with little statistically significant variation in comparison to PSCs with an annealed MeO-2PACz HTL (anneal-free MAPbI₃). Again, the J_{SC-JV} matches well with the calculated J_{SC-EQE} . To our knowledge, this represents the highest performance demonstrated for a PSC fabricated without any annealing treatments in a fully R2R compatible manner. We compare our work to other fully annealing-free approaches as discussed above in **Figure 6.20**.

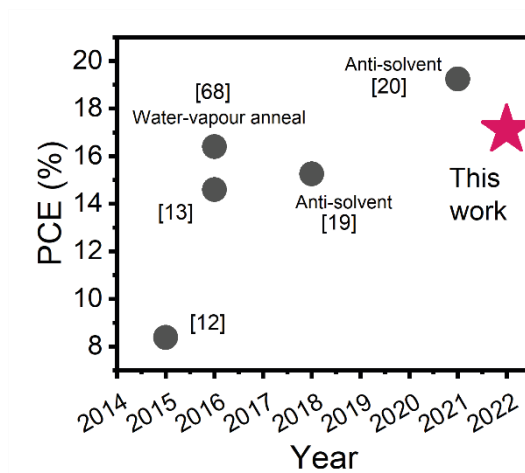


Figure 6.20: A comparison of reported device power conversion efficiencies (PCEs) in the literature for fully annealing-free fabrication of perovskite solar cells. The annotations indicate the use of processing steps with limited scalability.

Finally, we recently reported the use of gas-quenching to fabricate spray-coated MAPbI₃ perovskite films, and the spray deposition of MeO-2PACz as an HTL.^[39] We believe that the binary solvent precursor ink explored here will be a promising candidate to spray coat the perovskite without the necessity of annealing. Previously, our attempts to spray coat ACN-based precursors have been unsuccessful due to the higher vapor pressure of ACN (88.8 mm Hg at 25 °C) leading to the premature evaporation of the precursor droplets before reaching the substrate surface. Here, the 1: 9 THF: 2-ME ink is expected to have a sufficiently low vapor pressure to allow it to be spray-deposited *and* undergo room temperature removal of the casting solvents. We believe that spray coating fully annealing free devices would have direct commercial relevance as a route to extremely high-throughput R2R fabrication of PSCs.

6.3.4 Conclusions

We have developed a novel two-component solvent system combining THF and 2-ME to fabricate crystalline MAPbI₃ thin-films at room temperature following simple gas-jet-induced evaporation of the casting solvents. Without the THF, the pure 2-ME precursor inks form discontinuous perovskite films characterized by a large number of pinholes. By adding THF to the 2-ME, we are able to modify the vapor pressure of the binary system. This results in a lower degree of solvent coordination to the lead centers, a finding in agreement with theoretical predictions. The THF component therefore accelerates the solvent removal during the “gas-quench”. This results in a greater degree of nucleation with a dense and uniform film created having a smaller average grain size with respect to the pure 2-ME composition. We find however that if too much THF is incorporated, a rapid, top-down evaporation process occurs, resulting in a solidified top layer with a series of voids formed throughout the underlying film. At the optimized composition of 10 vol % THF, however, we tune the evaporation rate to obtain uniform, pinhole-free perovskite films. Using this approach, we fabricate *p-i-n* PSCs incorporating an annealing-free perovskite layer and demonstrate stabilized device efficiencies up to 18.0%. These PCEs are completely comparable to those demonstrated in devices incorporating annealed perovskite films, underpinning the practicality of our approach.

Finally, we removed the annealing step typically employed during the deposition of self-assembled monolayer molecules as HTLs. We observed only a small loss in device performance when forgoing the MeO-2PACz annealing process. By combining an anneal-free MeO-2PACz film with an anneal-free 1: 9 THF: 2-ME perovskite layer, we created devices having stabilized PCEs of up to 17.1%. This is the highest device performance demonstrated so far for a fully annealing-free PSC that is completely compatible with a high-speed, high-volume R2R process.

In summary this work demonstrates a facile route to fabricate efficient PSCs without any lengthy annealing steps to process either the charge transporting layers or the perovskite itself. The binary solvent precursor ink demonstrates good storage stability and is identified as an ideal candidate for rapid spray deposition. These results therefore represent a promising route for low-cost, high-speed, and high-volume industrial production of PSCs.

6.3.6 Acknowledgements

This work was partly funded by the Engineering and Physical Sciences Research Council (EPSRC) grants EP/S009213/1 (The integration of photovoltaic devices with carbon-fiber composites) and EP/V027131/1 (High-efficiency flexible and scalable halide-perovskite solar modules). E.J.C. and E.L.K.S. thank the EPSRC for a PhD studentship from the Centre for Doctoral Training in New and Sustainable PV, (EP/L01551X/1). T.T. thanks the faculty of Science, University of Sheffield for a studentship. M.E. O’K. thanks the EPSRC for a PhD studentship from the Centre for Doctoral Training in Polymers and Colloids (EP/L016281/1). The XPS instrument belongs to the Sheffield Surface Analysis Centre, a facility led by Professor Graham Leggett and run from the Department of Chemistry at the University of Sheffield. We acknowledge Diamond Light Source for time on beamline I07 under proposal SI30612-1 for the GIWAXS measurements and thank Dr. Hadeel Hussain and Dr. Rachel Kilbride for assistance with measurements, and Dr. Daniel Toolan and Karl-Augustin Zaininger for use of the *in situ* blade coater during these experiments.

6.3.7 Conflicts of Interest

D.G. Lidzey is co-founder and Chairman of materials science company Ossila that retails products for research and development of optoelectronic devices, including perovskite solar cells. C.J. Wood is an employee of Power Roll Ltd. who are developing solar cell devices based on perovskites. H. J. Snaith is co-founder and CSO of Oxford PV Ltd.

6.3.8 References

- [1] NREL, “Best Research Cell Efficiencies,” can be found under <https://www.nrel.gov/pv/cell-efficiency.html>, **2022**.
- [2] Y. Deng, E. Peng, Y. Shao, Z. Xiao, Q. Dong, J. Huang, / *Energy Environ. Sci* **2015**, *8*, 1544.
- [3] K. Hwang, Y.-S. S. Jung, Y.-J. J. Heo, F. H. Scholes, S. E. Watkins, J. Subbiah, D. J. Jones, D.-Y. Y. Kim, D. Vak, *Adv. Mater.* **2015**, *27*, 1241.
- [4] A. T. Barrows, A. J. Pearson, C. K. Kwak, A. D. F. Dunbar, A. R. Buckley, D. G. Lidzey, *Energy Environ. Sci.* **2014**, *7*, 2944.
- [5] N. Rolston, W. J. Scheideler, A. C. Flick, J. P. Chen, H. Elmaraghi, A. Sleugh, O. Zhao,

- M. Woodhouse, R. H. Dauskardt, *Joule* **2020**, *4*, 2675.
- [6] F. Hilt, M. Q. Hovish, N. Rolston, K. Brü, C. J. Tassone, R. H. Dauskardt, *2102 | Energy Environ. Sci* **2018**, *11*, 2102.
- [7] K. Bruening, B. Dou, J. Simonaitis, Y. Y. Lin, M. F. A. M. van Hest, C. J. Tassone, *Joule* **2018**, *2*, 2464.
- [8] Z. Song, C. L. McElvany, A. B. Phillips, I. Celik, P. W. Krantz, S. C. Waththage, G. K. Liyanage, D. Apul, M. J. Heben, *Energy Environ. Sci.* **2017**, *10*, 1297.
- [9] J. Panidi, D. G. Georgiadou, T. Schoetz, T. Prodromakis, *Adv. Funct. Mater.* **2022**, 2200694.
- [10] C. Polyzoidis, K. Rogdakis, E. Kymakis, *Adv. Energy Mater.* **2021**, *11*, 2101854.
- [11] I. Mathews, S. Sofia, E. Ma, J. Jean, H. S. Laine, S. C. Siah, T. Buonassisi, I. M. Peters, *Joule* **2020**, *4*, 822.
- [12] Z. Su, F. Hou, F. Jin, L. Wang, Y. Li, J. Zhu, B. Chu, W. Li, *Org. Electron.* **2015**, *26*, 104.
- [13] D. Zhao, W. Ke, C. R. Grice, A. J. Cimaroli, X. Tan, M. Yang, R. W. Collins, H. Zhang, K. Zhu, Y. Yan, *Nano Energy* **2016**, *19*, 88.
- [14] F. Zhou, H. Liu, X. Wang, W. Shen, *Adv. Funct. Mater.* **2017**, *27*, 1606156.
- [15] X. Zheng, B. Chen, C. Wu, S. Priya, *Nano Energy* **2015**, *17*, 269.
- [16] M. Yin, F. Xie, H. Chen, X. Yang, F. Ye, E. Bi, Y. Wu, M. Cai, L. Han, *J. Mater. Chem. A* **2016**, *4*, 8548.
- [17] X. Fang, Y. Wu, Y. Lu, Y. Sun, S. Zhang, J. Zhang, W. Zhang, N. Yuan, J. Ding, *J. Mater. Chem. C* **2017**, *5*, 842.
- [18] M. M. Byranvand, S. Song, L. Pyeon, G. Kang, G.-Y. Lee, T. Park, *Nano Energy* **2017**, *34*, 181.
- [19] J. Jiang, S. Wang, X. Jia, X. Fang, S. Zhang, J. Zhang, W. Liu, J. Ding, N. Yuan, *RSC Adv.* **2018**, *8*, 12823.
- [20] H. Dong, S. Pang, F. He, H. Yang, W. Zhu, D. Chen, H. Xi, J. Zhang, Y. Hao, C. Zhang, *Sol. RRL* **2021**, *5*, 2100097.
- [21] C. Dong, J. Chen, C.-H. Chen, Y.-R. Shi, W.-F. Yang, K.-L. Wang, Z.-K. Wang, L.-S. Liao, *Nano Energy* **2022**, *94*, 106866.
- [22] M.-R. Ahmadian-Yazdi, M. Eslamian, *Mater. Today Commun.* **2018**, *14*, 151.
- [23] X. Zhang, F. Zabihi, H. Xiong, M. Eslamian, C. Hou, M. Zhu, H. Wang, Q. Zhang, *Chem. Eng. J.* **2020**, *394*, 124887.

- [24] H. Xiong, F. Zabihi, H. Wang, Q. Zhang, M. Eslamian, *Nanoscale* **2018**, *10*, 8526.
- [25] B. Yang, O. Dyck, J. Poplawsky, J. Keum, S. Das, A. Puretzky, T. Aytug, P. C. Joshi, C. M. Rouleau, G. Duscher, D. B. Geohegan, K. Xiao, *Angew. Chemie Int. Ed.* **2015**, *54*, 14862.
- [26] A. Dubey, N. Kantack, N. Adhikari, K. M. Reza, S. Venkatesan, M. Kumar, D. Khatiwada, S. Darling, Q. Qiao, *J. Mater. Chem. A* **2016**, *4*, 10231.
- [27] C. Wu, K. Wang, J. Li, Z. Liang, J. Li, W. Li, L. Zhao, B. Chi, S. Wang, *Matter* **2021**, *4*, 775.
- [28] G. S. Shin, W.-G. Choi, S. Na, S. O. Ryu, T. Moon, *Electron. Mater. Lett.* **2017**, *13*, 72.
- [29] Z. Wang, X. Zhu, J. Feng, C. Wang, C. Zhang, X. Ren, S. Priya, S. (Frank) Liu, D. Yang, *Adv. Sci.* **2021**, *8*, 2002860.
- [30] K. Wang, C. Wu, Y. Hou, D. Yang, T. Ye, J. Yoon, M. Sanghadasa, S. Priya, *Energy Environ. Sci.* **2020**, *13*, 3412.
- [31] Q. Liu, Y. Zhao, Y. Ma, X. Sun, W. Ge, Z. Fang, H. Bai, Q. Tian, B. Fan, T. Zhang, *J. Mater. Chem. A* **2019**, *7*, 18275.
- [32] G. Wang, L. Liao, L. Chen, C. Xu, Y. Yao, D. Liu, P. Li, J. Deng, Q. Song, *Org. Electron.* **2020**, *86*, 105918.
- [33] K. H. Hendriks, J. J. van Franeker, B. J. Bruijnaers, J. A. Anta, M. M. Wienk, R. A. J. Janssen, *J. Mater. Chem. A* **2017**, *5*, 2346.
- [34] Y. Deng, C. H. Van Brackle, X. Dai, J. Zhao, B. Chen, J. Huang, *Sci. Adv.* **2019**, *5*, eaax7537.
- [35] S. Chen, X. Dai, S. Xu, H. Jiao, L. Zhao, J. Huang, *Science (80-.)*. **2021**, *373*, 902.
- [36] D.-K. Lee, D.-N. Jeong, T. K. Ahn, N.-G. Park, *ACS Energy Lett.* **2019**, *4*, 2393.
- [37] J. W. Yoo, J. Jang, U. Kim, Y. Lee, S.-G. Ji, E. Noh, S. Hong, M. Choi, S. Il Seok, *Joule* **2021**, *5*, 2420.
- [38] J. Li, J. Dagar, O. Shargaieva, M. A. Flatken, H. Köbler, M. Fenske, C. Schultz, B. Stegemann, J. Just, D. M. Többens, A. Abate, R. Munir, E. Unger, *Adv. Energy Mater.* **2021**, *11*, 2003460.
- [39] E. J. Cassella, E. L. K. Spooner, T. Thornber, M. E. O’Kane, T. E. Catley, J. E. Bishop, J. A. Smith, O. S. Game, D. G. Lidzey, *Adv. Sci.* **2022**, *9*, 2104848.
- [40] F.-M. Raoult, *J. Phys. Théorique Appliquée* **1889**, *8*, 5.
- [41] G. C. Fonger, *Toxicology* **1995**, *103*, 137.
- [42] G. C. Fonger, P. Hakkinen, S. Jordan, S. Publicker, *Toxicology* **2014**, *325*, 209.

- [43] H. Zhang, K. Darabi, N. Y. Nia, A. Krishna, P. Ahlawat, B. Guo, M. H. S. Almalki, T. Sen Su, D. Ren, V. Bolnykh, L. A. Castriotta, M. Zendejdel, L. Pan, S. S. Alonso, R. Li, S. M. Zakeeruddin, A. Hagfeldt, U. Rothlisberger, A. Di Carlo, A. Amassian, M. Grätzel, *Nat. Commun.* **2022**, *13*, 1.
- [44] S. Rahimnejad, A. Kovalenko, S. M. Forés, C. Aranda, A. Guerrero, *ChemPhysChem* **2016**, 2795.
- [45] O. Shargaieva, H. Näsström, J. A. Smith, D. Többens, R. Munir, E. Unger, *Mater. Adv.* **2020**, *1*, 3314.
- [46] J. C. Hamill, J. Schwartz, Y.-L. Loo, *ACS Energy Lett.* **2018**, *3*, 92.
- [47] G. Gritzner, S. Sperker, *J. Solution Chem.* **1988**, *17*, 1133.
- [48] K. W. Lau, M. H. H. Aron, M. H. J. Yen, E. Y. Fung, S. Grzybicki, R. Matamoros, J. C. Curtis, *Inorganica Chim. Acta* **1994**, *226*, 137.
- [49] A. S. Tutantsev, N. N. Udalova, S. A. Fateev, A. A. Petrov, W. Chengyuan, E. G. Maksimov, E. A. Goodilin, A. B. Tarasov, *J. Phys. Chem. C* **2020**, *124*, 11117.
- [50] C. M. Hansen, *Hansen Solubility Parameters*, CRC Press, **2007**.
- [51] A. Sharenko, C. Mackeen, L. Jewell, F. Bridges, M. F. Toney, **2017**, DOI 10.1021/acs.chemmater.6b04917.
- [52] J. Kim, B. Park, J. Baek, J. S. Yun, H.-W. Kwon, J. Seidel, H. Min, S. Coelho, S. Lim, S. Huang, K. Gaus, M. A. Green, T. J. Shin, A. W. Y. Ho-baillie, M. G. Kim, S. Il Seok, *J. Am. Chem. Soc.* **2020**, *142*, 6251.
- [53] A. Al-Ashouri, A. Magomedov, M. Roß, M. Jošt, M. Talaikis, G. Chistiakova, T. Bertram, J. A. Márquez, E. Köhnen, E. Kasparavičius, S. Levenco, L. Gil-Escrig, C. J. Hages, R. Schlatmann, B. Rech, T. Malinauskas, T. Unold, C. A. Kaufmann, L. Korte, G. Niaura, V. Getautis, S. Albrecht, *Energy Environ. Sci.* **2019**, *12*, 3356.
- [54] Y. Yu, F. Zhang, T. Hou, X. Sun, H. Yu, M. Zhang, *Sol. RRL* **2021**, 2100386.
- [55] O. Almora, D. Baran, G. C. Bazan, C. Berger, C. I. Cabrera, K. R. Catchpole, S. Erten-Ela, F. Guo, J. Hauch, A. W. Y. Ho-Baillie, T. J. Jacobsson, R. A. J. Janssen, T. Kirchartz, N. Kopidakis, Y. Li, M. A. Loi, R. R. Lunt, X. Mathew, M. D. McGehee, J. Min, D. B. Mitzi, M. K. Nazeeruddin, J. Nelson, A. F. Nogueira, U. W. Paetzold, N. Park, B. P. Rand, U. Rau, H. J. Snaith, E. Unger, L. Vaillant-Roca, H. Yip, C. J. Brabec, *Adv. Energy Mater.* **2021**, *11*, 2002774.
- [56] T. Baikie, Y. Fang, J. M. Kadro, M. Schreyer, F. Wei, S. G. Mhaisalkar, M. Graetzel, T. J.

- White, *J. Mater. Chem. A* **2013**, *1*, 5628.
- [57] P. Scherrer, *Nachrichten von der Gesellschaft der Wissenschaften zu Göttingen, Math. Klasse* **1918**, *2*, 98.
- [58] A. S. Thind, X. Huang, J. Sun, R. Mishra, *Chem. Mater.* **2017**, *29*, 6003.
- [59] J. Cao, X. Jing, J. Yan, C. Hu, R. Chen, J. Yin, J. Li, N. Zheng, *J. Am. Chem. Soc.* **2016**, *138*, 9919.
- [60] A. A. Petrov, I. P. Sokolova, N. A. Belich, G. S. Peters, P. V. Dorovatovskii, Y. V. Zubavichus, V. N. Khrustalev, A. V. Petrov, M. Grätzel, E. A. Goodilin, A. B. Tarasov, *J. Phys. Chem. C* **2017**, *121*, 20739.
- [61] T. Su, X. Li, Y. Zhang, F. Zhang, Z. Sheng, *Phys. Chem. Chem. Phys.* **2017**, *19*, 13147.
- [62] L. Tian, W. Zhang, Y. Huang, F. Wen, H. Yu, Y. Li, Q. Wang, C. Peng, Z. Ma, T. Hu, L. Du, M. Zhang, *ACS Appl. Mater. Interfaces* **2020**, *12*, acsami.0c06558.
- [63] S. Moghadamzadeh, I. M. Hossain, M. Jakoby, B. Abdollahi Nejjand, D. Rueda-Delgado, J. A. Schwenzer, S. Gharibzadeh, T. Abzieher, M. R. Khan, A. A. Haghighirad, I. A. Howard, B. S. Richards, U. Lemmer, U. W. Paetzold, *J. Mater. Chem. A* **2020**, *8*, 670.
- [64] M. E. O’Kane, J. A. Smith, T. I. Alanazi, E. J. Cassella, O. Game, S. van Meurs, D. G. Lidzey, *ChemSusChem* **2021**, *14*, 2537.
- [65] N. K. Noel, S. N. Habisreutinger, B. Wenger, M. T. Klug, M. T. Hörantner, M. B. Johnston, R. J. Nicholas, D. T. Moore, H. J. Snaith, *Energy Environ. Sci.* **2017**, *10*, 145.
- [66] X. Wang, Y. Fan, L. Wang, C. Chen, Z. Li, R. Liu, H. Meng, Z. Shao, X. Du, H. Zhang, G. Cui, S. Pang, *Chem* **2020**, *6*, 1369.
- [67] C. Bracher, B. G. Freestone, D. K. Mohamad, J. A. Smith, D. G. Lidzey, *Energy Sci. Eng.* **2018**, *6*, 35.
- [68] B. Wang, Z. G. Zhang, S. Ye, H. Rao, Z. Bian, C. Huang, Y. Li, *J. Mater. Chem. A* **2016**, *4*, 17267.
- [69] F. Ali, C. Roldán-Carmona, M. Sohail, M. K. Nazeeruddin, *Adv. Energy Mater.* **2020**, *10*, 2002989.
- [70] P. B. Paramonov, S. A. Paniagua, P. J. Hotchkiss, S. C. Jones, N. R. Armstrong, S. R. Marder, J.-L. Brédas, *Chem. Mater.* **2008**, *20*, 5131.
- [71] P. J. Hotchkiss, S. C. Jones, S. A. Paniagua, A. Sharma, B. Kippelen, N. R. Armstrong, S. R. Marder, *Acc. Chem. Res.* **2012**, *45*, 337.

[72] G. Ashiotis, A. Deschildre, Z. Nawaz, J. P. Wright, D. Karkoulis, F. E. Picca, J. Kieffer, *J. Appl. Crystallogr.* 2015, *48*, 510.

Chapter 4 Conclusions and Further Work

Chapter 4 targeted the development of three key new for spray-coated PSCs. Firstly, the deposition and rinsing processes for spray-coated carbazole-based self-assembled molecule (SAM) were developed and optimized. Within the wider community, such SAMs have become an extremely promising material for charge-transport within PSCs. These materials hold the promise of combining low-costs, stability, versatility, and efficiency. Chapter 4 corroborates the versatility of MeO-2PACz, demonstrating no loss in PCE of devices incorporating a spray-coated MeO-2PACz layer versus a spin-coated MeO-2PACz layer. Secondly, a gas-assisted spray processing (GASP) route was developed. Here, an “air-knife” moved over the substrate surface induces crystallisation of the perovskite film by encouraging evaporation of the casting solvent. This process improves upon other typical “one-step” crystallisation techniques for spray-coated PSCs, such as anti-solvent bathing and vacuum-flash assisted processing routes, which are inherently limited to batch processing, rather than roll-to-roll. Finally, the perovskite layer is cast from a 2-methoxyethanol solvent system: the increased volatility of the solution vs. ubiquitous DMF: DMSO-based precursor solutions is expected to facilitate faster deposition and fabrication speeds. Combining these three technologies, we create devices having state-of-the-art power conversion efficiencies of up to 20.8%.

Improvements and Future work:

- **Investigate a “spray-rinsing” approach.** Within this work, the spray-coated SAM is dip rinsed. Whilst this approach could be upscaled, it would consume large volumes of solvent and pose logistical issues. Instead, an approach which combines the spray deposition of the rinsing solvent along with its air bladed removal should be explored.
- **Explore non-toxic solvents.** Clearly, solvent toxicity is a critical factor for commercial production of PSCs. The workplace exposure limit of 2-methoxy ethanol is insufficient for an industrial process (only 1 ppm over an 8-hour time-

weighted average exposure time, versus 10 ppm for DMF.) Future work should, therefore, focus on “green” solvent alternatives that combine both sufficient Workplace Exposure Limits (WELs) and facilitate surface-wetting onto the SAM charge-transporting layers. A promising candidate would be an ethanol : DMSO-based precursor.^[1]

- **Explore methods to alleviate surface-wetting issues associated with the SAMs.** Alternatively, the surface-wetting issues associated with the SAMs could be alleviated *via* other routes than solvent-engineering. Recently, Al-Ashouri et al. have reported the use of a secondary SAM component to the hole-transporting layer solution.^[2] The secondary component contains phosphonic acid groups at the ‘head’ of the chemical structure, this increasing the surface energy of the coated substrate and thereby alleviating the wettability issues. More recently, Zheng et al. have shown that the carbazole-based SAMs can be incorporated directly into the perovskite precursor solution.^[3] Using this approach, the SAMs still self-assemble onto the underlying substrate during perovskite film processing. Both of these approaches should be explored to spray-deposit a SAM hole-transporting layer with sufficient wettability to enable subsequent deposition of perovskite thin-films from a broader range of precursor solvent systems. This would broaden the number of non-toxic solvents available to be explored.
- **Explore the spray-deposition of SAMs over large areas.** The SAMs are an extremely promising hole-transporting material, however, they must now be explored in larger area cells. Some groups have reportedly encountered coverage problems when upscaling the carbazole-based SAMs.^[4] Here, the exploration of “seed” layers to encourage the conformality of the SAM coverage could be investigated. Some promising results have been reported for NiO_x seed layers.^[5]

Whilst high-performing devices were realised in Chapter 4, MAPbI₃ is only a “fruit fly” of the perovskite field. Therefore, in Chapter 5, the GASP protocol was applied to a methylammonium-free perovskite composition, creating devices having highly comparable efficiencies to spin-coated reference cells. Such MA-free compositions are expected to confer enhanced device stability under thermal stress, due to the exclusion of thermally unstable MA molecules. However, these compositions suffer from a high

degree of crystalline defects. This necessitates the exploration of passivation strategies to achieve comparable device efficiencies as MA-containing perovskites. To this end, a spray-coated, surface passivating, post-treatment was developed. Here, an alkyl ammonium-halide molecule, i-BABr, was spray-coated onto the annealed perovskite surface. After a short annealing treatment, the i-BABr formed a 2D perovskite phase at the film surface. The formation of this perovskite phase resulted in an increased photoluminescent efficiency and enhanced device V_{OC} , attributed to the reduction in nonradiative recombination at the interface. Using this process, devices were created having efficiencies of up to 19.8%, analogous to cells with a spin-coated passivation layer. Importantly, the stabilised efficiency of this best-performing cell was 19.4%, representing a significant improvement upon the stabilised efficiency of the unpassivated, spray-coated cell (16.6%).

Improvements and Future work:

- **Explore alternative casting solvents for the passivating treatment.** In order to avoid the deterioration of the underlying perovskite by the polar casting-solvent (isopropanol), future spray-coated, surface passivating treatments should be cast from nonpolar solvents, such as chloroform^[6] or an alternative with a suitable WEL.
- **Incorporate a passivating agent into the bulk perovskite layer.** A number of groups have reported on the synergistic effect of combining bulk and surface passivating treatments. “Dual-passivation” approaches have been shown to have a significantly greater improvement on the perovskite film quality in comparison to either surface- or bulk- passivation alone.^[7,8]
- **Extend the GASP process to other perovskite compositions.** Within this thesis, both MAPbI_3 and a CsFA-based perovskite have been fabricated via spray coating in combination with an air-knife. This gas-assisted spray coating process should now be explored with other perovskite compositions. Specifically, the development of spray-coated narrow- and wide- bandgap perovskite compositions would open avenues of exploration towards spray-coated tandem solar cells. Indeed, the National Renewable Energy Laboratory recently reported the benefits of gas-quenching for preferential texturing of spin-coated wide bandgap perovskites to reduce defect densities in the perovskite thin-film.^[9]

Finally, in Chapter 6, a novel, binary solvent system was developed to deposit highly crystalline, spin-coated MAPbI₃ films under room temperature conditions without an annealing post-deposition treatment. Avoiding the use of lengthy annealing times is highly desirable to maximise the throughput speed of PSC fabrication. By adding tetrahydrofuran to a 2-methoxyethanol precursor ink, the increased volatility coupled with reduced solvent co-ordination facilitated rapid nucleation of the perovskite, induced by a gas-quench. Here, the optimum THF concentration (10 vol %) created uniform, densely packed films of small perovskite grains which realised devices having stabilised efficiencies of up to 18.0%. This value is commensurate with the stabilised efficiencies realised by devices having an annealed perovskite active layer. Revisiting MeO-2PACz (the SAM spray-coated in Chapter 4), it was found that this molecule could form an efficient hole-extracting layer without the necessity for a post-deposition annealing step. Combining both an annealing-free SAM and the volatile THF: 2-ME MAPbI₃ precursor ink, spin-coated, fully annealing free PSCs were created having stabilised efficiencies of up to 17.1%. Considering the work presented in Chapter 4, this device stack is therefore identified as a route towards extremely high-throughput spray-coated PSCs.

Improvements and Future work:

- **Investigate the presence of trapped solvent in the as-cast perovskite thin-films.** It was also noted that vacuum processing steps for the electrode deposition are likely to remove entrapped solvent. In a high-speed, R2R industrial process, the electrode is, however, likely to be printed (rather than evaporated.) It is necessary, therefore, to explore whether solvent is trapped in the as-prepared perovskite thin-films when no vacuum is applied. Nuclear Magnetic Resonance (NMR) studies of the as-cast perovskite film would reveal the presence of remaining solvents.
- **Further stability testing.** To improve upon this work, more comprehensive exploration of the intrinsic stability of annealing-free devices should be explored. These intrinsic factors (independent of any protective encapsulation environment) include light, temperature, and electrical bias. The “Consensus statement for stability assessment and reporting for perovskite photovoltaics” details a number of suitable tests.^[10] In addition, a deeper understanding of the optoelectronic properties of annealing-free PSCs should be explored.

- **Investigate the creation of annealing free devices on flexible (polymeric) substrates.** Such low-temperature processed PSCs are extremely relevant to the field of flexible PV, where thermal tolerance of plastic substrates is a critical consideration. Flexible PSCs, specifically integrated with “Internet of Things” applications, are expected to reduce the barrier cost to market entry of PSCs by up to an order of magnitude.^[11,12] High-speed, roll-to-roll fabrication of annealing-free devices on such plastic substrates is therefore of significant research interest.
- **Develop an annealing-free electron transporting layer, to enable fully spray-coated, annealing free devices.** Although PCBM (Phenyl-C₆₁-butyric acid methyl ester or Phenyl-C₇₀-butyric acid methyl ester) is typically annealed to remove the chlorobenzene casting solvent (b.p. 132 °C), incorporating a volatile solvent, such as chloroform (b.p. 61 °C), could enable annealing-free fabrication of this charge-transporting layer. Zhang et al. recently identified a dual layer of SnO₂ and PCBM as an efficient electron-transporting layer for *p-i-n* PSCs.^[13] We have previously demonstrated spray-coated SnO₂ ETLs,^[14] therefore, this system is an ideal candidate for future exploration of spray-coated ETLs for fully spray-coated *p-i-n* cells.
- **Development of a spray-compatible back electrode.** Thermal evaporation of the back electrode is a significant bottleneck to the manufacturing speed of cells. Moreover, the cost of the incumbent coinage metal electrodes will significantly affect the LCOE of the technology. Alternatives, such as carbon-based electrodes should be explored.^[15,16]

This work has since been the inspiration for a number of other developments within our lab. Notably, the use of an “air-knife” in combination with spray coating (developed in Chapter 4) has now also enabled the fabrication of state-of-the-art spray-coated organic solar cells. We have also applied the GASP deposition of the MA-free perovskite (detailed in Chapter 5) to non-planar substrates, successfully fabricating PSCs over curved surfaces^[17] – one of the unique benefits that spray coating offers.

Revisiting the aims of the thesis (**Section 1.2**), this work has successfully developed five industrially-relevant processing techniques for the fabrication of PSCs. The objectives, and how they have been met, are discussed below.

- **Spray-coated self-assembled monolayers.** This process has been developed in Chapter 4, with the process being fully compatible with R2R coating.
- **Gas-quenching to control the crystallisation of spray-coated perovskite thin-films.** Chapters 4 and 5 demonstrated the broad applicability of using an “air-knife” to facilitate the crystallisation of spray-coated perovskite precursor solutions. The enhanced crystallisation control enabled the creation of state-of-the-art spray-coated PSCs.
- **Solvent-engineering to facilitate surface wetting of spray-coated precursor solutions onto SAMs.** The surface-wetting issues associated with the nonpolar SAMs was overcome by the use of 2-methoxy ethanol-based solvent system to enable spray coating onto MeO-2PACz in Chapter 4.
- **Develop a spray-coated surface-passivating treatment.** This has been achieved in Chapter 5 by spray-deposition of an alkylammonium halide onto the deposited perovskite, demonstrating a clear improvement in the performance metrics of the passivated PSCs.
- **Develop a precursor solution that enables the circumvention of lengthy annealing times of perovskite thin-films.** In Chapter 6, a volatile precursor solution was demonstrated to enable room-temperature crystallisation of MAPbI₃, negating the need for long annealing treatments. This approach will now be explored for R2R-compatible deposition techniques.
- **Consider at all times the “golden triangle” of solar technologies.** The technologies developed within this thesis have significantly advanced the efficiency of spray-coated PSCs. The processes developed are also compatible with high-speed, R2R deposition. The faster the deposition speed, the lower the effective cost of energy, therefore enabling low-cost manufacture. A critical cost-consideration remaining relates to the toxicity of the perovskite precursor solvents used. Also, more comprehensive studies are required to understand the device stability of both spray-coated and annealing-free cells.

Whilst the results presented within this thesis advance the field of spray-coated PSCs, the innovations remain as proof-of-concept, prototype devices. Each technique must now be upscaled to larger active areas. Spray-coated devices are currently lagging behind all other scalable perovskite deposition techniques, in both device active areas and PCEs.^[18] This must be urgently addressed in order to evidence the viability of spray coating for industrial production of PSCs. Considering the complexity of the optimisation parameter space, machine learning techniques could prove an invaluable tool to develop spray-coated PSCs. Sequential machine learning methods work well for optimising problems with multiple variables. Researchers from MIT and Stanford University have now demonstrated a method to incorporate the researchers' domain knowledge within the predictive cycle, accelerating research into open-air processing of PSCs.^[19] Therefore, such machine learning techniques should be explored to accelerate the development of spray-coated PSCs and propel the movement towards commercialisation. Specifically, a focus should be made to integrate spray-coated PSCs into tandem architectures, which are widely accepted as the "closest to market" approach to PSC commercialisation.

This work has significantly advanced the field of PSCs by enhancing the toolkit of techniques available to engineer high-performing devices in a roll-to-roll compatible manner.

References

- [1] H.-S. Yun, H. W. Kwon, M. J. Paik, S. Hong, J. Kim, E. Noh, J. Park, Y. Lee, S. Il Seok, *Nat. Energy* 2022 **2022**, 1.
- [2] A. Al-Ashouri, M. Marčinskas, E. Kasparavičius, T. Malinauskas, A. Palmstrom, V. Getautis, S. Albrecht, M. D. McGehee, A. Magomedov, *ACS Energy Lett.* **2023**, *8*, 898.
- [3] X. Zheng, Z. Li, Y. Zhang, M. Chen, T. Liu, C. Xiao, D. Gao, J. B. Patel, D. Kuciauskas, A. Magomedov, R. A. Scheidt, X. Wang, S. P. Harvey, Z. Dai, C. Zhang, D. Morales, H. Pruetz, B. M. Wieliczka, A. R. Kirmani, N. P. Padture, K. R. Graham, Y. Yan, M. K. Nazeeruddin, M. D. McGehee, Z. Zhu, J. M. Luther, *Nat. Energy* **2023**, DOI 10.1038/s41560-023-01227-6.
- [4] J. Li, J. Dagar, O. Shargaieva, M. A. Flatken, H. Köbler, M. Fenske, C. Schultz, B. Stegemann, J. Just, D. M. Többens, A. Abate, R. Munir, E. Unger, *Adv. Energy Mater.*

2021, *11*, 2003460.

- [5] N. Phung, M. Verheijen, A. Todinova, K. Datta, M. Verhage, A. Al-Ashouri, H. Köbler, X. Li, A. Abate, S. Albrecht, M. Creatore, *ACS Appl. Mater. Interfaces* **2022**, *14*, 2166.
- [6] J. J. Yoo, S. Wiegbold, M. C. Sponseller, M. R. Chua, S. N. Bertram, N. Titan Putri Hartono, J. S. Tresback, E. C. Hansen, J.-P. Correa-Baena, V. Bulovic, T. Buonassisi, S. Sik Shin, M. G. Bawendi, *2192 | Energy Environ. Sci* **2019**, *12*, 2192.
- [7] S. Gharibzadeh, P. Fassel, I. M. Hossain, P. Rohrbeck, M. Frericks, M. Schmidt, T. Duong, M. R. Khan, T. Abzieher, B. A. Nejjand, F. Schackmar, O. Almora, T. Feeney, R. Singh, D. Fuchs, U. Lemmer, J. P. Hofmann, S. A. L. Weber, U. W. Paetzold, *Energy Environ. Sci.* **2021**, *14*, 5875.
- [8] M. Degani, Q. An, M. Albaladejo-Siguan, Y. J. Hofstetter, C. Cho, F. Paulus, G. Grancini, Y. Vaynzof, *Sci. Adv.* **2021**, *7*, 7930.
- [9] Q. Jiang, J. Tong, R. A. Scheidt, X. Wang, A. E. Louks, Y. Xian, R. Tirawat, A. F. Palmstrom, M. P. Hautzinger, S. P. Harvey, S. Johnston, L. T. Schelhas, B. W. Larson, E. L. Warren, M. C. Beard, J. J. Berry, Y. Yan, K. Zhu, *Science (80-.)*. **2022**, *378*, 1295.
- [10] M. V Khenkin, E. A. Katz, A. Abate, G. Bardizza, J. J. Berry, C. Brabec, F. Brunetti, V. Bulović, Q. Burlingame, A. Di Carlo, R. Cheacharoen, Y.-B. Cheng, A. Colsmann, S. Cros, K. Domanski, M. Dusza, C. J. Fell, S. R. Forrest, Y. Galagan, D. Di Girolamo, M. Grätzel, A. Hagfeldt, E. Hauff, H. Hoppe, J. Kettle, H. Köbler, M. S. Leite, S. Liu, Y.-L. Loo, J. M. Luther, C.-Q. Ma, M. Madsen, M. Manceau, M. Matheron, M. McGehee, R. Meitzner, M. Khaja Nazeeruddin, A. Flavia Nogueira, Ç. Odabaşı, A. Osherov, N.-G. Park, M. O. Reese, F. De Rossi, M. Saliba, U. S. Schubert, H. J. Snaith, S. D. Stranks, W. Tress, P. A. Troshin, V. Turkovic, S. Veenstra, I. Visoly-Fisher, A. Walsh, T. Watson, H. Xie, R. Yıldırım, S. Mohammed Zakeeruddin, K. Zhu, M. Lira-Cantu, *Nat. Energy* **n.d.**, DOI 10.1038/s41560-019-0529-5.
- [11] B. Parida, A. Singh, A. K. Kalathil Soopy, S. Sangaraju, M. Sundaray, S. Mishra, S. (Frank) Liu, A. Najar, *Adv. Sci.* **2022**, *9*, 2200308.
- [12] C. Polyzoidis, K. Rogdakis, E. Kymakis, *Adv. Energy Mater.* **2021**, *11*, 2101854.
- [13] J. Zhang, J. Mcgettrick, K. Ji, J. Bi, T. Webb, X. Liu, D. Liu, A. Ren, Y. Xiang, B. Li, V. Stolojan, T. Watson, S. D. Stranks, W. Zhang, *ENERGY Environ. Mater.* **2023**, *1*.
- [14] J. E. Bishop, C. D. Read, J. A. Smith, T. J. Routledge, D. G. Lidzey, *Sci. Rep.* **2020**, *10*, 6610.

- [15] L. J. Sutherland, D. Vak, M. Gao, T. A. N. Peiris, J. Jasieniak, G. P. Simon, H. Weerasinghe, *Adv. Energy Mater.* **2022**, *12*, 2202142.
- [16] D. Beynon, E. Parvazian, K. Hooper, J. Mcgettrick, R. Patidar, T. Dunlop, Z. Wei, P. Davies, R. Garcia-Rodriguez, M. Carnie, M. Davies, T. Watson, D. Beynon, E. Parvazian, K. Hooper, J. Mcgettrick, R. Patidar, T. Dunlop, Z. Wei, M. Carnie, M. Davies, T. Watson, P. Davies, R. Garcia-Rodriguez, *Adv. Mater.* **2023**, 2208561.
- [17] T. Thornber, O. S. Game, E. J. Cassella, M. E. O’Kane, J. E. Bishop, T. J. Routledge, T. I. Alanazi, M. Togay, P. J. M. Isherwood, L. C. Infante-Ortega, D. B. Hammond, J. M. Walls, D. G. Lidzey, *ACS Appl. Mater. Interfaces* **2022**, *14*, 37587.
- [18] F. Wang, Y. Han, D. Duan, C. Ge, H. Hu, G. Li, *Energy Rev.* **2022**, *1*, 100010.
- [19] Z. Liu, N. Rolston, A. C. Flick, T. W. Colburn, Z. Ren, R. H. Dauskardt, T. Buonassisi, *Joule* **2022**, *6*, 834.